Total Cross-Sections for the $(\gamma, \pi^+\pi^-)$ process on ^{2}H and ^{12}C from 550–1105 MeV

A Thesis
Submitted to the Faculty of Graduate Studies and Research
In Partial Fulfillment of the Requirements
for the Degree of
Doctor of Philosophy
in Physics
University of Regina

by
Akihisa Shinozaki
Regina, Saskachewan
June, 2002

Abstract

This thesis presents data analysis and results of the $(\gamma, \pi^+\pi^-)$ experiment with graphite and deuterized polyethylene targets. The first part of the thesis describes the experiment and the data calibration. A detailed description of the pion momentum reconstruction by a drift chamber system is presented. An assessment of the detector performance is then provided. The evaluated performance is adopted by a Monte Carlo simulation so that an unbiased comparison between the data and the simulation may be possible. The latter half of the thesis describes the physical interpretation of the experimental data. The total cross sections for various reaction processes are presented by fitting the data with the simulation. The photon energy is largely below the ρ^0 production threshold and this is the first time an experiment of this kind has been performed on complex nuclei. The present analysis seems to be consistent with a nuclear matter model of the ρ^0 meson. The polarization of the ρ^0 meson is also investigated.

Acknowledgments

I am deeply thankful to my supervisors Dr. G. J. Lolos and Dr. G. M. Huber and to Dr. Z. Papandreou for their superior suggestions, ideas, understanding, and patience. They proofread and surveyed every part of this work for my errors. I also wish to acknowledge their financial support from their NSERC grants as well as for the Teaching Assistantships provided by the Department of Physics throughout this thesis preparation.

I am immensely grateful to the Faculty of Graduate Studies and Research for the Graduate Scholarship and Teaching Assistantships from 1998 to 2001. I also owe them a debt of gratitude for awarding me the Gerhard Herzberg Fellowship in 1998.

I gratefully acknowledge the financial support from Spencer Middleton & Jack Spencer Gordon Middleton Scholarship in 1997. I also would like to express my deep gratitude for HUGS at CEBAF '98 Summer Program.

I would like to thank all members of the TAGX collaboration, the INS-ES staff, and the fellow graduate students for their warm and invaluable assistance. INS-ES also financially supported the ES144 experiment.

Contents

List of Tables

List of Figures

Chapter 1

Introduction

In The Standard Model, the strong interactions are described by quantum chromodynamics (QCD). In QCD, the strong force is carried by gluons and acts on the color-charged particles, which are quarks and gluons. There are six quark flavors currently known to exist and each has very different mass (the "current mass"). Two flavors of quarks, namely, up and down, are very light (1–10 MeV/c^2 [1]) and chiral symmetry is a very good approximation toward the solution of the dynamical systems. The strength of the strong force is characterized by the coupling constant, α_s. It changes with the space-time distance ("running coupling constant") of the interaction. Equivalently, it is expressed in terms of the four-momentum transfer Q of a probed process by [2]

$$\alpha_s(Q) = \frac{\alpha_s(\Lambda)}{1 + \frac{33-2n_f}{6\pi}\alpha_s(\Lambda)\log\left(\frac{Q}{\Lambda}\right)},$$

where n_f is the number of quark flavors. The parameter Λ can take any value of Q but fixes $\alpha_s(\Lambda)$ by experimental measurements. Since the particle data gives [1]

$$\alpha_s(M_Z) = 0.1185, \quad (M_Z = 91.19 \text{ GeV}),$$

one finds that α_s is infinitely large at $Q \simeq 48$ MeV and gradually decreases as Q increases. Up to $Q \simeq 280$ MeV, which can be translated to a distance of $1/Q \simeq 0.7$ fm, α_s is over 0.5. In this relatively low energy or large distance region, the perturbative approach to the QCD problem breaks down. Physically, the quarks and gluons are confined inside colorless hadrons and the light quarks are condensed ($\langle 0|\bar{q}q|0\rangle \neq 0$). Because of the quark condensate, each quark acquires the effective mass (~310 MeV/c^2 [3]) much larger than its own current mass and the "very accurate" chiral symmetry is spontaneously broken. This implies a phase boundary between the "hot and dense" quark-gluon plasma and the "frozen state" of hadrons.

Topics regarding the structure of the phase boundary have received significant attention in the past decades. Most notably, Brown and Rho have theorized the so-called Brown-Rho scaling law which predicts that vector meson masses in the normal nuclear medium are roughly 20% smaller than those in vacuum [4]. The scaling law is based on the effective Lagrangian, which incorporates the QCD principles that the chiral symmetry is partially restored and the scale invariance does not hold under the nuclear medium environment. Subsequently, a similar result was arrived at by Hatsuda and Lee based on QCD sum rules [5]. There are a number of experimental results which seem to be consistent with these predictions at least qualitatively. The CERES collaboration has reported that the dilepton mass spectra, $m_{e^+e^-}$, from the Pb-Au collisions at CERN-SPS, seem to have an enhancement in the region 0.3–0.7 GeV/c^2 [6]. This is commonly believed to be a consequence of the mass modification of the ρ and ω mesons, both of which have the decay channel $\rho/\omega \to e^+e^-$. In interpreting K^+-^{12}C scattering data, Brown *et al.* proposed the mass modification of the ρ and ω [7]. The experiment KEK-PS E325 also measured the mass of the electron-positron pair from the p-A collisions and found that Cu target has pronounced mass in the region in 0.3–0.7 GeV/c^2 as compared to a CH$_2$ target in the $m_{e^+e^-}$ spectra[8]. The most direct evidence so far for modifications, however, may be the TAGX experiment which measured the ^{3}He$(\gamma, \pi^+\pi^-)X$ reaction [9, 10]. It is claimed that from the direct observation of $\rho^0 \to \pi^+\pi^-$ from the dipion spectra, the in-medium ρ^0 invariant mass peak is as small as 640 MeV/c^2. In the mean time, theoretical developments have also made remarkable progress. Rather than relying on QCD principles, the complete hadronic description of the ρ in-medium mass spectral function has been derived by Peters *et al* [11]. Rapp and Wambach have summarized extensive theoretical models on the QCD phase transition which may explain data from the heavy iron collisions experiment [12].

It is hoped that the present analysis of the $(\gamma, \pi^+\pi^-)$ experiment with the graphite and deuterized polyethylene (CD$_2$) targets will be able to contribute to this novel aspect of nuclear physics. The experiment was originally proposed to the Institute of Nuclear Study Electron Synchrotron PAC by G. M. Huber and Z. Papandreou as spokesmen of the TAGX collaboration and it was accepted as the ES144. Since the ^{3}He$(\gamma, \pi^+\pi^-)X$ experiment had been already carried out as ES134, the experiment was primarily intended to chart the ρ^0 in-medium mass versus nuclear density. Particularly, the ^{12}C data provide a direct observation of the $\rho^0 \to \pi^+\pi^-$ decay in normal nuclear density, because the photon energy (1 GeV) lies in the sub-threshold region of photo production so that 80% of the photo-produced ρ^0 decays take place inside the carbon nucleus [13]. However, the $(\gamma, \pi^+\pi^-)$ measurement on a complex nucleus below the ρ^0 threshold region ($E_{\gamma th}$ = 1086 MeV) is a novel experiment and the experimental data themselves should be interesting. Below threshold, the ρ^0 production is certainly a rare process and most reaction strength is associated with $\Delta\pi$ production or double-Δ excitation. It is, therefore, very important to identify the various processes as unambiguously as possible. The technique for this procedure is an important part of this thesis. There is common criticism to the interpretation of our collaboration's earlier $^3\text{He}(\gamma, \pi^+\pi^-)X$ experiment because the photon energy is below threshold and one cannot be certain if the result is free from the limited phase space. This work aims to clarify this issue in the course of this thesis.

The organization of this thesis is the following: In Chapter 2, the experimental procedure, the data calibration, the detector analysis, and the data selection are presented. The experimental procedure deals with the TAGX spectrometer, the photon tagging system, and the data acquisition. In the calibration, a number of procedures to reconstruct the momentum of a charged particles by the drift chamber system are presented. In fact, the straw drift chamber was specially installed for the ρ^0 experiments (ES134 and ES144) so that the momentum resolution would be improved. The improvement of the momentum resolution certainly provides an improved resolution for the dipion invariant mass, one of the most important ingredients to identify ρ^0 events. The performances of the other detector parts are also evaluated. At the end of the chapter, data are selected by applying cuts to create the carbon and deuteron spectra. Chapter 3 describes the TAGX Monte Carlo simulation. Its foundation includes a comprehensive description of the detector system. The previously evaluated TAGX performance is embedded in the simulation. The most important part is the creation of the $\gamma A \to \pi^+\pi^- X$ reaction. Various theoretical ideas, experimental data, and the present techniques for the analysis are discussed there. The total cross sections for various processes are given in Chapter 4, derived by fitting the data distributions with the Monte Carlo simulations. There, the physical interpretations for the results as well as the fitting procedure are offered. The Thesis is summarized in Chapter 5.

Chapter 2

Experiment and Data Calibration

The experimental facilities consist of the high-energy electron synchrotron, a spectrometer with several kinds of particle detectors, and an online data acquisition system. Extensive off-line data analysis of the detectors and apparatus was performed after the completion of the experiment. The analysis aims to extract the most important variables for the reaction cross sections.

2.1 The $^{12}C/^{2}D(\gamma,\pi^+\pi^-)$ Experiment

The $^{12}C/^{2}D(\gamma,\pi^+\pi^-)$ experiment was carried out using the 1.3-GeV Electron Synchrotron in the Institute of Nuclear Study at Tokyo. Graphite and deuterized polyethylene, CD_2, were used to investigate carbon and deuteron nuclei. The photon energy throughout the experiment was 550–1100 MeV.

As shown in Fig.2.1, the electron beam from the synchrotron is steered to the photon tagging system. The tagged photon beam enters the TAGX spectrometer. Simultaneous detection of two charged particles in the TAGX spectrometer constitute an event trigger, which records data from the entire TAGX detector system as well as photon flux information and synchrotron energy. This section describes each element of the experimental apparatus.

2.1.1 Photon Tagging System and Photon Flux

The electron beam was extracted from the electron synchrotron when the beam energy had reached its maximum value in the synchrotron acceleration cycle. The duration of the extraction was 5–10 ms and the synchrotron repetition rate was 21.5 Hz, resulting

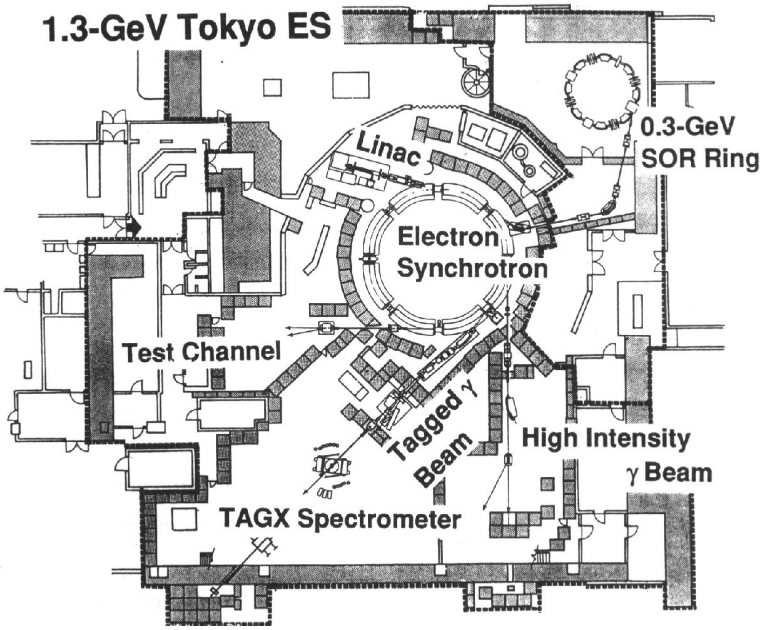

Figure 2.1: Layout of Electron Synchrotron at the Institute of Nuclear Study. Drawing is from Ref.[14].

in a duty factor of 10–20%, which is defined as the ratio of time that beam is available over total time the accelerator is on.

During the extraction period, the photon energy changed with time sinusoidally by ~10% [15], therefore the extraction time was recorded in order to obtain the actual electron energy. This was done by the energy tag module (ETM) which determined the actual electron energy from the beam peak energy and the trigger timing.

The extracted electron beam was transported to the photon tagging system shown in Fig.2.2. The main components of the system were the radiator (Pt, 100 μm), the tagging dipole magnet (11.7 kG), and a two-plane tagging array of scintillation counters. The high energy electron radiated a photon at the radiator and was then swept by the dipole magnet to a corresponding focal point of its trajectory on a plane of scintillation counters called the tagging counter plane. Each tagging counter lay at the focal point for every 10 MeV/c interval and the 32 tagging counter array covers the range of 95–405 MeV/c scattered electron momentum. The second tagging plane is comprised of eight tagging counters ("backing counters") and its coincidence signal with the front plane was used to minimize the accidental background. Once the synchrotron energy is

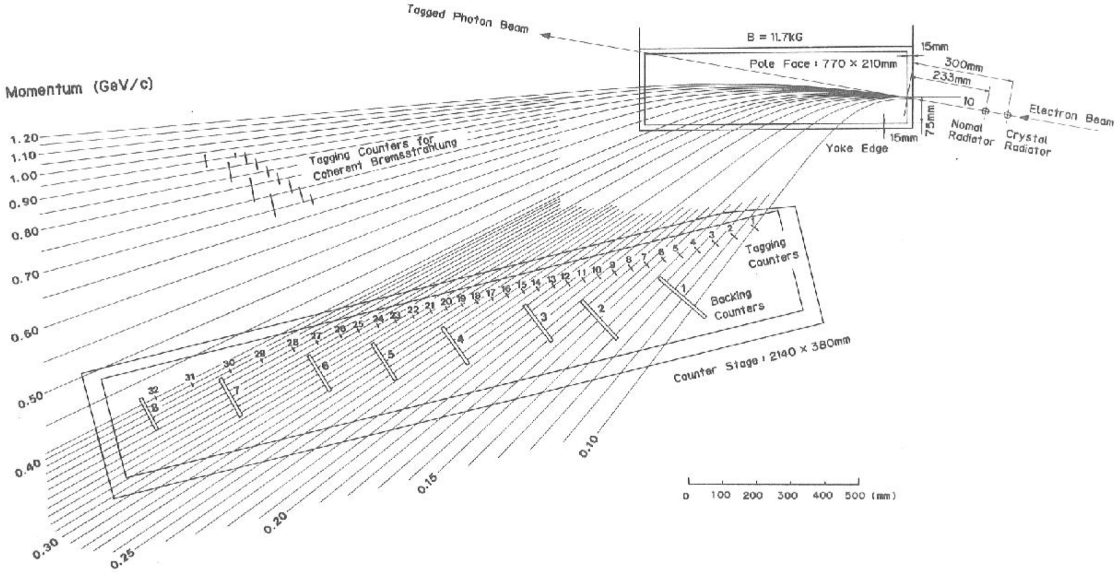

Figure 2.2: The INS photon tagging system. Electron trajectories are placed at the focal points for each trajectory. Drawing is from Ref.[15].

determined by the ETM ($E_e(t)$) and the hit tagging counter is identified (tag#=i), the tagged photon energy is given by*:

$$E_\gamma = E_e(t) - \Delta E - E_{\mathrm{tag}}(i), \quad E_{\mathrm{tag}}(i) = 10i + 90 \text{ [MeV]}.$$

ΔE is a sum of energy losses of the electron beam. One such loss originates from the beam extraction from the synchrotron and the other from the radiator of the tagging system. When $E_e = 1.2$ GeV, $\Delta E \simeq 5.95 + 0.24 = 6.2$ MeV [15].

However, the number of tagged photons is not the same as the number of tagging counter hits because not all the photons arrive at the target due to the collimation of the photon beam. The correction can be made by measuring the ratio of number of arriving photons to the number of hits in the tagging counter, which is called the tagging efficiency. In order to measure the tagging efficiency, one had to replace the target with a lead glass Čerenkov counter, which had a high (~100%) photon detection efficiency and could also count individual photons at low beam intensities. This was done regularly or whenever it was believed the experimental conditions had changed.

---

*Throughout this thesis, E_γ indicates the photon energy in the laboratory frame.

The actual tagging efficiency is given by:

$$\eta_i = \frac{M_{\rm in}(i) - M_{\rm out}(i) - M'_{\rm out}(i)}{N_{\rm in}(i) - N_{\rm out}(i)},$$

where $M(i)$ indicates the number of coincident hits between the Čerenkov counter and i'th tagging counter and $N(i)$ is the number of i'th tagging counter hits. Subscripts "in" and "out" denote whether or not the radiator is inserted in the path of the beam. M' is the number of accidental coincidences. Typically, η_i = 80–90%. The actual number of counter hits and the efficiency are shown in Appendix A. There was a significant background that could trigger the tagging counters even without the radiator. So, the off/on ratios $R_i = N_{\rm out}(i)/N_{\rm in}(i)$ were also measured frequently. Their values were less than a few %. The number of tagged photons is given by:

$$N_\gamma = \sum_i N_{\rm in}(i)(1 - R_i)\eta_i.$$

Because there were three experiments performed at different top ES energies, namely, E_e(top) = 1.040, 1.180, and 1.200 MeV, the resulting photon spectrum has a shape as shown in Fig.2.3.

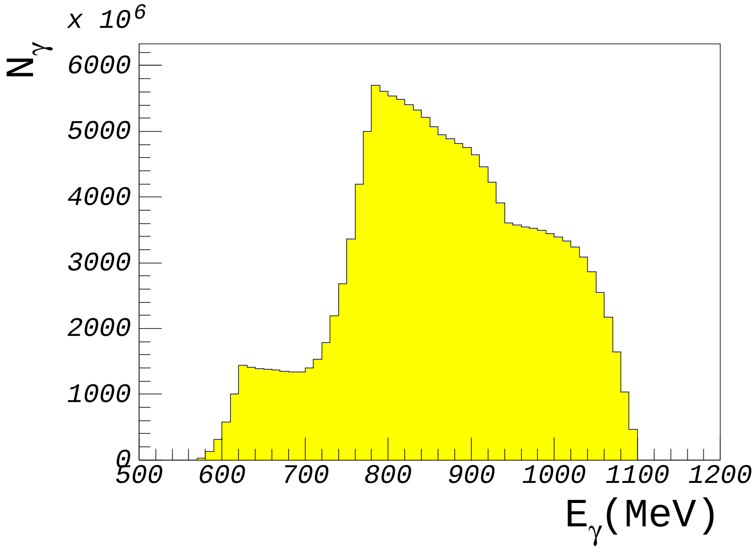

Figure 2.3: Tagged photon spectrum for this experiment. The photon spectra with three different ES energies (1.040, 1.180, and 1.200 MeV) are combined in this figure.

2.1.2 TAGX Spectrometer and Target

Fig.2.4 shows the top view of the TAGX Spectrometer. The TAGX Spectrometer con-

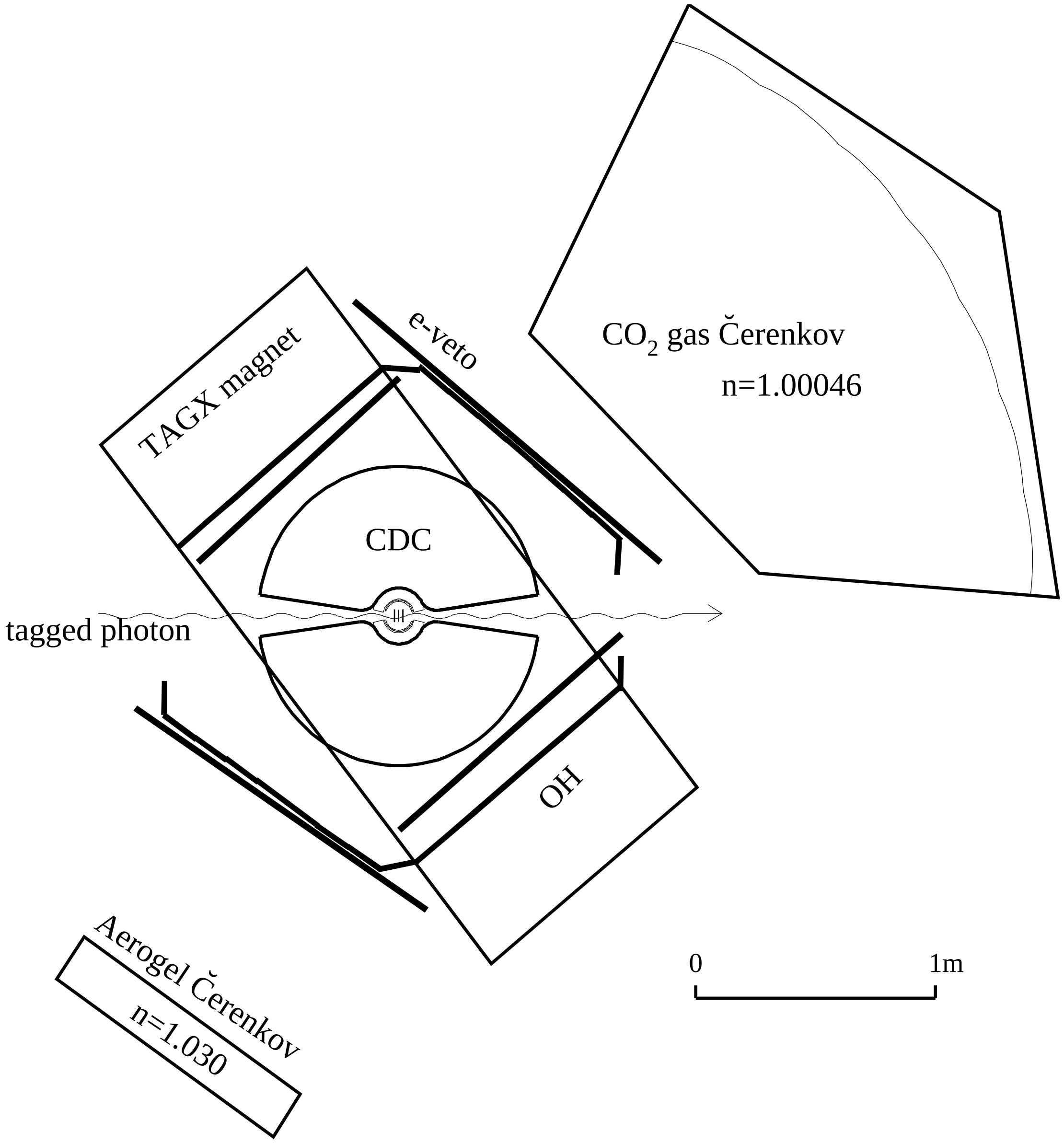

Figure 2.4: Top view of all TAGX spectrometer elements.

sisted of the dipole magnet, the Inner Hodoscope (IH), the Outer Hodoscope (OH), the Cylindrical Drift Chamber (CDC), the Straw Drift Chamber (SDC), and the electron veto counter (e-veto). In addition to them, the beam veto counters and the Aerogel and CO_2 gas Čerenkov counters were set up for this experiment. The target lay at the center of the magnetic field. The spectrometer covered the target center with a solid angle of approximately π sr. Most of the detectors were symmetric about the vertical plane that contained the beam axis. Detector parts which lay in the right or left with respect to the beam direction were labeled accordingly. Each component is described as follows:

Magnet The TAGX magnet had a 60 cm vertical gap and the maximum field strength was nearly 6 kG near the target center. The magnetic field had been mapped for input to the trajectory tracking algorithm [29].

IH The Inner Hodoscopes consisted of twelve scintillation counters, six in each side. Six paddles covered 15–160 degrees and were located 6.1 cm from the target center (see Fig.2.5). The IH and OH defined the trigger and the time of flight.

OH The Outer Hodoscopes assembled an outer array of plastic scintillation counters as shown in Fig.2.6. It consisted of 33 paddles, 17 on the right and 16 on the left. They were located 80–100 cm from the center and covered 10–170 degrees on each side. Each scintillator extended 59 cm vertically. There were two PMTs mounted on each OH at the top and the bottom so that the vertical particle position might be found from their timing difference.

CDC The CDC contained a number of drift cells. The chamber was filled with argon-ethane gas mixture. Each drift cell consisted of six grounded (cathode) wires placed at the corners of a hexagon and a sense (anode) wire at the center. An array of drift cells composed a layer. There were twelve layers radially arranged as shown in Fig.2.5, but only nine were used for the readout. The first and ninth layers lay at 13.8 cm and 50.7 cm from the center, respectively, and covered approximately 10–170 degrees. There were a total of 636 sense wires to be read out from the CDC. The CDC was designed to measure the planar momentum and position of charged particles.

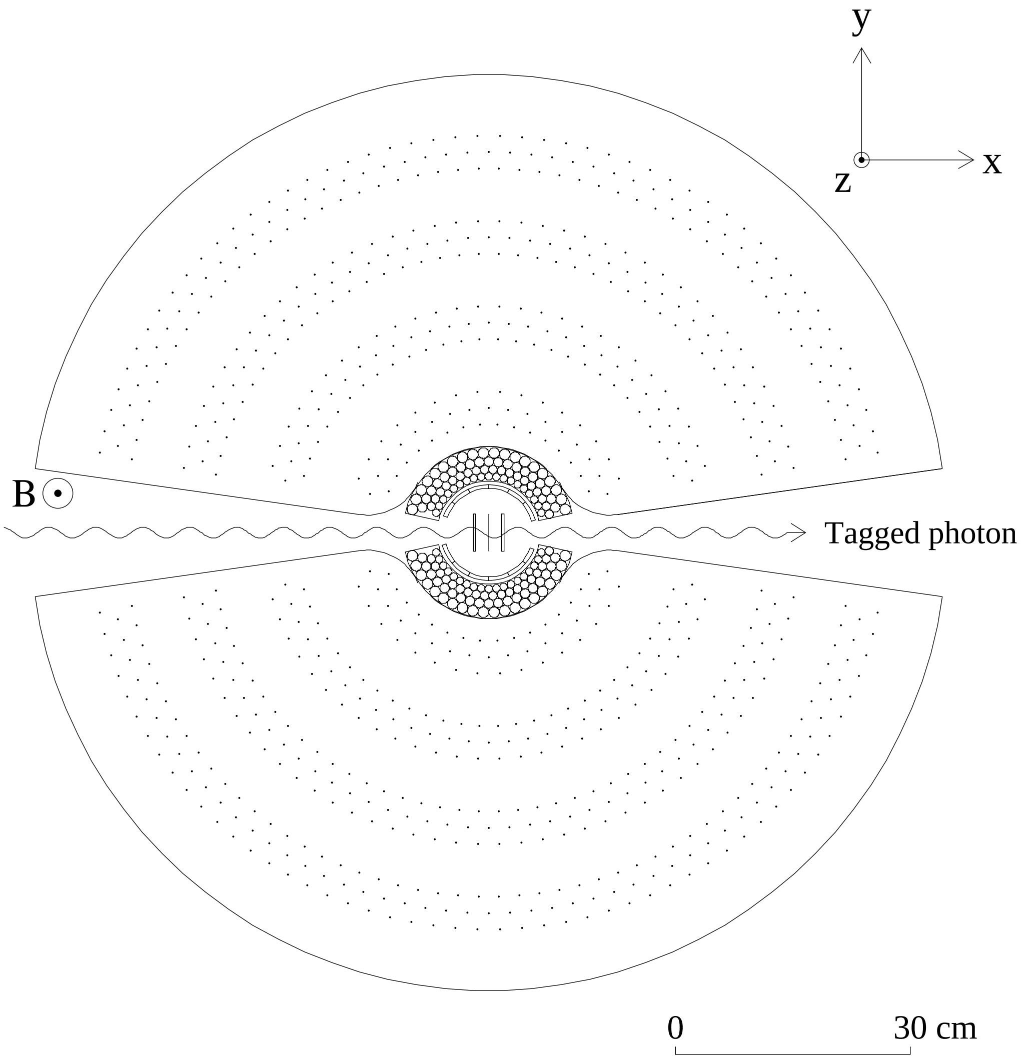

Figure 2.5: The top view of the TAGX spectrometer at the target proximity. The CDC has 12 layers of drift cells. Each point represents a sense wire. The SDC consists of four layers of the straw tubes. Circles represent the tubes. The IH comprises of 12 paddles made out of plastic scintillator. The target materials are at the center. The TAGX coordinate (see sec.2.2.1) is presented at the upper right corner.

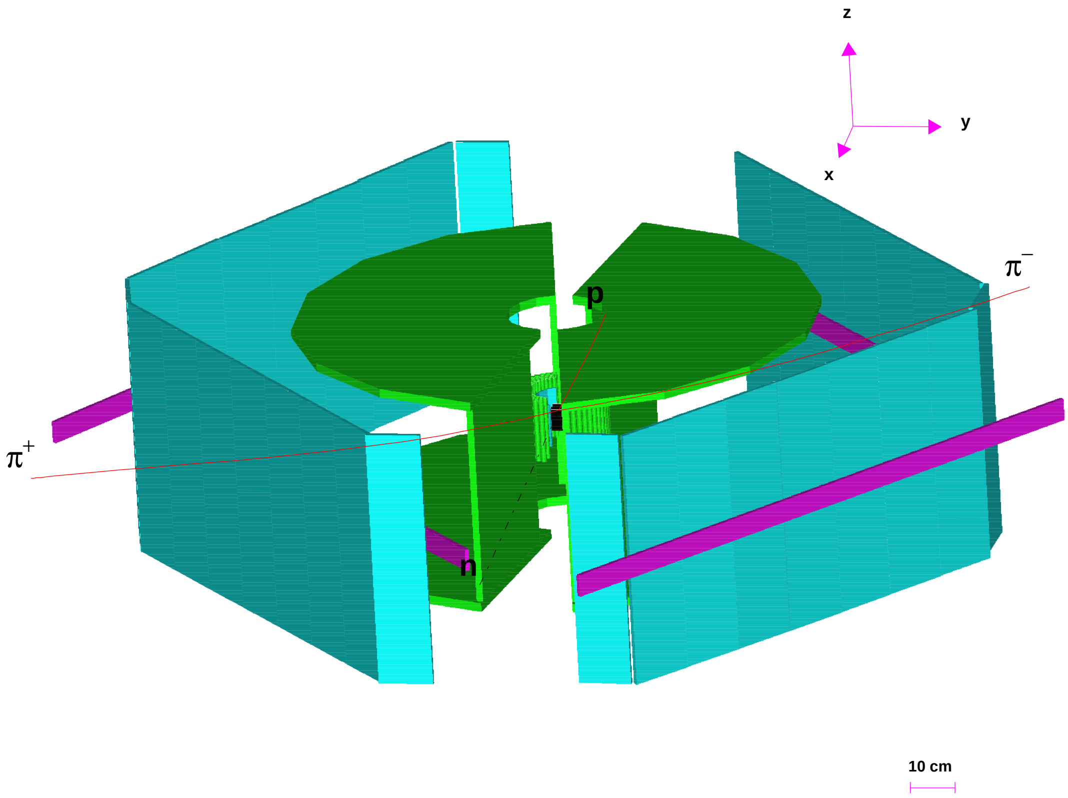

Figure 2.6: The TAGX spectrometer drawn by GEANT. From inside, target materials, the IH, the SDC straws, the CDC end-plates, the OH, and the e-veto are drawn. The TAGX coordinate (see sec.2.2.1) is presented at the upper right corner. The photon beam coincides with the x-axis. The Čerenkov detectors and beam veto counters are not drawn.

SDC A single cell of the SDC consisted of a cylindrical straw tube which was grounded and filled with argon-ethane gas and a sense wire at the center of the tube. The SDC comprised four layers of straws with radius of 0.48–0.68 cm (see also Fig.2.5). Each layer in each side had 19 or 20 straws. The first and fourth layers' sense wires were 7.2 cm and 10.2 cm from the target center, respectively, and covered approximately 20–160 degrees. The SDC was designed to improve upon the CDC track reconstruction measurements.

e-veto There were four e-veto paddles, two in each side. One of them covered 10–90 degrees (forward) and the other 90–170 degrees (backward) and both lay just behind or in front of the OH paddles (see Fig.2.6). Their vertical dimension was 5 cm, and therefore covered only ±2.5 cm from the medium plane. The e-veto counters were to reduce the EM background (i.e. electron and positron) at the trigger level. The forward e-veto counters had been found to be the most effective of all veto counters.

Aerogel Čerenkov Fig.2.7 illustrates the aerogel Čerenkov counter. It was also located along the medium plane but further back from the target. The aerogel was 9 cm thick and 12 cm in height. The index of refraction was 1.030. The pion threshold for producing the Čerenkov light was 570 MeV/c, which was above the pion momentum of this experiment in this backward scattering angle region. The produced Čerenkov light was reflected by the mirror behind the aerogel and directed into one of eight PMTs. Their ADC and TDC data were recorded to be analyzed later.

CO_2 gas Čerenkov A schematic side view of the pressurized CO_2 Čerenkov counter is illustrated in Fig.2.8. It was positioned behind the OH paddles (see Fig.2.4). The Čerenkov window was 60 cm high. There were seven spherical-parabolic concave mirrors inside the gas container. Each of them is focused on the medium plane and on the corresponding PMT mounted at the top of the container. Pressure of the CO_2 gas was approximately 1.2 atm and its index of refraction was 1.00046, resulting in an electron threshold of 17 MeV/c. Its ADC and TDC data were recorded for off-line analysis.

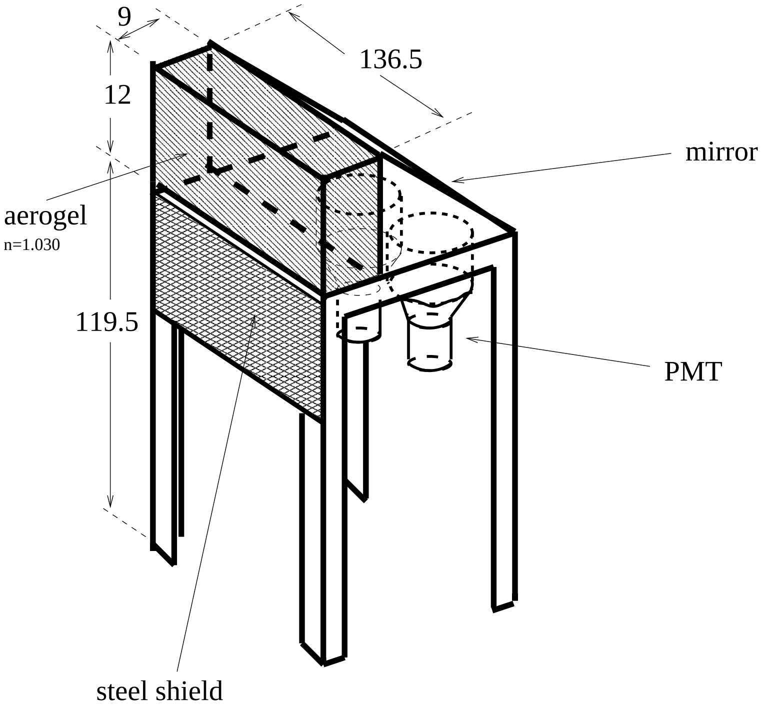

Figure 2.7: Schematic view of the aerogel Čerenkov counter used for this experiment. Only two PMTs out of eight are drown in this figure. Dimensions are in cm.

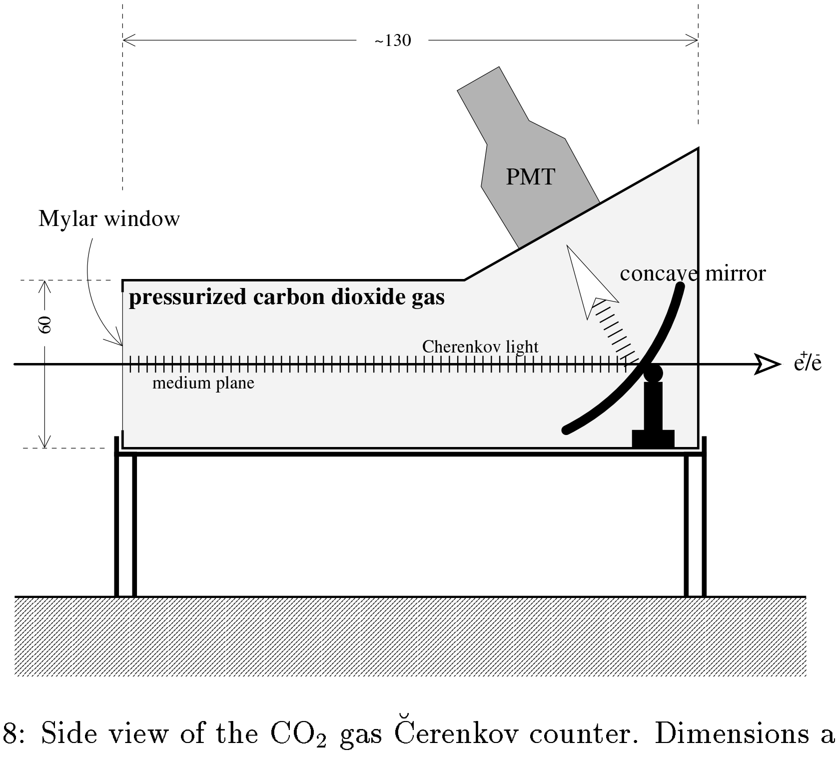

Figure 2.8: Side view of the CO_2 gas Čerenkov counter. Dimensions are in cm.

Beam Veto There were beam veto-up and down counters. The beam veto counters faced the photon beam but the up (down) scintillator was well above (below) the medium plane so that only the beam halo was eliminated. The signals were inserted into the trigger veto.

A schematic view of the target is illustrated in Fig.2.9. Detailed data for each target are shown in Tab.2.1.

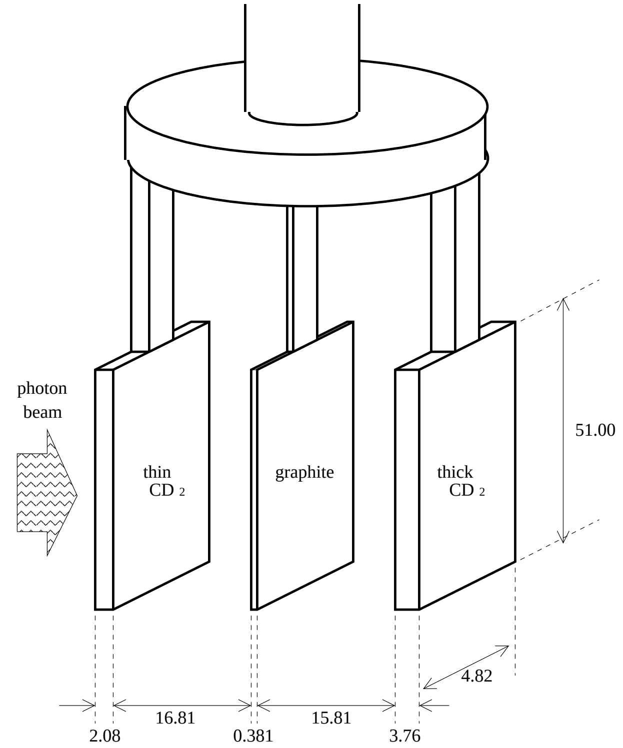

Figure 2.9: Schematic view of target used for this experiment. Dimensions are in mm.

Table 2.1: Target specifications

	graphite	thinCD_2	thickCD_2
thickness [mm]	0.381	2.08	3.76
density [g/cm^3]	1.7	1.08	1.08
carbon nuclei [$10^{21}/cm^2$]	3.51	8.41	15.2
deuteron nuclei [$10^{21}/cm^2$]	0.00	16.8	30.4

2.1.3 Trigger

The trigger was formed as the coincidence between one of the left IH counters, one right IH, one left OH, one right OH, the tagging counter, and the absence of the electron veto counter. But the actual trigger was a little more complicated in order to optimize the data taking efficiency, so it was produced in two levels. The first level of trigger was called the pre-trigger (PT), which was a coincidence signal of the sum of the backing tag counter, the left and right IH, and the absence of an inhibit signal. It can be written as, $\mathrm{PT}=\sum \mathrm{TagB} \otimes \mathrm{IHL} \otimes \mathrm{IHR} \otimes \overline{\mathrm{Inhibit}}$, where IHL and IHR indicate the sum of IH left and right signals, respectively. The Inhibit signal was the sum of forward right and left side e-veto counters (SR1 and SL1), the beam veto counters, (BVU and BVD), PT, MT, and IchBin signals. That is,

$$\mathrm{Inhibit} = \mathrm{SL1} \bigoplus \mathrm{SR1} \bigoplus \mathrm{BVU} \bigoplus \mathrm{BVD} \bigoplus \mathrm{PT} \bigoplus \mathrm{MT} \bigoplus \mathrm{IchBin}.$$

The MT and IchBin signals will be described later. The diagrammatic representation is drawn in Fig.2.10. Once the PT was issued, the TDC common start signals, such as

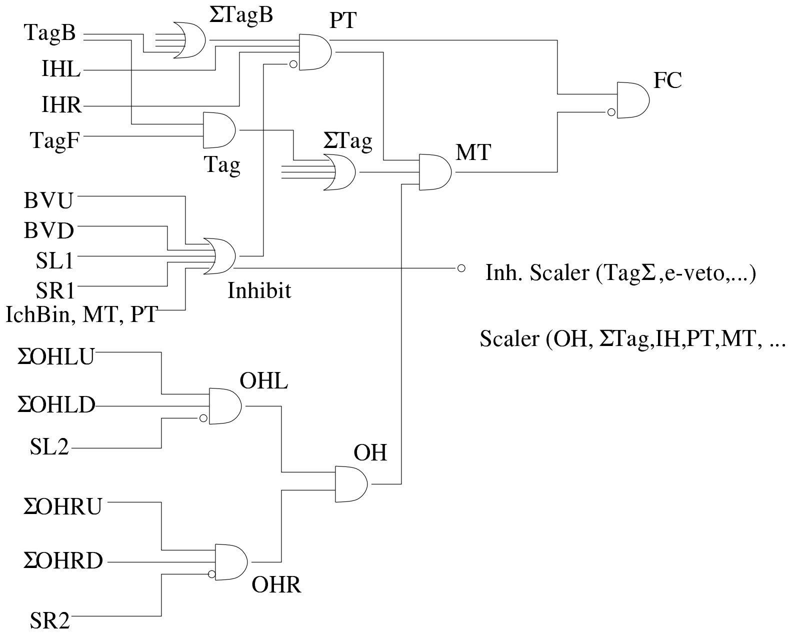

Figure 2.10: Trigger circuitry. L and R indicate left and right side of the detector. U and D indicate up and down ends of the detector. SR(L)1 and SR(L)2 are the left (right) side of forward and backward e-veto signals, respectively. BV denotes the beam veto counter.

the SDC, CDC, OH, were set and the ADC gates were opened.

The OHL signal was formed by the coincidence between the sum of left-side OH UP (OHLU), the sum of left-side OH Down (OHLD), and the absence of the backward-left e-veto signal (SL2), or OHL $= \sum_i \mathrm{OHLU}_i \otimes \sum_i \mathrm{OHLD}_i \otimes \overline{\mathrm{SL2}}$. Similarly, OHR $= \sum_i \mathrm{OHRU}_i \otimes \sum_i \mathrm{OHRD}_i \otimes \overline{\mathrm{SR2}}$. As shown in the diagram, the OH signal was the coincidence between OHL and OHR: OH=OHL$\otimes$OHR.

The tagger signal, Tag, was the coincidence signal between the tagging counter, TagF, and backing tag counter, TagB. The sigma tag signal, $\sum$Tag, was the sum of all tagging counters.

Now the main trigger, MT, was formed as the coincidence among PT, OH, and $\sum$Tag. When a MT was created, all the ADC, TDC, ETM and scaler information were transported to the memory module and eventually to the computer hard drive. This process took a significant amount of time (2 ms [17]), so a computer busy signal, IchBin, was used to inhibit the electronics to avoid creating the next MT. The MT itself also issued Inhibit in order to cover the signal delay of IchBin.

When a PT was produced but a MT was not, all TDC starts and ADC gates had to be reset. This was done by creating a fast clear signal, FC, which was the coincidence between PT and $\overline{\mathrm{MT}}$.

Throughout the experiment, the $\sum$Tag rate, which represents roughly the tagged photon rate, was kept around 3×10^5/s. PT and MT rates were $\sim 8\times10^2$/s and $\sim$10/s, respectively. The computer live time rate was also monitored to check the trigger and beam condition. It was given by:

$$\eta_{\mathrm{com}} = \frac{\text{Number of Inhibited } \sum\text{Tag scaler counts}}{\text{Number of } \sum\text{Tag scaler counts}}.$$

The value was found to be $\sim 70\%$. The value for each set of runs is listed in Tab.2.2.

2.2 Data Calibration and TAGX Performance

This section describes the way data are processed to obtain the time of flight and momentum with maximum resolution. The identification of the detected particle necessitates the measurement of both quantities. The quality of the EM background separation in the off-line analysis depends on this process. The performance of the detector elements is evaluated at the end.

Table 2.2: Computer live-time rate η_{com}. N_{trig} is the number of main triggers. Experiment numbers were assigned to distinguish sets of runs based on the value of the synchrotron beam energy.

Exp.#	E_e(top) [MeV]	N_{trig} [$\times 10^6$]	η_{com} [%]
33	1200	19.87	72.30
34	1040	9.83	64.92
35	1180	6.20	69.19

2.2.1 TAGX Software Overview

The Regina TAGX Software is a set of utility programs that process the data accumulated by the TAGX data acquisition system in order to produce physical observables such as mass and momentum, which are then accessible for physics analysis. The software was originally created on the FACOM system at INS and transferred to the UNIX system for our ρ^0 experiments. The transformation was to improve the real-time computing power and the management of high-speed automated data-acquisition and analysis system [17].

The Regina TAGX software was modeled after the off-line part of the INS TAGX software. Many modifications had been made for the following reasons:

1. The computer environment in Regina was different from that of INS. The Fortran and C compilers of the SUN OS at INS were incompatible with that of the DEC Alpha in Regina.
2. The new detector, SDC, and a new layer in the Cylindrical Drift Chamber (CDC) (see Fig.2.5) were installed to the TAGX spectrometer for the first time for the ρ^0 experiments. The software had to be changed accordingly.
3. The TAGX software at INS was not a completed version in the conventional sense because it was in the process of being transferred from FACOM to UNIX at INS. This software was not user friendly and it was necessary to standardize it.
4. Several criticisms and bugs in the programs were pointed out by the TAGX group members.

The original software in the FACOM environment was developed by S. Kasai,

K. Maruyama, Y. Murata, K. Niki, H. Harada, *et al.* The on-line part of UNIX version was developed by H. Yamashita, K. Miyamoto *et al* [17]. As for the off-line part, the CDC calibration and new layer installation was performed by H. Yamashita. The SDC software installation was performed by G. Garino *et al* [16]. The IH and OH counter calibration was performed by H. Hirosawa and H. Yamashita. DEC Alpha version has been developed by F. Farzanpay, M. Iurescu, A. Weinerman, N. Knecht, Z. Papandreou and the author.

Organization of TAGX Software

The main utilities of the Regina TAGX software are the following;

CDC-T_0 Calibration: This utility program determines the CDC drift time offset, CDC-T_0, from the CDC-TDC distribution. A CDC-T_0 parameter file is created.

CDC-XT Calibration: In this calibration, the relationship between X (drift length) and T (drift time) is determined in a parameterized function method. A CDC-XT parameter file is created.

CDC Analysis: The program calculates the planar momentum of the recognized particle track in the CDC, using determined parameters above. The calculated data are recorded in the TAGX data structure.

SDC-T_0 Calibration: This utility finds the SDC timing offset SDC-T_0 out of the SDC-TDC spectrum. TDC cut parameters are also created. The parameters are stored in a SDC-T_0 file.

SDC-XT Calibration: The relationship between the drift length and drift time for a SDC cell is found with this utility, similar to CDC-XT. It generates the SDC-XT parameter file.

SDC-CDC Analysis: Using determined SDC parameters, the CDC track obtained by CDC Analysis is modified into a longer SDC-CDC track so that the planar momentum is improved. The calculated quantities are recorded in a TAGX data structure.

Scintillation Counter Calibration: In this utility program, the timing offsets of the scintillation counters are determined so that time-of-flight information and vertical position will be extracted in the Scintillation Counter Analysis. The obtained parameters are recorded in corresponding parameter files.

Scintillation Counter Analysis: Final analysis determines the detected particle's rest mass using the planar momentum and time-of-flight information. The calculated quantities are stored in a TAGX data structure.

The CDC Analysis, SDC-CDC Analysis and Scintillation Counter Analysis involve processing TAGX data, whereas the rest of the programs are for the purpose of finding parameters (see Fig.2.11). Details of the above description will be found in the later sections.

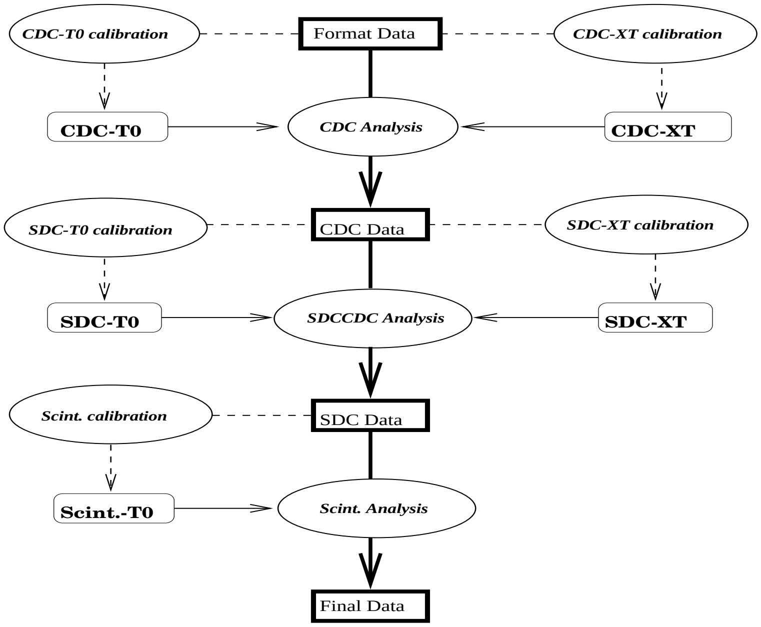

Figure 2.11: Data flow and associated software packages. Ovals, round rectangles and rectangles indicate software packages, parameters and TAGX data, respectively.

Structure of TAGX Data

The TAGX data have a specific structure; Experiment, Run, Loop, and Event. A run corresponds to one data file, which is created by one run of data acquisition. The experiment is usually assigned to a series of runs that have the same experimental conditions, such as the same ES energy (see Tab.2.2). Each loop consists of variable number of events, typically 50–60 events, since data taken are temporarily accumulated in the memory modules (60 kB) and when the buffer in either module becomes full, it is transfered to a UNIX Workstation [17]. Scaler data (e.g. Tagging counters) are also stored in this unit. Each event corresponds to a TAGX main trigger and contains a Format Block, and a Calibrated Block. (By convention, the initial TAGX data are called Format Data and the processed data are called Calibrated Data.) The Format Block is a data block which specifies the impacted detectors and their information (TDC and ADC). The Calibrated Block is reserved for trajectory data that is to be created by the TAGX software and is initially empty. Each calibrated block consists of an event header and a number of track sections. The header specifies the number of tracks, hit tagging counters, the photon energy, and so on. Each section of track contains information of momentum, time-of-flight, mass, *etc.*

TAGX Coordinate

Throughout this section, the TAGX coordinate system is used. It is a Cartesian coordinate system in which the direction of the tagged photon beam is defined as the x-axis and the direction of the TAGX magnetic field is defined as z-axis. The y-axis is subsequently determined by employing the right-hand rule (see Fig.2.5).

2.2.2 CDC-T_0 Calibration

The original description of determining the CDC-T_0 may be found in Y. Murata's report [22]. When the software was implanted into the UNIX system, the originals were entirely replaced with the PAW macro programs with different method developed by M. Iurescu and F. Farzanpay [19]. The author chose to retain and enhance the original method, which is described below.

Theory

The objective of the CDC-T_0 Calibration is to find a TDC offset, T_0, for each CDC wire so that the drift time, T_d, is calculated by

$$T_d = T_0 - T_s, \tag{2.1}$$

where T_s is the TDC value, since the TDC module is used with the common stop mode, that is, the start signal is from the CDC wire and the stop signal is from the IH. T_0 can then be found from the TDC value spectrum as follows.

Let the drift length, X, be a random variable with a certain probability distribution function, $f_X(x)$. Define an ideal drift time, T, such that T and X are related with a smooth function

$$X = h(T), \quad \text{with} \quad h(0) = 0, \quad \frac{dh}{dT} \geq 0. \tag{2.2}$$

Then, T has a probability distribution function of*

$$f_T(t) = f_X\left(h(t)\right)\frac{dh}{dt}.$$

The measured drift time, T_d, differs from T because the secondary electron is created around the ionization. By writing $f_D(d)$ as the probability density function of $D = T_d - T$, the probability density function of T_d may be given by:

$$\begin{aligned} f_{T_d}(t_d) &= \int f_D(t_d - t) f_T(t) dt \\ &= \int f_D(t_d - t) f_X(h(t)) \frac{dh}{dt} dt. \end{aligned} \tag{2.3}$$

For the proof of eq.(2.3), please see Appendix B. $f_{T_d}(t_d)$ corresponds to the drift time spectrum. Using eq.(2.1), the TDC density function is now found as

$$f_{T_s}(t_s) = f_{T_d}(t_d)\left|\frac{dt_d}{dt_s}\right| = f_{T_d}(T_0 - t_s) = \int f_D(T_0 - t_s - t) f_X\left(h(t)\right)\frac{dh}{dt}dt. \tag{2.4}$$

Assuming the drift cell has a radius of R, X can take only $0 \leq X \leq R$ values. So $f_X(x)$ is non zero only if $x \in [0, R]$. If the secondary electron is always created at the ionization point (no diffusion), then $f_D(t) = \delta(t)$ and

$$\begin{aligned} f_{T_s}(t_s) &= \int_{h^{-1}(0)}^{h^{-1}(R)} f_D(T_0 - t_s - t) f_X(h(t)) \frac{dh}{dt} dt \\ &= \begin{cases} f_X(h(T_0 - t_s)) \left.\dfrac{dh}{dt}\right|_{t = T_0 - t_s} & (T_0 - h^{-1}(R) \leq t_s \leq T_0) \\ 0 & (\text{otherwise}) \end{cases} . \end{aligned}$$

Therefore, if there is no diffusion in the drift cell, the TDC value should be distributed in a limited range with the maximum value of T_0.

---

*If two random variables X and Y are related with a monotonically increasing or decreasing function $Y = g(X)$, their probability density functions, $f_X(x)$ and $f_Y(y)$, are related with $f_Y(y) = f_X(g^{-1}(y))\left|dx/dy\right|$. For the proof, please see Ref.[24].

Note that the term, *ideal drift time*, is used to express that there is a direct relationship to the drift distance. The measured drift time cannot be represented by eq.(2.2) because of the diffusion. So the real XT-relation, $X = g(T_d)$, is *not* the same as eq.(2.2), even though they are expected to be similar. This means that in general $g(0) = 0$ does not hold.

TDC Spectrum Fitting Function and Real Data

It may be reasonable to assume the drift length distribution function, $f_X(x)$, has a uniform distribution;

$$f_X(x) = \begin{cases} 1/R & (0 \leq x \leq R) \\ 0 & (\text{otherwise}) \end{cases} . \tag{2.5}$$

Also, the diffusion distribution function, $f_D(d)$, may be approximated by a Normal distribution,

$$f_D(d) = \frac{1}{\sqrt{2\pi}\,\sigma_D} \exp\left(-\frac{d^2}{2\sigma_D^2}\right), \tag{2.6}$$

where σ_D represents the typical time resolution of the cell. Substituting eqs.(2.5) and (2.6) into eq.(2.4), yields

$$f_{T_s}(t_s) = \int_0^{h^{-1}(R)} f_D(T_0 - t_s - t)\frac{1}{R}\frac{dh}{dt}dt. \tag{2.7}$$

Expanding $\dfrac{dh}{dt}$ around $t = 0$, i.e.,

$$\frac{dh}{dt} = \sum_{n=0}^{\infty} c_n t^n,$$

yields

$$\begin{aligned} f_{T_s}(t_s) \quad &= \quad \sum_{n=0}^{\infty} \frac{c_n}{\sqrt{\pi}R} \int_{-Z_d}^{Z_R - Z_d} \{\sqrt{2}\sigma_D(z + Z_d)\}^n e^{-z^2} dz \\ &\underset{Z_R \to \infty}{\longrightarrow} \quad \sum_{n=0}^{\infty} \frac{c_n(\sqrt{2}\sigma_D)^n}{\sqrt{\pi}R} \left\{ e^{-Z_d^2} \sum_{m=0}^{n-1} a_m Z_d^m \right. \\ &\qquad \left. + \, (1 + \operatorname{erf}(Z_d)) \sum_{m=0}^{n/2} \binom{n}{2m} Z_d^{n-2m} \right\} \end{aligned} \tag{2.8}$$

where $Z_d = \frac{T_0 - t_s}{\sqrt{2}\sigma_D}$, $Z_R = \frac{h^{-1}(R)}{\sqrt{2}\sigma_D}$ and a_m are constants. $\operatorname{erf}(z)$ is known as the error function;

$$\operatorname{erf}(z) \equiv \frac{2}{\sqrt{\pi}} \int_0^z e^{-z'^2} dz',$$

which is available in the CERN library. This is the basic form of the TDC spectrum fitting function to find the TDC-T_0, σ_D, and c_n. The choice of the chamber gas and the electric field makes the drift speed fairly constant[†] so the actual fitting function takes up to $n = 3$ and only the upper portion of TDC spectrum is fitted (see Fig.2.12).

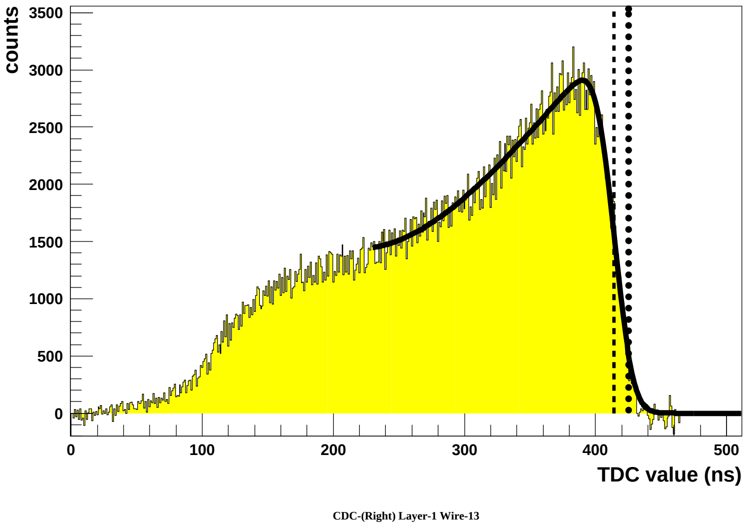

Figure 2.12: An example of the CDC-TDC spectrum. The thick solid line is the fitted curve, the dashed line is the T_0 value found from the fit and the dotted line is the value of $T_0 + \sigma_D$. In the fitting process, the overflow TDC channel near 500 ns is removed and the noise is subtracted. The noise level is estimated by averaging the region $0 \leq$(TDC value)≤ 60.

2.2.3 CDC-XT Calibration

The determination of the XT relation is an iterative process. The decision whether or not to proceed to the next iteration was done by measuring a new Residual Root Mean Square (RRMS) peak. If the peak does not differ much from the previous value, then the XT relation is said to have converged. In the following section, the initial XT relation samples, a new XT-relation set, and the RRMS peak are described and then the real data are presented.

The original CDC-XT calibration code developed by K. Niki, Y. Murata S. Kasai, and K. Maruyama was transformed into the UNIX version with the ninth layer installa-

---

[†] Both CDC and SDC uses Ar-C_2H_6 (50%-50%, 1 atm) gas and the electric field in the drift cell is 0.3 kV/cm or larger. Referring to Ref.[23], the CDC drift speed is 50 μm/ns ±7% in the region of 1 mm or more away from the sense wire.

tion by H. Yamashita. The DEC Alpha version of the copy was created by M. Iurescu, A. Weinerman and the author.

Principle

Obviously, the XT relation has to be determined in such a way that the drift length, X, predicts the distance between the charged particle trajectory and the sense wire with the desired accuracy. If X is found, then the trajectory is determined (see sec.2.2.4). The drift distance is also found independently from the determined trajectory. The difference between X determined from the drift time, T_d, and the "actual" drift length, which is called the residual, therefore has to be minimized. If a trajectory is found with n sense wires, the trajectory can give n drift distances at once. The goodness of the minimization can be parameterized with RRMS,

$$s_X = \sqrt{\frac{1}{n-3}\sum_{i=1}^{n}\delta_i^2} \tag{2.9}$$

where

$$\begin{aligned}
\delta_i &= X_i(T_{di}) - X_i(\text{track}) \qquad \text{(residual of } i\text{'th sense wire)} \\
X_i(T_{di}) &= \text{(drift distance from the drift time of } i\text{'th sense wire)} \\
X_i(\text{track}) &= \text{(drift distance of } i\text{'th sense wire from the track)} \\
n-3 &= \text{(number of degrees of freedom, see eq.(2.19))}.
\end{aligned}$$

It would be ideal if the $X_i(T_{di})$ could be determined such that the RRMS of each track is minimized. However, it is impossible to do so, because there would be too many parameters to be determined and the number of degrees of freedom becomes negative. So, in order to determine $X_i(T_{di})$, sample data of $X_i(\text{track})$ versus T_{di} are stored and fitted with a fifth order polynomial. The polynomials, $g_i(T_{di})$ are now the new $X_i(T_{di})$ or the XT relation of the i'th wire*.

The sample XT-relation data are selected from the data sample based on well-defined tracks, so that the resulting $g_i(T_{di})$ are not affected by accidental data. Momentum, Target Miss, number of tracks per event, and number of fitting points, n, in CDC

---

*Finding $g_i(T_{di})$ wire by wire is not practical since there are not enough sample data collected so it is determined layer by layer.

are the used observables in finding a well-defined track. The number of fitted points is $n = 9$ (all layers fired) is required. Other sampling data cuts are described in Ref.[19].

If the residual, δ_i, has a Normal distribution with standard deviation, σ_X, then

$$\zeta = \frac{n-3}{\sigma_X^2} s_X^2$$

has the χ^2_{n-3} distribution. The explicit form of the χ^2_{n-3} distribution function yields the following probability density function of s_X:

$$\begin{aligned} f_{\mathrm{RRMS}}(s_X) &= f_{\chi^2_{n-3}}(\zeta) \left| \frac{d\zeta}{ds_X} \right| \\ &= \frac{\zeta^{\frac{n-3}{2}-1} e^{-\frac{\zeta}{2}}}{2^{(n-3)/2}\Gamma((n-3)/2)} \frac{2(n-3)}{\sigma_X^2} s_X \\ &= \frac{2}{\Gamma\left(\frac{n-3}{2}\right)} \left(\frac{n-3}{2\sigma_X^2}\right)^{\frac{n-3}{2}} s_X^{n-4} \exp\left(-\frac{n-3}{2\sigma_X^2} s_X^2\right). \end{aligned}$$

This function has a peak at $s_X^{(\mathrm{peak})} = \sigma_X \sqrt{\frac{n-4}{n-3}}$. Since it is proportional to σ_X, the quality of the XT relation can be evaluated by finding the peak value of the RRMS distribution, and the position resolution is given by

$$\sigma_X = \sqrt{\frac{n-3}{n-4}}\, s_X^{(\mathrm{peak})}. \tag{2.10}$$

Real Data

The actual residual, δ_i, is not a Normal random variable because the drift cell is not actually cylindrical and the electron avalanche at the sense wire makes it larger. Also the track fitting function does not assume any multiple scattering. The resulting RRMS does not exactly obey $f_{\mathrm{RRMS}}(s_X)$ (see Fig.2.13). The peak value is typically 260 μm so eq.(2.10) gives $\sigma_X \simeq 290\ \mu$m.

2.2.4 CDC Analysis

The purpose of the CDC Analysis is to find a charged particle's trajectory in the CDC so as to determine its planar momentum, the emission angle and the vertex position. The following sections describe how these quantities were initially determined, and then present subsequent modifications and improvements. The main part of this analysis relies on determining the particle trajectory. The spline curve fitting method developed

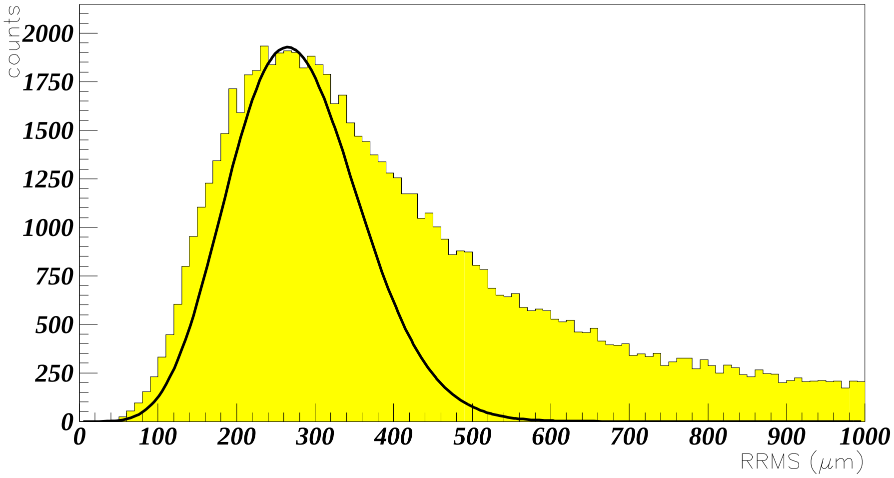

Figure 2.13: The RRMS Distribution. The curve represents the function $f_{\mathrm{RRMS}}(s_X)$. Data are from tracks with nine fitting points only.

by H. Wind is used for this purpose. The main authors of the FACOM version are K. Maruyama, Y. Murata and K. Niki. Transformation into the UNIX environment, while implementing the ninth layer, was performed by H. Yamashita. From the UNIX version to the DEC Alpha version, the transformation with some modifications has been performed by M. Iurescu, A. Weinerman, F. Farzanpay and the author.

Track Fitting Function in the xy-plane

A trajectory made by a particle having electric charge $q = Qe$, ($e = 1.602 \times 10^{-19}$ C) with its xy-plane momentum, P_{xy}[MeV/c], in the inhomogeneous magnetic field, $B_z(x,y)$[kG], has a radius of curvature*,

$$r(x,y)[\mathrm{cm}] = -\frac{P_{xy}[\mathrm{MeV/c}]}{0.2998 Q B_z(x,y)[\mathrm{kG}]}. \tag{2.11}$$

The negative sign is added so that when $B_z > 0$, positively (negatively) charged particles assume negative (positive) radii. This is because a particle trajectory, $y = y(x)$, in the TAGX dipole magnet ($B_z \geq 0$) has the radius of curvature,

$$r(x,y) = \frac{(1+y'^2)^{3/2}}{y''}. \tag{2.12}$$

---

*In this chapter, units are in this system unless explicitly specified.

Substituting eq.(2.11) into eq.(2.12) yields

$$y'' = -\frac{0.2998QB_z}{P_{xy}}\left(1+y'^2\right)^{3/2}, \tag{2.13}$$

where coordinates are measured in cm. Rotating the system about the z-axis such that the trajectory becomes a one valued function and then integrating eq.(2.13) along the new x-axis twice yields the track fitting function,

$$\tilde{y}(\tilde{x}) = A_1 + A_2\tilde{x} - \frac{0.2998Q}{P_{xy}}\int_{c_1}^{\tilde{x}}\int_{c_2}^{\xi_2} B_z(\xi_1)\left[1+\{\tilde{y}'(\xi_1)\}^2\right]^{3/2} d\xi_1 d\xi_2, \tag{2.14}$$

where $(\tilde{x},\tilde{y})$ is the rotated TAGX coordinate of (x,y), and $A_1=\tilde{y}(c_1)$ and $A_2=\tilde{y}'(c_2)$ are constants of integration.

Momentum in the xy-plane

Finding the planar momentum, P_{xy}, is an iterative process. The planar trajectory, the residuals, and RRMS are also obtained simultaneously. Suppose the trajectory points and the derivatives $(\tilde{x}_i,\tilde{y}_i;\tilde{y}_i')$, $i=1,\cdots,n$, are given in a certain iteration. The least square fit to the points is performed to find the regression curve of eq.(2.14)[†];

$$\begin{aligned}
\hat{\beta} &= ({}^tMM)^{-1}\,{}^tMU & (2.15)\\
\hat{U} &= M\beta & (2.16)\\
\hat{y}_i' &= \beta_2+\beta_3 J_i & (2.17)\\
\hat{\alpha}_i &= \mathrm{Tan}^{-1} y_i', & (2.18)
\end{aligned}$$

where

$$\beta = \begin{pmatrix}\beta_1\\ \beta_2\\ \beta_3\end{pmatrix} = \begin{pmatrix}A_1\\ A_2\\ \frac{0.2998Q}{P_{xy}}\end{pmatrix}, \quad U = \begin{pmatrix}\tilde{y}_1\\ \vdots\\ \tilde{y}_i\\ \vdots\\ \tilde{y}_n\end{pmatrix}, \quad M = \begin{pmatrix}1 & \tilde{x}_1 & I_1\\ \vdots & \vdots & \vdots\\ 1 & \tilde{x}_i & I_i\\ \vdots & \vdots & \vdots\\ 1 & \tilde{x}_n & I_n\end{pmatrix},$$

$$\begin{aligned}
I_i &= -\int_{\tilde{x}_1}^{\tilde{x}_i}\int_{\tilde{x}_1}^{\xi_2} B_z(\xi_1)\left[1+\{\tilde{y}'(\xi_1)\}^2\right]^{3/2} d\xi_1 d\xi_2,\\
J_i &= -\int_{\tilde{x}_1}^{\tilde{x}_i} B_z(\xi_1)\left[1+\{\tilde{y}'(\xi_1)\}^2\right]^{3/2} d\xi_1.
\end{aligned}$$

[†] $\hat{x}$ denotes an estimator of x. Ref.[24] defines, "An estimator is a rule that tells how to calculate an estimate based on the measurements contained in a sample."

I_i and J_i are computed by a combination of cubic spline fitting and Simpson's integral. The original description may be found in Ref.[18]. Y. Murata coded the program using Fujitsu Scientific Library and CERN Library [21]. If $\varepsilon_i = \tilde{y}_i - \hat{y}_i$ obeys a Normal distribution with mean 0 and standard deviation σ_Y, then the unbiased estimator‡ of σ_Y^2 is given by

$$s_Y^2 = \frac{1}{n-3}\sum_{i=1}^{n} \varepsilon_i^2 = \frac{{}^tUU - {}^t\hat{\beta}\,{}^tMU}{n-3}, \tag{2.19}$$

where the number of degrees of freedom becomes $n-3$ because there are n independent random variables, ε_i, and the track curve eq.(2.14) has three unknown parameters. It should to be noted that the residual δ_i is not the same as ε_i because δ_i is the difference in drift distance. An approximation to δ_i can easily be obtained by

$$\delta_i \simeq (\hat{y}_i - \tilde{y}_i)\cos\hat{\alpha}_i. \tag{2.20}$$

This is valid when $|\tilde{y}''| \approx 0$ or when $\tilde{x}_i$ is close to the actual $\tilde{x}_i$. In other words, the approximation converges to the fully calculated value when the iteration is converged. The new momentum is calculated to be,

$$P_{xy} = \frac{0.2998}{|\beta_3|}, \tag{2.21}$$

under an assumption that the particle's electric charge takes $q = \pm e$ or $Q = \pm 1$. The sign of Q takes the sign of β_3. The iteration is terminated when the difference between the old P_{xy} and new one is less than 0.5%. The new coordinates are determined as follows:

$$\begin{aligned} \tilde{x}_i &\simeq \tilde{w}_{xi} - g_i(T_{di})\sin\hat{\alpha}_i, \\ \tilde{y}_i &\simeq \tilde{w}_{yi} + g_i(T_{di})\cos\hat{\alpha}_i, \end{aligned}$$

where (w_{xi}, w_{yi}) is the sense wire position and T_{di} is the drift time of i'th wire. Again, the approximation is valid when $|\tilde{y}''| \approx 0$ or when $\left|\tilde{x}_i^{\text{old}} - \tilde{x}_i^{\text{new}}\right| \approx 0$.

Rotation Angle As described above, the CDC fitting points are determined from the least square method. The method finds the elements of β minimizing s_Y. It is desirable, however, to minimize RRMS or s_X instead of s_Y, because s_Y takes only the

---

‡If an estimator $\hat{x}$ of a parameter x has an expectation value $\mathrm{E}(\hat{x}) = x$, then $\hat{x}$ is called an unbiased estimator.

rotated y-axis into account. Eq.(2.20) shows that if each $\alpha_i = 0$, then $s_X = s_Y$. So by rotating the coordinate system such that each $\alpha_i \approx 0$, the minimization of RRMS may be improved. From geometrical considerations, one may find that the rotation angle is

$$\theta_R = \tan^{-1}\frac{w_{xn} - w_{x1}}{w_{yn} - w_{y1}}.$$

Vertex Position and Emission Angle in the xy-Plane

Since the TAGX magnetic field is nearly uniform in the vicinity of the target center, it can be assumed that the curvature of the trajectory is constant in that region. So the vertex point is calculated as an intersection point between two approximated trajectory circles, which must be determined first.

The momentum vector in the unrotated TAGX coordinate system is

$$(P_x, P_y)_1 = P_{xy}(\cos\phi_1, \sin\phi_1), \quad \phi_1 = \alpha_1 + \theta_R$$

Subscript "1" denotes the first fitting point. Because this vector is tangent to the circle, the circle center is given by

$$(x_c, y_c) = (x_1, y_1) + r_c(\cos\phi_c, \sin\phi_c), \quad \phi_c = \phi_1 \pm \frac{\pi}{2} \quad \text{for } \mp \text{ charge,} \tag{2.22}$$

where $r_c = |r(x_1, y_1)|$ and $r(x, y)$ is given by eq.(2.11). There are two candidates of the vertex point given by

$$(x_v, y_v)^{\pm} = (x_c, y_c)^{(1)} + r_c^{(1)}(\cos(\Psi \pm \psi), \sin(\Psi \pm \psi)), \tag{2.23}$$

where [§]

$$\Psi = \tan^{-1}\frac{y_c^{(2)} - y_c^{(1)}}{x_c^{(2)} - x_c^{(1)}} \tag{2.24}$$

$$\psi = \mathrm{Cos}^{-1}\frac{(r_c^{(1)})^2 + d^2 - (r_c^{(2)})^2}{2dr_c^{(1)}} \tag{2.25}$$

$$d = \sqrt{(x_c^{(2)} - x_c^{(1)})^2 + (y_c^{(2)} - y_c^{(1)})^2}, \tag{2.26}$$

and superscript "(i)" indicates the variable of i'th trajectory. The geometrical meaning of the variables may be gleaned from Fig.2.14. It is assumed that the vertex position

---

[§] The initial capital letter for names of the inverse of the trigonometric functions indicates the principal value whereas the normal label denotes the general angles. Specifically, $\tan^{-1}$ is used for the Fortran intrinsic function, `atan2`.

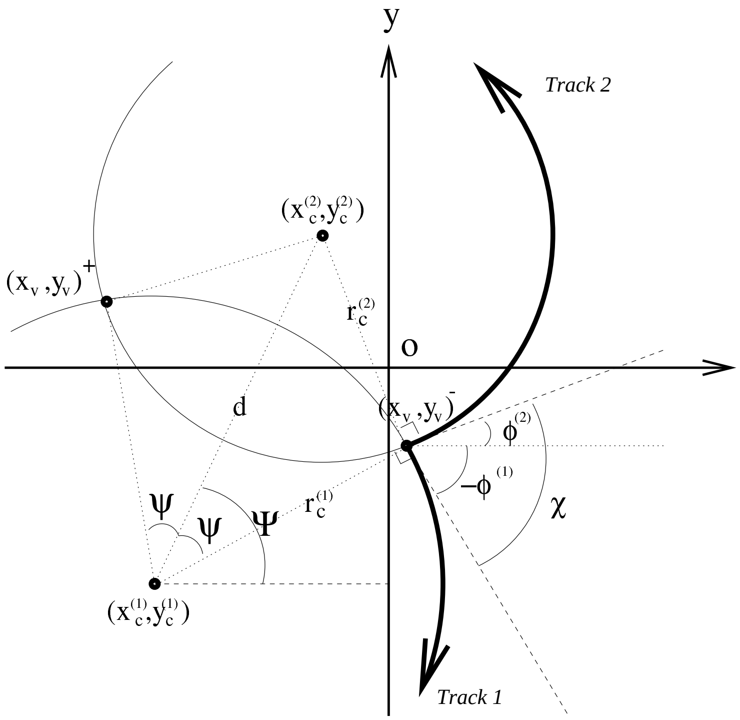

Figure 2.14: Two candidates of the vertex position. Track#1 assumes positively charged and the track#2 negative. Note that $\phi^{(i)}$ and Ψ are general angles so that $-\phi^{(1)}$ may be relevant for the case of this figure when one defines that $-\pi \leq \phi \leq \pi$.

is either $(x_v, y_v)^+$ or $(x_v, y_v)^-$, whichever is closer to the origin since the origin is the center of the target system. Finally, the azimuthal emission angle for the i'th trajectory is given by

$$\phi^{(i)} = \tan^{-1} \frac{y_v - y_c^{(i)}}{x_v - x_c^{(i)}} \mp \frac{\pi}{2} \quad (\text{for } \pm \text{ charge}). \tag{2.27}$$

2.2.5 SDC T_0 Calibration

In this section, the method of determining the SDC T_0 created by G. Garino is discussed. His method was almost completely maintained in the DEC Alpha version.

Determination of Relative T_0

The SDC position resolution is expected to be $\sim 150\,\mu$m [16]. If the drift speed is 50 μm/ns, the drift time resolution then is 3ns. So T_0 has to be determined within a few ns precision. Because the SDC-XT parameters were also determined layer by layer, the T_0's of each individual SDC cell in the same layer had to be aligned with each other within this precision. For this reason, each wire's TDC spectrum was placed on top of a reference spectrum, so that it was easy to discern by how many ns it had to be shifted to match with the reference spectrum (see Fig.2.15). The shifted value was considered as the relative T_0. Now, the T_0 value is found by

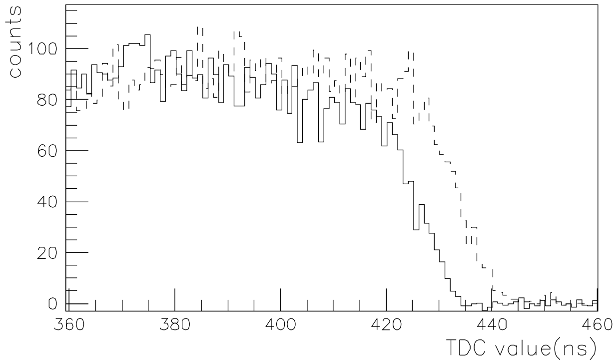

Figure 2.15: Matching two SDC-TDC spectra. The thick solid line is the reference spectrum. Each wire TDC is presented as a dashed line and shifted to match the reference. The dashed line is positioned to the right when negative T_R is given so that eq.(2.28) is satisfied.

$$T_0 = T_G + T_R, \tag{2.28}$$

where T_R is the relative T_0 and T_G is the reference value called the global T_0. This value was determined from one of the SDC wires that was in optimal shape, which will be described below.

The TDC spectrum which will be used to determine T_R, has to result from the tracks that triggered the IH, so that T_0 is not smeared by accidentals. To ensure of this, the following conditions were applied to create the spectrum:

1. Events with only two tracks are allowed.
2. The vertex position is less than 5 cm from the target center.
3. The wire that fired is in a geometrical range corresponding to hit IH paddle.

It was observed that T_R often differs by a few ns from the one determined using data without these conditions. This is due to the fact that the SDC is very noisy because it is close to the beam and there is a problem of cross talk between neighbour straw tube cells. The origin of the cross talk problem is not well understood.

Determination of Global T_0

The determination of T_G becomes somewhat redundant because, unlike the CDC-XT relation, the SDC-XT does not demand $X = 0$ at $T_d = 0$. But it is better to set the T_G value systematically so that one can make direct comparison of the same variable from a different run. So the TDC fitting function presented by eq.(2.8) is also employed to determine T_G (see Fig.2.16).

TDC Cut

The SDC has a problem of high multiplicity, which makes it difficult to carry out identification of the best SDC tracks. So the background hits have to be eliminated as much as possible before the detailed analysis. In this utility, the TDC lower and higher limits are set by eye (see Fig.2.17). The determined cut will be applied for SDC-XT calibration and SDC-CDC Analysis.

2.2.6 SDC-XT Calibration

The SDC chamber consists of only four layers of straw tubes in a very small region, so it is very difficult to find a particle trajectory with reasonable confidence by using

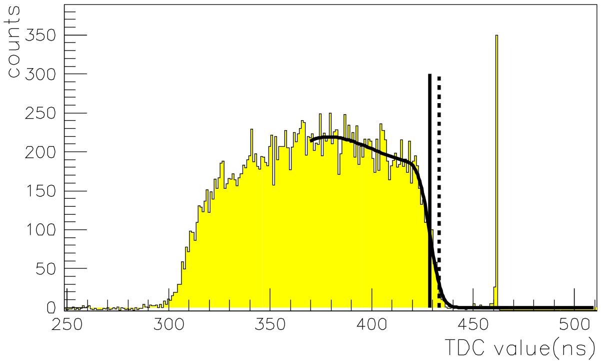

Figure 2.16: Fitting function for the SDC-TDC spectrum. The solid curve is the fitted function given by eq.(2.8). The solid straight line indicates the fitted T_0 value and the dashed line represents $T_0 + \sigma_D$.

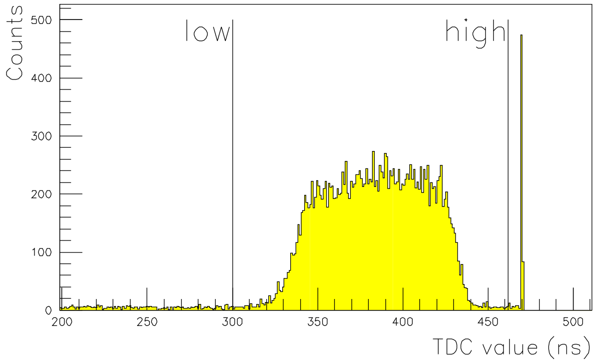

Figure 2.17: Cuts on the SDC-TDC value. Accepted region is inside the limits of high and low lines. The values are set by human eye.

only the SDC information. Instead, the SDC-CDC trajectory is interrogated iteratively with exactly the same method used in the CDC Analysis. However, only the SDC-XT relation is improved in this iteration. Because the SDC straw tubes are small compared to the CDC cell and the SDC spatial resolution is better, the given SDC-CDC RRMS is not expected to be improved greatly from one iteration to another. The SDC-XT relation is found by minimizing the SDC residuals.

The SDC-XT calibration in the UNIX environment created by G. Garino has been modified while being transformed into the DEC Alpha version by the author. Originally, the XT relation was determined with a SDC straight track, which will be discussed in the SDC Analysis. That resulted in many and long iterations of determination as the track created only with the SDC information is spurious. The modification is due to a finding that the SDC-CDC misalignment is within the observational error [25] so that one can joint the SDC track with a CDC track without a coordinate transformation, which has to be otherwise determined altogether.

SDC Residual

Determination of the SDC-XT relation means the minimization of the SDC residual. It is the SDC residuals that have to be minimized, even though SDC-CDC RRMS is automatically minimized when finding the SDC-CDC trajectory. Assuming each SDC drift cell has the same spatial resolution, σ_X, the collective residual, δ, which is the collection of δ_i from all layers, has a Normal distribution with mean 0 and standard deviation σ_X. The standard deviation can easily be evaluated once the SDC-XT samples are collected, and represents the goodness of the SDC-XT relation.

The real collective residual distribution is shown in Fig.2.18. It can be seen that the distribution is very well approximated by a Normal distribution. From the Gaussian fitting, one can find that the averaged SDC spatial resolution is typically 150 μm.

SDC-XT Relation Table

The extraction of an accurate XT relation is important for obtaining good position resolution. A parameterized function as the SDC-XT relation is rather artificial and might not be able to reflect an unexpected behavior. For this reason, a look-up table method was established. The method is explained as the following:

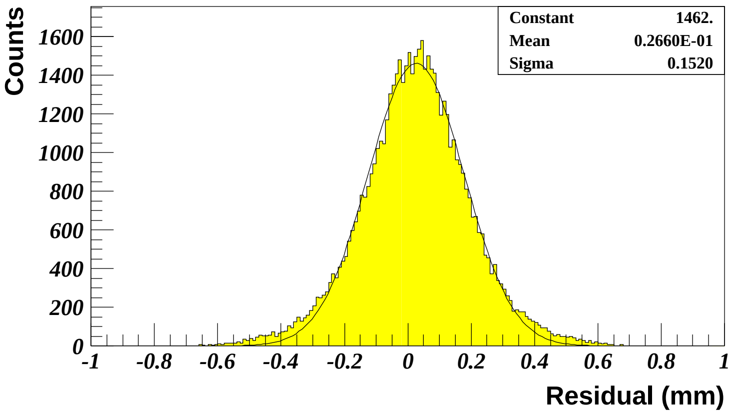

Figure 2.18: Distribution of the SDC residual. The curve is the fitted Gaussian. In this case, the SDC spatial resolution is found as 152 μm.

Suppose the XT samples, (T_{di}, X_i), $i = 1, \cdots, N$, are collected for a SDC layer, where N is a very large number, so that the points can cover every possible XT relation. To obtain an estimation of the drift distance for a certain drift time, T, one may select the points (T_{di}, X_i) that are in the region $|T - T_{di}| \leq \Delta T$. The mean value of X_i in the region is the estimation of $X(T)$. By taking the finite value of ΔT, a data table, X versus T, can be made. The resulting table is called the XT-table. The XT relation is assumed to have converged when the improvement of the residual from the previous iteration is less than 0.5%.

The real XT-table is made by taking $\Delta T_d = 0.5$ ns so that X can be obtained every 1 ns. The weak point of this method is, therefore, discontinuity and non-smoothness of the relation. The converged XT-relation has to be inspected especially when enough sampling data are not available. Fig.2.19 shows the good conversion of the relation, which is smooth and continuous over the entire relation.

2.2.7 SDC-CDC Analysis

The objective of this step is to improve each CDC trajectory by using the SDC information and subsequently modify the planar momentum, the emission angle and the vertex position. There might be several ways of extending the trajectory into the SDC. G. Garino created the following procedure:

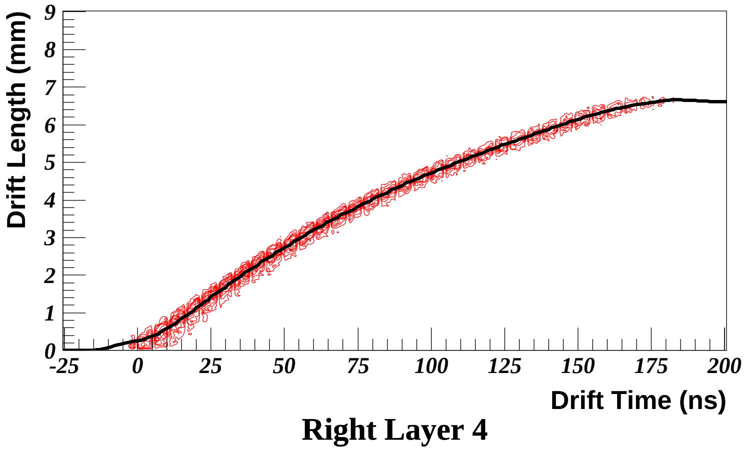

Figure 2.19: The SDC-XT relation. The smooth line is the determined XT relation. The straight horizontal part of the line in the large drift-time region is artificially set at the straw radius. The data sample is presented in the contour plot.

1. Create a number of candidate SDC tracks which may be an extension of the CDC track.
2. Select the best SDC track candidate and create the SDC-CDC trajectory.

Description of these steps will be found below. The improvements will be presented in sec.2.2.10.

SDC Analysis

Clustering The job of clustering is the grouping of the SDC hit wires. The term *hit wire* means that the wire whose TDC value is in the region determined by the TDC cut. A SDC cluster is defined as a group of three or four hit wires that forms one of the eight wire pattern shown in Fig.2.20. For the three-hit case, any one of the wires within the pattern can be absent.

Wire-Side Pattern Assignment Even after finding a cluster, an ambiguity remains. In principle, one cannot tell which side of the wire the secondary electron came from by only looking at the drift time itself. Since the ambiguity (of the wire-side pattern) cannot be resolved in a straightforward way, the job is to simply assign the wire side pattern to each possible track. There are 2^4 wire patterns conceivable for a 4-wire cluster.

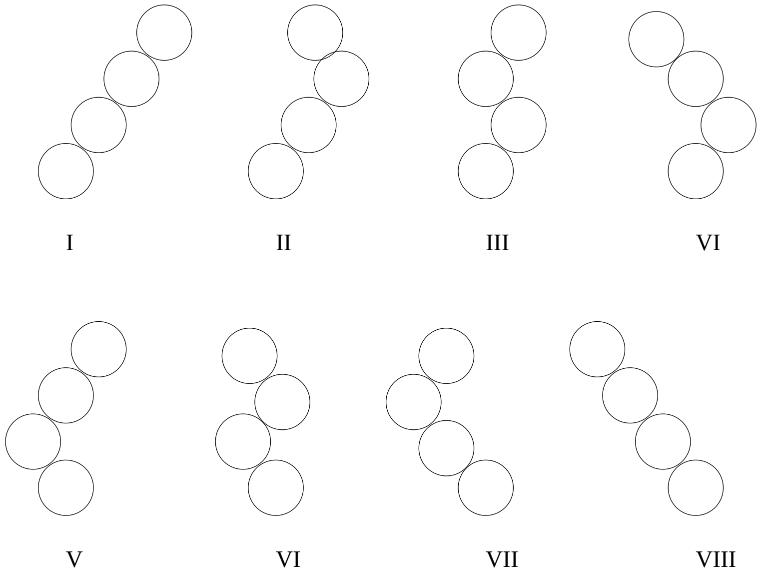

Figure 2.20: Eight wire patterns for the SDC cluster. Each of the four circles represents the SDC cell from one layer.

However, most of the patterns are not probable because of the wire configuration (see Fig.2.21). Usually, two to four patterns are selected out of the possibility. Even though the SDC straw configuration is known, the selection rule is based on the Monte Carlo simulation [16] to make sure not to lose any possible patterns. But every permutation is selected for a 3-wire cluster. Therefore, there are two to four SDC tracks per 4-wire cluster and 8 tracks per 3-wire cluster.

SDC Track Construction The SDC track is a straight line. There are a few reasons for this:

1. The condition of a valid SDC track is merely a collection of reasonable SDC hit positions and low SDC-RRMS. The positions found will be used as the initial points of the SDC-CDC track.

2. A straight line approximation is very fast and reasonable. To see this, suppose the worst case in which a very low planar-momentum particle (60 MeV/c) in the magnetic field ($B_z = 5.0$ kG) went through the SDC. The deviation of the straight line from the circle within the SDC is estimated to be 140 μm, which is still less than the SDC position resolution.

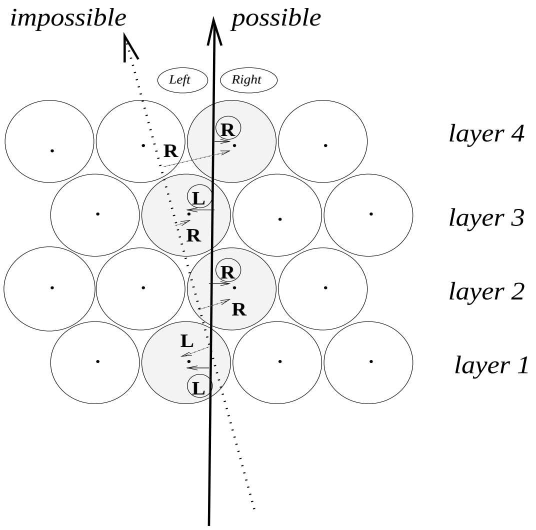

Figure 2.21: Schematic diagram of assigning the wire side pattern. Filled circles indicates the cluster. Wire side is defined from the point of view of the trajectory. In this particular case, wire hit pattern (L,R,L,R) is a possible SDC track. But (L,R,R,R) is impossible to construct a straight line trajectory.

The SDC track is a straight line that produces a minimum SDC RRMS. The solution of this problem is not linear. The process of finding the line, however, makes use of the least square method, by carefully rotating the system so that the residuals are always along the y-axis.

Suppose a cluster with wire coordinates (w_{xi}, w_{yi}), $(i = 1, n$ where $n = 3$ or $4)$, after the wire pattern is assigned. One can find the regression line of the n wires with the least square method:

$$\begin{aligned} \text{slope} \quad &: \quad m_0 = \frac{\mathrm{E}(w_x)\mathrm{E}(w_y) - \mathrm{E}(w_x w_y)}{\mathrm{E}^2(w_x) - \mathrm{E}(w_x^2)} && (2.29) \\ \text{intercept} \quad &: \quad b_0 = \mathrm{E}(w_y) - m_0 \mathrm{E}(w_x) && (2.30) \end{aligned}$$

Rotating the TAGX coordinate system along the z-axis by $\theta_0 = \tan^{-1} m_0$, the first approximation of the hit points is calculated to be:

$$\begin{aligned} \tilde{x}_i &= \tilde{w}_{xi} \\ \tilde{y}_i &= \tilde{w}_{yi} + P_i g_i(T_{di}) \end{aligned}$$

where $P_i = \pm 1$ have been determined by the wire side pattern assignment and $g_i(T_{di})$ is found from the XT-table. The next step is to correct the rotation angle, θ_0. By finding the line of regression for points $(\tilde{x}_i, \tilde{y}_i)$, i.e.,

$$\begin{aligned} \text{slope} &: \; m_1 = \frac{\mathrm{E}(\tilde{x})\mathrm{E}(\tilde{y}) - \mathrm{E}(\tilde{x}\tilde{y})}{\mathrm{E}^2(\tilde{x}) - \mathrm{E}(\tilde{x}^2)} \\ \text{intercept} &: \; b_1 = \mathrm{E}(\tilde{y}) - m_1 \mathrm{E}(\tilde{x}), \end{aligned}$$

the corrected rotation angle is found as

$$\theta_1 = \theta_0 + \mathrm{Tan}^{-1} m_1.$$

After the I'th correction of the rotation, one can find it to be:

$$\theta_I = \theta_0 + \sum_{i=1}^{I} \mathrm{Tan}^{-1} m_i,$$

where m_i is the slope of the regression line of the i'th iteration. Since each step does not involve any approximation, the series $\{\theta_i\}$ converges very fast. The real analysis terminates at the 7th iteration or when $|\theta_{i-1} - \theta_i| < 10^{-3}$ deg. The SDC RRMS is given by:

$$s_X = \sqrt{\frac{1}{n-2} \sum_{i=1}^{n} \frac{(\tilde{y}_i - m_I \tilde{x}_i - b_I)^2}{1 + m_I^2}}.$$

Assume that

$$\zeta = \frac{(n-2)s_X^2}{\sigma_X^2}$$

has a χ^2 distribution with $n-2$ degrees of freedom. Suppose one decides to reject at the 0.1% level, corresponding to $\zeta = 13.8$ for $n = 4$. Then 4-point SDC tracks whose RRMS $> 500\,\mu$m may be eliminated from the candidate. However, the SDC track here is a straight line, even if it is a good approximation. SDC tracks with more than 2 mm RRMS are excluded from further analysis.

SDC-CDC Trajectory

The principle of finding the SDC-CDC trajectory is the same as that of the CDC trajectory (see sec.2.2.4). The initial set of points in the iteration, however, is the CDC track points and the SDC track points determined on page 47. So even if the SDC track is a straight line, the final SDC-CDC track would not be affected, simply because SDC-CDC track points have to be around the curve, eq.(2.14).

If there are a number of SDC tracks, the program searches for the SDC track that makes SDC-CDC RRMS minimum. The SDC track that has the smallest SDC RRMS of all candidates, does not always provide the best SDC points. The candidate which is chosen statistically is shown in Fig.2.22. One requirement is that the CDC track should not deteriorate by combining it with the SDC track. However, because the SDC is a small device located near the target, it is very advantageous to find the counterpart of a CDC track. So the SDC-CDC track is created as long as the combined RRMS is less than 4 mm, which is large enough to accomodate all the possible SDC-CDC tracks. If no SDC track is used, the CDC track alone is used in the subsequent analysis.

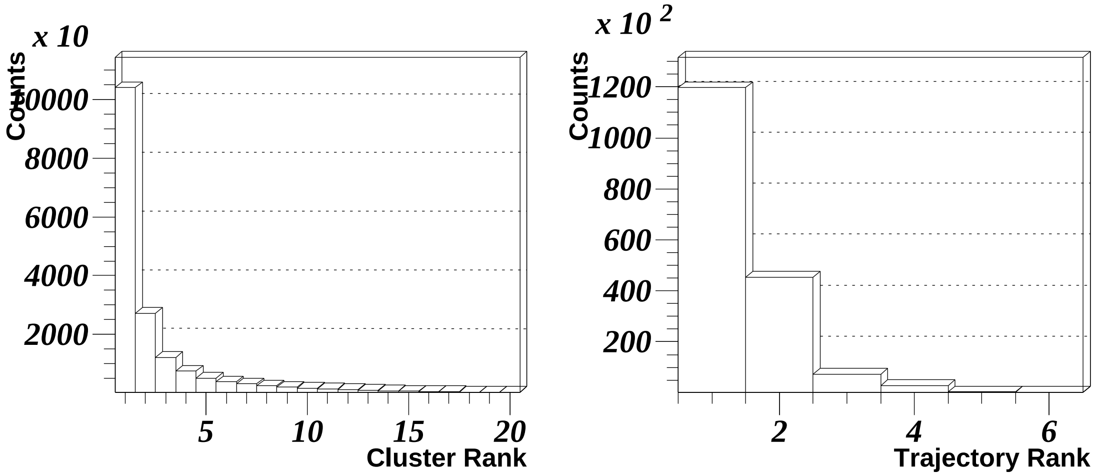

Figure 2.22: Rank of the SDC track candidate. At left is a chosen cluster rank distribution and at right is a chosen trajectory rank distribution. The trajectory rank is an enumeration of the candidate tracks in order of smaller RRMS to larger. The cluster rank is an enumeration of the clusters in order of smaller RRMS of rank-1 trajectory to larger.

2.2.8 Scintillation Counter Calibration

The scintillation counter here refers to the IH, OH and Tagging counters. The objectives of the calibration are:

1. to determine the z-component of the OH hit position of the SDC-CDC track.
2. to determine the SDC-CDC track's time of flight between the IH and OH.

Originally, the calibration code was created by S. Kasai in the FACOM environment. It was adopted in the UNIX environment by H. Hirosawa. Although the DEC Alpha version was first created by A. Weinerman, some methods and conclusions contradicted Hirosawa's [20]. The author adopted Hirosawa's method, which is more consistent.

Time Chart

Fig.2.23 shows the schematic representation of the event timing which eventually determines the scintillation counter TDC values. IH-T_0 in the figure include any kind of timing differences among the IH paddles such as PMT response timing, cable delay, etc. OH-T_0 is also defined similarly but excludes the light propagation time in the scintillator, which will be determined explicitly. The chart ignores all the common timing delay associated with the same counter such as the cable delay, since they introduce only constants in the timing and are not essential in determining timing differences.

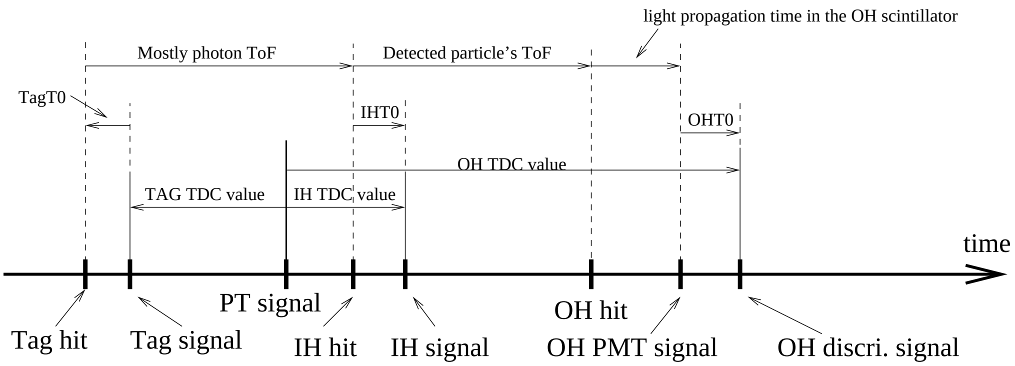

Figure 2.23: Scintillation counter timing diagram. The pre-trigger timing (TDC common start timing) is usually the same as the IH stop timing (self triggered). But this diagram shows the most general case in which the pre-trigger timing was determined by another IH. The light propagation time in the IH scintillator was ignored.

IH-T_0 determination

By referring to the timing chart in Fig.2.23, one may derive the following expression:

$$(\text{photon TOF}) = \{T(\text{Tag}_i) + T_0(\text{Tag}_i)\} - \{T(\text{IH}_j) - T_0(\text{IH}_j)\} + (\text{const.}) \qquad (2.31)$$

where $T(\text{Tag}_i)$ and $T(\text{IH}_j)$ are the TDC values for IH i'th and Tag j'th counters, respectively. The photon TOF in eq.(2.31) actually excludes the incident electron's time of flight between the tagging radiator and the tagging counter and includes the detected particle's time of flight between the reaction point and the IH. By fixing the tagging counter paddle number, i, "photon TOF" and $T_0(\mathrm{Tag}_i)$ are fixed so that relative value of IH-T_0 may be found from eq.(2.31). But the relative value is essential, so the actual IH-T_0 is defined as

$$T_0(\mathrm{IH}_j) = T(\mathrm{IH}_j) - T(\mathrm{Tag}_{i=30}). \tag{2.32}$$

The quantity should not change from one event to another, so the IH-T_0 may be found at the peak of the distribution of the right hand side of eq.(2.32).

OH-T_0 determination

Since each OH has two-ended (up and down) readout, the detected particle's time of flight from IH to OH may be calculated by two ways (see Fig.2.23):

$$\begin{aligned} \mathrm{TOF} &= \{T(\mathrm{OHU}_i) - t_l(\mathrm{OHU}_i)) - T_0(\mathrm{OHU}_i)\} - \{T(\mathrm{IH}_j) - T_0(\mathrm{IH}_j)\} & (2.33) \\ \mathrm{TOF} &= \{T(\mathrm{OHD}_i) - t_l(\mathrm{OHD}_i) - T_0(\mathrm{OHD}_i)\} - \{T(\mathrm{IH}_j) - T_0(\mathrm{IH}_j)\}, & (2.34) \end{aligned}$$

where t_l is the light transmission time from the OH scintillator hit position to the light guide. This may actually be given by

$$\begin{aligned} t_l(\mathrm{OHU}_i) &= \frac{z_{\mathrm{max}} - z(\mathrm{OH}_i)}{v_{\mathrm{eff}\,i}} & (2.35) \\ t_l(\mathrm{OHD}_i) &= \frac{z(\mathrm{OH}_i) - z_{\mathrm{min}}}{v_{\mathrm{eff}\,i}}, & (2.36) \end{aligned}$$

where $z(\mathrm{OH}_i)$ is the z-component of the i'th OH hit position, $v_{\mathrm{eff}\,i}$ is the effective light speed in the scintillator, and z_{max} and z_{min} are the z-coordinate of the OH scintillator upper and lower edges ($z_{\mathrm{max}} = -z_{\mathrm{min}} = 29.75$ cm). Subtracting eq.(2.33) from eq.(2.34), the difference takes the following form:

$$T(\mathrm{OHD}_i) - T(\mathrm{OHU}_i) = t_l(\mathrm{OHD}_i) - t_l(\mathrm{OHU}_i) + T_0(\mathrm{OHD}_i) - T_0(\mathrm{OHU}_i). \tag{2.37}$$

By combining eqs.(2.35), (2.36) and (2.37), one can find

$$z(\mathrm{OH}_i) = \frac{v_{\mathrm{eff}\,i}}{2}\{T(\mathrm{OHD}_i) - T(\mathrm{OHU}_i) + T_{Z0i}\}, \tag{2.38}$$

where T_{Z0i} or OH-Z_0 is defined as

$$T_{Z0i} \equiv T_0(\mathrm{OHU}_i) - T_0(\mathrm{OHD}_i). \tag{2.39}$$

One may find OH-Z_0 from the electron runs where most of the events are confined on the $z = 0$ plane, or by finding the central value of the $T(\mathrm{OHU}_i) - T(\mathrm{OHD}_i)$ distribution with the hadronic events. The value $v_{\mathrm{eff}i}$ may also be determined from the width of this distribution because $z_{\min} \leq z(\mathrm{OH}_i) \leq z_{\max}$.

Now, by adding eq.(2.33) and eq.(2.34), one may eliminate the $z(\mathrm{OH}_i)$ terms to conclude:

$$\mathrm{TOF} = \frac{T(\mathrm{OHU}_i) + T(\mathrm{OHD}_i)}{2} - T_0(\mathrm{OH}_i) - \{T(\mathrm{IH}_j) - T_0(\mathrm{IH}_j)\}, \tag{2.40}$$

where

$$T_0(\mathrm{OH}_i) \equiv \frac{T_0(\mathrm{OHU}_i) + T_0(\mathrm{OHD}_i)}{2} + \frac{z_{\max} - z_{\min}}{2v_{\mathrm{eff}i}}. \tag{2.41}$$

The observable $T_0(\mathrm{OH}_i)$ or OH-T_0 is needed to obtain the time of flight of the trajectory but in addition $T_0(\mathrm{OH}_{\mathrm{up}i})$ and $T_0(\mathrm{OHD}_i)$ are unknown. Instead, since it is fairly easy to find proton tracks (see sec.2.3), one can make use of these tracks to obtain the OH-T_0. The time of flight for a proton with the three-dimensional trajectory length and momentum, l and P, which are obtained from information given by the SDC-CDC trajectory and from the $z(\mathrm{OH}_i)$ value as described in the next section, may theoretically be given by:

$$\mathrm{TOF(proton)} = \frac{l}{c}\sqrt{1 + \left(\frac{m_p c^2}{Pc}\right)^2}, \quad (m_p = 938.3\ \mathrm{MeV/c^2}). \tag{2.42}$$

Substituting eq.(2.42) into eq.(2.40) yields

$$T_0(\mathrm{OH}_i) = \frac{T(\mathrm{OHU}_i) + T(\mathrm{OHD}_i)}{2} - \{T(\mathrm{IH}_j) - T_0(\mathrm{IH}_j)\} - \frac{l}{c}\sqrt{1 + \left(\frac{m_p c^2}{Pc}\right)^2}. \tag{2.43}$$

The distribution of the right hand side of eq.(2.43) produced by proton tracks exhibits a sharp peak, which is to be identified as the OH-T_0.

2.2.9 Scintillation Counter Analysis

This is the final step of the calibration. The author adopted codes developed by H. Yamashita and H. Hirosawa. To this code, the computation of the planar trajectory length is added in order to more accurately determine the spiral trajectory length and three-dimensional momentum. Previously, it had been simply substituted with a straight line segment in two dimensions between the IH and OH hit positions. Using the determined IH-T_0, OH-Z_0 and OH-T_0 values, the z component of the OH hit position and the time of flight can be determined from eqs.(2.38) and (2.40). The following physical quantities are obtained in this analysis:

$$\begin{aligned}
\text{dip angle}: \quad & D && = \mathrm{Tan}^{-1}\frac{z(\mathrm{OH})}{l_{xy}} \\
\text{polar emission angle}: \quad & \theta && = \frac{\pi}{2} - D \\
\text{three-dimensional momentum}: \quad & P && = \frac{P_{xy}}{\cos D} \\
\text{three-dimensional trajectory length}: \quad & l && = \frac{l_{xy}}{\cos D} \\
\text{particle speed}: \quad & v && = \frac{l}{\mathrm{TOF}} \\
\text{particle rest mass}: \quad & m && = \frac{P}{c}\sqrt{\left(\frac{c}{v}\right)^2 - 1},
\end{aligned}$$

where l_{xy} and P_{xy} are the xy-plane trajectory length and momentum, respectively. The calculation of l_{xy} is described below and P_{xy} is obtained from the SDC-CDC analysis.

Two-Dimensional Path Length

The two-dimensional trajectory length, l_{xy}, is necessary to obtain the various physical quantities shown above. The equations of motion in the xy-plane for a particle with electric charge, $q = Qe$, and momentum, P_{xy}, in the magnetic field, $\vec{B} = (0, 0, B_z(x, y))$, are given by

$$\left\{ \begin{array}{rcl} \ddot{x} & = & \omega \dot{y} \\ \ddot{y} & = & -\omega \dot{x} \end{array} \right. , \quad \omega[\mathrm{rad./ns}] = 0.2998 \frac{Q v_{xy}[\mathrm{cm/ns}] B_z[\mathrm{kG}]}{P_{xy}[\mathrm{MeV/c}]}. \tag{2.44}$$

The general solution of this system may be found as,

$$\left\{ \begin{array}{rcl} \dot{x} & = & v_{xy} \cos\theta \\ \dot{y} & = & -v_{xy} \sin\theta \end{array} \right. , \quad v_{xy} = \mathrm{const.}, \tag{2.45}$$

where

$$\theta(t) \equiv \int^t \omega(x, y) dt. \tag{2.46}$$

Switching the parameter from t[ns] to θ[rad.], i.e.,

$$\frac{dx}{d\theta} = \frac{\dot{x}}{\omega}, \quad \frac{dy}{d\theta} = \frac{\dot{y}}{\omega},$$

one may find the trajectory length in the xy-plane as,

$$l_{xy} = \int_{\theta_{\min}}^{\theta_{\max}} \sqrt{\left(\frac{dx}{d\theta}\right)^2 + \left(\frac{dy}{d\theta}\right)^2} d\theta = \int_{\theta_{\min}}^{\theta_{\max}} |r(\theta)| \, d\theta, \tag{2.47}$$

where $r = v_{xy}/\omega$ is given by eq.(2.11). One may find the parameter θ from the direction of $\vec{v} = (\dot{x}, \dot{y})$ by using eq.(2.45) without performing the integration of eq.(2.46). This makes the integration of eq.(2.47) easier because the fitting points and the momentum vectors are already known from the SDC-CDC Analysis (note that $\vec{P}//\vec{v}$). The actual computation for eq.(2.47) employs the trapezoidal rule.

2.2.10 Spectrometer Performance

Chamber Detection Efficiencies

Let $\eta_i^{(j)}$ be the CDC i'th layer detection efficiency, when more than j fitting points are required to reconstruct a CDC track. Because an SDC-CDC track cannot be constructed without constructing a CDC track first, it may be evaluated as

$$\eta_i^{(j)} = \frac{N_i}{M_i},$$

where M_i is the number of $(j+1)$-fitting-point CDC tracks requiring always an i'th layer hit and N_i is the number of j-fitting-point CDC tracks without using i'th layer. Similarly, the SDC detection efficiency may be given by

$$\eta_S^{(j)} = \frac{\text{(number of SDC-CDC tracks)}}{\text{(number of } j\text{-fitting-point CDC tracks)}}.$$

As j increases, $\eta^{(j)}$ are expected to increase, because the definition of a track becomes better defined. However, it is also anticipated that $\eta^{(j)}$ do not change much for specific j values when a certain confidence level is achieved. So by observing $\eta^{(j)}$ with respect to j, it may be possible to find an effective j or the validity of $j = 5$ may be tested.

Using proton and pion tracks*, it is observed that $\eta^{(j)}$ does not increase significantly with increasing j (see Tab.(2.3) and Fig.(2.24)). This test supports the validity of $j = 5$, since the difference between $\eta^{(5)}$ and $\eta^{(7)}$ is 4% at most.

Planar Momentum Resolution

If one knows the spatial resolution, $\sigma_X[\mu\text{m}]$, the magnetic field, B[kG], the length, L[cm], and the number of data points, N, of a drift chamber, then the momentum resolution

---

*IH and OH hits are also required because time-of-flight information is necessary to identify the particle.

Table 2.3: Detection efficiencies of the CDC layers and the SDC. For definition of $\eta^{(j)}$, please see the text.

layer	$\eta^{(5)}$(%)	$\eta^{(6)}$(%)	$\eta^{(7)}$(%)	$\eta^{(8)}$(%)
SDC	95.2 ±0.50	95.6± 0.51	96.1±0.52	96.7 ± 0.55
CDC1	91.9 ±0.49	93.0± 0.50	94.8±0.53	96.7 ± 0.64
CDC2	87.5 ±0.47	88.4± 0.48	90.0±0.51	92.4 ± 0.60
CDC3	95.8 ±0.50	96.6± 0.52	97.8±0.55	98.9 ± 0.65
CDC4	93.5 ±0.50	94.2± 0.51	95.2±0.54	96.8 ± 0.64
CDC5	96.7 ±0.51	97.1± 0.52	97.4±0.55	98.0 ± 0.65
CDC6	96.9 ±0.51	97.4± 0.52	97.9±0.55	98.7 ± 0.65
CDC7	93.4 ±0.50	94.1± 0.51	95.3±0.54	96.0 ± 0.63
CDC8	93.3 ±0.49	94.0± 0.51	95.2±0.54	96.3 ± 0.63
CDC9	87.0 ±0.47	87.6± 0.48	88.6±0.51	89.7 ± 0.58
CDC avr.	92.9 ±0.16	93.6± 0.17	94.7±0.18	95.9 ± 0.21

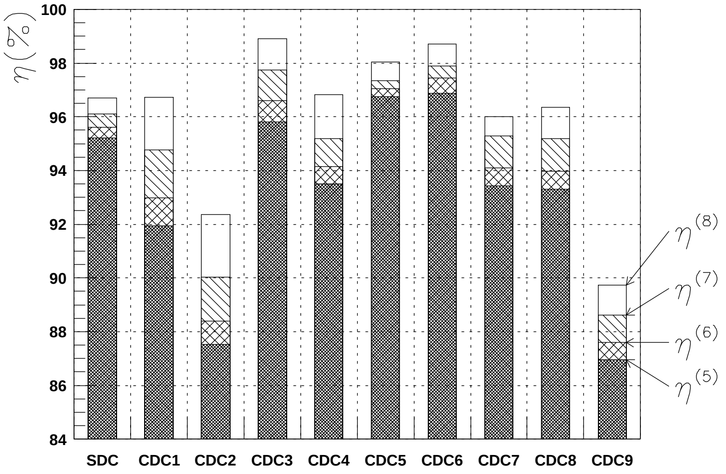

Figure 2.24: Detection efficiency comparison. Bar graphs from the top to bottom are $\eta^{(8)}$,$\eta^{(7)}$,$\eta^{(6)}$, and $\eta^{(5)}$, respectively. Errors are ignored. For definition of the values, please see the text.

of a trajectory with momentum, P[GeV/c], may be given by [30]

$$\frac{\sigma_P}{P} = \sqrt{\frac{720}{N+4}}\frac{\sigma_X P}{3BL^2}.$$

Clearly, the momentum resolution may be parametrized as a first order function of the momentum.

From the property of the least square estimators, the variances of the determined parameters in eq.(2.15) are given by

$$\mathrm{Var}(\hat{\beta}_j) = c_{jj}\sigma_Y^2 \tag{2.48}$$

where c_{jj} are the diagonal matrix elements of $({}^tMM)^{-1}$. From eq.(2.21), the standard deviation of the error P_{xy} may be given by

$$\sigma_{P_{xy}} \simeq \left|\frac{\partial P_{xy}}{\partial \beta_3}\right| \sqrt{c_{33}\sigma_Y^2} = \frac{0.2998}{\beta_3^2}\sqrt{c_{33}}\,\sigma_Y.$$

It is now possible to make an estimator of $\sigma_{P_{xy}}$ as

$$\hat{\sigma}_{P_{xy}} = \frac{0.2998}{\hat{\beta}_3^2}\sqrt{c_{33}}\,s_Y.$$

In Fig.2.25, an estimator of the planar momentum resolution,

$$\frac{\hat{\sigma}_{P_{xy}}}{P_{xy}} = \frac{\sqrt{c_{33}}}{0.2998}P_{xy}s_Y,$$

is plotted versus P_{xy}. The plot shows a widespread distribution because $\hat{\sigma}_{P_{xy}}/P_{xy}$ depends on the number of fitting points. Denoting n_S and n_C as the number of fitting points in the SDC and CDC, respectively, n_S takes on values 3 or 4 and n_C takes on values $5 \leq n_C \leq 9$. Writing,

$$\frac{\sigma_{P_{xy}}}{P_{xy}} = aP_{xy} + b, \tag{2.49}$$

one can find the coefficients a and b with respect to (n_S, n_C) by fitting the $\sigma_{P_{xy}}/P_{xy}$ versus P_{xy} scatter plot. The fitting results with the upgraded TAGX (SDC+CDC 9 layers) are shown in Tab.2.4. The weighted average gives

$$\frac{\sigma_{P_{xy}}}{P_{xy}} = 0.090P_{xy} + 0.12 \times 10^{-3}.$$

Similar analyses under an assumption that the new TAGX features were not made use of, yielded

$$\text{CDC 9 layers}: \quad \frac{\sigma_{P_{xy}}}{P_{xy}} = 0.131P_{xy} + 2.16 \times 10^{-3};$$

$$\text{CDC 8 layers}: \quad \frac{\sigma_{P_{xy}}}{P_{xy}} = 0.139P_{xy} + 2.12 \times 10^{-3}.$$

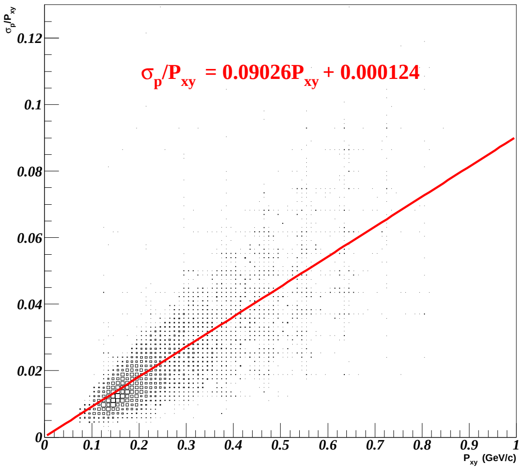

Figure 2.25: Scatter plot of the momentum resolution versus momentum. Data are only from pion tracks. In order to optimize the fitting, cuts with RRMS$\leq$ 600 μm and $\sqrt{x_v^2 + y_v^2} \leq$ 4cm are applied.

Table 2.4: Planar momentum resolution parameters. Coefficients of the momentum resolution found by fitting the scatter plot as shown in Fig.(2.25). *Entry* is the number of pion tracks in percent. RRMS $\leq$ 600 μm and $\sqrt{x_v^2 + y_v^2} \leq$ 4 cm are applied.

n_S	n_C	*entry* [%]	a [(GeV/c)$^{-1}$]	b [$\times 10^{-3}$]	$\sigma_{P_{xy}}$ [MeV/c] at P_{xy} = 300 MeV/c
0	5	0.39	0.074	45.27	20.2
3–4	5	1.40	0.113	5.18	11.7
0	6	0.47	0.093	37.51	19.6
3–4	6	6.38	0.103	1.79	9.8
0	7	0.57	0.137	10.72	15.5
3–4	7	18.68	0.093	0.92	8.6
0	8	0.69	0.118	6.81	12.7
3–4	8	37.28	0.082	1.60	7.9
0	9	0.27	0.118	0.04	10.6
3–4	9	33.86	0.073	1.84	7.1
average			0.090	0.12	8.1

Therefore, if the the planar momentum is 300 MeV/c, the planar momentum resolution improves 5% by adding the 9th layer and 35% by adding the SDC. The overall TAGX modification improves the momentum resolution by 38%. A Monte Carlo simulation Ref.[26] gives the three-dimensional momentum resolution,

$$\frac{\sigma_P}{P} = 0.09P + 0.01,$$

with $n_S = 0$, $5 \leq n_C \leq 8$. Comparing with the results above, this equation is a little too optimistic to be applied to this experiment.

Vertex Position Resolution

Because the SDC is located very close to the target, the vertex position resolution is also expected to be improved by the new enhancements of TAGX. The results indeed show a clear improvement, as depicted in Fig.2.26.

Azimuthal-Angle Resolution

The angular resolution of a drift chamber with the spatial resolution, σ_X(cm), the length, L(cm), and equally-spaced N data points can be written as [30]

$$\sigma_\phi = \frac{\sigma_X}{L}\sqrt{\frac{192}{N+4.9}}.$$

Inserting the values appropriate for TAGX ($N = 13$, $L \simeq 442$ mm, and $\sigma_X \approx 0.29$ mm) yields

$$\sigma_\phi \simeq 0.42[\text{deg./mm}]\sigma_X \approx 0.12^\circ.$$

The variation in the multiple scattering through material of thickness x in radiation lengths is given by [1]

$$\theta_0 = \frac{13.6 \text{ MeV}}{\beta c P}\sqrt{x}(1 + 0.038 \ln x).$$

When substituting the SDC+CDC value of $x = (3.5 + 4.0) \times 10^{-3}$ [16, 29], one obtains $\theta_0 = 0.34^\circ$ for charged pions of $P = 200$ MeV/c. This is larger than the data fitting uncertainty estimate. In other words, the azimuthal-angle resolution is expected to depend on the position resolution, particle species, and the planar momentum. In the analysis below, the charged pion's angular resolution is parametrized as

$$\sigma_\phi = a s_X + b, \tag{2.50}$$

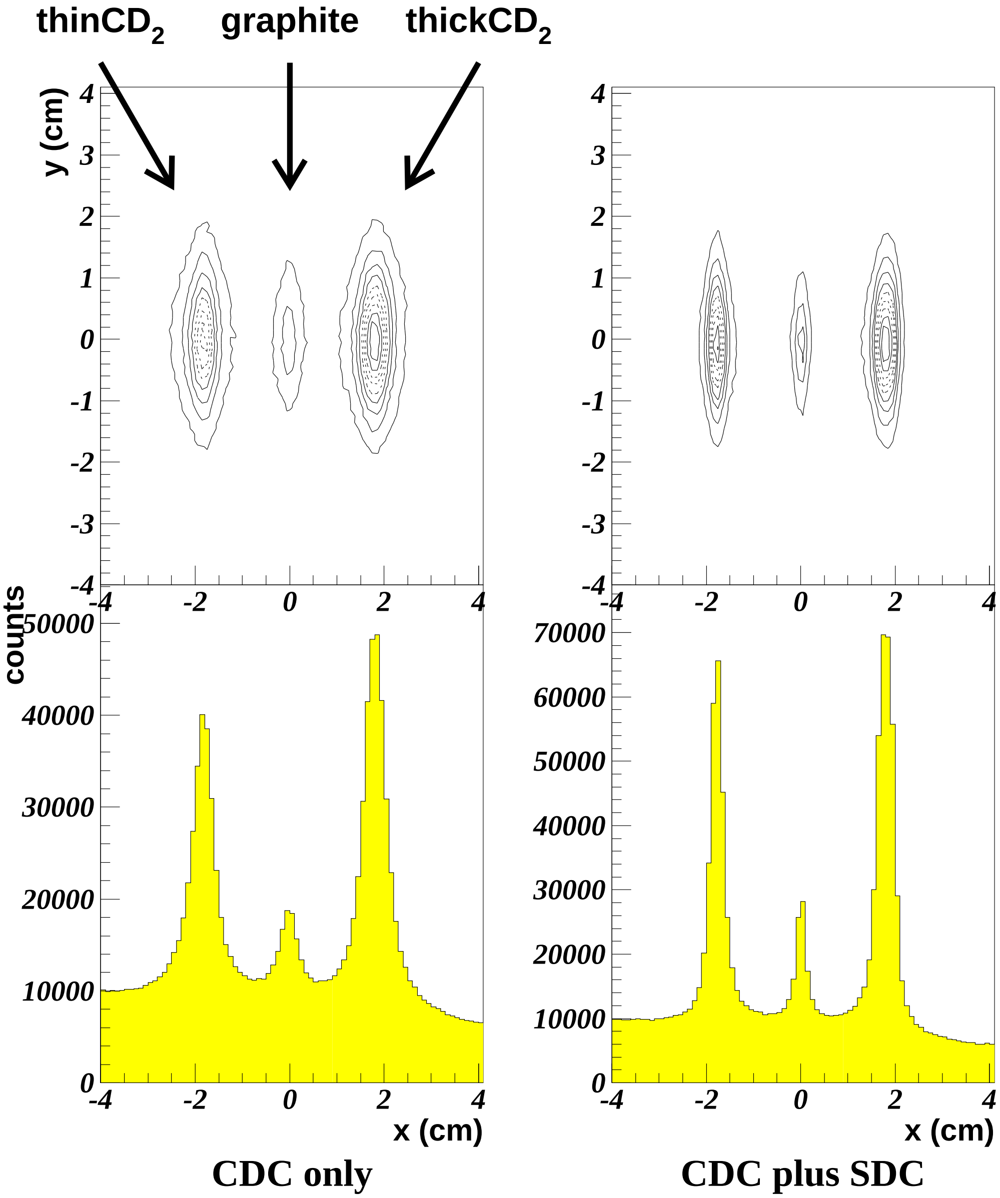

Figure 2.26: Comparison of the vertex position distribution before and after the TAGX modification. In the top panels are two-dimensional contour plots and in the bottom ones their x-projection. The data shown here are after the first stage of event rejection (see sec.2.3.3).

since the angular uncertainty due to the multiple scattering is ultimately reduced to the fitting quality.

The SDC-CDC analysis employing eqs.(2.17) and (2.18) provides the planar emission angle presented by eq.(2.27). Using eq.(2.48), one may estimate the angular resolution as follows:

$$\begin{aligned}\sigma_\phi &= \left|\frac{d\alpha}{dy'}\right| \sqrt{\left(\frac{\partial y'}{\partial \beta_2}\right)^2 \mathrm{Var}(\hat{\beta}_2) + \left(\frac{\partial y'}{\partial \beta_3}\right)^2 \mathrm{Var}(\hat{\beta}_3)} \\ &= s_Y \cos^2 \alpha \sqrt{c_{22} + c_{33}(\tan\alpha - A_2)^2 \left(\frac{P_{xy}}{0.2998}\right)^2}.\end{aligned}$$

Tab.2.5 shows the estimation of the coefficients in eq.(2.50) obtained by fitting the σ_ϕ versus s_X scatter plot with the line. Fig.2.27 illustrates the example. The results indicate that the SDC-incorporated trajectory has better angular resolution, as expected, and that proton tracks give a slope coefficient a that is ~1.5 larger from that for pions.

Table 2.5: Coefficients of the azimuthal-angle resolution found by fitting the scatter plot σ_ϕ versus s_X. An example of the plot is shown in Fig.2.27.

n_S	n_C	a [deg./mm]	b [deg.]	σ_ϕ[deg.] at $s_X = 0.3$ mm
0	5	3.12	0.525	1.46
3–4	5	1.86	0.127	0.69
0	6	2.39	0.346	1.06
3–4	6	1.56	0.091	0.56
0	7	2.22	0.110	0.78
3–4	7	1.50	0.023	0.47
0	8	2.16	0.013	0.66
3–4	8	1.27	0.050	0.43
0	9	1.00	0.143	0.44
3–4	9	1.18	0.051	0.41
average		1.46	0.021	0.46

Scintillation Counter Timing Resolution

The TAGX momentum detection threshold is ~40 MeV/c. If the particle trajectory is identified as an electron or positron,

$$\beta(e^\pm) = \left(1 + \left(\frac{m_e c}{P(e^\pm)}\right)^2\right)^{-1/2} \geq 1 - 10^{-4}, \quad \text{when } P(e^\pm) \geq 40 \text{ MeV/c}.$$

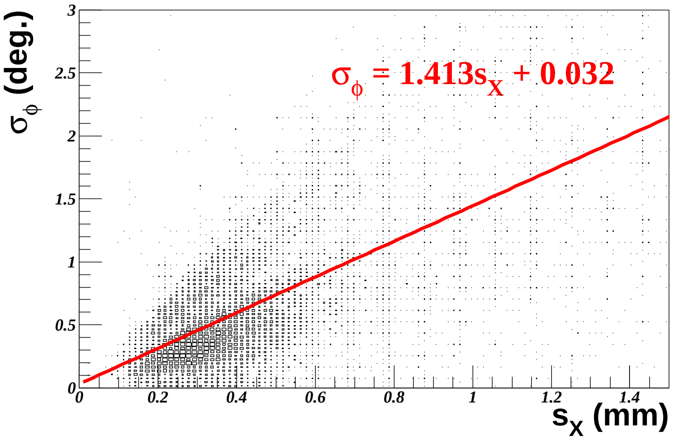

Figure 2.27: Scatter plot of the azimuthal-angle resolution (σ_ϕ) versus RRMS (s_X). Data are from pion tracks only. A momentum cut, $150 \leq P \leq 500$ MeV/c, is applied to suppress the $e^\pm$ contamination.

However, TAGX does not have the required sensitivity to resolve such values of β. The ratio, $\beta = l/(ct)$, measured by the TAGX with the EM background events gives 1.03±0.187 (see Fig.2.28). The origin of the error is the error of the time of flight between IH and OH (t) and that of the trajectory length (l). The relationship may be written by

$$\sigma_\beta^2 \simeq \mathrm{E}\left(\frac{1}{t^2}\right)\left(\frac{\sigma_l^2}{c^2} + \sigma_t^2\right), \tag{2.51}$$

where σ indicates each quantity's RMS error. But these errors are actually associated with the scintillation counter timing resolution. The time-of-flight resolution, σ_t, may be written in terms of the OH and IH timing resolutions. Using (2.40), one obtains,

$$\sigma_t^2 = \frac{\sigma_{\mathrm{OH}}^2}{2} + \sigma_{\mathrm{IH}}^2. \tag{2.52}$$

The trajectory length, l, on the other hand, is given by $l = \sqrt{l_{xy}^2 + z^2}$ and z is given by eq.(2.38). Using these equations, one may find that,

$$\sigma_l^2 = \mathrm{E}\left(\frac{l_{xy}^2}{l^2}\right)\sigma_{l_{xy}}^2 + \mathrm{E}\left(\frac{z^2}{l^2}\right)\sigma_z^2 \tag{2.53}$$

$$\sigma_z^2 = \frac{v_{\mathrm{eff}}^2}{2}\sigma_{\mathrm{OH}}^2. \tag{2.54}$$

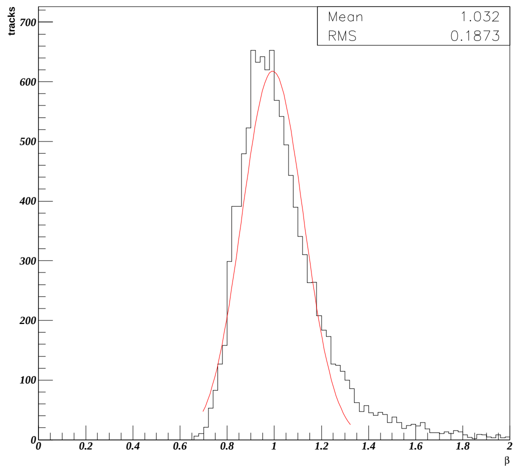

Figure 2.28: Electron/positron beta distribution. A Gaussian fit gives $\sigma_\beta = 0.13 \pm 0.001$.

Substituting eqs.(2.52-2.54) into eq.(2.51), the following expression is found:

$$\sigma_\beta^2 \simeq \mathrm{E}\left(\frac{1}{t^2}\right)\left[\left\{1-\mathrm{E}\left(\frac{z^2}{l^2}\right)\right\}\frac{\sigma_{l_{xy}}^2}{c}+\left\{\frac{v_{\mathrm{eff}}^2}{c^2}\mathrm{E}\left(\frac{z^2}{l^2}\right)+1\right\}\frac{{\sigma_{\mathrm{OH}}}^2}{2}+\sigma_{\mathrm{IH}}^2\right]. \qquad (2.55)$$

During the experiments, the IH timing resolution was found to be $\sigma_{\mathrm{IH}} = 0.36\ \mathrm{ns} \pm 8\%$. The OH-$Z_0$ analysis yields the effective light-transmission speed in the OH scintillator and it was found to be $v_{\mathrm{eff}} \approx 12 \pm 1$ cm/ns. Subsequently the analysis of the EM background events results in

$$\begin{aligned}\sigma_\beta &= 0.130 \pm 0.001,\\ \mathrm{E}\left(\frac{1}{t^2}\right) &= 0.118 \pm 0.004\ \mathrm{ns}^{-2},\\ \mathrm{E}\left(\frac{z^2}{l^2}\right) &= (3.0 \pm 0.1) \times 10^{-3}.\end{aligned}$$

Because there are still two unknown variables, $\sigma_{l_{xy}}$ and σ_{OH} in eq.(2.55), only their upper limits can be determined:

$$\begin{aligned}\sigma_{l_{xy}} &\leq 3.5\ \mathrm{cm} \pm 82\%,\\ \sigma_{\mathrm{OH}} &\leq 0.17\ \mathrm{ns} \pm 82\%.\end{aligned}$$

Following this, eqs.(2.52) and (2.54) provide the resolutions of the time of flight and the z-component of the OH hit position:

$$\sigma_t \leq 380 \pm 60\ \mathrm{ps},$$

$$\sigma_z \leq 1.4 \pm 1.3\,\mathrm{cm}$$

These values have large errors but they are within agreement with the other independent analysis from Ref.[29].

Error of the Three Dimensional Momentum

The three dimensional momentum is reconstructed by

$$P = \frac{l}{l_{xy}} P_{xy} = P_{xy}\sqrt{1 + \frac{z^2}{l_{xy}^2}},$$

where P_{xy} is the planar momentum, l_{xy} the planar trajectory length, z the OH hit position in the z-direction, and $l = \sqrt{l_{xy}^2 + z^2}$ the three dimensional trajectory length. So the errors of z, l_{xy}, and P_{xy} propagate into the error of P. Assuming that a variable, x, is measured slightly off by Δx from the true value where x may be P_{xy}, z, or l_{xy}, the error in P may be written by

$$\Delta P = \frac{\partial P}{\partial P_{xy}} \Delta P_{xy} + \frac{\partial P}{\partial z} \Delta z + \frac{\partial P}{\partial l_{xy}} \Delta l_{xy},$$

or

$$\frac{\Delta P}{P} = \frac{\Delta P_{xy}}{P_{xy}} + \frac{z^2}{l^2}\left(\frac{\Delta z}{z} - \frac{\Delta l_{xy}}{l_{xy}}\right).$$

Due to the TAGX geometry, $(z/l)^2 \lesssim 0.10$. In other words, up to 10% of the relative errors in each z and l_{xy} contributes to the relative error of P. It was found in the previous section, that $\Delta_{l_{xy}}/l_{xy} \lesssim 0.04$. In the worst case scenario, the error in l_{xy} may contribute 0.4% to the relative error of P, which is fairly comparable to the contribution from the planar momentum resolution.

Čerenkov Detection Efficiency

Assessing the detection efficiency of the aerogel and CO_2-gas Čerenkov detectors involves both particle ID and tracking. Since neither of them are known particularly well, the assessment is not very easy. Here, the detector performance is evaluated from a dedicated experimental run where the particle ID does not play a role. This run was originally carried out to determine the OH-Z_0 parameter (see eq.(2.39)). In this run, the electron veto counters were removed from the trigger and one could assume that almost all events were from the EM reaction, $\gamma \rightarrow e^+e^-$[†]. But both aerogel and CO_2-gas Čerenkov detectors were so far away from the chamber tracking device, that the particle tracking could only be guessed at and this might not be very reliable. The track was extrapolated to the detectors with a straight line from the OH hit position since the magnetic field outside the magnet yoke was very weak[‡]. Because it was not so clear that the track actually had hit the detector or a specific PMT, the neighbour PMTs were examined as well. If the adjacent PMT indeed had a signal, it was assumed that the track actually had hit the PMT. If none of the adjacent PMTs had signals, only the original PMT was taken to be inefficient. Fig.2.29 shows the resulting Čerenkov detection efficiencies. It turned out that neither efficiency was particularly good. The cause was the high TAGX

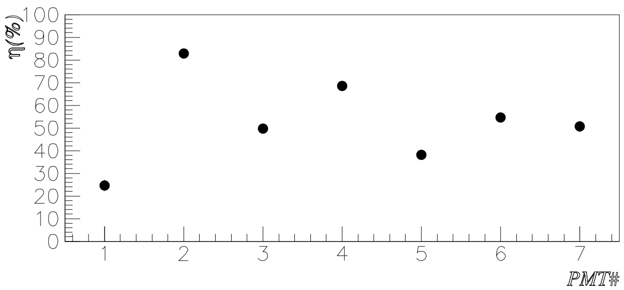

CO_2 gas

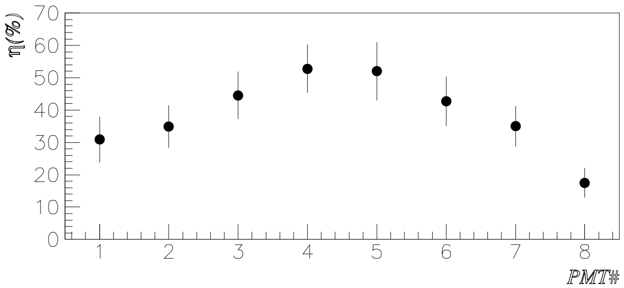

Aerogel

Figure 2.29: Detection efficiencies for the Čerenkov counters. Data are from a special run without the e-veto and Čerenkov counters in the trigger (see text).

[†] For graphite with 1 GeV photon energy, $\sigma_{total}(\gamma \rightarrow e^+e^-) = \frac{7}{9}(A/X_0N_A) \simeq 0.36$ barn [1]. Ref.[42] shows $\sigma_{abs}(\gamma\mathrm{C}) \lesssim 200\ \mu\mathrm{barn}/A$. The pair production is more than 150 times more probable than any hadronic events to happen.

[‡] The mirrors of both aerogel and gas counters were approximately 2 m away from the target center. Knowing the position resolution at the OH ($\sim$ 90 cm away from the center, $\sim$ 2 cm position resolution), one might guess that the extrapolated track has $\sim$ 5 cm position resolution.

magnetic field at the PMT location and which was determined during the experiment. Efforts to increase magnetic-field shielding of the PMT's, over and above their μ-metal shields, were not entirely successful due to the large field gradients at the PMT location.

2.3 Experimental Data

A total of about 36M events were calibrated before proceeding to do particle identification and to select events of interest. This section describes the final stage of data processing. The data processing code the author uses for this purpose is a modified version of the standardized program developed by G. Huber, Z. Papandreou and F. Farzanpay.

2.3.1 Particle Identification

For purposes of particle identification, the three-dimensional momentum, P, versus the reciprocal of beta, $1/\beta$, can be used to identify a particle. The underlying idea of this scheme is that they are directly related in terms of mass, m:

$$P = \frac{mv}{\sqrt{1-(v/c)^2}} = \frac{mc}{\sqrt{\beta^{-2}-1}}. \tag{2.56}$$

Fig.2.30 shows data and the PID boxes which were used for the later analysis. In $\beta \approx 1$ region, one cannot separate $e^+(e^-)$ and $\pi^+(\pi^-)$ because of the time of flight resolution. With these PID boxes, it is expected that the high momentum $e^\pm$ will be misidentified as $\pi^{\pm}$[*]. e^+e^- contamination must be dealt with in the later analyses.

2.3.2 Energy Loss Estimation

The pion momenta from the photo production are different from those measured by the calibration, because pions lose energy in the target and detectors. The actual pion momentum at the creation location may be calculated by taking the energy loss into account.

It is fairly easy to calculate the energy loss through the detectors because they are all cylindrical so the energy loss does not depend strongly on the direction of the particle momentum. But the target is not radially symmetric so one has to make certain assumptions to estimate the energy loss in it. Here, the reaction point is assumed to

---

[*] The $e^\pm$ curves for eq.(2.56) would essentially be $\beta = 1$ in Fig.2.30.

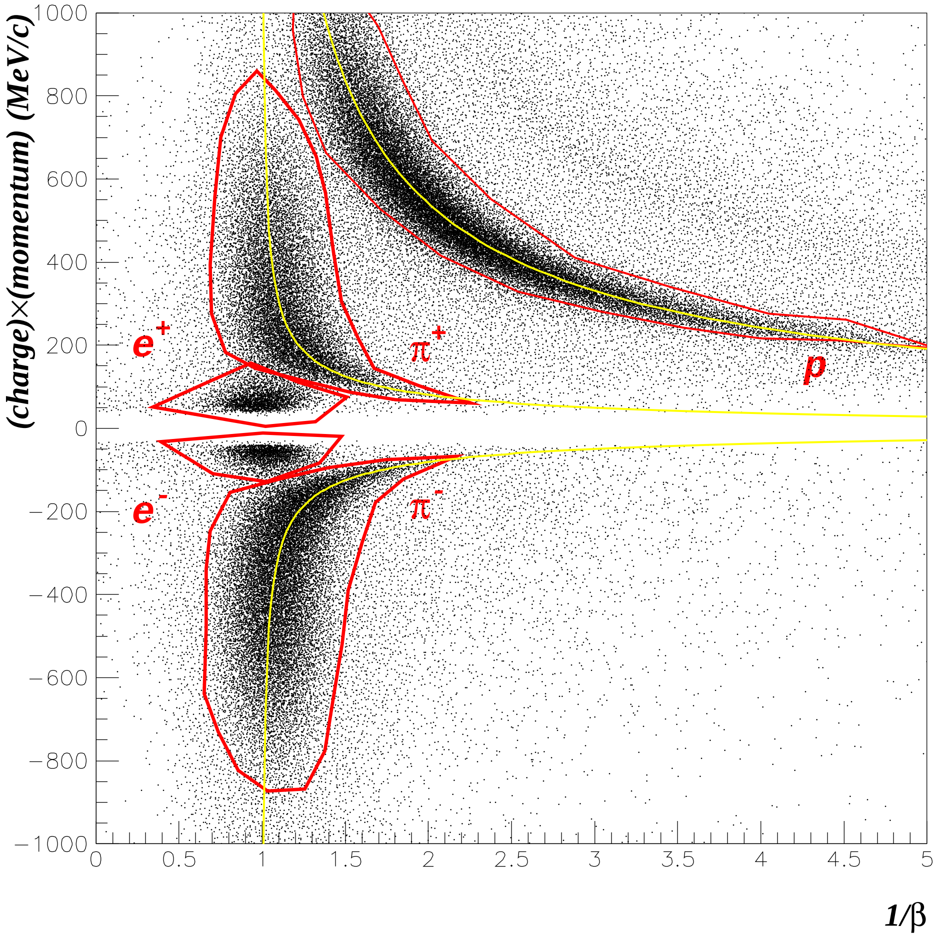

Figure 2.30: Momentum×charge versus $1/\beta$. Thick solid lines indicate the PID boxes. Thin white curves are $P = \pm m_\pi c/\sqrt{\beta^{-2}-1}$ and $P = m_p c/\sqrt{\beta^{-2}-1}$. The first stage of the event rejection is carried out, which is described in sec.2.3.3.

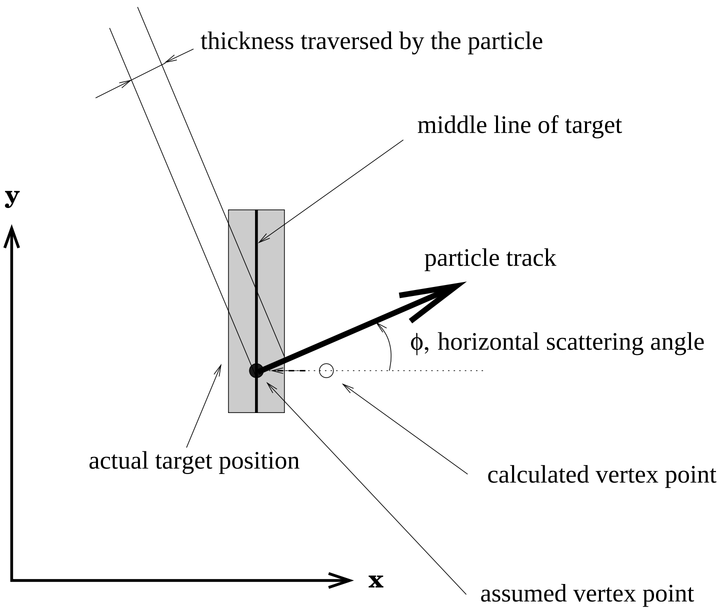

Figure 2.31: Vertex position and target thickness traversed by a track.

be at the middle of the target if the vertex point found is closest to that target (see Fig.2.31). Then the track is approximated with a straight line and the target thickness traversed by the particle is calculated. This yields the energy loss from the Bethe-Bloch equation. The results of the calculation are shown in Fig.2.32. There are peaks around the azimuthal scattering angle, $\phi = \pm 90°$, because on average the particle passes the largest length through the target. Typically, ~3 MeV for pions and ~5 MeV for protons were added to obtain the final kinetic energy because of the energy losses in the IH and the SDC materials.

2.3.3 $(\gamma, \pi^+\pi^-)$ Event Selection

Before proceeding to the detailed event selection, a sequence of crude event rejections, which may be called the first stage of the event selection, has already taken place. The first-stage event selection was carried out with the calibration process. This incorporated several sets of event rejections, each of which was accompanied by a step of the data analysis illustrated in Fig.2.11. Each set of the event rejections is described as follows:

Format Data → CDC Data The basic condition is that at least one, but less than five, trajectories were successfully reconstructed in each side of the CDC. A se-

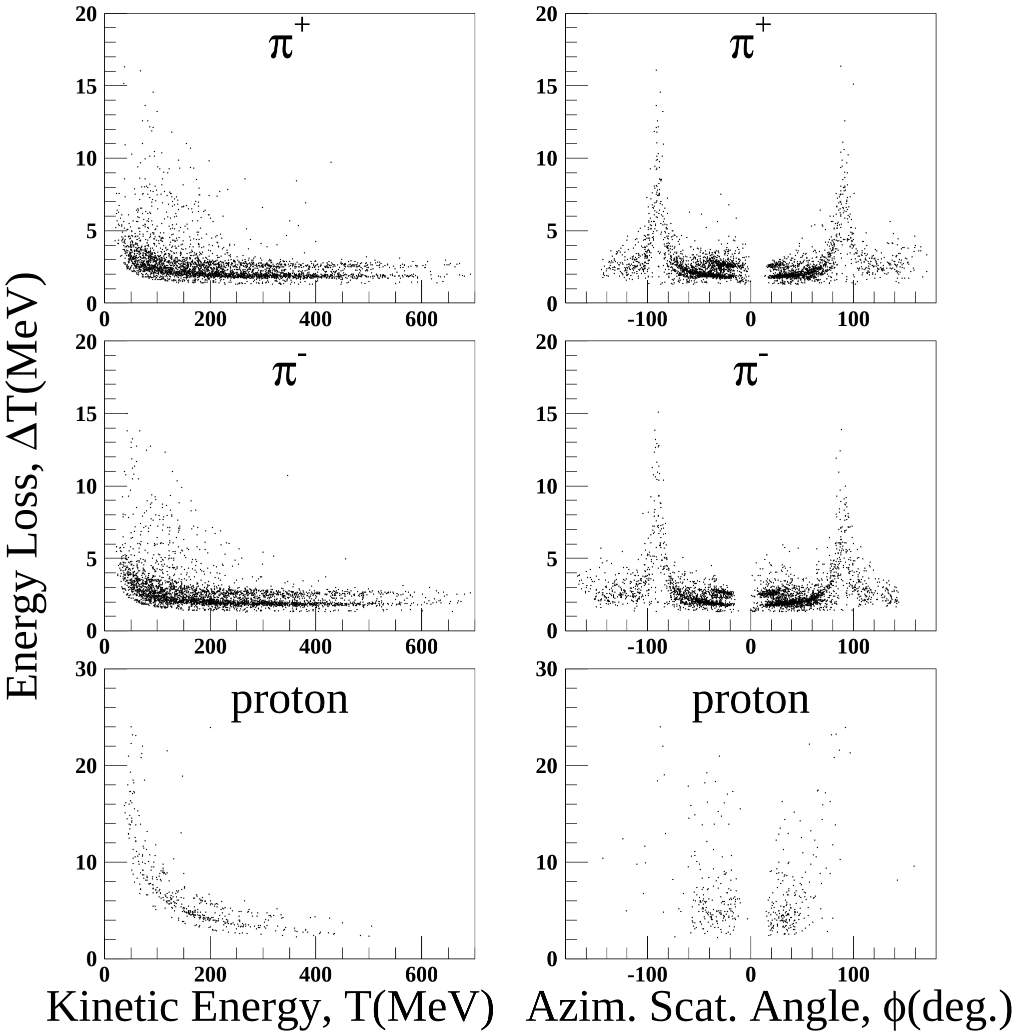

Figure 2.32: Estimation of the energy loss in the target and the TAGX detectors. The left panel is the energy loss versus particle kinetic energy. The right panel is the energy versus azimuthal scattering angle. The multiple lines in the plot are a result of the three layers of the target (see Fig.2.9).

ries of cuts was also placed on the number of TDC and ADC signals of the IH, OH and CDC, such that the cuts were consistent with the trajectory condition. Approximately 65% of the events in the Format Data sample (36M events) were rejected. Thus, the CDC Data were created with ~12.6M events.

CDC Data → SDC Data Once the SDC-CDC trajectories were finalized, events in which the closest vertex point is more than 5 cm away from the target center were rejected. Another ~11M events were thus rejected. This reduced the SDC Data to 1.89M events. Only 5.3% of the Format-Data events survived at this point.

SDC Data → Final Data Events were rejected if the photon energy could not be uniquely determined. The most common cause was a multiple hit in the tagging counter array[†]. An entire loop was also rejected if the scaler data had been recorded in a poor condition so that the photon flux could not be adequately estimated. Another 11k events were rejected as a result. The Final Data consisted of 1.86M events.

In addition, an entire run was rejected if the parameters were so poorly determined that the estimated resolutions for the planar momentum or the time of fight could not meet expectations. The cause was due to some hardware problem identified during the experiment. 1.68M events passed to the next stage of analysis.

The second stage of the event selection focussed on the double-pion production events by eliminating possible EM and other events. Events to be rejected were selected in a sequence of logical tests. The selection was based on:

1. At least one of (gas and aerogel) Čerenkov has a valid TDC value. The valid values include the electron peak region (6.2%).
2. At least one of the trajectories belongs to either e^+ or e^- box presented in Fig.2.30 (15.5%).
3. There is one track identified as π^+ *or* there is no track as π^-. Fig.2.30 was used for the identification (70.8%).

[†] There is an exceptional case where two consecutive tagging counters had been hit simultaneously. In this case, the photon energy was taken as the average value of the two and thus the event was retained.

4. There are more than two pions identified (0.037%).
5. There is no intersection between π^+ and π^- tracks (the argument of Cos^{-1} becomes larger than 1 in eq.(2.25)) *or* the vertex between π^+ and π^- tracks is more than 5 cm away from the target center (1.3%).
6. At least one track does not belong to any of the boxes presented in Fig.2.30 (1.1%).
7. There are more than one proton identified (0.0062%).
8. $|\cos\chi| \geq 0.99$, where $\chi = \phi(\pi^+) - \phi(\pi^-)$ is a difference of the $\pi^\pm$ azimuthal emission angles (see Fig.2.14) (0.13%).

If any of criteria 1–8 is true, the event was eliminated. The numbers in the parenthesis indicate the fraction of events rejected by the test *in this sequence* over 1.68M events. The conditions of the tests overlap each other, so the values do not indicate the ratios of such events. The last cut consists of two separate conditions. The upper part of the cut, $\cos\chi \geq 0.99$ aims to further suppress the possibility of e^+e^- events, which correspond to small opening angles. The lower part is for elimination of a poorly defined vertex point. Better vertex definition results in better separation between carbon and deuterium data because their separation only depends on the vertex position, as will be discussed in the following sections. From eqs.(2.23)–(2.26), one may find that the resolution of the vertex point is roughly proportional to $\Delta r_c/\sqrt{2(1+\cos\chi)}$, where Δr_c represents a typical size of error of r_c, radii of the trajectory circles. As a result of these cuts, only 4.6% of 1.68M events or 77k events survived as potentially good events. Cuts after Test 3 do not appear to be effective in terms of the presented percentage, but the last one, for example, eliminated about 2.8% from the data which survived up to Test 7.

2.3.4 Background Subtraction

After the EM background elimination in the previous section, there still remained a persistent background component that creates the uniform feature in the vertex position (see Fig.2.26 for example). The last attempt to eliminate this feature was to identify the background and subtract it from the signal. The background and signal component of the data may be estimated with the x-component of the vertex position. The foreground events may be assumed to have the vertex position at the proximity of the real target position. The qualitative estimate was done by fitting the distribution with a function,

$$\begin{aligned} f(x) &= b_0 + b_1 x + \sum_{i=1}^{3} A_i \{ g(x; \sigma_S, x_i, d_i) + r g(x; \sigma_C, x_i, d_i) \} \qquad (2.57) \\ g(x; \sigma, x_i, d_i) &= \frac{1}{2d_i} \left\{ \mathrm{erf}\left(\frac{x - (x_i - d_i/2)}{\sqrt{2}\sigma} \right) - \mathrm{erf}\left(\frac{x - (x_i + d_i/2)}{\sqrt{2}\sigma} \right) \right\} \end{aligned}$$

where $A_0, A_i, \sigma_S, \sigma_C$, and r are parameters to be determined, and x_i and d_i are the central target position and the thickness, respectively, which are known (see Fig.2.9). The function $g(x; \sigma, x_i, d_i)$ represents the vertex distribution around the i'th target with the σ diffusion parameters. When $d_i \to 0$, it approaches a Normal distribution, $N(x_i, \sigma^2)$. It may be formally obtained by applying a theorem presented in Appendix B letting

$$f_X(x) = \begin{cases} 1/d_i, & (|x - x_i| \le d_i/2) \\ 0, & (\text{otherwise}) \end{cases} \quad , \quad f_U(u) = \frac{1}{\sqrt{2\pi}\sigma} \exp\left(-\frac{u^2}{2\sigma^2} \right) .$$

It was assumed that $\sigma_S(\sigma_C)$ would give the position resolution when the track had been reconstructed with SDC(CDC only). The parameter r would be related to a ratio of number of CDC-only tracks to that of the SDC-CDC tracks. A_i estimated a magnitude of the foreground signal and $b_0 + b_1 x$ strength of the background.

Fig.2.33 shows the distribution and the function $f(x)$. The fitting found that

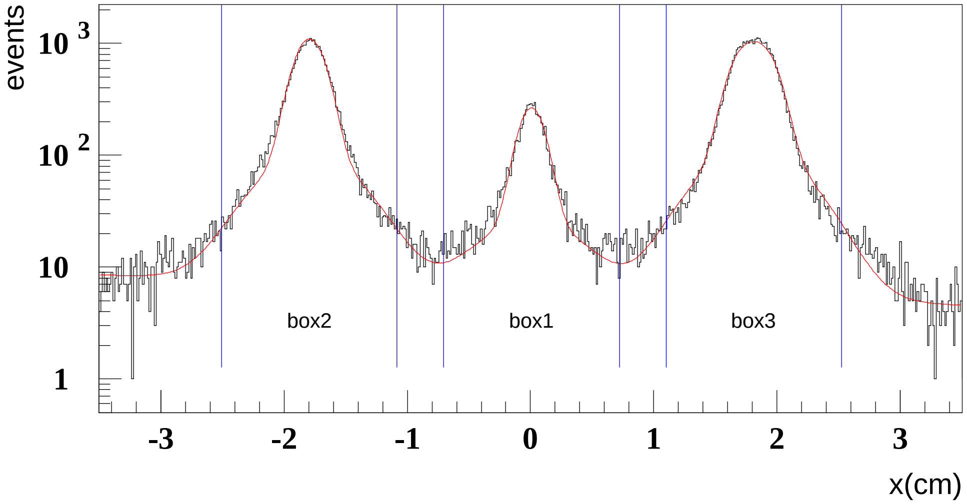

Figure 2.33: Distribution of the x-component of the vertex position. The smooth curve represents the fitting function, $f(x)$ (see text). The vertical lines indicate the borders of the boxes determined from the fitting.

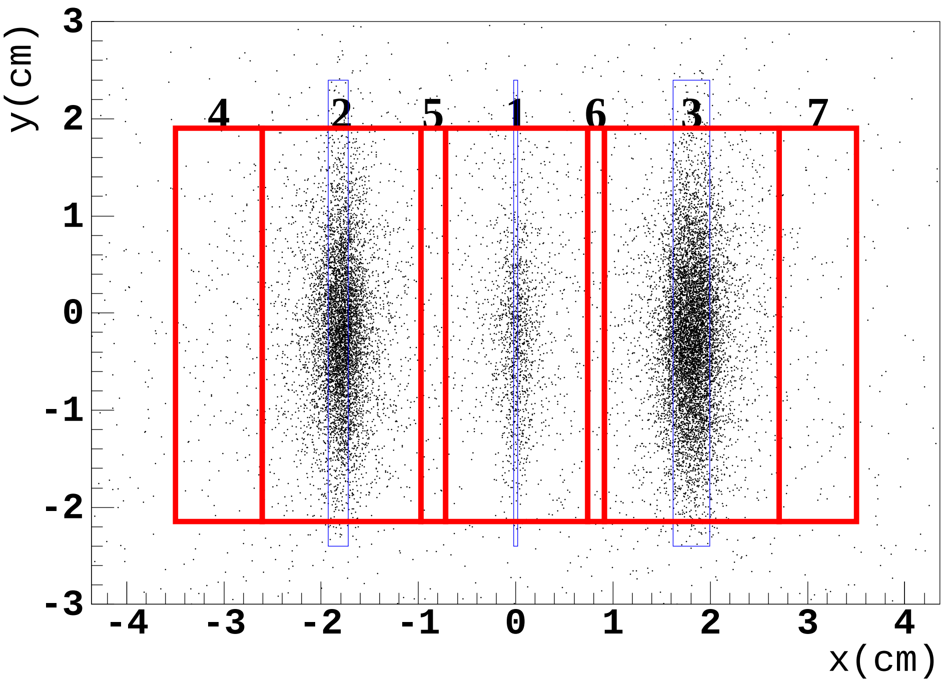

Figure 2.34: Vertex position scatter plot in the xy-plane. Thin squares with thiner lines indicate the actual target position. Central box is the graphite target. The thicker lines indicate the box cut. This figure defines the number of box as shown.

$$r = 0.294 \pm 0.011, \quad \sigma_S = 0.1015 \pm 0.001 \text{ cm}, \quad \sigma_C = 0.365 \pm 0.008 \text{ cm}.$$

Since these σ's should estimate the foreground region, the data were cut by $|x - x_i| \leq d_i/2 + 1.96\sigma_C$, or at the 95% confidence interval. A similar process was carried out on the y-component of the vertex. Because the y-distribution represents the interacting position of the photon beam, the fitting function was taken as a Gaussian distribution added with a linear term or

$$h(y) = a_0 + a_1 y + \frac{a_2}{\sqrt{2\pi}\sigma_{\text{beam}}} \exp\left(-\frac{(y - y_0)^2}{2\sigma_{\text{beam}}^2}\right),$$

where a_0, a_1, a_2, y_0, and σ_{beam} were constant parameters to be determined. The fitting found that $\sigma_{\text{beam}} = 0.784 \pm 0.004$ cm. Border lines were drawn at the 99% confidence interval or $|y - y_0| \leq 2.58\sigma_{\text{beam}}$. Together with the x-position cut, a box cut was now created as shown in Fig.2.34. Seven boxes are defined in the figure.

One may estimate the total number of background B_i in the box$\#i$ by performing the integration on the first two terms in eq.(2.57). That is,

$$B_i = \int_{x_i - t_i/2}^{x_i + t_i/2} (b_0 + b_1 x) dx = t_i (b_0 + b_1 x_i),$$

where t_i is the thickness of the box. When $i \leq 3$, $t_i = d_i + 2 \times 1.96\sigma_C$. Tab.2.6 lists the result of the integration. It reveals that more than 10% of the graphite data in box#1 are background. Also, boxes#4-7 are not completely dominated by the background; this makes the background subtraction a little more complicated.

Table 2.6: Estimation of number of background events, B_i. Y_i are the total number of events in the box#i. t_i is the thickness of the box. Boxes are defined in Fig.2.34.

box#	t_i[cm]	B_i/Y_i[%]	Y_i
1	1.468	11.44	6695
2	1.638	2.97	28733
3	1.806	2.68	35145
4	0.887	63.66	727
5	0.249	48.78	266
6	0.165	42.30	204
7	0.787	91.05	451

In order to obtain the foreground spectrum, one had to construct the background spectrum first. It was done with the data in boxes#4 and 7, which were subtracted from the data in boxes#2 and 3, respectively. The subtraction may be expressed by:

$$dY_{BG} = dY_4 - \frac{Y_4 - B_4}{Y_2} dY_2 + dY_7 - \frac{Y_7 - B_7}{Y_3} dY_3,$$

where dY represents the differential yield. Boxes#2 and #3 also contain some background, but the contribution is only about 3%. Data in box#5 and #6 were not used because they contain as much as 20% of the carbon data spilled over from box#1, which is different from the CD_2 signal. The true events in box#1, or the carbon spectrum, were now constructed by

$$dY_{\mathrm{C}} \equiv dY_{\mathrm{C}}(\#1) = dY_1 - \frac{B_1}{B_4 + B_7} dY_{BG}. \tag{2.58}$$

And the CD_2 spectrum was given by

$$\begin{aligned} dY_{\mathrm{CD_2}} &\equiv dY_{\mathrm{CD_2}}(\#2) + dY_{\mathrm{CD_2}}(\#3) \\ &= \left(dY_2 - \frac{B_2}{B_4 + B_7} dY_{BG} \right) + \left(dY_3 - \frac{B_3}{B_4 + B_7} dY_{BG} \right). \end{aligned} \tag{2.59}$$

2.3.5 Deuteron-Carbon Data Separation

It is obvious that the CD$_2$ data are composed of the carbon and deuteron data so that one may write

$$dY_{\mathrm{CD}_2}(\#i) = dY_{\mathrm{D}}(\#i) + dY_{\mathrm{C}}(\#i), \quad (i = 2 \text{ or } 3). \tag{2.60}$$

In order to obtain the deuteron spectrum, however, one has to know the carbon spectrum *in* the CD$_2$ spectrum. Because $dY_{\mathrm{C}}(\#2 \text{ or } 3)$ is unknown, one has to substitute the graphite spectrum, $dY_{\mathrm{C}}(\#1)$, which is already known from eq.(2.58). Adequate coefficients for the substitution may be found from the formula of the yield of the $(\gamma, \pi^+\pi^-)$ events expressed by:

$$dY(\vec{p}_{\pi^+}, \vec{p}_{\pi^-}) = \eta(\vec{p}_{\pi^+}, \vec{p}_{\pi^-}) N_\gamma N_T d\sigma(\vec{p}_{\pi^+}, \vec{p}_{\pi^-}), \tag{2.61}$$

where N_γ is the number of photons, N_T the number of target nuclei per unit area, $d\sigma$ the differential cross section, and η the detection efficiency. Following eq.(2.61), one may write

$$dY_{\mathrm{C}}(\#i) = \eta(\#i) N_\gamma N_{\mathrm{C}}(\#i) d\sigma_{\mathrm{C}}, \quad (i = 1, 2, 3). \tag{2.62}$$

These equations yield

$$dY_{\mathrm{C}}(\#i) = \frac{N_{\mathrm{C}}(\#i)\eta(\#i)}{N_{\mathrm{C}}(\#1)\eta(\#1)} dY_{\mathrm{C}}(\#1), \quad (i = 2 \text{ or } 3). \tag{2.63}$$

Substituting eq.(2.63) into eq.(2.60) yields

$$\begin{aligned} dY_{\mathrm{D}} &\equiv dY_{\mathrm{D}}(\#2) + dY_{\mathrm{D}}(\#3) \\ &= dY_{\mathrm{CD}_2} - \frac{N_{\mathrm{C}}(\#2)\eta(\#2) + N_{\mathrm{C}}(\#3)\eta(\#3)}{N_{\mathrm{C}}(\#1)\eta(\#1)} dY_{\mathrm{C}}. \end{aligned} \tag{2.64}$$

Now, the deuteron spectrum can be obtained in principle since dY_{CD_2} is given by eq.(2.59) and $N_{\mathrm{C}}(\#i)$ are listed in Tab.2.1. There is, however, a problem that the coefficient of $dY_{\mathrm{C}}(\#1)$ also depends on the pion momenta implicitly through the dependence of η. In principle, then, finding $\eta(\vec{p}_{\pi^+}, \vec{p}_{\pi^-})$ is possible but hardly useful. Usually, one wants to obtain a distribution which is the integrated form of the many-fold differential yield. The invariant mass spectrum is such an example. In such case, if one wants to extract $\eta(m_{\pi^+\pi^-})$, for instance, the knowledge of the carbon differential cross section will be required in order to properly weigh the distribution of the pion momenta. One can proceed to obtain a reliable carbon differential cross section from this experiment and then find an appropriate acceptance such as $\eta(m_{\pi^+\pi^-})$. For the present analysis, however, an easier approach was taken, instead. It was decided that the ratios $\eta(\#2)/\eta(\#1)$ and $\eta(\#3)/\eta(\#1)$ should be fixed. Although the precise effect of this methodology cannot be predicted with sufficient confidence, by giving these ratios some errors, the resulting spectrum may be justified. The fixed values of ratios were determined by taking an algebraic average of the results obtained by the Monte Carlo simulations made by assuming various reaction mechanisms that are described in the next chapter. The systematic error was taken from the standard deviation of the results. The determined values were photon-energy dependent and $\eta(\#2)/\eta(\#1) = 1.070 \pm 0.061$ and $\eta(\#3)/\eta(\#1) = 0.741 \pm 0.084$ for the highest energy bin (see Tab.3.3). It was found that each absolute value of η was strongly dependent on the reaction mechanism but the ratios were moderately stable (see Fig.3.11).

As shown in Fig.2.3, the photon energy distribution is highly non-uniform and very wide. It is desirable to make the photon energy range as narrow as possible to study the physics of the multi-pion photo-production. The data have to be separated into photon energy bins, but at the same time, have sufficient statistics to be properly analyzed. The actual data were separated into four photon energy ranges such that the number of events were equally distributed. The limits of the bins used are listed in Tab.2.7. Some examples of the present experimental data such as the dipion invariant mass spectra are presented in Appendix C.

Table 2.7: Photon energy bins and number of deuterium and carbon events in this experiment.

E_γ [MeV]	N_γ [$10^{10}\gamma$]	Y_{D} [events]	Y_{C} [events]
550– 810	10.41	6580± 554	1300±40.9
810– 890	8.23	6743± 439	1352±41.8
890– 975	6.95	6543± 420	1455±43.5
975–1105	6.44	6379± 466	1546±45.4
total	32.04	26245±2257	5653±87.9

Chapter 3

Monte Carlo Simulation

The primary objective of the Monte Carlo simulations for this experiment is to extract the TAGX acceptance, which is the remaining quantity necessary to extract the reaction cross section. However, the TAGX has only a π-sr geometrical acceptance, so in order to obtain the effective acceptance, knowledge of all double pion photo-production processes is required. In fact, this knowledge is a primary goal of this Thesis. Clearly, this task will involve careful assumptions based in part on information in the literature. One has to assume which reaction channels are relevant and then to assign a differential cross section to each. When the differential cross section is set, then the TAGX acceptance for a reaction will be found by simulating the performance of the TAGX spectrometer. The entire process is achieved with a simulation code, the TAGX Monte Carlo Simulation.

3.1 Concepts of the TAGX Monte Carlo Simulation

In order to reproduce the experimental data, the following four major steps have been established in the TAGX Monte Carlo Simulation:

1. Generation of the $(\gamma, \pi^+\pi^-)$ reaction events.
2. Transportation of the produced charged particles (mostly pions and protons) in the TAGX spectrometer.
3. Detection of the events with the virtual TAGX detector system.
4. Processing of Monte Carlo events, carried out in an identical manner to the data analysis treatment.

The generated Monte Carlo format is exactly the same as that of the experimental data and this facilitates their comparison. Because the double pion photo-production mechanism is the ultimate object of interest of the analysis, Step 1 is described in the following sections. The structure of the TAGX Monte Carlo Simulation presented here is based on the original code developed by K. Benslama.

The GEANT package is used for Step 2. Essentially, it deals with the energy loss, decay and other reactions while transporting a particle in the detector medium subject to the TAGX magnetic field. To ensure that the complex geometry of the TAGX was programmed correctly into the software, the GEANT drawing package was utilized as shown in Fig.2.6. Because the Čerenkov and beam veto counters were considered to be unimportant for these simulations, their presence was not included in the simulation. The reason for this is that leptonic background was not simulated in the Monte Carlo.

Particle detection with the TAGX (Step 3) is obviously the element most directly related with the overall TAGX acceptance. It dictates each detector efficiency as well as the resolution. Most of them have been obtained in the analysis described in the previous chapter. The following values were utilized for the actual simulation:

- The OH detection efficiency = 100%.
- The e-veto detection efficiency = 90%.
- Detection efficiencies for SDC and CDC = values in Tab.2.3.
- Resolution of the TOF between IH and OH = 380 ps.
- Resolution of the OH z-position = 1.3 cm.
- SDC-CDC momentum resolution = values in Tab.2.4.
- SDC-CDC azimuthal angle resolution = values in Tab.2.5.
- Resolution of the planar trajectory length = 1.5 cm.
- The IH signal is *on* when $C\Delta T_{\mathrm{IH}} \geq V_{th}$ is satisfied where

$$\begin{aligned}
C &= 30\ \mathrm{mV/MeV}\ \text{(IH pulse height conversion factor)} \\
\Delta T_{\mathrm{IH}} &= \text{calculated by GEANT}\ \left(\begin{array}{l}\text{transported particle's energy loss in-} \\ \text{side the IH scintillator}\end{array}\right) \\
V_{th} &= 10\ \mathrm{mV}\ \text{(IH discriminator threshold)}
\end{aligned}$$

The IH pulse height conversion factor was obtained from Ref.[28]. The threshold value of the IH discriminator as well as the OH and e-veto detection efficiencies were estimated according to the experimental record. The relative detection efficiencies among the OH paddles were found by comparing their counting rates during the experiment. A specific paddle, OHL14, was corrected to 75%. The event detection of the TAGX in the simulation was defined as

$$\text{MC Trigger} = \text{IHL} \bigotimes \text{IHR} \bigotimes \text{OHL} \bigotimes \text{OHR} \bigotimes \overline{\text{e-veto}},$$

which is analogous to the real trigger condition.

In Step 4, the second stage of the event selection described in sec.2.3.3 was applied to the Monte Carlo events. Because the Čerenkov detectors were not simulated, the Čerenkov cut (Test 1 on page 70) was omitted, which is an exception. A sample output of the simulation is displayed in Fig.3.1. The resolution imposed in Step 3 seems to reproduce the data distribution very well. This should lead to the extraction of meaningful detection acceptances from the simulation.

3.2 Generation of Events

The number of $(\gamma, \pi^+\pi^-)$ events to be simulated must follow dY in eq.(2.61) with $\eta = 1$. In order to determine the dY, one has to find each factor in the right hand side. The number of photons, N_γ, is given by the actual distribution shown in Fig.2.3. The number of targets is also available as shown in Tab.2.1. Therefore, only the differential cross section has to be evaluated. The simplest way to obtain the cross section is via the method of the plane wave impulse approximation (PWIA), in which one assumes that a particular transition from one state to another occurs instantly without any other interactions taking place either before or after. When the quasifree process, $\gamma A \to \pi^+\pi^- NB$, is written with the diagram shown in Fig.3.2, the off-shell PWIA yields [32]

$$d\sigma_{\text{PWIA}} = \frac{|\mathcal{M}_{el}|^2 S(\vec{p}, E)}{4(k \cdot p)} d\Phi_4(k + p_A; k_1, k_2, p', p_B), \tag{3.1}$$

where the spectral function, $S(\vec{p}, E)$, may be understood as a joint probability density function of a nuclear nucleon having its momentum, $\vec{p}$, and leaving the residual system, B, with the invariant missing energy, $E = m_N + m_B - m_A$[*]. $\mathcal{M}_{el}$ is the off-shell Lorentz-

---

[*] In this section, units are set with $\hbar = c = 1$. One may find that $E = -Q$, where Q is the Q value, the kinetic energy released by the reaction, $A \to NB$.

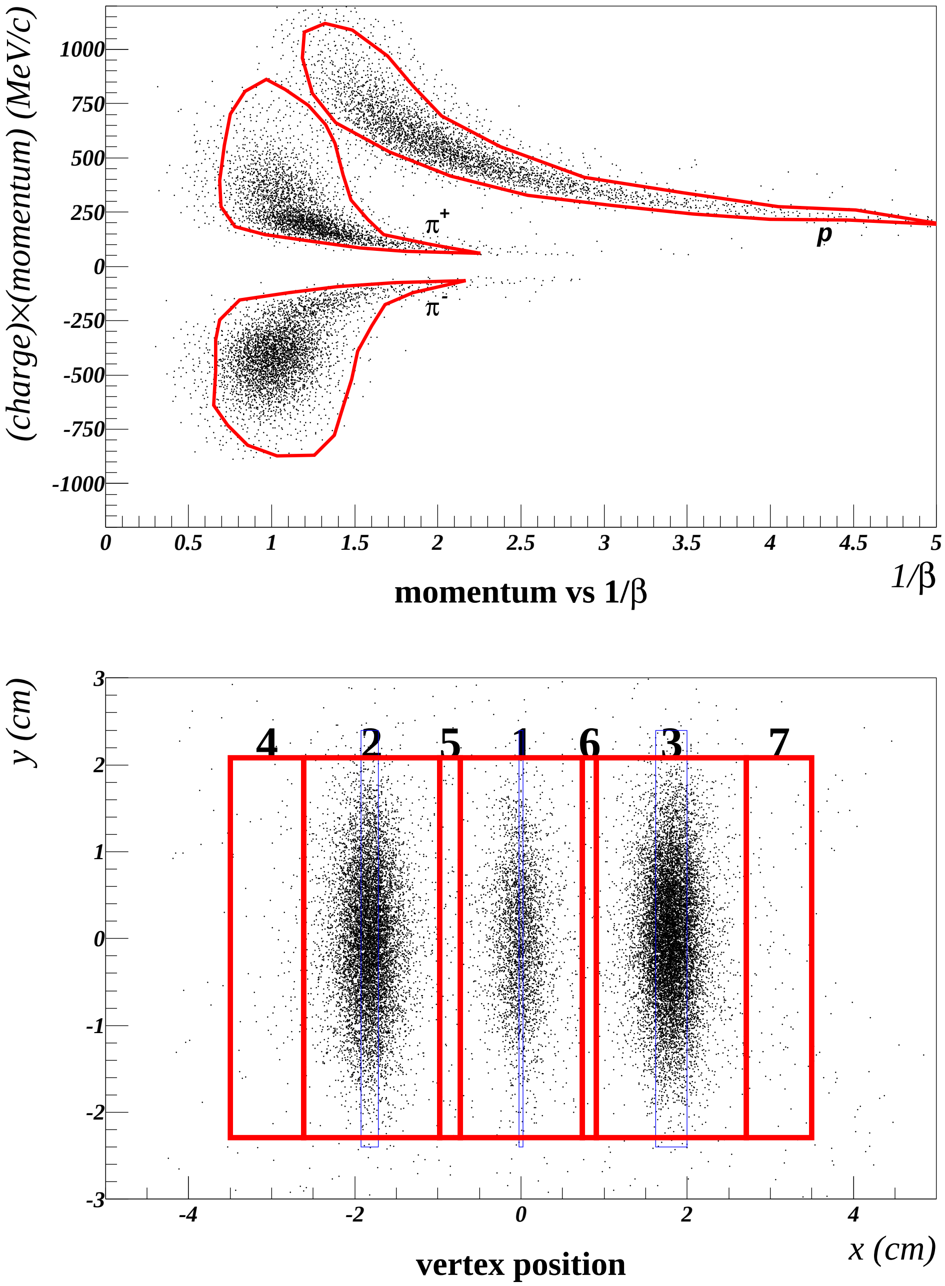

Figure 3.1: The PID plot (up) and vertex position (down) in the $^{12}C(\gamma, \Delta^{++}\pi^{-})^{11}B$ simulation. The solid lines are the same cuts used in the data analysis described in the previous chapter. For comparison, please see Fig.2.30 for PID and Fig.2.34 for vertex. Details of the event generation are described in sec.3.2. The electron/positron bands are absent in the top panel because they were not simulated.

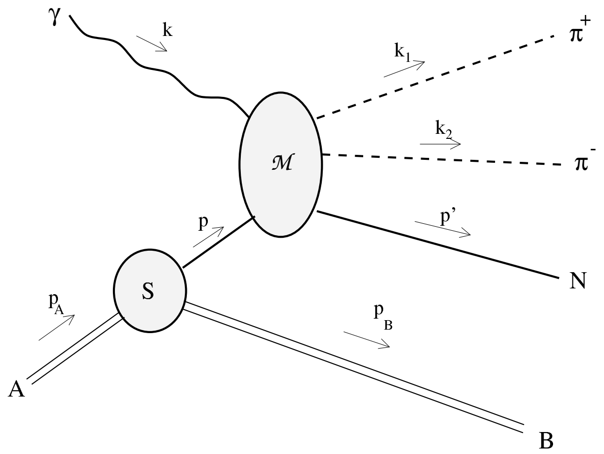

Figure 3.2: The diagram of the plane-wave impulse approximation for the quasifree reaction $\gamma A \to \pi^+\pi^- NB$. S denotes the spectral function and $\mathcal{M}$ represents the quasifree transition amplitude.

invariant transition amplitude for the elementary process, $\gamma N \to \pi^+\pi^- N$, and $d\Phi_n$ is an element of the n-body phase space given by [31]

$$d\Phi_n(P; p_1, p_2, \cdots, p_n) = (2\pi)^4 \delta^{(4)}(P - \sum_{i=1}^{n} p_i) \prod_{i=1}^{n} \frac{d^3 p_i}{(2\pi)^3 2E_i}.$$

So within the PWIA, finding the differential cross section is reduced to finding the amplitude $\mathcal{M}_{el}$ and the spectral function $S(\vec{p}, E)$. J. A. Gómez Tejedor *et al.* [44] have considered all the relevant processes with a hadronic model Lagrangian so it is certainly possible to obtain the amplitude $\mathcal{M}_{el}$ in an elaborate way. However, a much more practical approach is taken here, since model-independent results are desirable and this approach may be sufficient to reproduce the data. An additional benefit is that a simpler approach enables one to understand the reaction in a straightforward fashion.

The TAGX simulation code which originally developed by G. Huber formed the basic structure of this event generation code. Particularly, the code makes use of the n-body generator; the program developed in CERN is also an important part of the author's version as well. Essentially, the CERN program gives $d\Phi_n$.

In the following sections, a number of phenomenological reaction amplitudes will be introduced. It will be shown that the quasi-free assumption alone is not sufficient to reproduce the data so non-quasifree processes and final-state interactions are included, and described thereafter. It should be noted that only the form of the differential cross section is important here, because the absolute value of each individual total cross section will be determined in the next chapter. Therefore, all normalization constants will be omitted in the discussion below.

3.2.1 Elementary Amplitudes

There is an extensive database in the literature to determine many of the elementary photo-production-channel amplitudes. In particular, γp experiments including the 1 GeV photon energy region were conducted in 1960s and 1970s at DESY [33], CEA [34], and Frascati [35] using a hydrogen bubble chamber. A through study of multiple pion photo-production compiled by D. Lüke and P. Söding in 1971 is a valuable source of information [36]. The latest total cross section measurement for the $p(\gamma, \pi^+\pi^-)$ reaction up to 800 MeV photon energy at Mainz is in complete agreement with those of the preceding bubble-chamber experiments, but with much better precision [37]. Data on the γn reactions are, on the other hand, very sparse. A deuteron bubble chamber experiment at Frascati may be the most important constraint on γn amplitudes [38, 39].

Fig.3.3(a) shows the double pion photo production cross sections extracted from the DESY experiment by the ABBHHM collaboration. One can observe that the $\Delta^{++}\pi^-$ production is the dominant process below 1100 MeV, approximately the ρ^0 photo-production threshold, and it accounts for more than 70% of the double pion photo production cross section. The $\gamma n \to \pi^+\pi^- n$ cross sections in Fig.3.3(b) were extracted by F. Carbonara *et al.* from the Frascati deuterium experiment assuming that the proton was a spectator. The cross section also shows dominant $\Delta^-\pi^+$ production, the charge symmetric reaction of $\Delta^{++}\pi^-$. Both teams analyzed data by fitting the Dalitz plot, i.e., $m^2(N\pi)$ versus $m^2(2\pi)$, with the resonances and an assumed phase space background.

While all the $p(\gamma, \Delta^{++}\pi^-)$ data are similar, different models were used to try to interpret the data. Both the Frascati and CEA groups used the intermediate isobar model, which assumes that the reaction proceeds via a mixture of intermediate higher isobar states. The model considered all or some of $N^*(1440)P_{11}$, $N^*(1520)D_{13}$, $N^*(1680)F_{15}$, and $\Delta(1950)F_{37}$ resonances as the intermediate states. The DESY group adopted the gauge-invariant one pion exchange (OPE) model. Both the intermediate isobar model and the OPE model were not entirely successful in explaining the details of the data.

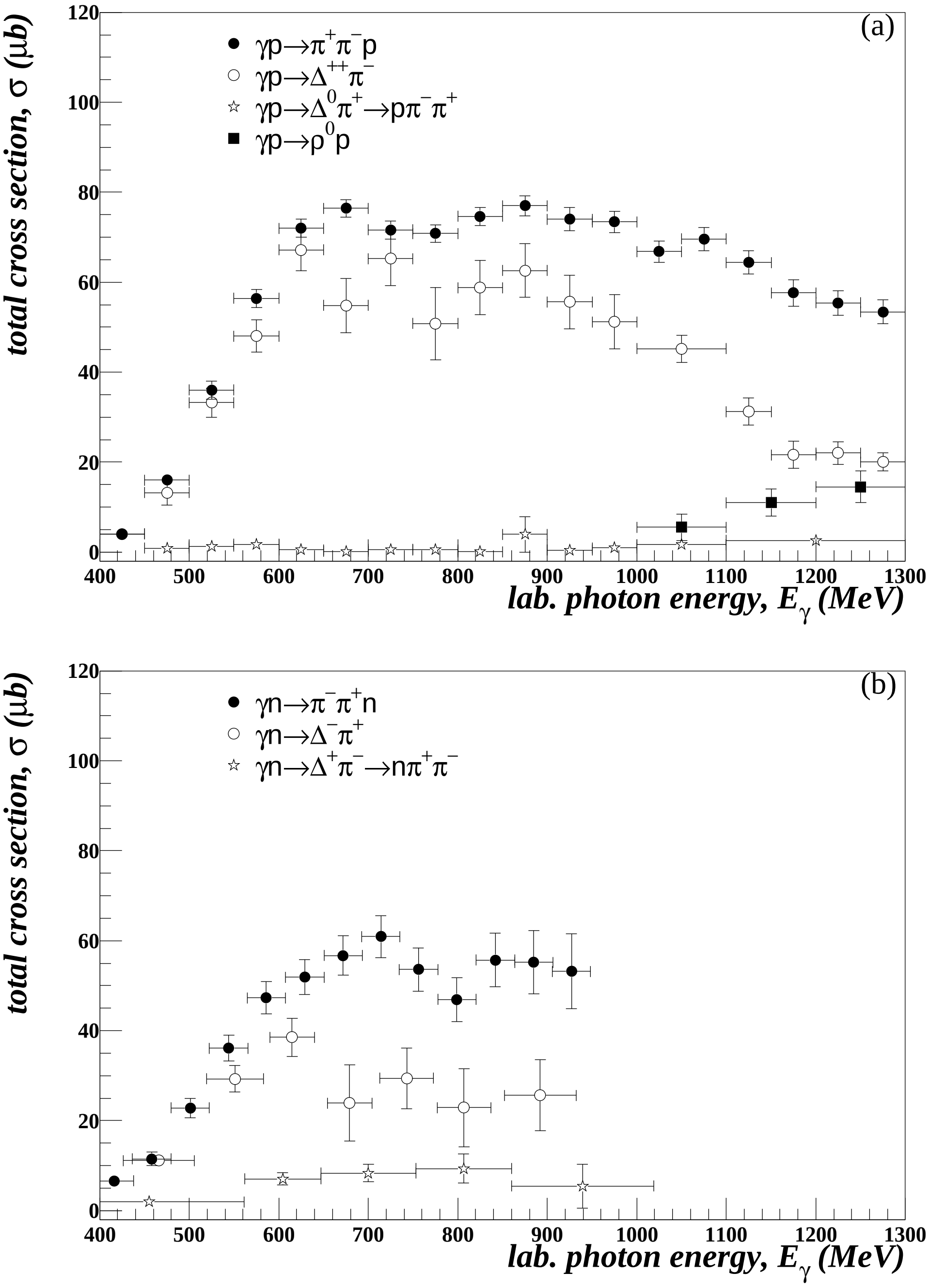

Figure 3.3: Total $\pi^+\pi^-$ photo production cross section as a function of laboratory photon energy on (a) a proton target measured by the ABBHHM collaboration [33]; and (b) on a neutron with the deuterium target by F. Carbonara *et al* [39].

The model was improved later on by including all four isobar states [40]. Fig.3.4 shows the $\Delta^{++}(1232)$ decay angular distributions, $W(\cos\theta_J)$, and the differential cross sections, $d\sigma/d\Delta^2$, for the reaction $\gamma p \to \Delta^{++}\pi^-$ in many different photon energy regions obtained by the ABBHHM collaboration in comparison with this model. Here, the decay angle is presented in the Gottfried-Jackson system [41]. The definition of θ_J is illustrated in Fig.3.5. It is the angle between the scattered proton momentum and that of the incident photon in the $p\pi^+$ center-of-mass frame. This system is useful in studying the nature of the exchanged particle because the quantization axis is (anti-)parallel to the momentum transfer [45]. Δ^2 is the absolute value of the square of the four-momentum transfer between incoming proton and Δ^{++}, or, $\Delta^2 \equiv -(p-(p'+k_1))^2$. More recently, a photo-nuclear absorption experiment at the photon energies of up to 1.2 GeV at Frascati has reported clearer evidence of photo excitations of these isobar

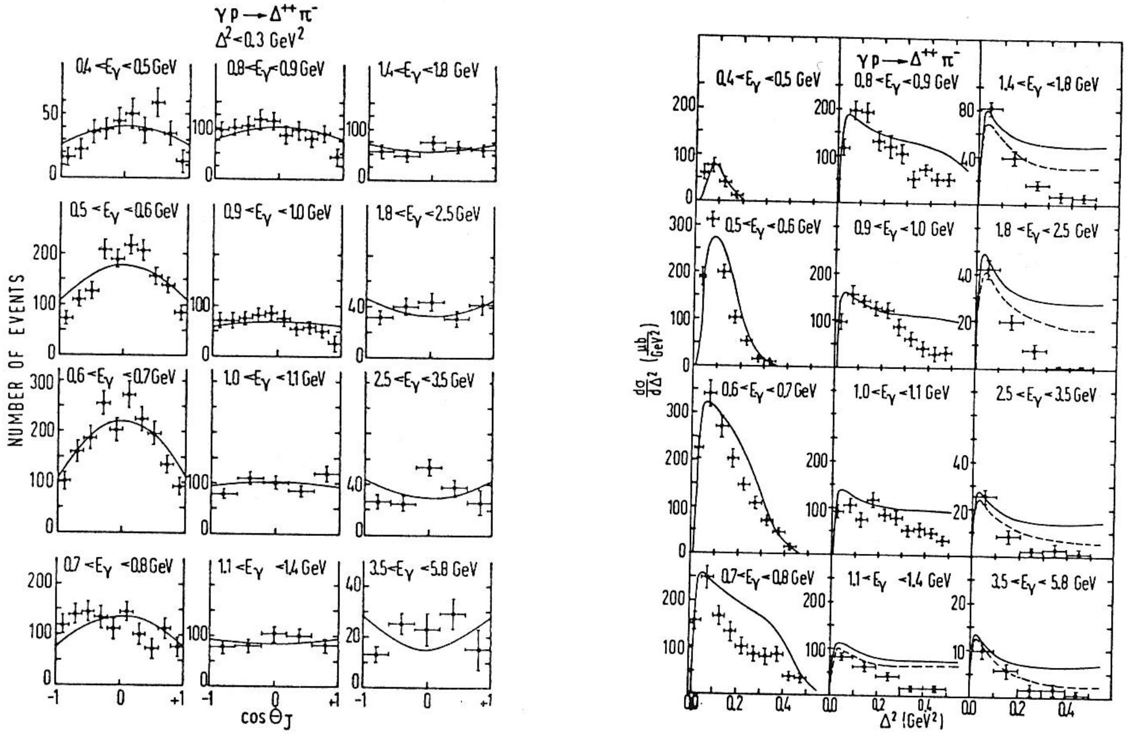

Figure 3.4: DESY data on the reaction $\gamma p \to \Delta^{++}\pi^-$ for various intervals of the photon energy, E_γ obtained by the ABBHHM collaboration. At left is the decay angular distribution of the Δ^{++} with $\Delta^2 \leq 0.3$ GeV^2, where Δ^2 is the absolute value of the square of the four-momentum transfer between incoming proton and Δ^{++}. At right is the differential cross sections $d\sigma/d\Delta^2$. The curves are the gauge-invariant OPE model with the inclusion of higher isobar states. Figure is from Ref.[33].

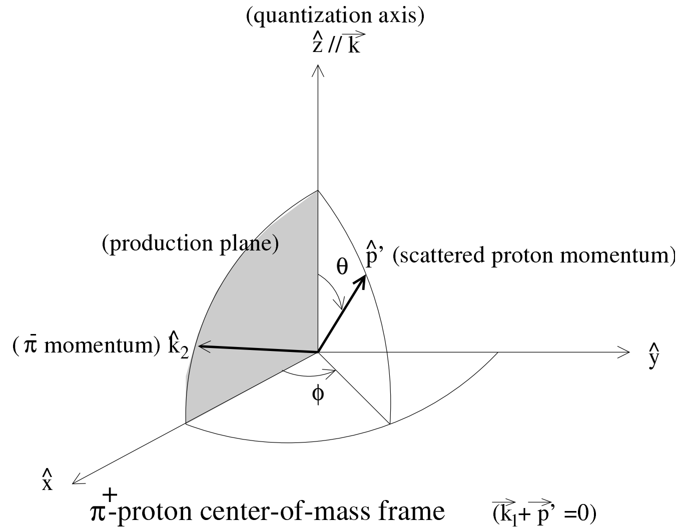

Figure 3.5: $\Delta^{++} \to p\pi^{+}$ decay angles (θ and ϕ) in the Gottfried-Jackson system [41].

states in the nuclear environment [42].

Perhaps the presence of the higher isobar resonances means that one has to incorporate them in the simulations to properly reproduce the data. However, explicitly simulating the resonances is a rather cumbersome approach because these isobar excitations in general interfere with each other and with other processes such as the OPE, the Δ exchange, or the contact interaction (Δ Kroll-Ruderman term), and largely unknown branching ratios have to be adjusted. As will be explained further in sec.4.1, simulating this interference is not particularly reliable under the present scope of this thesis. While the simulation as such is not perfect, it should be also noted that the present data may not discern a minor interference or even differences between similar processes. Particularly, the scattered nucleons were not detected in most cases when the simultaneous observation of two-pion momenta was the requirement in this experiment. Here, a much more practical approach to the problem was taken from the fact that all the isobar resonances decay to either $N\pi$, $N^{*}(1440)\pi$, $\Delta(1232)\pi$, $N\rho$, $N\eta$, or $N(\pi\pi)^{I=0}_{\text{s-wave}}$ [1]. The idea is to simulate these decay modes independently and then take the incoherent sum to reproduce the quasifree data. The interference among the processes which lead to the same decay mode would be simulated implicitly and adequately if the resulting differential cross sections yield the empirical values. It is, therefore, preferable to construct each Lorentz-invariant amplitude phenomenologically based on the empirical differential cross sections.

It can be shown from the properties of an element of n-body phase space [1],

$$d\Phi_n(P; p_1, \cdots, p_n) = d\Phi_2(q; p_1, p_2) d\Phi_{n-1}(P; q, p_3 \cdots, p_n) \frac{dq^2}{2\pi}$$

that $N(\pi\pi)^{I=0}_{\text{s-wave}}$ and $(N\pi\pi)_{\text{3BPS}}$ are exactly the same if the $(\pi\pi)^{I=0}_{\text{s-wave}}$ system is produced isotropically, where $(N\pi\pi)_{\text{3BPS}}$ is the $N\pi\pi$ system following the three-body Lorentz-invariant phase space. Also, if the $N^*(1440)$ is produced and decayed isotropically and the width of 350 MeV/c^2 is sufficiently large, then the $(N\pi\pi)_{\text{3BPS}}$ process is a good approximation to the $N^*\pi$ process. Since there are no angular information data on the photo-produced $N^*(1440)$ or $(\pi\pi)^{I=0}_{\text{s-wave}}$ system, an isotropic distribution in the total center-of-mass frame may be assumed. Therefore, the $(N\pi\pi)_{\text{3BPS}}$ simulation will represent both $N(\pi\pi)^{I=0}_{\text{s-wave}}$ and $N^*(1440)\pi \to N\pi\pi$. It should be understood that all the other conceivable quasifree processes such as the $N^*(1440)\pi$ production through the OPE are also represented by this simulation. Now all that is needed to simulate the quasifree double-pion photo production is to generate the four different final states, namely $\Delta(1232)\pi$, $N\rho$, $N\eta$, and $(N\pi\pi)_{\text{3BPS}}$.

$\Delta(1232)\pi$ Process

Because elementary $\Delta^{++}(1232)\pi^-$ production is a dominant process in the kinematic region of this experiment, this channel has been extensively investigated by many groups [36]. For the current simulation, it is assumed that the quasifree production amplitude is expressed by

$$\left|\mathcal{M}(\gamma p \to \Delta^{++}\pi^-)\right|^2 = W_*(\cos\theta_{\text{cm}}) W_\Delta(\cos\theta_J, \phi_J) f_\Delta(m_{p\pi^+}),$$

where θ_{cm} is the angle between the $\Delta(1232)$ momentum and that of the incoming proton in the center-of-mass rest frame. $W_*(\cos\theta_{\text{cm}})$ represents the distribution of this angle and was expressed by the Legendre polynomials,

$$W_*(\cos\theta_{\text{cm}}) = \frac{1}{2} + \sum_{l=1}^{\infty} A_l(s) P_l(\cos\theta_{\text{cm}}), \quad s = (p+k)^2. \tag{3.2}$$

$W_\Delta(\cos\theta_J, \phi_J)$ is the Δ decay angular distribution in the Gottfried-Jackson system, $m_{p\pi^+}$ is the $p\pi^+$-invariant mass, and f_Δ is the Δ resonance factor. Because the Δ has spin 3/2 and decays into a spin-1/2 nucleon and a spin-0 pion, the decay products generate the orbital angular momentum, $l = 1$ (p-wave). The orientation of the p-wave depends on the polarization of the Δ. Therefore, the angular distribution of the decay can be expressed in terms of the Δ density matrix elements [41],

$$\begin{aligned} W_\Delta(\cos\theta,\phi) &= \frac{3}{4\pi}\left\{\frac{1}{6}(1+4\rho_{33}) + \frac{1}{2}(1-4\rho_{33})\cos^2\theta \right. \\ & \left. -\frac{2}{\sqrt{3}}\mathrm{Re}(\rho_{3-1})\sin^2\theta\cos 2\phi - \frac{2}{\sqrt{3}}\mathrm{Re}(\rho_{31})\sin 2\theta\cos\phi\right\}. \end{aligned}$$

The coefficients $A_l(s)$ up to $l = 5$, as well as the the three density matrix elements, $\rho_{33}(s)$, $\mathrm{Re}(\rho_{3-1}(s))$, and $\mathrm{Re}(\rho_{31}(s))$, in the Gottfried-Jackson system, were all expressed with parameterized functions of s. This was aimed to reproduce the DESY data by the ABBHHM collaboration [33] which agree with other experiments and cover the photon energies of this experiment. The Δ resonance factor was given by the Breit-Wigner shape presented by Jackson [45],

$$\left.\begin{aligned} f_\Delta(m) &= \frac{m}{q(m)}\frac{\Gamma_\Delta(m)}{(m^2-m_0^2)^2+m_0^2\Gamma_\Delta^2(m)} \\ \Gamma_\Delta(m) &= \Gamma_0\left(\frac{q(m)}{q(m_0)}\right)^3\frac{2.2m_\pi^2+q^2(m_0)}{2.2m_\pi^2+q^2(m)} \\ q(m) &= \frac{\sqrt{(m^2-(m_\pi+m_N)^2)(m^2-(m_\pi-m_N)^2)}}{2m}. \end{aligned}\right\} \qquad (3.3)$$

The Bright-Wigner mass and full width, m_0, Γ_0 in the nuclear media were taken from Ref.[42]. The following values were actually used:

	m_0 [MeV]	Γ_0 [MeV]
deuteron	1241	161
carbon	1268	170

Similarly,

$$\left|\mathcal{M}(\gamma n \to \Delta^-\pi^+)\right|^2 = W_*(\cos\theta_{\mathrm{cm}})W_\Delta(\cos\theta_J,\phi_J)f_\Delta(m_{\pi^-n}), \qquad (3.4)$$

was assumed by symmetry.

The $\Delta^0\pi^+$ production cross section obtained by the DESY experiment in Fig.3.3 is present but very small. The result is in rough agreement with the CEA result, although the DESY group assumed that the $\Delta^0\pi^+$ process interferes with the $\Delta^{++}\pi^-$, whereas the CEA group did not. On the basis of isospin conservation, the production cross section ratio would be [34]

$$\frac{\sigma(\gamma p\to\Delta^0\pi^+\to p\pi^+\pi^-)}{\sigma(\gamma p\to\Delta^{++}\pi^-\to p\pi^+\pi^-)} = \left\{\begin{array}{ll} 1/9, & (I_s = 1/2 \text{ or OPE}) \\ 4/9, & (I_s = 3/2) \end{array}\right. ,$$

where I_s is the s-channel isospin. Both data gave less than 1/9 for most of the energy region.

There is no angular information for this reaction, so the isotropic assumption could be employed, unlike that of the $\Delta^{++}\pi^-$ case. However, as will be shown in the missing mass distribution, the angular dependence of the Δ rendered by the factor $W_*(\cos\theta_{\rm cm})$ is an important feature of the process[†]. In addition, there seems to be no particular reason to assume that the angular distribution of the $\Delta^0\pi^+$ process must be very different from that of the $\Delta^{++}\pi^-$ process. Therefore, it seems reasonable to simulate the $\Delta^0\pi^+$ process with the amplitude of

$$\left|\mathcal{M}\left(\begin{array}{lll}\gamma p & \rightarrow & \Delta^0\pi^+ \\ & & \hookrightarrow \pi^- p\end{array}\right)\right|^2 = W_*(\cos\theta_{\rm cm})W_\Delta(\cos\theta_J)f_\Delta(m_{\pi^- p}). \tag{3.5}$$

This amplitude is exactly the same as that of the $\Delta^-\pi^+$ process which is given by eq.(3.4) when the neutron is replaced with the proton. In other words, if one does not detect the nucleon and does not have the angular information, it is impossible to distinguish the two quasifree processes, $\Delta^0\pi^+$ and $\Delta^-\pi^+$. Similar arguments may also be used for the $\Delta^{++}\pi^-$ and $\Delta^+\pi^-$ processes. Though the present experiment occasionally observed the proton tracks, such evens were not statistically significant. It was therefore decided that only the $\Delta^{++}\pi^-$ and $\Delta^-\pi^+$ reactions, which are more important than the $\Delta^0\pi^+$ and $\Delta^+\pi^-$ and may be separable without proton detection, were considered in the present analysis. In any case, $\Delta^0\pi^+$ ($\Delta^+\pi^-$) is included implicitly in the $\Delta^-\pi^+$ ($\Delta^{++}\pi^-$) process, since they have similar distributions.

Quasifree ρ^0 Production

High energy photo production (E_γ = 5–10 GeV) of ρ^0 from various nuclei was extensively studied around 1970 at Cornell [52, 53], DESY [54], and SLAC [55]. A review of these data may be found in Ref.[56]. However, most of the data are concentrated on the coherent production, which completely dominates at forward production angle, particularly on heavier nuclei. A sizable contribution from incoherent photo production may be seen in ρ^0 photo production on deuteron [52]. It shows the same t distribu-

---

[†] Because the Δ^{++} tends to scatter in the backward direction (original direction of the proton), more energetic pions are generated by the $\Delta^{++}\pi^-$ process than by the $(N\pi\pi)_{\rm 3BPS}$ process, which is assumed to be completely isotropic. As a result, the missing-mass distributions exhibit significant differences between them (see Figs.4.1 and 4.20).

tion, $d\sigma/dt$, as was observed on hydrogen[‡]. The elementary reaction $\gamma p \to \rho^0 p$ is even more extensively studied at CEA [57], DESY [33, 54], SLAC [58, 59], and Cornell [52]. Ref.[60] by G. Wolf provides a useful summary. Exclusive ρ^0 production by muons,

$$\mu + N \to \mu + N + \rho^0$$

on deuterium, carbon and calcium were investigated by the NMC at the CERN-SPS [62] and may also be a useful reference. For the present analysis, following the experimental results given above, it is assumed that the transition amplitude for the quasifree (incoherent) process is given by

$$\left|\mathcal{M}(\gamma N \to \rho^0 N \to \pi^+\pi^- N)\right|^2 = e^{At} W(\cos\theta, \phi) f_\rho(m_{\pi^+\pi^-}), \tag{3.6}$$

where $W(\cos\theta, \phi)$ is the $\rho^0 \to \pi^+\pi^-$ decay angular distribution and f_ρ is the ρ-resonance factor. The factor e^{At} gives a strong forward-scattering effect, characteristic of the diffractive process, with the slope parameter $A \approx 6$ GeV^{-2}.

Because a spin-1 ρ^0 decays into two spin-0 pions, the orbital angular momentum of the pions must be a p-wave ($l = 1$) state. Like the $\Delta(1232)\pi$ process, when the incident photon is not polarized, the decay distribution can be expressed in terms of three elements of the ρ^0 density matrix, $\rho_{\lambda\lambda'}$, by [61]

$$\begin{aligned} W(\cos\theta, \phi) &= \frac{3}{4\pi}\left\{\frac{1}{2}(1-\rho_{00}) + \frac{1}{2}(3\rho_{00}-1)\cos^2\theta \right. \\ &\quad \left. -\sqrt{2}\mathrm{Re}(\rho_{10})\sin 2\theta\cos\phi - \mathrm{Re}(\rho_{1-1})\sin^2\theta\cos 2\phi\right\}, \\ &\quad \left(\mathrm{tr}[\rho] \equiv \sum_\lambda \rho_{\lambda\lambda} = \rho_{00} + \rho_{11} + \rho_{-1-1} = 1\right). \end{aligned}$$

Each diagonal element, $\rho_{\lambda\lambda}$, may be interpreted as a probability of having the helicity λ ($\lambda = 0, \pm 1$). Since a real photon has helicity ± 1 (transverse), $\rho_{00} = 0$ (or $\rho_{11} + \rho_{-1-1} = 1$) means the reaction conserves helicity[§], while $\rho_{00} = 1$ signifies the helicity as being completely flipped. When the decay distribution is integrated with respect to the azimuthal angle, it may become clearer:

$$W(\cos\theta) = \int_0^{2\pi} W(\cos\theta, \phi)d\phi = \frac{3}{4}\left\{(1-\rho_{00}) + (3\rho_{00}-1)\cos^2\theta\right\}.$$

[‡] $t \equiv q^2$, $q \equiv k' - k = p - p'$ where $\gamma(k) + N(p) \to \rho^0(k') + X(p')$. When a reaction is coherent or quasifree double-pion photo production ($p'^2 = p^2$), it can be shown that $t \leq 0$.

[§] It is certainly possible that the photon with helicity $\lambda = +1(-1)$ creates the ρ with $\lambda = -1(+1)$, which can be considered a helicity flip, but these processes ($\Delta\lambda = 2$) would be completely overwhelmed by the helicity conserving process.

In order to characterize the density matrices, however, one must specify the reference frame because the ρ helicity is frame dependent. Studies have shown that high energy photo production conserves the s-channel helicity when $t \geq -0.4$ GeV^2. But helicity flipping becomes also apparent when $-0.8 \leq t \leq -0.4$ GeV^2 (see, e.g., Ref.[58]). When the reaction is s-channel helicity conserving, the helicity system is a convenient choice [60]. It is defined in the rest frame of the dipion system. However, the z-axis (quantization axis) coincides with the direction of the dipion momentum in the rest frame of the total center-of-mass system. The y-axis is normal to the production plane (a plane which includes the z-axis and the photon momentum). The π^+ momentum specifies the decay angles. The definition is depicted in Fig.3.6. As will be described later, it is very difficult to isolate the ρ^0 signal near the production threshold, so the phenomenological polarization is not known in this photon energy region. For the present simulation, it was decided to independently simulate the helicity conserving and flipping processes, irrespective of the t value. Specifically, the simulation assumes either polarization of

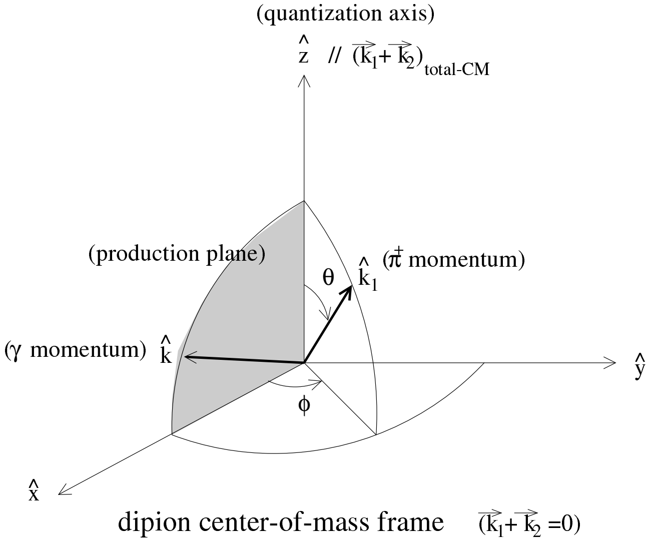

Figure 3.6: The dipion decay angles in the helicity system [61]. "total-CM" should refer to the γ-N rest frame when the quasifree reaction is considered. This would become the γ-A rest frame for the coherent production.

$$\begin{aligned} W(\cos\theta_{qH}) &= \frac{3}{4}\sin^2\theta_{qH} \quad \text{for transverse } \rho^0 \ (\lambda_{\rho^0}=\pm 1); \\ W(\cos\theta_{qH}) &= \frac{3}{2}\cos^2\theta_{qH} \quad \text{for longitudinal } \rho^0 \ (\lambda_{\rho^0}=0), \end{aligned}$$

where the subscript "qH" denotes the quasifree helicity system. Details of this angle are described in Appendix. D.

There are a few models as for the shape of the ρ^0 resonance. For the present simulation, the Jackson type p-wave Breit-Wigner shape is taken [45]. It is given by

$$\left.\begin{aligned} f_\rho(m) &= \frac{m}{q(m)} \frac{\Gamma_\rho(m)}{(m^2 - m_0^2)^2 + m_0^2 \Gamma_\rho^2(m)} \\ \Gamma_\rho(m) &= \Gamma_0 \left(\frac{q}{q(m_0)} \right)^3 \frac{2q^2(m_0)}{q^2 + q^2(m_0)} \\ q(m) &= \sqrt{\frac{m^2}{4} - m_\pi^2} \end{aligned}\right\} \tag{3.7}$$

with $\Gamma_0 = 150.7$ MeV, $m_0 = 770$ MeV. However, it has been shown by P. Söding [63] that the experimentally observed ρ^0 mass is reduced by about 30 MeV/c^2 due to an interference effect between the resonance and the Drell-type process¶ which is an OPE process with the virtual pion diffractively scattered by the target as shown in Fig.3.7. Other references in the literature use the Ross and Stololsky factor, $(m_0/m_{\pi^+\pi^-})^{n(t)}$, for the ρ^0 shape [60], which multiplies the Breit-Wigner factor and causes a skewed ρ^0 mass shape.

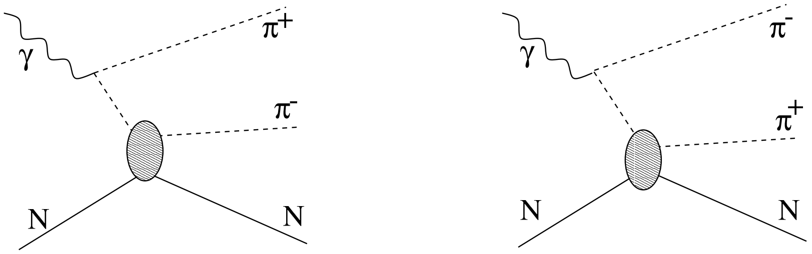

Figure 3.7: The diagrams for the Drell-type background. The exchanged pion is diffractively scattered by the target nucleon [64]. The diffraction causes the interference with the ρ^0 production process. See also, e.g., Refs.[63, 60] for the interference with the ρ^0 process.

The shape of the resonance is particularly important for this broad ρ^0 resonance at the threshold region because there is simply not enough energy to equally distribute the invariant mass below and above the peak. Therefore, restrictions due to available phase-space force the population to occupy the lower invariant mass regions, which are

---

¶This should not be confused with the term for the Drell-Yan process, $q\bar{q} \to \gamma^* \to l^+l^-$.

strongly dependent on the form of the lower part of the mass spectrum. The dipion invariant mass distributions at various photon energies are demonstrated in Fig.3.8, where two types of mass formulae are compared. The ρ^0 cross sections near the threshold estimated by the ABBHHM collaboration [33] and the ABHHM collaboration [49] at DESY are examples where the uncertainty in the line shape affected the ρ^0 cross-section determination. Both teams happened to use three different types of resonance spectra, but a different set (e.g. the Breit-Wigner, the Breit-Wigner with the Ross-Stololsky factor, and the Söding model were used by the ABBHHM collaboration) and the systematic differences are clearly visible. The lower the photon energy becomes, the larger are the deviations of the cross section with different line shapes presented. As much as a 35% difference is seen at 1.4 GeV photon energy, well above the threshold in Ref.[33]. One can therefore conclude that the resonance shape is a very sensitive and relevant issue. The Fermi motion, in case of a nuclear target, adds another complication because it causes the threshold photon energy to fluctuate depending on the direction of the Fermi momentum. However, this is expected to be less significant because the momentum distribution decays exponentially (see Fig.3.9), whereas the resonance factor has a much slower decreasing tail (see Fig.3.8). The explicit calculation is performed in Appendix E.

Because the exact shape of the ρ^0 resonance is not known, the present Jackson type resonance shape imposes this model dependency on the present analysis and result. In order to reduce the risk of this particular model dependency propagating into the final results of other reaction channels, the Drell-type background simulation was introduced separately from the ρ^0 simulation. The scheme is that the Drell simulation adjusts the skewness of the resonance so that the true resonance may be contained within the ρ^0 and Drell simulations. The Drell amplitude was taken as

$$|\mathcal{M}(\text{Drell process})|^2 = e^{At}$$

with $A = 6\ \text{GeV}^{-2}$. The detailed structure of the Drell process, such as the pion propagator, were all omitted in this form. When this is presented later, one should be cautious in interpreting the cross section or its spectra because the Drell simulation here is not designed to simulate the Drell process only. For both the ρ^0 and Drell simulations,

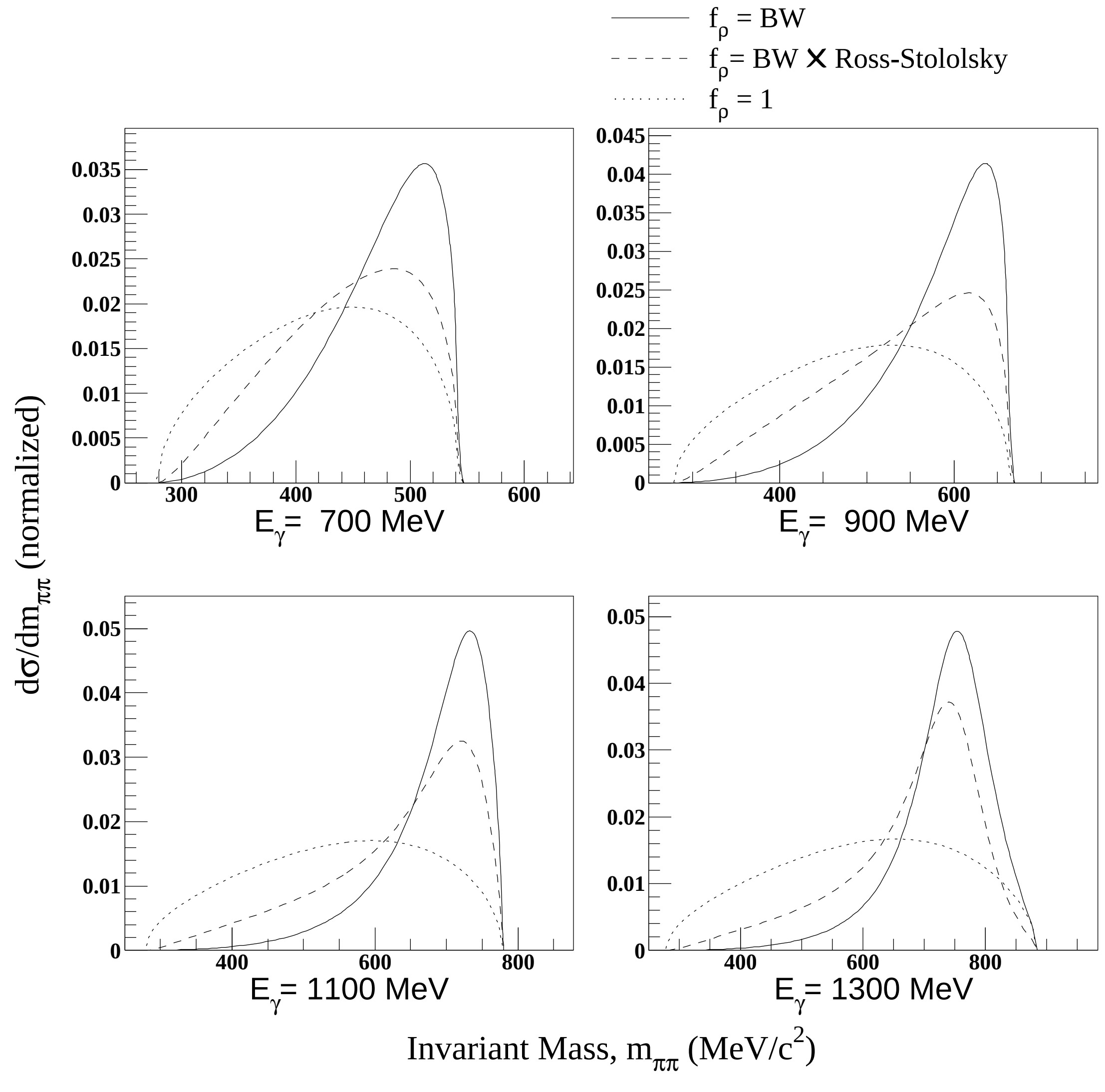

Figure 3.8: An estimate of the dipion invariant mass distribution $d\sigma/dm_{\pi\pi}$ for the reaction $\gamma p \rightarrow \rho^0 p$ at four different laboratory photon energies. The solid line is the Breit-Wigner shape given by eq.(3.7). The dashed line is the Breit-Wigner multiplied by $(m_0/m)^4$. The dotted line is the flat spectrum, $f_\rho = 1$. See eq.(E.2) for detail.

the cross section ratios were assumed to be

$$\frac{\sigma(\gamma n \to \rho^0 n)}{\sigma(\gamma p \to \rho^0 p)} = \frac{\sigma(\mathrm{Drell}\gamma n)}{\sigma(\mathrm{Drell}\gamma p)} = 1,$$

on the basis of the isospin symmetry.

ρ^0 production can occur via s-channel resonances, which create a weak t dependence in the differential cross section. In the high energy region, the diffractive production seems to dominate, but the intermediate resonance processes could be significant at the lower energies. In fact, it is predicted that there is an enhancement around $E_\gamma = 760$ MeV in the ρ^0 production cross section because of a large coupling of $N^*(1520)$ to the $N\rho$ decay mode [65]. However, identifying the process, $\gamma p \to N^*(1520)^* \to N\rho^0$, would be difficult because of the flat t dependence. In order to isolate this process, one may have to analyze the data in a more sophisticated manner, such as simultaneous study of the ρ^0 decay angles with respect to the ρ^0 scattering angles. The present simulation only focuses on the diffraction-like ρ^0 production.

Mass Shift of the ρ^0 in the Nuclear Medium

It has been an interesting topic of hadron physics that an enhancement in the e^+e^--pair invariant mass below the ρ/ω resonance region, observed in the heavy-ion experiments at CERN-SPS [6] and in the $p+A$ reactions at KEK [8], is an indication of the modified ρ^0 mass in a hot and dense hadronic medium predicted by theories [4, 5] inspired by chiral symmetry restoration. A rather direct ρ^0 mass measurement has also been reported by the TAGX collaboration using $^3\mathrm{He}(\gamma, \pi^+\pi^-)X$ [9, 10], which may be summarized as

$$m_\rho^* \approx 655 \text{ MeV}, \quad \Gamma_\rho^* \approx 151 \text{ MeV}, \quad (E_\gamma = 800\text{–}1120 \text{ MeV}).$$

It leads to the medium modified ρ^0 simulation with an amplitude of

$$\left|\mathcal{M}(\gamma N \to \rho^{0*} N)\right|^2 = e^{At} f_{\rho^{0*}}(m_{\pi^+\pi^-})$$

where $m_0 = 655$ MeV and $\Gamma_0 = 150.7$ MeV.

Later theoretical models (see, e.g., Refs.[65, 66]), on the other hand, have predicted a small decrease of the central mass but a dramatic broadening of the width. If it is actually the case, a part of the broadened ρ^0 events should be registered in the Drell simulation, since both would create an invariant mass spectrum that mainly follows the phase space. In a way, it is understood that the Drell process correspond to a ρ resonance shape (or the ρ spectral function) with $f_\rho = \text{const}$. In other words, it is not possible from the present analysis to distinguish the broadened ρ^0 from the Drell-type background. Therefore, it should be understood that the Drell simulation could also include the modified ρ^0 with a strongly widened mass spectrum.

$(N\pi\pi)_{\mathrm{3BPS}}$ Production

As described above, the simulation is intended to accommodate $(\pi\pi)^{I=0}_{\text{s-wave}}$ and $N^*(1440)\pi$ production. The interference term between $\Delta^{++}\pi^-$ and $\Delta^0\pi^+$ could also be registered, if it has sufficient strength. Evidently, one may write

$$|\mathcal{M}\left(\gamma N \to (N\pi\pi)_{\mathrm{3BPS}}\right)|^2 = \text{const.}$$

η Production

The isobar resonances which have the largest branching ratio decaying into the η meson are $N^*(1535)S_{11}$ and $N^*(1650)S_{11}$ [1]. The η has charged decay modes,

$$\begin{aligned} \Gamma(\eta \to \pi^+\pi^-\pi^0)/\Gamma_{\text{total}} &= 23.1 \pm 0.5\% \\ \Gamma(\eta \to \pi^+\pi^-\gamma)/\Gamma_{\text{total}} &= 4.77 \pm 0.13\%, \end{aligned}$$

which may be detected by TAGX. In the simulation, the production amplitude is assumed to take the following form:

$$|\mathcal{M}(\gamma N \to \eta N)|^2 = f_{N^*(1535)}(m_{\eta N}) + f_{N^*(1650)}(m_{\eta N}),$$

where $f_{N^*}(m)$ is a N^* resonance factor given by [45]

$$\begin{aligned} f_{N^*}(m) &= \frac{m}{q(m)} \frac{\Gamma_{N^*}(m)}{(m^2 - m_0^2)^2 + m_0^2\Gamma^2_{N^*}(m)} \\ \Gamma_{N^*}(m) &= \Gamma(N^* \to \eta N)\frac{q(m)}{q(m_0)}\frac{m_0}{m} \\ q(m) &= \frac{\sqrt{(m^2 - (m_\eta + m_N)^2)(m^2 - (m_\eta - m_N)^2)}}{2m} \end{aligned}$$

with $m_0 = 1535$ or 1650 MeV. The partial widths are given by [1]

$$\begin{aligned} \Gamma(N^*(1535) \to \eta N) &= 55\% \times 150 \text{ MeV} \\ \Gamma(N^*(1650) \to \eta N) &= 10\% \times 150 \text{ MeV.} \end{aligned}$$

With this form, the η is produced isotropically in the photon-nucleon center of mass frame, which conforms to the s-wave decay of the resonances. The recent differential cross section data from the $\gamma + d \to \eta + X$ experiment near the threshold conducted at the Mainz Microtron (MAMI) [48] clearly shows the s-wave production of η. The same experiment also finds that $\sigma(\gamma n \to \eta n)/\sigma(\gamma p \to \eta p) \simeq 0.68$. This is also incorporated in the present simulation.

Three Pion Production

The threshold photon energy for an elementary multi-pion photo-production is given by

$$E_{\gamma th}(n) = n m_\pi \left(1 + \frac{n}{2}\frac{m_\pi}{m_N}\right),$$

where n is the number of pions produced. Although the quadruple-pion photo-production threshold on proton is 723 MeV, the cross section is negligible below 1 GeV [33]. Based on the available energy in this experiment, multiple-pion photo-production is manifest only up to three pions. Besides the η production, conceivable three-pion production processes such as

$$\begin{array}{rl} \gamma + N \;\to N^{**} \to & N^*(1440) + \pi \\ & \hookrightarrow \Delta + \pi \end{array}$$

could be important to account for our experimental data. In fact, this particular process should appear if $N^*(1440)\pi$ production, approximated by the $(N\pi\pi)_{\mathrm{3BPS}}$ simulation, is present at all, because the $\Delta\pi$ is another important decay mode for the $N^*(1440)$ [1]. By isospin invariance, it may be shown that quasi-free 3π production with this type of process has a cross section ratio,

$$\begin{aligned} \pi^+\pi^-\pi^0 : \pi^+\pi^+\pi^- &= 5:2 \qquad \text{(proton target)} \\ \pi^+\pi^-\pi^0 : \pi^+\pi^-\pi^- &= 5:2 \qquad \text{(neutron target)} \end{aligned}$$

where double-neutral pion production is omitted. The transition amplitude is assumed constant so that the final state of the $N3\pi$ follows the four-body phase space, that is,

$$d\sigma(\mathrm{QF}3\pi) = \frac{|\mathcal{M}_{el}(\mathrm{QF}3\pi)|^2 S(\vec{p}, E)}{4(k \cdot p)} d\Phi_5(k + p_A; k_1, k_2, k_3, p', p_B),$$

with $\mathcal{M}(\mathrm{QF}3\pi) = \mathrm{const}$.

3.2.2 Coherent 2π Production

The $\gamma d \to \pi^+\pi^- d$ Reaction

As mentioned above, there have been a number of studies on coherent ρ^0 photo production with the most relevant reference being the DESY experiment by the ABHHM collaboration [49], which investigated the coherent 2π photo production on deuterium near the ρ^0 threshold region. There, forward angle 2π differential cross sections were fitted by an exponential function,

$$\frac{d\sigma}{dt} = Ae^{Bt}$$

with $B \approx 24$ GeV^{-2}. The s-channel helicity conservation was observed for the ρ^0 resonance region when $|t|$ is small ($0.04 \leq |t| \leq 0.20$ GeV^2). These results are reflected in the present simulation, which assumes that

$$\begin{aligned} \left|\mathcal{M}(\gamma d \to \rho^0 d \to \pi^+\pi^- d)\right|^2 &= e^{Bt} W(\cos\theta_{cH}) f_\rho(m_{\pi^+\pi^-}) \qquad (3.8) \\ |\mathcal{M}(\text{coherent Drell-type background})|^2 &= e^{Bt}, \end{aligned}$$

where $W(\cos\theta_{cH})$ is the ρ^0 decay angular distribution in the coherent helicity system depicted in Fig.3.6. The system has a preferred quantization axis when the s-channel helicity is conserved. The axis differs from the quasifree helicity system because the four-momentum of the center of mass (s-channel) is the sum of four-momenta between the incident photon and the target nucleus, instead of the target nucleon. As is done for the quasifree process, the simulation considers two polarized states in this system:

$$\begin{aligned} W(\cos\theta_{cH}) &= \frac{3}{4}\sin^2\theta_{cH} \quad \text{for helicity conserving (transverse polarization);} \\ W(\cos\theta_{cH}) &= \frac{3}{2}\cos^2\theta_{cH} \quad \text{for helicity flipping (longitudinal polarization).} \end{aligned}$$

Phase Space Background

In addition to the Drell-type background, the phase space background,

$$\left|\mathcal{M}\left(\gamma d \to (\pi^+\pi^- d)_{\rm 3BPS}\right)\right|^2 = \text{const.}$$

is also considered. The reason for this is to cover the model-dependent forward producing factor e^{24t}. This phase space background process will not be considered for carbon since carbon simulations take a different approach to the differential cross section as written below.

The γC $\rightarrow$ $\pi^+\pi^-$C Reaction

For coherent ρ^0 production on carbon, the optical model gives the coherent ρ^0 amplitude written as [56]

$$f_c = 2\pi f_0 \int_0^\infty \int_{-\infty}^\infty \rho(b,z) J_0(bq_b) e^{iq_z z} \exp\left\{ -\frac{\sigma_{VN}}{2}(1 - i\beta_V) \int_z^\infty \rho(b,z')dz' \right\} dzbdb, \quad (3.9)$$

where f_0 is the spin and isospin independent part of the photo-production amplitude of the boson V on nucleus, b and z are coordinates respectively orthogonal and parallel to the direction of flight of the incoming photon, $\rho(b,z)$ is the nuclear matter distribution, $\vec{q}$ is the momentum transfer to the nucleus. The overall production amplitude may be then written as

$$\left|\mathcal{M}(\gamma\text{C} \rightarrow \rho^0\text{C} \rightarrow \pi^+\pi^-\text{C})\right|^2 = |f_c|^2 f_\rho(m_{\pi^+\pi^-}) W(\cos\theta_{cH}).$$

f_0 is taken as a constant. σ_{VN} and $\beta_V \equiv \text{Re}[f_{VN}(0)]/\text{Im}[f_{VN}(0)]$ (f_{VN} is the VN elastic scattering amplitude) are very roughly approximated with the $\pi^0 N$ values. This π^0 approximation serves merely to provide the diffractive nature of the process that brings about the carbon version of the factor e^{Bt} in eq.(3.8). To obtain the $\pi^0 N$ scattering amplitude and the total cross section, please see Appendix F.

In the coherent production, the target nuclei are assumed to remain intact for both deuteron and carbon cases. This simplifies the form of the differential cross section to

$$d\sigma = \frac{|\mathcal{M}|^2}{4E_\gamma m_A} d\Phi_3(k + p_A; k_1, k_2, p_A).$$

3.2.3 Non-Quasifree Processes

For the non-quasifree process on deuterium, the cross section may be given by

$$d\sigma = \frac{|\mathcal{M}|^2}{4E_\gamma m_d} d\Phi_4(k + p_d; k_1, k_2, p_p', p_n'). \quad (3.10)$$

The corresponding reaction on carbon may be assumed as one in which the incident photon interacts with a proton-neutron pair (quasi-deuteron). In this case, one has to know the quasi-deuteron equivalent of the spectral function in carbon in order to write a correct PWIA cross section. For the present analysis, it is devised that the quasi-deuteron spectral function is a product of two nucleon spectral functions. One then may be able to write the cross section as

$$d\sigma = \frac{|\mathcal{M}|^2 S(\vec{p_p}, E_1) S(\vec{p_n}, E_1)}{4k \cdot (p_p + p_n)} d\Phi_5(k + p_A; k_1, k_2, p'_p, p'_n, p_B). \tag{3.11}$$

Consideration of this process seems to become relevant when one observes fairly large cross sections for double $\Delta(1232)$ photo-production on deuterium measured by M. Asai *et al.* [47] and Y. Wada *et al.* [46], as shown in Fig.4.14. The cross section is quite large ($\sim$40 μb) so it is important to incorporate the process into the simulation. The amplitude may be simply written by

$$\left|\mathcal{M}(\gamma d \to \Delta^{++}\Delta^{-})\right|^2 = f_\Delta(m_{p\pi^+}) f_\Delta(m_{n\pi^-}),$$

where f_Δ is the resonance factor given by eq.(3.3). The process, $\gamma d \to \Delta^+\Delta^0 \to \pi^+\pi^- pn$, is also present, in principle, but the cross section is expected to be about 1/81 of that of $\Delta^{++}\Delta^-$ by the vector meson dominance model and isospin symmetry [47]. This is small enough to ignore in the present analysis.

Following the work of M. Asai [47], the four-body phase space background (4BPS) is also considered. It is given by

$$\left|\mathcal{M}\left(\gamma + A \to (\pi^+\pi^- pn)_{\mathrm{4BPS}} + X\right)\right|^2 = \mathrm{const.}$$

which is to be substituted only in eqs.(3.10) or (3.11). This is designed to exclude the $\Delta^{++}\Delta^-$ process from other possible double-resonance channels such as $N^*\Delta$ or $2N^*$ or any deuteron quasifree processes that give rise to significant FSI, which cannot be dealt with the usual three-body phase space treatment. (It is possible to view a quasifree reaction followed by a quasi-elastic scattering or FSI as a kind of transition involving two nucleons.) The FSI for carbon will be treated explicitly in a later section.

3.2.4 Nuclear Spectral Functions

The spectral function introduced in sec.3.2 may be written in the factorized form [32],

$$S(\vec{p}, E) = \sum_\alpha \rho_\alpha(|\vec{p}|) P_\alpha(E),$$

where α indicates the nucleon state. $\rho_\alpha(|\vec{p}|)$ is a probability density function of the nucleon in the state α having its magnitude of momentum in the rest frame of the nucleus, $|\vec{p}|$. $P_\alpha(E)$ is a probability density function of the α-state nucleon leaving the residual system with the invariant missing energy, $E = m_B + m_N - m_A$.

Deuterium Spectral Function

$\rho_\alpha(|\vec{p}|)$ used for the simulation is from the MCEEP simulation package [50], designed to simulate $(e, e'X)$ experiments. The function is displayed in Fig.3.9. As for the missing energy, it is clearly,

$$P_\alpha(E) = \delta(E + m_d - m_p - m_n).$$

Carbon Spectral Function

As $\rho_\alpha(|\vec{p}|)$ for carbon was not immediately available, one for ^{16}O from MCEEP was used instead. This is shown in Fig.3.9. In the simulation, both proton and neutron were assumed to take the same form as

$$S(\vec{p}, E) = \rho_{P_{3/2}}(|\vec{p}|)P_{P_{3/2}}(E) + \rho_{S_{1/2}}(|\vec{p}|)P_{S_{1/2}}(E)$$

with

$$\begin{aligned} P_{P_{3/2}}(E) &= \frac{2}{3} \cdot \int a_{\epsilon_B^*} \delta\left(E + m(^{12}\mathrm{C}) - m_p - m(^{11}\mathrm{B}_{\mathrm{g.s.}}) - \epsilon_B^*\right) d\epsilon_B^* \\ P_{S_{1/2}}(E) &= \frac{1}{3} \cdot \frac{1}{\pi} \frac{\Gamma/2}{(E - E_C)^2 + (\Gamma/2)^2}. \end{aligned}$$

The parameters may be found from the $^{12}\mathrm{C}(e, e'p)$ experiments. Ref.[32] gives the ^{11}B excited state values of $\epsilon_B^* = 0,\ 2.125,\ 5.021,\ 6.79$ MeV with $a_{\epsilon_B^*} = 74,\ 13,\ 9,\ 4\%$, respectively, and $E_C = 38$ MeV, $\Gamma = 23$ MeV. Values for the ^{11}C excited states were assumed to be the same.

3.2.5 Final State Interactions

In the picture of the independent particle model, the target nucleus may be considered as a many-body system of nucleons. When quasifree elementary or quasi-deuteron processes are considered, the final state $\pi^+\pi^-N$ system may still interact with the other spectator nucleons. Consideration of the final state interactions (FSI) is meant to correct the initially generated particle momenta so that a more realistic simulation will be performed. The importance of this correction may be estimated from the concept of the mean free path of the final state particles.

For the deuterium target, FSI were not considered because it is a loosely bound two-body system and experimental results seem to agree with the quasifree assumptions

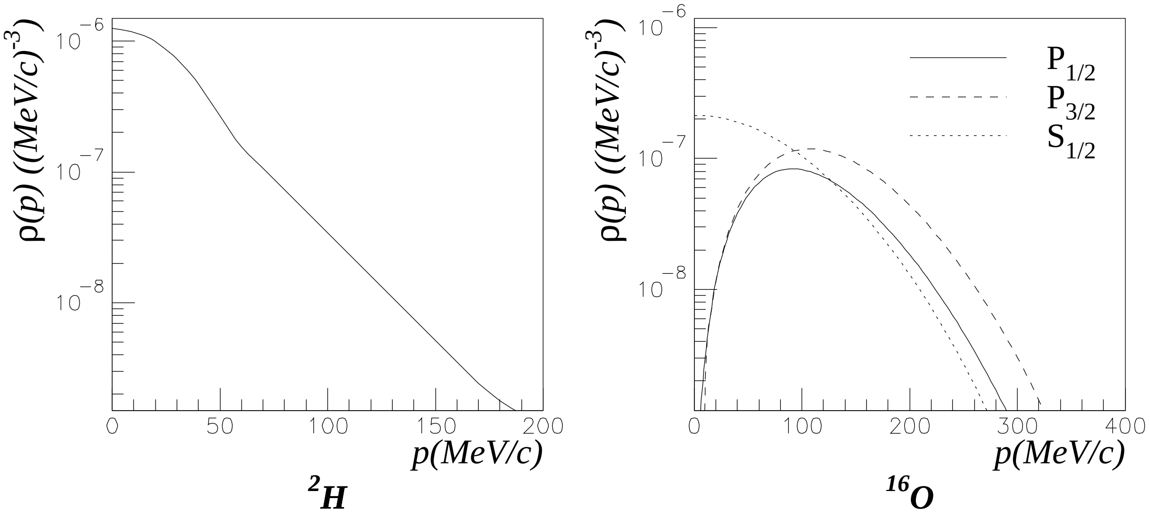

Figure 3.9: Deuteron and oxygen spectral functions from Ref.[32]. The carbon spectral function was replaced with the oxygen $P_{3/2}$ and $S_{1/2}$ states.

very well. In addition, non-quasi free processes have already been explicitly considered. However, for the carbon target, the inclusion of FSI is unavoidable since the produced pion energies are within the Δ excitation region, where the mean free path of the pions is typically shorter than the nuclear radius. Specifically, the mean free path in the nuclear medium for pions of $p_{\rm lab} = 300$ MeV/c is ~0.9 fm [43]. For protons of $p_{\rm lab} = 550$ MeV/c, it is ~5 fm [70]. The precise calculation of FSI is a complicated task and is possibly not worthwhile because of experimental limitations. To make the calculation easier, pion and proton FSI are simulated independently.

The computation of the pion FSI in the present simulation makes use of calculations adopted for a study of the $(\pi, 2\pi)$ reaction, which attempts to correctly account for the total production cross section by considering the absorption of both incoming and outgoing pions [51]. When pion absorption for the outgoing pions is considered, the PWIA cross section given by eq.(3.1) may be corrected to

$$d\sigma = \int d^3 r \rho(\vec{r}) \frac{|\mathcal{M}_{el}|^2 S(\vec{p}, E)}{4(k \cdot p)} d\Phi_4(k + p_A; k_1, k_2, p', p_B) e^{-\chi(k_1, \vec{r})} e^{-\chi(k_2, \vec{r})}. \tag{3.12}$$

The shadowing effect for the photons is neglected because of the comparably small γN cross section below $E_\gamma = 1$ GeV [42]. When the pion laboratory kinetic energy is less than 95 MeV, the Δ-hole optical potential is applicable and the exponent takes the following form:

$$\chi(k_i,\vec{r}) = \int_0^\infty C(k_i^0)\left[C_{A2}\left(\frac{\rho}{\rho_0}\right)^\beta + C_{A3}\left(\frac{\rho}{\rho_0}\right)^\gamma\right]\rho(\vec{r}+\hat{k}_i l)dl. \tag{3.13}$$

Otherwise, the phenomenological approach gives

$$\chi(k_i,\vec{r}) = \int_0^\infty C'(k_i^0)\rho^2(\vec{r}+\hat{k}_i l)dl. \tag{3.14}$$

The parameters, C, C', C_{A2}, C_{A3}, β, and γ are taken from Ref.[51]. They are all functions of the pion energy, k_i^0. The terms multiplied by C_{A2} and C_{A3} account for the two-body and three-body absorptions, respectively. $\rho_0 = 3/4\pi r_0^3$ is the nuclear matter density for a nucleon with $r_0 = 1.2$ fm. The density for carbon, $\rho(\vec{r})$, assumes the Woods-Saxon form,

$$\rho(\vec{r}) = \frac{\rho_A}{1+\exp\left(\frac{r-R_A}{a}\right)}, \quad \text{with} \quad \rho_A = A\left[\int_0^\infty \frac{4\pi r^2 dr}{1+\exp\left(\frac{r-R_A}{a}\right)}\right]^{-1},$$

and $R_A = r_0 A^{1/3}$, $a = 0.53$ fm. Quasi-elastic scattering brings about the momentum modification. The probability per unit length in the nucleus is expressed by

$$P_Q = C(k_i^0)\left[\frac{\Gamma}{2} - \frac{\Gamma_P}{2} + C_Q\left(\frac{\rho}{\rho_0}\right)^\alpha\right]\rho(\vec{r}+\hat{k}_i l),$$

where Γ, Γ_P, C_Q, and α are numerically available from Ref.[51] as functions of the pion energy. Now the probability of the quasi-elastic scattering for a pion is given by

$$1 - e^{-\chi_Q}, \quad \text{with} \quad \chi_Q = \int_0^\infty P_Q(\vec{r}, l)dl, \tag{3.15}$$

where the point of creation, $\vec{r}$ is fixed. In principle, one has to perform the three-fold integral with respect to the $\vec{r}$ similar to eq.(3.12). This is in addition to the three-fold integration with respect to the momentum transfer, from the nucleon to the pion under an appropriate potential field. Because the exact treatment for this step causes unnecessarily tedious calculations, a more intuitive — to the rigorous — approach was taken. First the $\pi^+\pi^-$ pair is created at a point $\vec{r}$ which is a random vector weighted by the nuclear density $\rho(\vec{r})$, and then the pions are quasi-elastically scattered by the constituent nucleons. The quasi-elastic scattering conforms to a phenomenological pion-nucleon scattering amplitude. The calculation is presented in Appendix F.

A correction to the pion absorption part given by eq.(3.12) was applied because the quasi-elastic scattering includes the charge exchange channels (e.g. $\pi^+ n \to \pi^0 p$). The exponent in eq.(3.12) may be rewritten by

$$\chi = \chi_A + \frac{\sigma_{\rm ex}}{\sigma_{\rm ex} + \sigma_{\rm el}} \chi_Q . \tag{3.16}$$

where $\sigma_{\rm ex}$ and $\sigma_{\rm el}$ are total cross sections for the charge exchange and elastic channel, respectively. Their computational steps are presented in Appendix F. χ_A and χ_Q are given by eq.(3.13) and (3.15), respectively.

The proton FSI are taken into account independently, by modifying the PWIA spectral function into the one with distorted wave impulse approximation (DWIA). It is given by [32]

$$S^D(\vec{p}_B, \vec{p}', E) = \frac{1}{(2\pi)^3} \int |\tilde{D}(\vec{p})|^2 S(|\vec{p}|, E) d^3p \tag{3.17}$$

with

$$\begin{aligned} \tilde{D}(\vec{p}) &= \int e^{i\vec{q}_r \cdot \vec{r}} D_{\vec{p}_r'}(\vec{r}) \rho(\vec{r}) d^3r \\ D_{\vec{p}_r'}(\vec{r}) &= \exp\left[-\frac{i m_p}{p_r'} \int_0^\infty U(\vec{r} + \hat{p}_r' l) dl \right] \\ \vec{q}_r &= \vec{p}_r'' - \vec{p}_r' \end{aligned} \tag{3.18}$$

where $\vec{p}_r''$ and $\vec{p}_r''$ are the initial and final proton momenta in the p-^{11}B center of mass frame, $U(\vec{r})$ is the p-^{11}B optical potential and $\rho(\vec{r})$ is the ^{11}B nuclear matter density. The method of calculating eq.(3.18) is described in Appendix G. The Monte Carlo method was used for the three-fold integral in eq.(3.17).

The FSI calculations above were added to the carbon simulations described in the earlier sections, except for coherent ρ^0 and η productions. This is justified because coherently produced ρ^0 and η are assumed to decay outside the carbon nucleus and the rest of the processes, such as Δ and QFρ^0, mostly decay inside the nucleus almost instantly after production. The lifetime of the η is about 5.58×10^{-22} seconds, which is long enough that one may reasonably assume that most of them can survive a traversal of the nucleus. The FSI of the η were not considered. On the other hand, the ρ^0, Δ and N^*, whose lifetimes are about 4×10^{-24} seconds or less, all decay before traveling ~1 fm, even at the theoretical limit of the speed of light. They were assumed to decay instantly after the production, which is a reasonable assumption because of the low photon energy boost. Finally, considering the FSI for the coherent ρ^0 process would be inappropriate, since the interaction keeps the nucleus intact.

3.3 TAGX Acceptance

The TAGX detection acceptance for the i'th target was computed by

$$\eta(\#i) = \frac{(\text{number of events survived in Step 4})}{(\text{number of events generated in Step 1})},$$

where Step 1 and 4 are defined in sec.3.1. Enumeration of the target here is in accordance with the target box# described in sec.2.3.4. To compare the TAGX acceptance for one reaction process to that of another, it would be more convenient to compare their average values. This may be given by

$$\bar{\eta} = \frac{\sum_{i=1}^{3} N_T(\#i)\eta(\#i)}{\sum_{i=1}^{3} N_T(\#i)}, \tag{3.19}$$

where $N_T(\#i)$ is the number of target nuclei per unit area in the i'th target. The values for $N_T(\#i)$ are listed in Tab.2.1. The TAGX simulations provided all values of $\eta(\#i)$ and the average acceptances for each photon energy bins are listed in Tab.3.1 for deuteron, and in Tab.3.2 for carbon simulation.

The average values for representative simulations are displayed in Fig.3.10. One first notices that the ρ^0 simulation has a very large acceptance compared with the other processes. This may be understood because the two pions are strongly correlated so that when one pion is detected in one side of the TAGX, there is a strong probability the other pion is detected on the other side. Also seen is the increasing acceptance with increasing photon energy for most cases. Another point is that the three body processes such as $\Delta^{++}\pi^-$ have larger acceptance than the four body processes such as $\Delta^{++}\Delta^-$.

Fig.3.11 shows acceptance ratios among the three individual experimental targets. The ratios show relatively moderate diversity between reactions as opposed to the absolute value. This led to a simpler way of extracting deuteron data from the CD_2 data which is discussed in sec.2.3.5. The acceptance ratios seem to depend on the photon energy so the parameters were determined for each photon energy bin. The determined values are tabulated in Tab.3.3.

Table 3.1: The average TAGX acceptances for the deuteron simulations. “T” and “L” in front of ρ^0 signifies transverse and longitudinal, respectively.

E_γ = 550– 810 MeV		E_γ = 810– 890 MeV	
process	$\bar{\eta}$[%]	process	$\bar{\eta}$[%]
coherent Tρ^0	8.54±0.07	coherent Tρ^0	9.30±0.07
coherent Lρ^0	3.94±0.04	coherent Lρ^0	4.27±0.04
coherent Drell	4.29±0.04	coherent Drell	4.54±0.04
d$\pi^+\pi^-$(3BPS)	1.58±0.03	d$\pi^+\pi^-$(3BPS)	1.56±0.03
$\Delta^{++}\pi^-$	2.40±0.02	$\Delta^{++}\pi^-$	3.32±0.03
$\Delta^-\pi^+$	2.09±0.01	$\Delta^-\pi^+$	2.82±0.02
QF Tρ^0	5.19±0.06	QF Tρ^0	6.08±0.06
QF Lρ^0	5.47±0.05	QF Lρ^0	6.48±0.05
QF Drell	3.13±0.02	QF Drell	3.54±0.02
QF ρ^0(655)	5.87±0.05	QF ρ^0(655)	6.49±0.05
N$\pi^+\pi^-$(3BPS)	2.41±0.02	N$\pi^+\pi^-$(3BPS)	2.63±0.02
$\Delta^{++}\Delta^-$	1.91±0.02	$\Delta^{++}\Delta^-$	2.07±0.01
pn$\pi^+\pi^-$(4BPS)	1.60±0.02	pn$\pi^+\pi^-$(4BPS)	1.79±0.02
QF η	1.64±0.01	QF η	1.30±0.01
QF 3π	1.04±0.01	QF 3π	1.62±0.01

E_γ = 890– 975 MeV		E_γ = 975–1105 MeV	
process	$\bar{\eta}$[%]	process	$\bar{\eta}$[%]
coherent Tρ^0	9.65±0.07	coherent Tρ^0	9.71±0.06
coherent Lρ^0	4.19±0.04	coherent Lρ^0	3.77±0.04
coherent Drell	4.40±0.05	coherent Drell	4.16±0.05
d$\pi^+\pi^-$(3BPS)	1.55±0.03	d$\pi^+\pi^-$(3BPS)	1.49±0.02
$\Delta^{++}\pi^-$	3.96±0.03	$\Delta^{++}\pi^-$	3.85±0.04
$\Delta^-\pi^+$	3.28±0.02	$\Delta^-\pi^+$	3.03±0.02
QF Tρ^0	6.74±0.06	QF Tρ^0	7.24±0.05
QF Lρ^0	6.91±0.04	QF Lρ^0	7.14±0.04
QF Drell	3.75±0.03	QF Drell	3.82±0.03
QF ρ^0(655)	6.59±0.05	QF ρ^0(655)	6.12±0.04
N$\pi^+\pi^-$(3BPS)	2.74±0.02	N$\pi^+\pi^-$(3BPS)	2.79±0.02
$\Delta^{++}\Delta^-$	2.14±0.01	$\Delta^{++}\Delta^-$	2.22±0.01
pn$\pi^+\pi^-$(4BPS)	1.94±0.02	pn$\pi^+\pi^-$(4BPS)	2.04±0.01
QF η	0.88±0.01	QF η	0.76±0.01
QF 3π	1.94±0.01	QF 3π	2.21±0.01

Table 3.2: The average TAGX acceptances for the carbon simulations. “T” and “L” in front of ρ^0 signifies transverse and longitudinal, respectively.

E_γ = 550– 810 MeV	
process	$\bar{\eta}$[%]
coherent Tρ^0	8.61±0.06
coherent Lρ^0	6.76±0.04
coherent Drell	4.52±0.04
$\Delta^{++}\pi^-$	1.67±0.02
$\Delta^-\pi^+$	1.54±0.01
QF Tρ^0	3.09±0.03
QF Lρ^0	3.39±0.03
QF Drell	2.13±0.02
QF ρ^0(655)	3.42±0.03
N$\pi^+\pi^-$(3BPS)	1.64±0.02
$\Delta^{++}\Delta^-$	1.50±0.02
pn$\pi^+\pi^-$(4BPS)	1.16±0.01
QF η	1.52±0.01
QF 3π	0.65±0.00

E_γ = 810– 890 MeV	
process	$\bar{\eta}$[%]
coherent Tρ^0	11.58±0.08
coherent Lρ^0	7.68±0.05
coherent Drell	4.84±0.04
$\Delta^{++}\pi^-$	2.12±0.02
$\Delta^-\pi^+$	1.95±0.02
QF Tρ^0	3.61±0.03
QF Lρ^0	4.02±0.03
QF Drell	2.43±0.02
QF ρ^0(655)	3.92±0.03
N$\pi^+\pi^-$(3BPS)	1.93±0.02
$\Delta^{++}\Delta^-$	1.60±0.02
pn$\pi^+\pi^-$(4BPS)	1.32±0.01
QF η	1.45±0.01
QF 3π	1.07±0.01

E_γ = 890– 975 MeV	
process	$\bar{\eta}$[%]
coherent Tρ^0	11.91±0.08
coherent Lρ^0	7.13±0.04
coherent Drell	4.77±0.05
$\Delta^{++}\pi^-$	2.35±0.02
$\Delta^-\pi^+$	2.21±0.02
QF Tρ^0	4.14±0.03
QF Lρ^0	4.34±0.03
QF Drell	2.70±0.02
QF ρ^0(655)	4.18±0.03
N$\pi^+\pi^-$(3BPS)	2.08±0.02
$\Delta^{++}\Delta^-$	1.67±0.01
pn$\pi^+\pi^-$(4BPS)	1.47±0.01
QF η	1.20±0.01
QF 3π	1.28±0.01

E_γ = 975–1105 MeV	
process	$\bar{\eta}$[%]
coherent Tρ^0	10.73±0.07
coherent Lρ^0	5.40±0.03
coherent Drell	4.45±0.05
$\Delta^{++}\pi^-$	2.55±0.02
$\Delta^-\pi^+$	2.32±0.02
QF Tρ^0	4.69±0.03
QF Lρ^0	4.49±0.02
QF Drell	2.80±0.02
QF ρ^0(655)	4.22±0.02
N$\pi^+\pi^-$(3BPS)	2.18±0.02
$\Delta^{++}\Delta^-$	1.79±0.01
pn$\pi^+\pi^-$(4BPS)	1.59±0.01
QF η	0.99±0.01
QF 3π	1.50±0.01

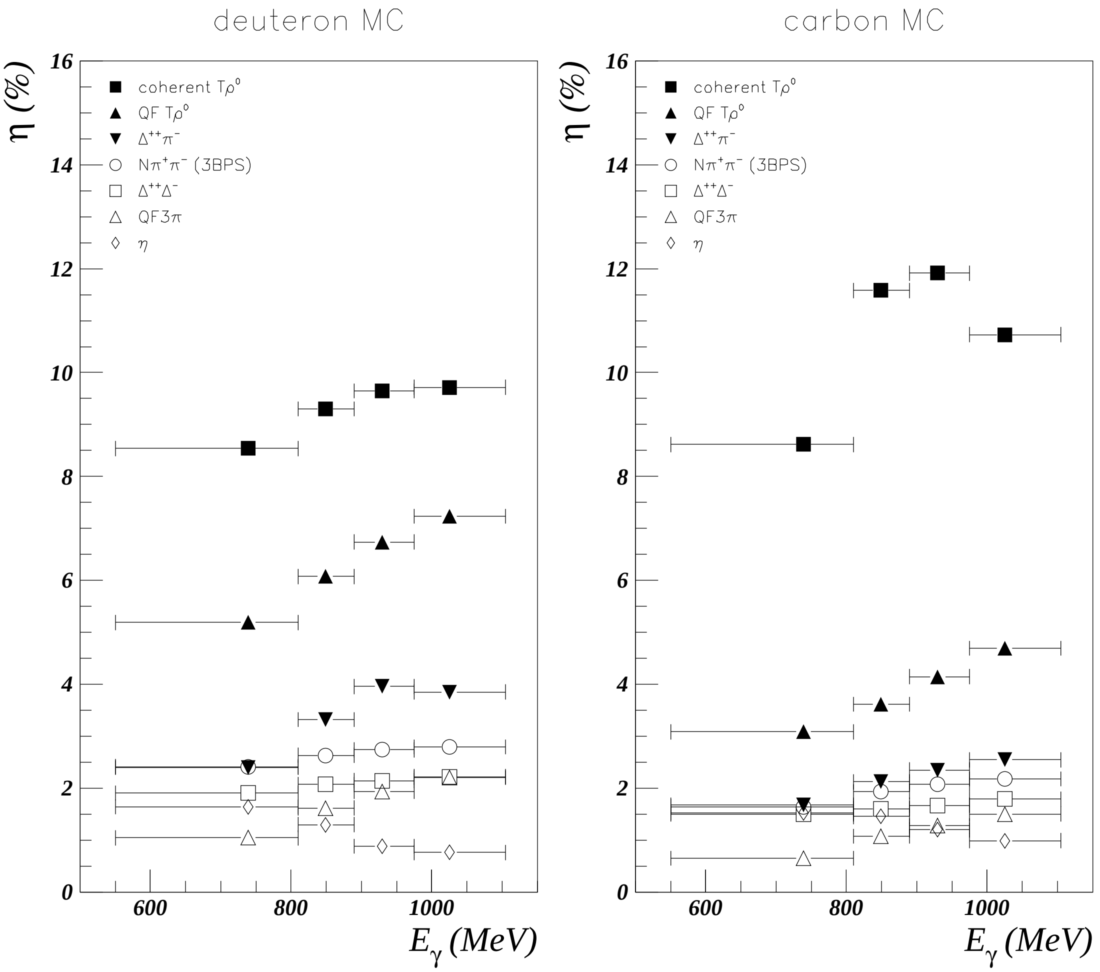

Figure 3.10: The TAGX acceptance obtained by the Monte Carlo simulation for representative processes. "T" in front of ρ^0 signifies transverse.

Table 3.3: The TAGX acceptance ratios determined from Fig.3.11. The target numbers are defined in sec.2.3.4.

E_γ[MeV]	$\eta(\#2)/\eta(\#1)$	$\eta(\#3)/\eta(\#1)$
550– 810	1.033± 0.055	0.821± 0.060
810– 890	1.042± 0.043	0.788± 0.070
890– 975	1.046± 0.058	0.775± 0.072
975–1105	1.070± 0.061	0.741± 0.084

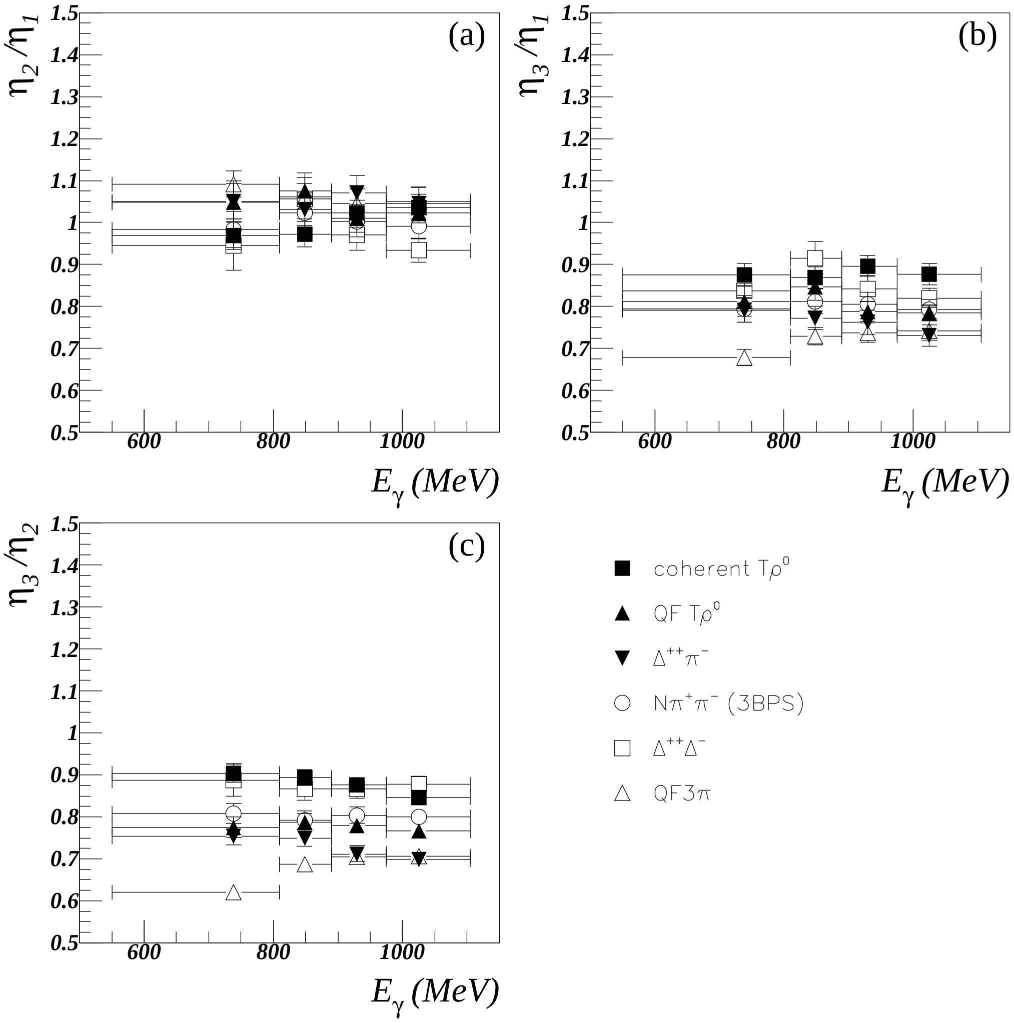

Figure 3.11: The carbon acceptance ratios. The subscript of η indicates the target position defined in sec.2.3.4.

Chapter 4

Data Analysis

Equipped with Monte Carlo simulations carried out as described in the previous chapter, the reproduction of the data and extraction of the total cross section can proceed. Reproduction of the data is done by fitting the distributions with the results of the simulations, by varying the strength of each individual simulation. When the strength is determined, the total cross section is obtainable from the TAGX acceptance. The present investigation, however, does not consider any interferences between the created simulations, so the produced Monte Carlo spectra are added incoherently.

4.1 Data Decomposition and the Monte Carlo Spectrum

4.1.1 Formalism of the Total Cross Section

The general form of the differential cross section for the $\gamma A \to \pi^+\pi^- X$ reaction is given by:

$$d\sigma(\gamma A \to \pi^+\pi^- X) = \frac{|\mathcal{M}(\gamma A \to \pi^+\pi^- X)|^2}{4E_\gamma m_A} d\Phi_3(k + p_A; k_1, k_2, p_X). \tag{4.1}$$

There may be a number of different reaction processes contributing to the reaction, so that the transition amplitude may be expressed as

$$\mathcal{M}(\gamma A \to \pi^+\pi^- X) = \sum_j \mathcal{M}_j, \tag{4.2}$$

where $\mathcal{M}_j$ represents a certain reaction process enumerated by the index, j. Denoting $Q = (k_1, k_2, p_X)$, one may write each of them as,

$$\mathcal{M}_j(Q) \propto \sqrt{\frac{d\sigma_j}{dQ}} e^{i(\Theta_j(Q)+\Phi_j)}, \quad \Theta_j(Q) = \tan^{-1}\frac{\mathrm{Im}(\mathcal{M}_j)}{\mathrm{Re}(\mathcal{M}_j)},$$

where Φ_j represents an overall phase, which does not depend on the kinematical variable, Q. From eqs.(4.1) and (4.2), the differential cross section is then given by,

$$\begin{aligned}\frac{d\sigma}{dQ}(\gamma A \to \pi^+\pi^- X) &= \left| \sum_j \sqrt{\frac{d\sigma_j}{dQ}} e^{i(\Theta_j(Q)+\Phi_j)} \right|^2 \\ &= \sum_j \frac{d\sigma_j}{dQ} + 2\sum_{j<k} \sqrt{\frac{d\sigma_j}{dQ}\frac{d\sigma_k}{dQ}} \cos\left\{\Theta_j(Q) - \Theta_k(Q) + \Phi_j - \Phi_k\right\}.\end{aligned}$$

Using eq.(2.61) with adequate detection efficiencies, one may conclude that the differential yield of the $\gamma A \to \pi^+\pi^- X$ reaction is written by

$$\frac{dY}{dQ}(\gamma A \to \pi^+\pi^- X) = \sum_j \frac{dY_j}{dQ} + 2\sum_{j<k} \sqrt{\frac{dY_j}{dQ}\frac{dY_k}{dQ}} \cos\left\{\Theta_j(Q) - \Theta_k(Q) + \Phi_j - \Phi_k\right\}.$$

The specific strength of the reaction in the data may be defined through

$$P_j = \int \frac{dY_j}{dQ} dQ \Big/ \int \frac{dY_{\rm data}}{dQ} dQ = \frac{Y_j}{Y_{\rm data}},$$

in other words as the number of events of reaction j over total number of events. By normalizing each reaction spectrum with

$$\frac{dX_j}{dQ} = \frac{Y_{\rm data}}{Y_j}\frac{dY_j}{dQ},$$

one may now write,

$$\frac{dY_{\rm data}}{dQ} = \sum_j P_j \frac{dX_j}{dQ} + 2\sum_{j<k} \sqrt{P_j P_k \frac{dX_j}{dQ}\frac{dX_k}{dQ}} \cos(\Theta_j - \Theta_k + \Phi_j - \Phi_k). \tag{4.3}$$

Integrating eq.(4.3) yields

$$1 = \sum_j P_j + 2\sum_{j<k} \sqrt{P_j P_k} \cos(\delta_j - \delta_k) = \left| \sum_j \sqrt{P_j} e^{\delta_j} \right|^2, \tag{4.4}$$

where

$$\cos(\delta_j - \delta_k) = \int \cos(\Theta_j - \Theta_k + \Phi_j - \Phi_k) \sqrt{\frac{dX_j}{dQ}\frac{dX_k}{dQ}} \frac{dQ}{Y_{\rm data}}. \tag{4.5}$$

If the simulated processes introduced in sec.3.2 are to reproduce the experimental spectra with appropriate values of P_j and $\Phi_j - \Phi_k$, eq.(4.3) would hold between the experimental data (left hand side) and the Monte Carlo simulation (right hand side). Then, from eq.(2.61), the total cross section for the reaction j is determined by,

$$\sigma_j = \frac{Y_{\rm data} P_j}{\eta_{\rm com} N_\gamma \sum_{i=1}^{3} N_T(\#i)\eta_j(\#i)} = \frac{Y_{\rm data} P_j}{\eta_{\rm com} N_\gamma N_T^{\rm tot} \overline{\eta}_j}, \quad \left(N_T^{\rm tot} = \sum_{i=1}^{3} N_T(\#i)\right) \tag{4.6}$$

where $\eta_{\rm com}$ is the TAGX computer live time rate presented in Tab.2.2 and $\overline{\eta_j}$ is the average TAGX acceptance for the simulation, j, given by eq.(3.19). The number of target nuclei for target#i, $N_T(\#i)$, are listed in Tab.2.1. The total yield, $Y_{\rm data}$, as well as the number of photons, N_γ, are tabulated in Tab.2.7. The total $\gamma A \to \pi^+\pi^- X$ cross section may be determined via,

$$\sigma(\gamma A \to \pi^+\pi^- X) = \frac{Y_{\rm data}}{\eta_{\rm com} N_\gamma N_T^{\rm tot}} \left(\sum_j \frac{P_j}{\overline{\eta_j}} + 2 \sum_{j<k} \frac{\sqrt{P_j P_k}}{\overline{\eta_{jk}}} \cos(\delta_j - \delta_k) \right),$$

where $\cos(\delta_j - \delta_k)$ is given by eq.(4.5). It is difficult to evaluate $\overline{\eta_{jk}}$, the average TAGX acceptance for the interference term. An obvious choice would be:

$$\overline{\eta_{jk}} \approx \sqrt{\overline{\eta_j}\,\overline{\eta_k}}.$$

One has to determine the strength, P_j, and the phase difference, $\Phi_j - \Phi_k$, in order to obtain the total cross sections. This may be accomplished by fitting the data spectrum, $dY_{\rm data}/dQ$, with a number of simulated distributions, dX_j/dQ, accompanied by the phase structure, $\Theta_j(Q)$.

4.1.2 Interference and Phase Structure

As demonstrated above, the interference effect can be studied when the phase structures, $\Theta_j(Q)$, are provided for the two interfering processes. It may be relatively easy to write them for, for instance, the ρ^0 excitations as

$$\Theta_{\rho^0}(k_1, k_2, p') = \tan^{-1}\left[\frac{(k_1 + k_2)^2 - m_\rho^2}{m_\rho \Gamma_\rho}\right] + \text{const}.$$

In case of the $\Delta\pi$ process, this would be

$$\Theta_{\Delta\pi}(k_1, k_2, p') = \tan^{-1}\left[\frac{(k_i + p')^2 - m_\Delta^2}{m_\Delta \Gamma_\Delta}\right] + \text{const.}, \quad (i = 1 \text{ or } 2).$$

Because the nucleon momentum, p' was not detected for most of the events in this experiment, this particular phase must be somewhat "blurred." This effect could be accounted if one interprets the difference of the phase in eq.(4.3) as

$$\Theta_j(k_1, k_2) - \Theta_k(k_1, k_2) = \int \{\Theta_j(k_1, k_2, p') - \Theta_k(k_1, k_2, p')\}\, d^3p'.$$

However, whether or not this phase will be accurate is not certain because the $\Delta\pi$ production is usually understood as a superposition of many processes (see sec.3.2); in addition some proton tracks are actually captured by the TAGX. In any case, considering any interference is not an consistent with the objectives of the analysis since the present method was originally devised to avoid investigating "subtle" interference effects. So, in this thesis, explicit consideration of the interference effects is forsaken in order to avoid exactly such model dependency. Should, however, the incorporation of interference be considered in the future, this is how a rigorous investigation needs be carried out. Now that the interference effects are ignored ($\Theta_j - \Theta_k + \Phi_j - \Phi_k = 90°$, $j \neq k$), the condition of the P_j given by eq.(4.4) becomes,

$$\sum_j P_j = 1, \quad P_j \geq 0. \tag{4.7}$$

4.1.3 Data Fitting

A number of $(\gamma, \pi^+\pi^-)$ events also contain $(\gamma, \pi^+\pi^- p)$ events. Such events form ~13% of the deuteron data and ~11% of the carbon data. These data may be particularly helpful in discriminating the quasifree γp reactions from γn reactions. However, the experimental errors for the $(\gamma, \pi^+\pi^- p)$ events are so large that it turned out that analyzing the two-pion events only gives better results and more information. Part of the reason is certainly that the $\pi^+\pi^-$ events are 7–9 times more. Nevertheless, $\pi^+\pi^- p$ events sometimes create a unique configuration of dipion momenta when two pions were captured in the same side of the TAGX, which cannot be possible without a proton track. The data fitting was, therefore, performed with the two-pion momenta. The fitting results were then compared with the $\pi^+\pi^- p$ events so that the outcome will be consistent.

In any two-pion detection experiment, the data are inherently six-dimensional (three components of momentum from each pion) in addition to the photon energy, which is already binned into four slices. This means that there are six independent variables to characterize the data. This is an important point, because unlike other experiments in which the scattered nucleon or nucleus is also detected, the detection of two pions does not allow the formation of Dalitz plots, so it is hard to distinguish one reaction from another by only a simple scatter plot. While the inclusive nature of the experiment is disadvantageous in determining quasifree and other cross sections, the multi-dimensional method not only enables one to compare those cross sections, thus providing feedback and confidence in the analysis, but it is also a desirable method when the acceptance is limited. A distorted spectrum due to fractional acceptance can only be understood with appropriate knowledge of many-fold differential cross section. Detailed knowledge of the differential cross section in turn improves the confidence in deducing the total cross section.

Perhaps a natural choice of the basis of the distribution is the two-pion momenta in 6-dimensional Euclidean space. However, there is a constraint to the distribution because neither the photon beam nor the target are polarized. Hence, the distribution is independent from the azimuthal angle of the dipion momentum. A better choice would therefore be a symmetric coordinate, $(|\vec{k}_1|, |\vec{k}_2|, \theta_1, \theta_2, \theta_{12})$, where θ_1 (θ_2) is the positive (negative) pion scattering angle and θ_{12} is an angle between positive and negative pion momenta. In the actual fitting process, the laboratory frame was chosen since it is readily accessible. Now the coordinate of the fitting is presented by, $Q = (|\vec{k}_1|, |\vec{k}_2|, \theta_1, \theta_2, \theta_{12})_{\mathrm{lab}}$.

Data fitting is performed with the MINUIT package from the CERN library. Subsequent sections describe the fitting results. Obviously, both the data and the simulation are always subjected to the same basic cuts which are defined in sec.2.3.3. When the data are subjected to a cut, the cut may suppress certain reaction processes and therefore relatively enhance other ones. This means that the parameter P_j also changes with the data set following the cuts. Once the P_j's are determined within a certain data set, the total cross sections σ_j are determined by eq.(4.6). The P_j suitable to another data set with a different cut then can be obtained via the same equation with the appropriate TAGX acceptance which differ from the original as well. In this way the Monte Carlo spectrum, $\sum_j P_j dX_j/dQ$, under different cuts may be obtained.

4.2 Deuteron Data Analysis

Tab.4.1 shows the deuteron fitting results, P_j and σ_j. In general, the reproducibility of the fit is very good in terms of the chisquare ($\chi^2/\mathrm{ndf} = 0.1$–$0.2$). This is mainly because the number of events is so limited that the error of the each bin in the five-dimensional coordinate is considerably large. It is also found that reproducing a one-dimensional spectrum is generally easy and successful. Fig.4.1 shows the missing-mass distributions for the data and the simulations at the highest photon energy bin. One may notice that the Monte Carlo simulation predicts a slightly lower mass peak than the data exhibits.

Table 4.1: The deuteron fitting result. “T” and “L” in front of ρ^0 signifies transverse and longitudinal, respectively.

E_γ = 550– 810 MeV χ^2/ndf = 0.100		
process	P_j[%]	σ[μb]
coherent Tρ^0	$0.0^{+1.15}_{-0.00}$	$0.0^{+0.33}_{-0.00}$
coherent Lρ^0	$4.4^{+2.27}_{-2.27}$	$2.6^{+1.64}_{-1.42}$
coherent Drell	$0.0^{+1.62}_{-0.00}$	$0.0^{+0.93}_{-0.00}$
d$\pi^+\pi^-$(3BPS)	$0.0^{+1.50}_{-0.00}$	$0.0^{+2.37}_{-0.00}$
$\Delta^{++}\pi^-$	$43.4^{+18.74}_{-18.74}$	$19.7^{+13.30}_{-10.32}$
$\Delta^-\pi^+$	$15.0^{+5.23}_{-5.23}$	$16.5^{+7.42}_{-6.54}$
QF Tρ^0	$0.0^{+1.79}_{-0.00}$	$0.0^{+0.86}_{-0.00}$
QF Lρ^0	$0.0^{+4.96}_{-0.00}$	$0.0^{+2.24}_{-0.00}$
QF Drell	$0.0^{+3.31}_{-0.00}$	$0.0^{+2.61}_{-0.00}$
QF ρ^0(655)	$0.0^{+2.24}_{-0.00}$	$0.0^{+0.94}_{-0.00}$
N$\pi^+\pi^-$(3BPS)	$10.8^{+11.38}_{-10.82}$	$10.3^{+12.45}_{-10.31}$
$\Delta^{++}\Delta^-$	$21.7^{+8.99}_{-8.99}$	$26.1^{+13.68}_{-11.97}$
pn$\pi^+\pi^-$(4BPS)	$24.1^{+9.53}_{-9.53}$	$34.7^{+17.68}_{-15.38}$
QF η	$2.7^{+9.02}_{-2.74}$	$3.8^{+13.90}_{-3.84}$
QF 3π	$0.7^{+5.98}_{-0.73}$	$1.6^{+14.29}_{-1.60}$
total multiπ	$100.0^{+0.00}_{-0.00}$	$115.3^{+28.98}_{-25.05}$

E_γ = 810– 890 MeV χ^2/ndf = 0.132		
process	P_j[%]	σ[μb]
coherent Tρ^0	$0.0^{+2.92}_{-0.00}$	$0.0^{+0.99}_{-0.00}$
coherent Lρ^0	$4.4^{+2.40}_{-2.40}$	$3.0^{+2.01}_{-1.75}$
coherent Drell	$1.3^{+2.91}_{-1.27}$	$0.8^{+2.08}_{-0.82}$
d$\pi^+\pi^-$(3BPS)	$0.0^{+0.58}_{-0.00}$	$0.0^{+1.19}_{-0.00}$
$\Delta^{++}\pi^-$	$46.3^{+12.24}_{-12.24}$	$19.0^{+8.81}_{-7.13}$
$\Delta^-\pi^+$	$18.0^{+3.92}_{-3.92}$	$18.7^{+5.70}_{-5.09}$
QF Tρ^0	$0.0^{+1.61}_{-0.00}$	$0.0^{+0.84}_{-0.00}$
QF Lρ^0	$0.0^{+2.48}_{-0.00}$	$0.0^{+1.20}_{-0.00}$
QF Drell	$0.0^{+2.15}_{-0.00}$	$0.0^{+1.90}_{-0.00}$
QF ρ^0(655)	$0.0^{+1.82}_{-0.00}$	$0.0^{+0.88}_{-0.00}$
N$\pi^+\pi^-$(3BPS)	$12.9^{+10.31}_{-10.31}$	$14.4^{+13.35}_{-11.67}$
$\Delta^{++}\Delta^-$	$19.7^{+7.46}_{-7.46}$	$27.8^{+13.33}_{-11.76}$
pn$\pi^+\pi^-$(4BPS)	$14.2^{+9.64}_{-9.64}$	$23.2^{+18.72}_{-16.31}$
QF η	$0.0^{+2.62}_{-0.00}$	$0.0^{+6.36}_{-0.00}$
QF 3π	$8.0^{+4.94}_{-4.94}$	$14.6^{+10.62}_{-9.33}$
total multiπ	$100.0^{+0.00}_{-0.00}$	$121.3^{+28.88}_{-29.78}$

E_γ = 890– 975 MeV χ^2/ndf = 0.141		
process	P_j[%]	σ[μb]
coherent Tρ^0	$0.0^{+1.04}_{-0.00}$	$0.0^{+0.38}_{-0.00}$
coherent Lρ^0	$5.7^{+2.90}_{-2.90}$	$4.5^{+2.82}_{-2.45}$
coherent Drell	$0.0^{+1.82}_{-0.00}$	$0.0^{+1.47}_{-0.00}$
d$\pi^+\pi^-$(3BPS)	$0.0^{+1.06}_{-0.00}$	$0.0^{+2.47}_{-0.00}$
$\Delta^{++}\pi^-$	$29.2^{+15.25}_{-15.25}$	$10.4^{+8.28}_{-6.27}$
$\Delta^-\pi^+$	$19.9^{+3.97}_{-3.97}$	$20.0^{+5.78}_{-5.16}$
QF Tρ^0	$0.0^{+1.24}_{-0.00}$	$0.0^{+0.65}_{-0.00}$
QF Lρ^0	$11.1^{+5.12}_{-5.12}$	$5.3^{+3.02}_{-2.65}$
QF Drell	$0.0^{+3.46}_{-0.00}$	$0.0^{+3.27}_{-0.00}$
QF ρ^0(655)	$0.0^{+2.36}_{-0.00}$	$0.0^{+1.27}_{-0.00}$
N$\pi^+\pi^-$(3BPS)	$6.9^{+11.94}_{-6.88}$	$8.3^{+16.09}_{-8.29}$
$\Delta^{++}\Delta^-$	$30.0^{+8.38}_{-8.38}$	$46.2^{+17.34}_{-15.33}$
pn$\pi^+\pi^-$(4BPS)	$7.2^{+17.50}_{-7.19}$	$12.3^{+33.04}_{-12.25}$
QF η	$0.0^{+0.84}_{-0.00}$	$0.0^{+3.41}_{-0.00}$
QF 3π	$6.8^{+6.76}_{-6.76}$	$11.6^{+13.18}_{-11.51}$
total multiπ	$100.0^{+0.00}_{-0.00}$	$118.4^{+36.22}_{-31.01}$

E_γ = 975–1105 MeV χ^2/ndf = 0.168		
process	P_j[%]	σ[μb]
coherent Tρ^0	$3.2^{+7.17}_{-3.18}$	$1.1^{+2.75}_{-1.10}$
coherent Lρ^0	$0.0^{+0.82}_{-0.00}$	$0.0^{+0.80}_{-0.00}$
coherent Drell	$1.8^{+5.33}_{-1.82}$	$1.5^{+4.80}_{-1.48}$
d$\pi^+\pi^-$(3BPS)	$0.0^{+1.66}_{-0.00}$	$0.0^{+4.09}_{-0.00}$
$\Delta^{++}\pi^-$	$33.3^{+9.50}_{-9.50}$	$10.3^{+5.72}_{-4.40}$
$\Delta^-\pi^+$	$12.7^{+4.38}_{-4.38}$	$14.2^{+6.28}_{-5.54}$
QF Tρ^0	$0.8^{+8.17}_{-0.84}$	$0.4^{+4.12}_{-0.39}$
QF Lρ^0	$19.3^{+4.24}_{-4.24}$	$9.1^{+2.79}_{-2.49}$
QF Drell	$0.0^{+6.72}_{-0.00}$	$0.0^{+6.39}_{-0.00}$
QF ρ^0(655)	$0.0^{+3.36}_{-0.00}$	$0.0^{+1.99}_{-0.00}$
N$\pi^+\pi^-$(3BPS)	$5.2^{+16.24}_{-5.17}$	$6.3^{+21.52}_{-6.26}$
$\Delta^{++}\Delta^-$	$22.6^{+7.61}_{-7.61}$	$34.4^{+14.89}_{-13.18}$
pn$\pi^+\pi^-$(4BPS)	$12.1^{+10.48}_{-10.48}$	$20.1^{+20.10}_{-17.58}$
QF η	$0.0^{+1.19}_{-0.00}$	$0.0^{+5.69}_{-0.00}$
QF 3π	$10.5^{+7.21}_{-7.21}$	$16.0^{+12.90}_{-11.38}$
total multiπ	$100.0^{+0.00}_{-0.00}$	$113.4^{+34.19}_{-36.77}$

The situation is similar in all photon energy bins. Because the peak position roughly agrees with the quasifree predictions, the disagreement seems to indicate the limitation of the PWIA approach for the quasifree processes. More accurate treatment to FSI seems to be necessary for a better reproduction.

Despite this imperfect reproducibility in the missing mass, the fitting result is not unreasonable. The following sections discuss the result by separating the data into three parts according to the missing-mass values. The three regions are defined as

$$\begin{aligned} m_X &\leq 1870 \text{ MeV/c}^2 && \text{(coherent region)} \\ 1870 \leq m_X &\leq 2000 \text{ MeV/c}^2 && \text{(quasifree region)} \\ m_X &\geq 2000 \text{ MeV/c}^2 && \text{(high missing-mass region).} \end{aligned}$$

It should be noted that this missing mass cut does not perfectly separate one process from another. The high dimensional fitting, in this sense too, becomes handy in disentangling the various processes.

4.2.1 Coherent Region

The total $\gamma d \to \pi^+\pi^- d$ cross section is plotted in Fig.4.2. This is the sum of the Tρ, Lρ, and the Drell-type background and the 3BPS background. The DESY data by P. Benz *et al.* (ABHHM collaboration) is also shown with the open circles in this figure. They show a good agreement. One should note, however, that their cross sections are restricted to the region of $-0.2 \leq t \leq -0.04$ GeV^2. Having no t-cut, the present data are actually expected to be larger than Benz's data. The situation may be understood from the actual t distribution observed in the experiment. Fig.4.3 indicates that most of forwardly produced processes, namely ρ^0 and Drell-type background both of which have the factor e^{24t} in the differential cross section, are in this t-cut region. The present determination is not sensitive enough to observe the effects of Benz's t-cut in the cross section.

The photon energy threshold on ^{2}H corresponding to the central value of the vacuum ρ^0 mass (770 MeV/c^2) is 928 MeV. The photon energy range for this experiment covers both below and above this threshold. P. Benz *et al.* determined the coherent ρ^0 cross section just above the threshold with three different models and because the shape of the resonance increasingly deviates from each other as the photon energy approaches

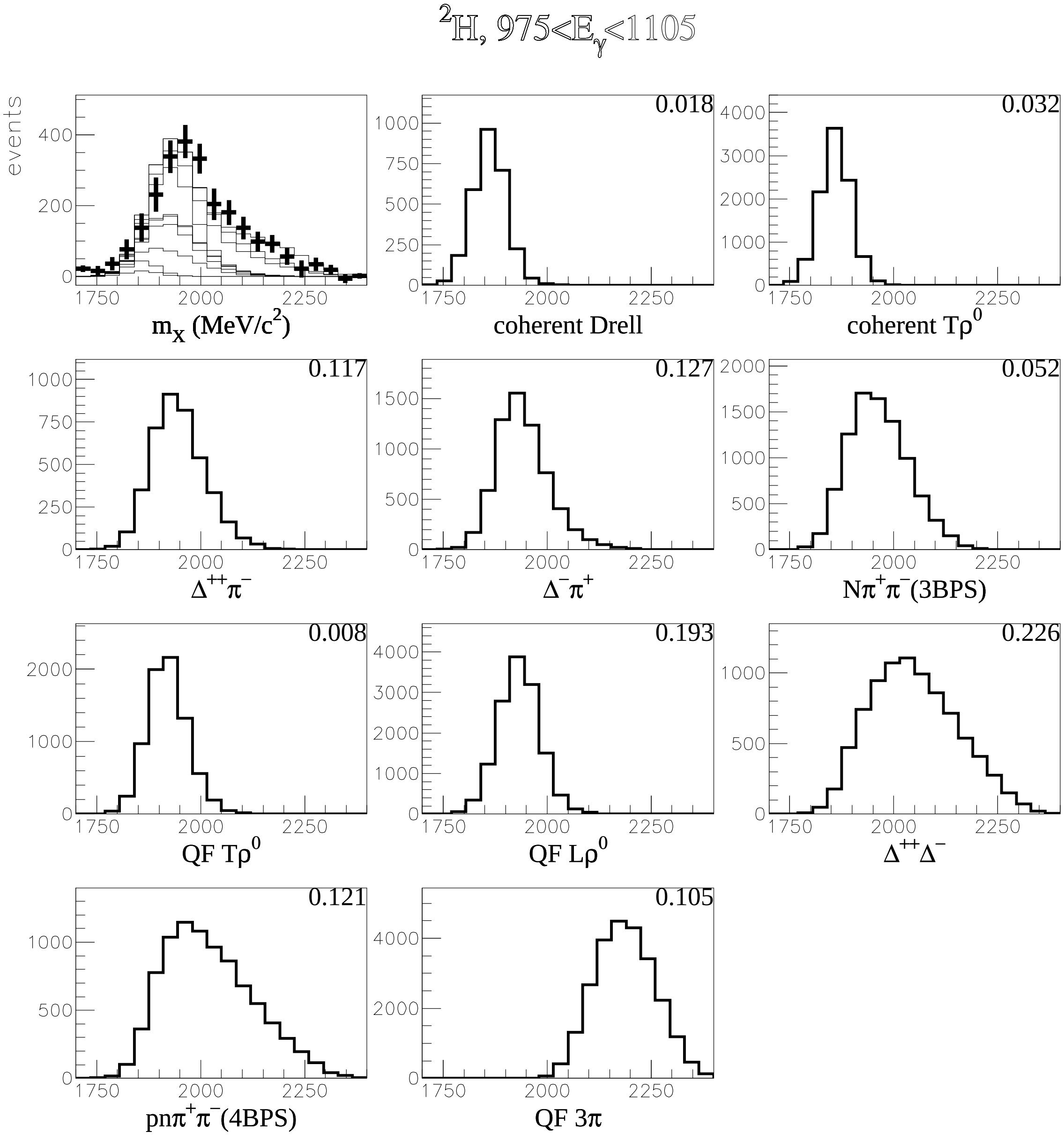

Figure 4.1: The deuteron missing-mass distribution. Data (+) and cumulative Monte Carlo simulation (rectangle lines) are superimposed in the top left panel. Each component of the simulation is displayed in the rest of the panels. The strength P_j for this particular data set is given in the upper right corner in each Monte Carlo panel.

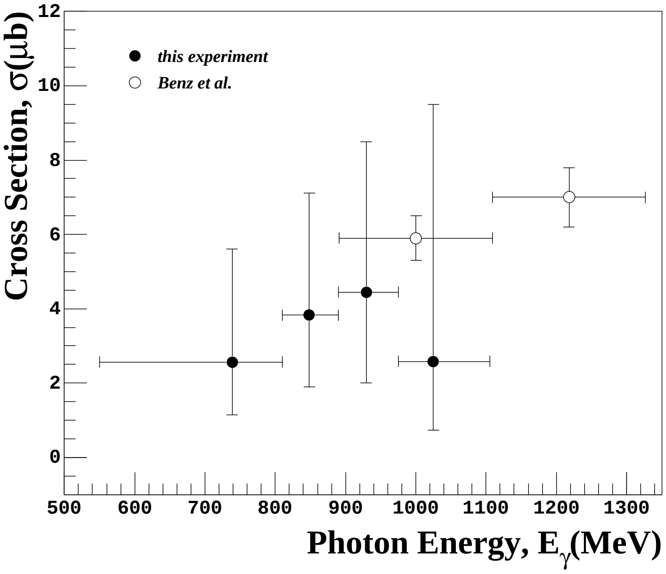

Figure 4.2: The $\gamma d \rightarrow \pi^+\pi^- d$ cross section obtained by this experiment (filled points) in comparison with Benz *et al.* [49] (open circles). Note that Benz's cross sections are for the region of $-0.2 \leq t \leq -0.04$ GeV^2 only.

the threshold, the different models give very different cross section (see *Quasifree* ρ^0 *Production* in sec.3.2.1 for more detail). In Fig.4.4, the cross section using so-called "interference model," which has the closest resonance shape as the one described in sec.3.2.2, is plotted against the present result. The figure shows agreement between Benz's ρ^0 and the sum of Tρ^0 and Lρ^0 from this work.

A striking feature in the result is that the ρ^0 cross section is completely dominated by the longitudinal ρ^0 below the threshold. A qualitative argument for this result may be given from the actual helicity decay angle distribution in Fig.4.5. As the numbers P_j in Fig.4.5 indicate, the missing-mass cut $m_X \leq 1870$ MeV/c^2 enhances the coherent processes only for about 40% of data. Whatever the proportion of the "leakage" is, all reactions except the longitudinally polarized ρ^0 give a distribution peaking around $\cos\theta_{cH} = 0$ partly because of the TAGX acceptance. But the data distribution is basically flat. The longitudinal ρ^0 has to be there to compensate at the edges of the distribution.

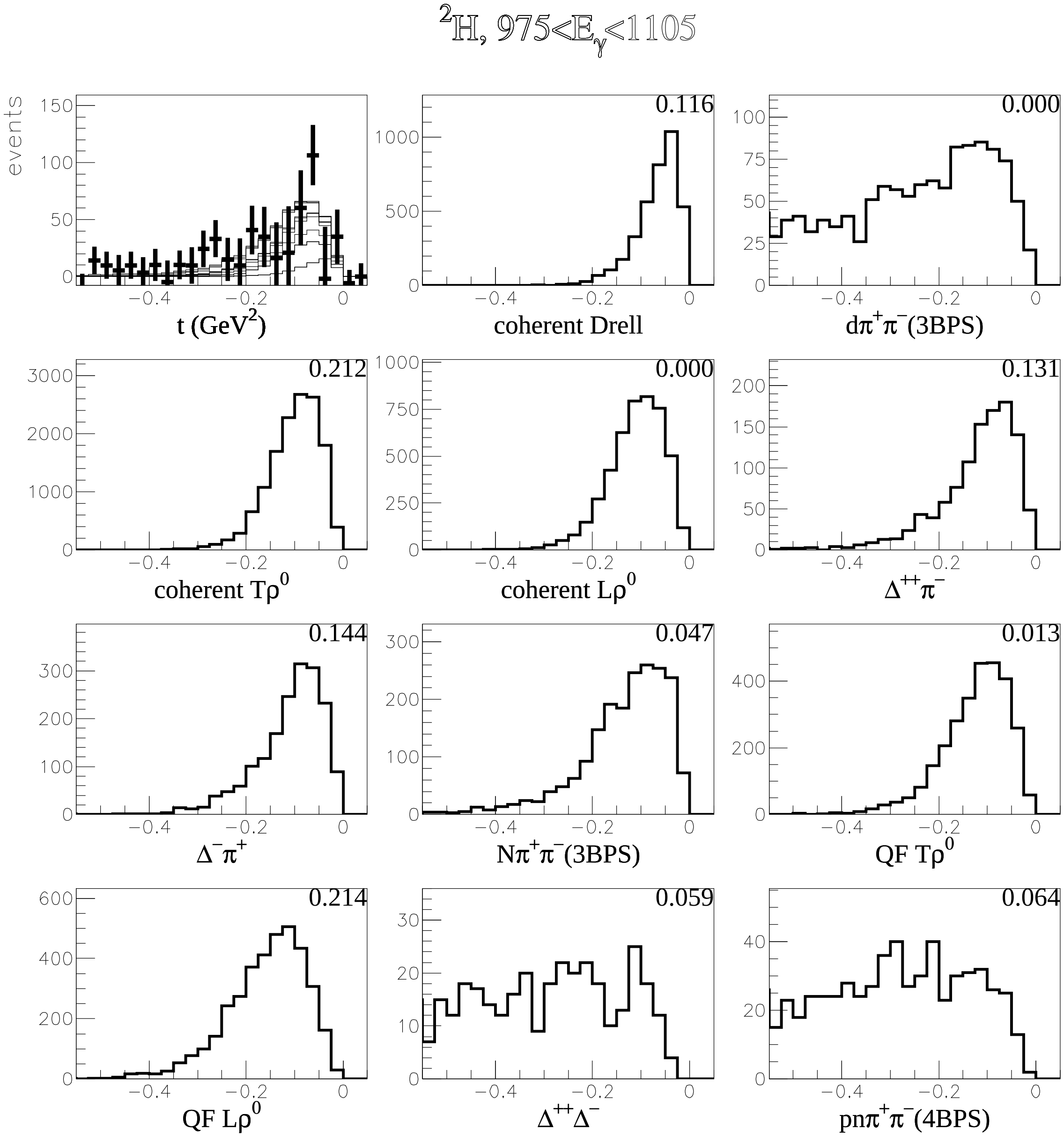

Figure 4.3: The t distribution in the coherent region, $m_X \leq 1870$ MeV/c^2. To interpret this figure, please refer to Fig.4.1. Note the P_j are no longer the same because of the missing-mass cut.

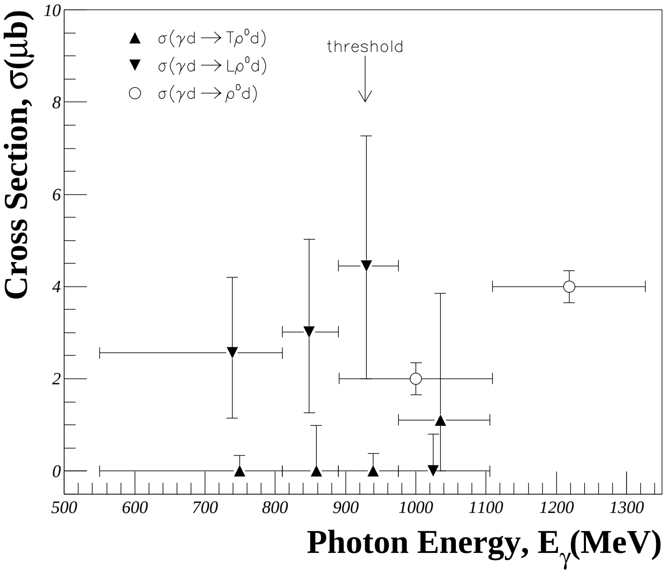

Figure 4.4: The $\gamma d \to \rho^0 d$ cross sections obtained by this experiment (filled triangles) in comparison with the DESY data by Benz *et al.* (ABHHM collaboration) [49] (open circles). "T" and "L" in front of ρ^0 denote transverse and longitudinal, respectively. The central E_γ values for Tρ^0 are shifted for clarity. Note that Benz's cross sections are for the region of $-0.2 \leq t \leq -0.04$ GeV^2 only.

4.2.2 Quasifree Region

$\Delta\pi$ Production Processes

One of the remarkable results in this missing mass region is the very small $\Delta\pi$ cross sections compared to the other experiments, such as the Frascati data by Carbonara *et al.* [39], resulting in the very small total quasifree cross section as clearly seen in Fig.4.6. The disagreement looks serious since there is a naive expectation of $\Delta\pi$ domination and relative reliability of the PWIA for the deuteron target. It is, thus, necessary to further investigate this issue. As for the fitting, the missing-mass distributions for the data shown in Fig.4.1 actually suggest even smaller quasifree cross sections because the data are seemingly "shifted" toward the higher mass regions. The high missing-mass part of the distribution cannot be accounted for from quasifree processes only. The apparent difference in the missing-mass distribution between the data and the simulation suggests that the fitting may have given the quasifree processes more strength than expected. However, this does not mean that the fitting process has a problem because the missing-mass distribution itself is not fitted. Also the good agreement in the ρ^0 production (see

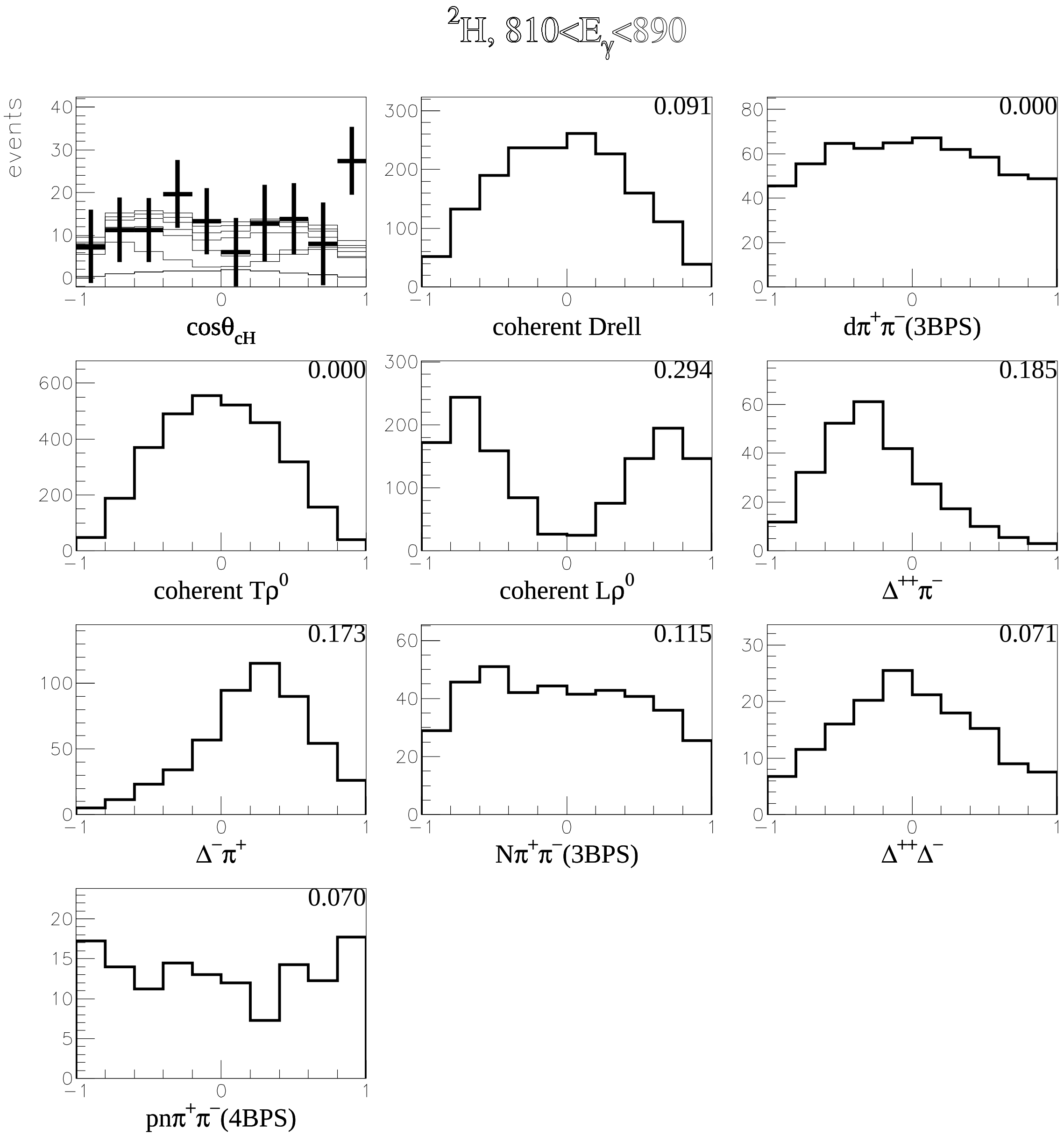

Figure 4.5: Distribution of $\cos\theta_{cH}$ in the coherent region ($m_X \leq 1870\mathrm{MeV/c}^2$). To interpret this figure, please refer to Fig.4.1.

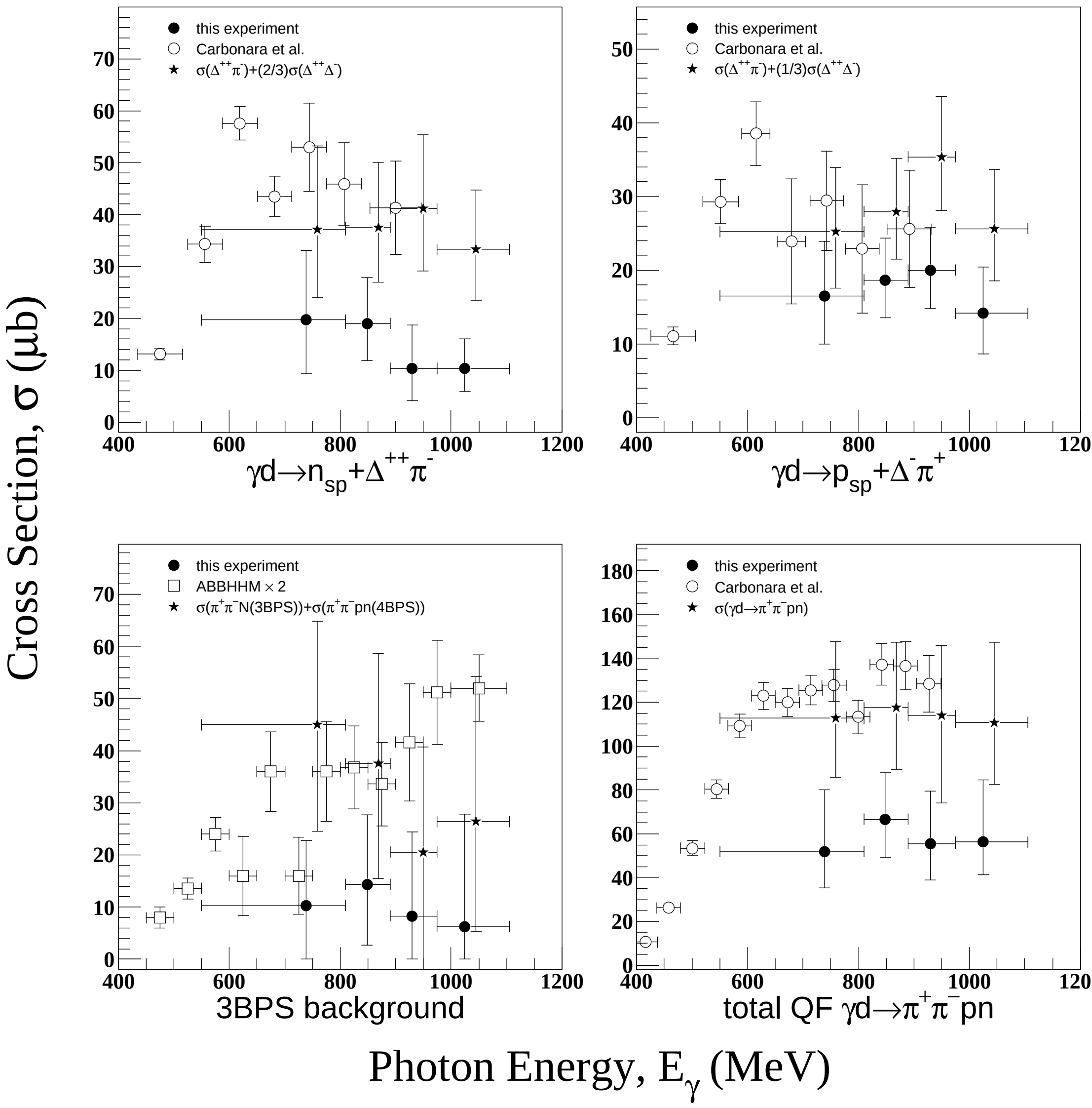

Figure 4.6: Deuteron quasifree cross sections. The closed circles are obtained by this experiment. The open circles are by Carbonara *et al* [39]. The open squares are from γp experiment by the ABBHHM collaboration [33]. These are multiplied by two for clarity. The filled stars ($\star$) are our quasifree cross sections plus the quasi-deuteron cross sections, i.e., $\Delta^{++}\Delta^{-}$ and $(\pi^{+}\pi^{-}pn)_{\text{4BPS}}$. In the $\Delta\pi$ panels, a rough cross section ratio $\Delta^{++}\pi^{-} : \Delta^{-}\pi^{+} = 2 : 1$ is considered when the $\Delta^{++}\Delta^{-}$ are added to the $\Delta\pi$. The ratio is devised entirely from Carbonara's data. For clarity, the filled stars are shifted toward larger E_γ value by 10 MeV.

below) and the underestimation of the 3BPS background suggests that the fitting did not misidentify the $\Delta\pi$ processes with other quasifree processes.

Instead, the main problem seems to stem from Carbonara's analysis, in which only quasifree processes were assumed with the struck nucleon having the larger momentum, four-body reaction processes such as double delta excitation were neglected. A few decades later, the double delta excitation process has been identified to be important. If the two-nucleon participating reactions are truly important, the PWIA quasifree process ought to be reduced in order to compensate for this. Therefore the disagreement between Carbonara's and present analyses may be a natural effect of the different PWIA approaches taken. Indeed, when the $\Delta\Delta$ cross section is added (the closed stars at the $\Delta\pi$ panels in Fig.4.6), there is a general agreement in the $\Delta\pi$ panels of Fig.4.6.

It may be a reasonable assumption that if a significant proportion of the $\Delta\pi$ process undergo FSI, then other quasifree processes do as well. A very similar test is done for the 3BPS background and the total quasifree cross section. At the 3BPS panel in Fig.4.6, the closed stars indicate the sum of $(\pi^+\pi^-N)_{\rm 3BPS}$ and $(\pi^+\pi^-pn)_{\rm 4BPS}$ processes. Although it is not certain that twice the value of the γp cross sections serves as a good prediction, the sum seems to agree with this prediction. In the total QF panel, the closed circles are the sum of all quasifree processes. These are $\Delta\pi$, QFρ^0, QF-Drell, and $(\pi^+\pi^-N)_{\rm 3BPS}$. The closed stars are the sum of, in addition, $\Delta\Delta$, and $(\pi^+\pi^-pn)_{\rm 4BPS}$ processes. Again, agreement between the closed stars and the open circles (Calbonara's data) can be seen.

The fitting result is also checked with events that included a proton track. The statistics in that data set are too limited to be reasonably fitted, but not too poor to be compared. Fig.4.7 shows distributions of the missing momentum in the laboratory frame which is given by

$$P_X = \left|\vec{k} - (\vec{k}_1 + \vec{k}_2 + \vec{p}_p)\right|_{\rm lab.}$$

The figure indicates that the Monte Carlo spectrum does not particularly overestimate the high missing momentum region. Also, the distributions of invariant masses,

$$m_{\pi^+p} = \sqrt{(k_1 + p_p)^2}, \qquad m_{\pi^-p} = \sqrt{(k_2 + p_p)^2}$$

in Figs.4.8 and 4.9 display good agreement between the data and simulation, which further contributes to the confidence of the fitting result. Once again one notes, in particular, that even with the missing-mass cut, the strength of the $\Delta^{++}\pi^-$ process is not underestimated. Finally, the $\Delta^0\pi^+$ component of the reaction does not seem to be important since the m_{π^-p} distribution is successfully reproduced without the $\Delta^0\pi^+$ process.

ρ^0 Production

The fitting finds no significant contribution from the modified-mass ρ^0 production or the Drell-type background. Only the unmodified ρ^0 gives non-zero cross sections. The total cross sections are displayed in Fig.4.10 together with proton data from the ABB-HHM collaboration [33] for comparison. The result shows that the incoherent ρ^0 are longitudinally polarized below the nominal photon energy threshold of 1086 MeV.

The signature of the longitudinal ρ^0 could be examined with the ρ^0 decay angle in the quasifree helicity system. However, because the scattered nucleons were not detected in most events, it is not possible to calculate the angle, θ_{qH}*. One could assume that, similar to the coherent angle, θ_{cH}, the target nucleon was at rest in the laboratory frame. Because of the Fermi motion of the nucleon, this is actually not the case. If the Fermi motion is neglected, it is possible to calculate "θ_{qH}" but this is no longer actual θ_{qH}. To avoid confusion, this angle can be denoted by θ'_{qH}. In other words, θ'_{qH} is an angle which ignores the Fermi motion. However, θ'_{qH} is a good approximation of θ_{qH} when the photon energy is much larger than the nucleon momentum. This is evident from Fig.4.11 which displays the $\cos\theta'_{qH}$ distributions. The shape of QF-Lρ^0 (QF-Tρ^0), which is proportional to $\cos^2\theta_{qH}$ ($\sin^2\theta_{qH}$), is well reproduced by the $\cos\theta'_{qH}$ distribution†.

Fig.4.11 is for the second highest photon energy bin in which the strength of the Tρ^0 is negligible. The data and the Monte Carlo distributions agree quite well. The $\cos^2\theta_{qH}$-like signature is not unique, but it is apparent that dominant $\Delta\pi$ and $\Delta^{++}\Delta^-$ processes give a $\sin^2\theta_{qH}$-like signature so that the longitudinal ρ^0 becomes more important than the transverse one in order to make the net spectrum agree with the data distribution. Since both the $(N\pi\pi)_{3\mathrm{BPS}}$ and $(\pi^+\pi^-pn)_{4\mathrm{BPS}}$ background processes exhibit somewhat similar signatures as the Lρ^0 does, it may be important to check that these processes are

---

*The definition of the quantization axis involves the Lorentz transformation to the γ-N rest frame (see Fig.3.6). Knowledge of the four momentum of the nucleon just before or after the reaction is necessary. For the explicit calculation of θ_{qH}, please see Appendix D.

†In the simulation, the Fermi motion for each event is simulated, thus, the precise θ_{qH} was used.

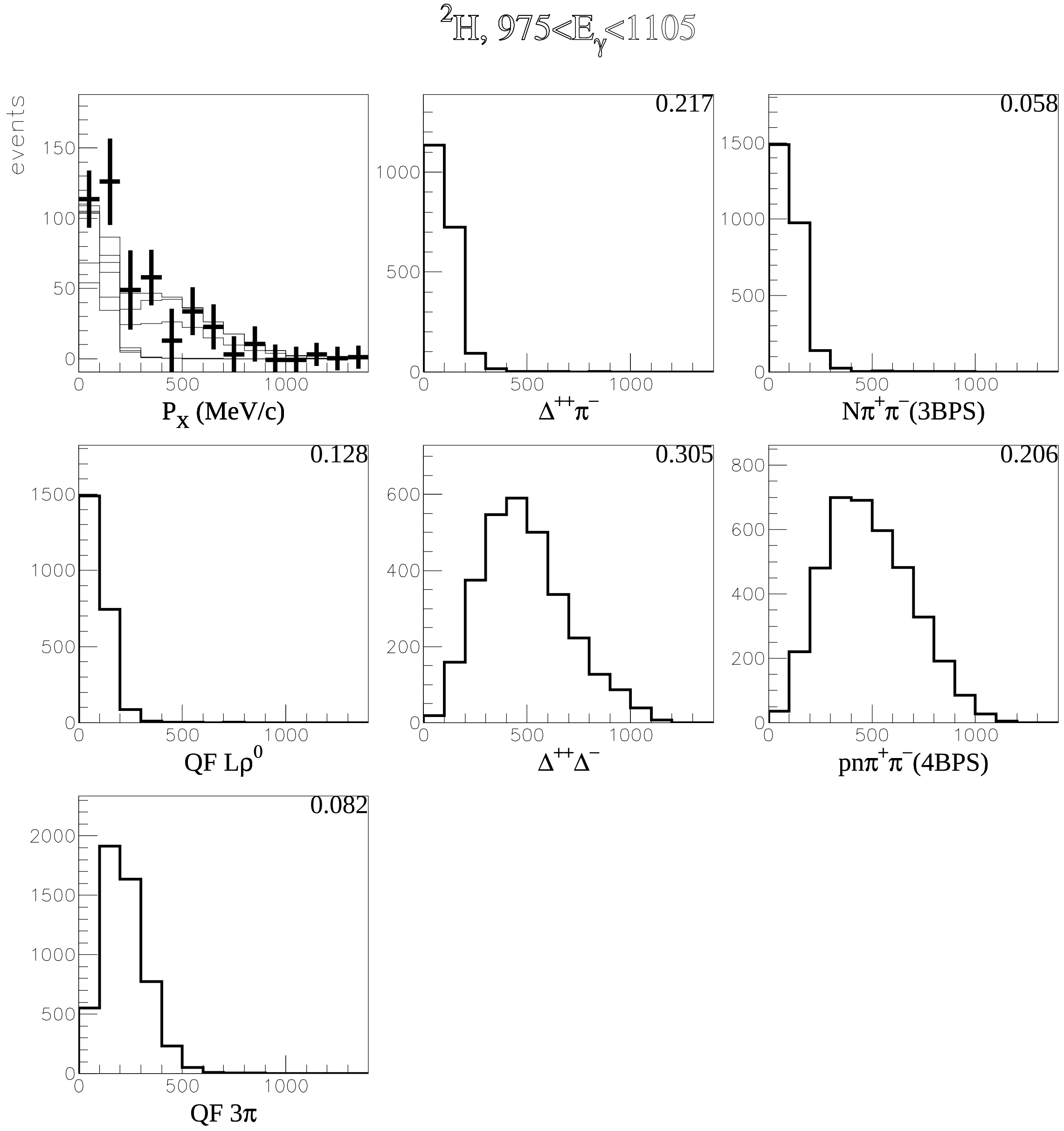

Figure 4.7: The missing-momentum distribution P_X with a proton track detected. No missing-mass cut is applied but only events with one proton and two pions detected are considered. To interpret this figure, please refer to Fig.4.1.

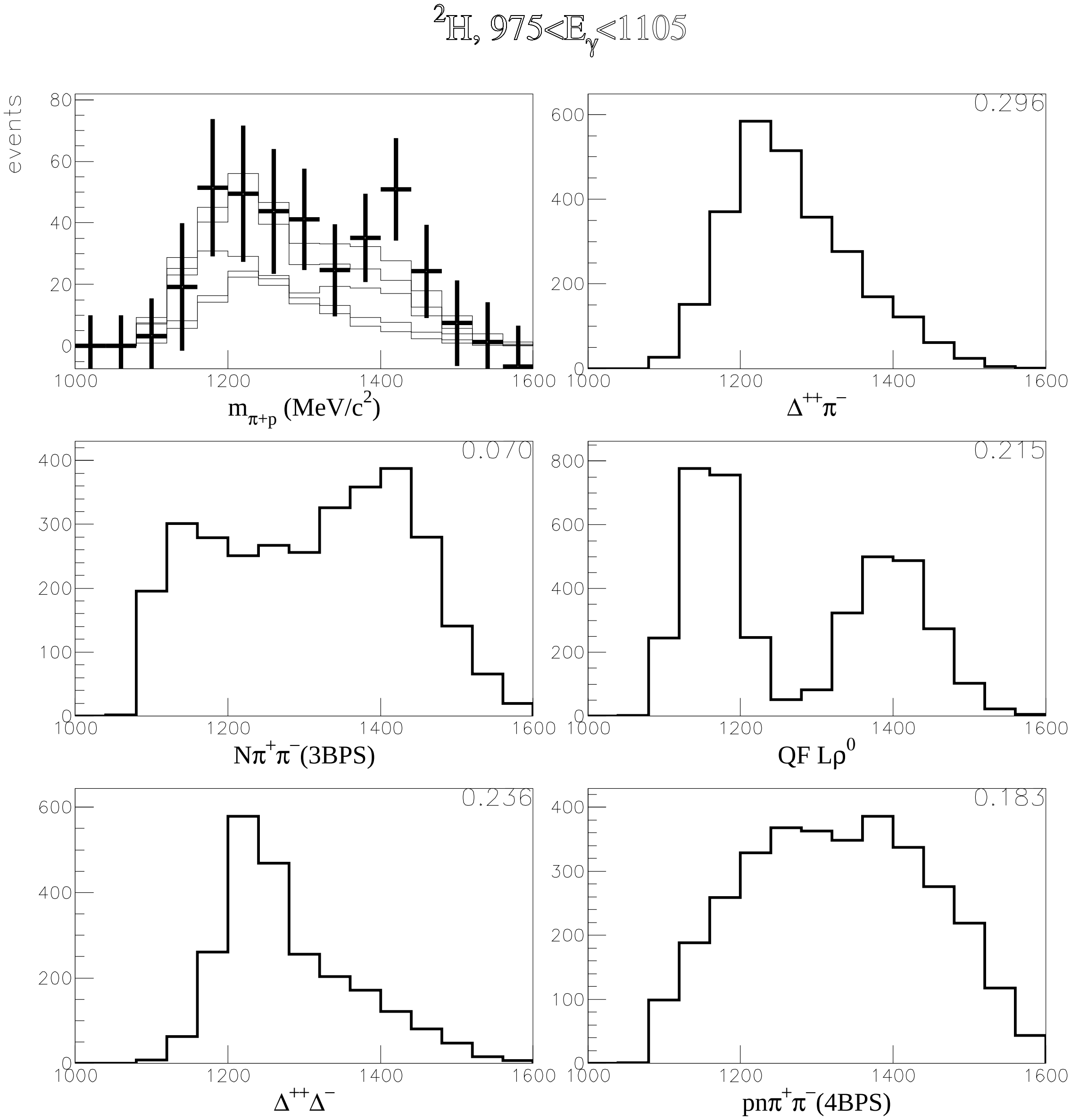

Figure 4.8: The π^+p invariant mass distribution in the quasifree region ($1870 \le m_X \le 2000$ MeV/c^2). To interpret this figure, please refer to Fig.4.1.

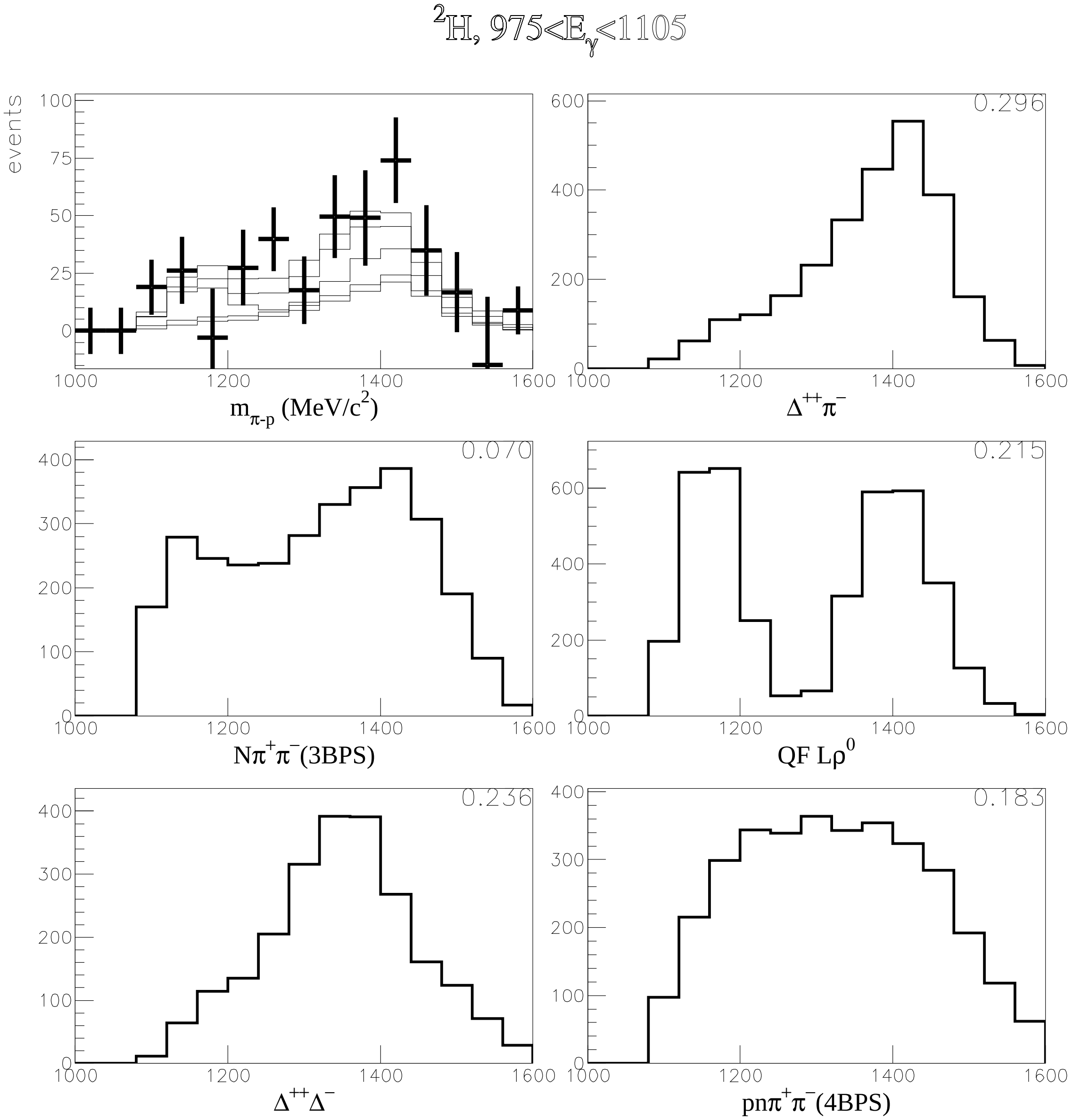

Figure 4.9: The $\pi^- p$ invariant mass distribution in the quasifree region ($1870 \leq m_X \leq 2000$ MeV/c^2). To interpret this figure, please refer to Fig.4.1.

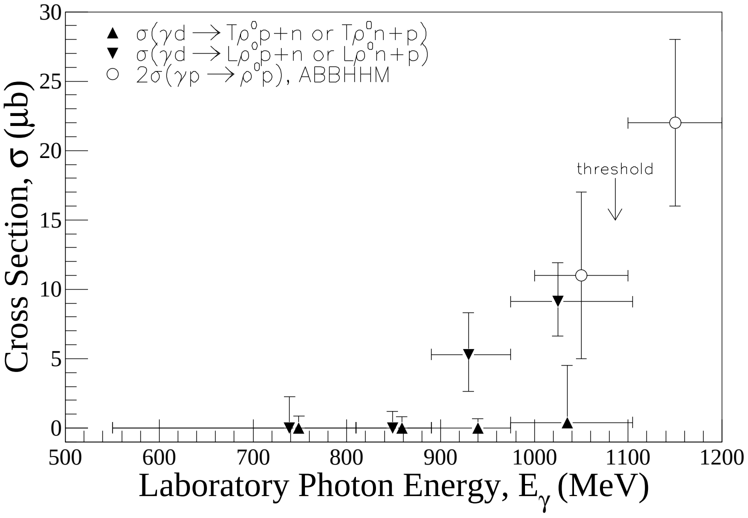

Figure 4.10: The deuteron quasifree cross section for the ρ^0 photo production (filled triangles). Open circles are the cross section for $\gamma p \to \rho^0 p$ from the ABBHHM collaboration [33]. They are multiplied by two to compare with our deuteron result. For clarity, the central Tρ^0 values are shifted by 10 MeV toward higher photon energy.

not as relevant as the Lρ^0. The dipion invariant mass distributions shown in Fig.4.12 may be a key ingredient to distinguish among processes. However, as shown in the figure, this variable is not as sensitive as one might expect. Most quasifree processes peak at a similar value due to the TAGX acceptance. A more useful variable turned out to be the opening angle distribution, $\theta_{\pi\pi} = \theta_{12}^{\mathrm{lab.}}$, which is displayed in Fig.4.13. Among the quasifree simulations, the QF-Lρ^0 peaks at the smallest value, $\cos\theta_{\pi\pi} \simeq -0.4$[‡]. This seems to be well suited to the data distribution. On the other hand, $(N\pi\pi)_{\mathrm{3BPS}}$ seems to be inhibited by the strong presence of the $\Delta^{++}\pi^-$ because both have a relatively large population at small opening angle ($\cos\theta_{\pi\pi} \geq 0.6$). Therefore they certainly appear to be combinatory reasons of enhancing the Lρ^0 instead of the backgrounds. The same may be true for any evidence that a ρ^0 mass shift has not been identified.

[‡] Qualitatively, a difference between the Tρ^0 and Lρ^0 in the opening angle distribution may be explained by the Lorentz boost from the rest frame of the ρ^0 to the laboratory. Suppose that the ρ^0 is produced in the same direction as the photon. In the ρ^0 rest frame, the Tρ^0 tends to distribute the pions vertical to the ρ^0 momentum in the total center-of-mass frame whose direction is likely very similar to that of the photon, whereas the Lρ^0 tends to release one of the pions toward its own direction leaving the other pion behind. The Lorentz transformation changes the directions of the pion momenta but the change is most pronounced when the original direction is perpendicular to the boost.

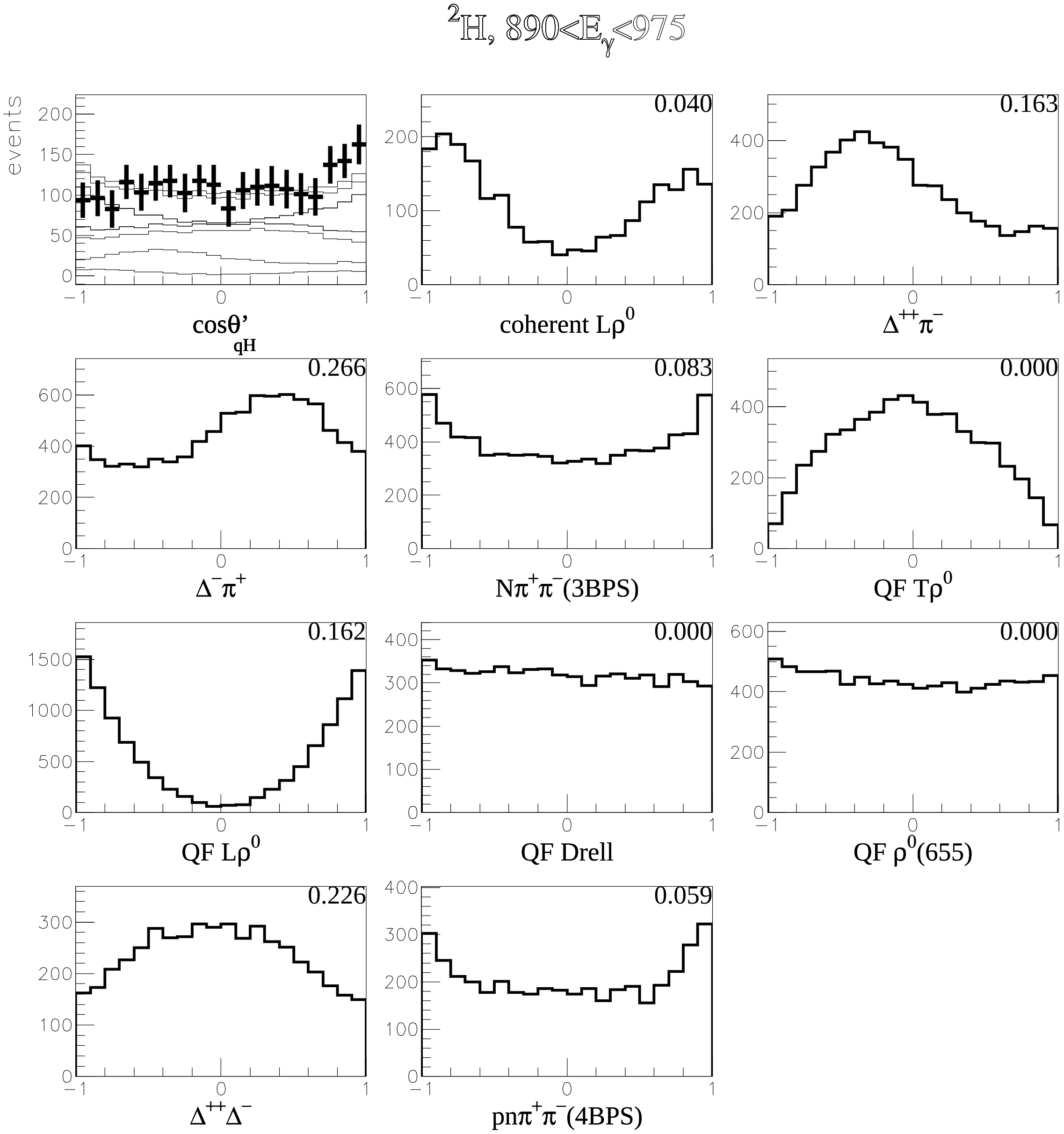

Figure 4.11: The $\cos\theta'_{qH}$ distribution in the quasifree region. To interpret this figure, please refer to Fig.4.1.

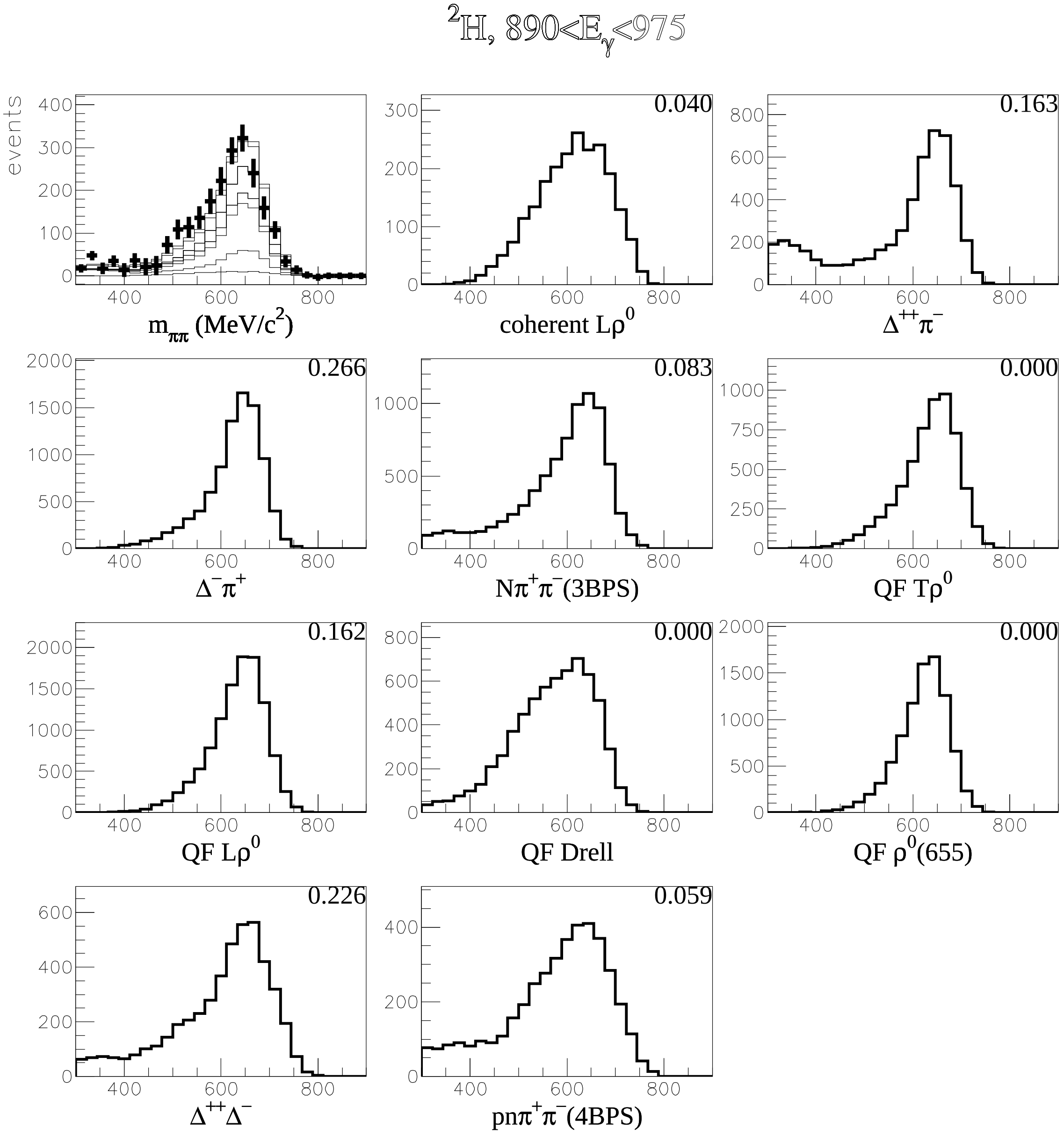

Figure 4.12: The dipion invariant mass distribution in the quasifree region. To interpret this figure, please refer to Fig.4.1.

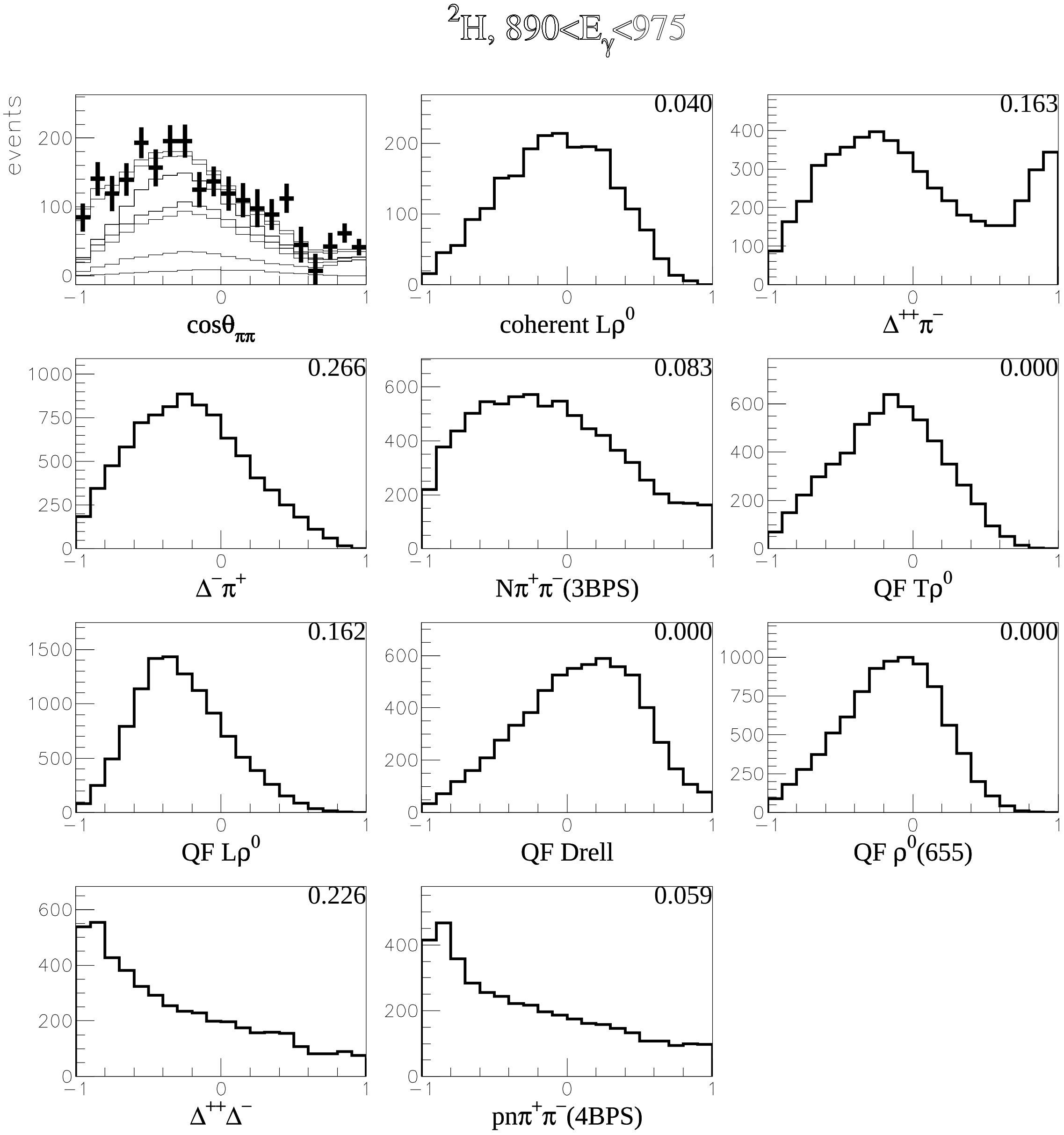

Figure 4.13: Distribution of the opening angle in the quasifree region. To interpret this figure, please refer to Fig.4.1.

4.2.3 High Missing-Mass Region

In this missing-mass region, reactions in which more than one nucleon participates or more than two pions are created are important. These reactions have a relatively small TAGX acceptance because the cross section becomes proportional to the many-body phase space with little correlation between the π^+ and π^-. The total cross section is inversely proportional to the acceptance so this region provides an important ingredient to determine the total multi-pion production cross section. At the same time, the inclusive nature of the experiment, together with the small fraction of the acceptance, makes this difficult to investigate conclusively. The five-dimensional analysis does not make it particularly easy to attain a high confidence. However, the parameters P_j for these processes are kept free in the fitting and they are determined just like the other parameters, thus some confidence in experimental data and in the fitting may be achieved by observing that the outcome is in accord with other accepted experimental results.

Fig.4.14 compares the results on $\Delta^{++}\Delta^-$ and the 4BPS background with data by Y. Wada *et al.* [46] and by M. Asai *et al* [47]. The cross sections are in agreement. The determination of the parameters for $\Delta^{++}\Delta^-$ and the 4BPS background certainly require differentiation between them, but they are found to be subtle in the one-dimensional spectra. The dipion decay angle, θ'_{qH}, in the quasifree region shown in Fig.4.11, which exhibits the same behavior as in the high missing-mass region for both $\Delta^{++}\Delta^-$ and the 4BPS background, may be the best projected distribution to observe a difference. An even better way to check the result is to analyze the events with a proton track. Fig.4.15 shows the π^+p invariant mass distribution in the high missing-mass region. The data distribution peaking around 1200 MeV/c^2 indicates the relatively strong presence of the $\Delta^{++}(1232)$ resonance, even in the region of high missing mass.

The results of three pion producing reactions, QFη and QF3π, are displayed in Fig.4.16. As for the η production, the cross section is compared with the $d(\gamma,\eta)X$ experiment near the threshold at MAMI by B. Krusche *et al.* [48] and with $p(\gamma,\pi^+\pi^-)p$ experiment at DESY by the ABBHHM collaboration [33]. This experiment agrees with those but within relatively large error bars due to particularly small TAGX acceptance (see Fig.3.10). The present QF$(3\pi N)$ background cross sections show a small contribu-

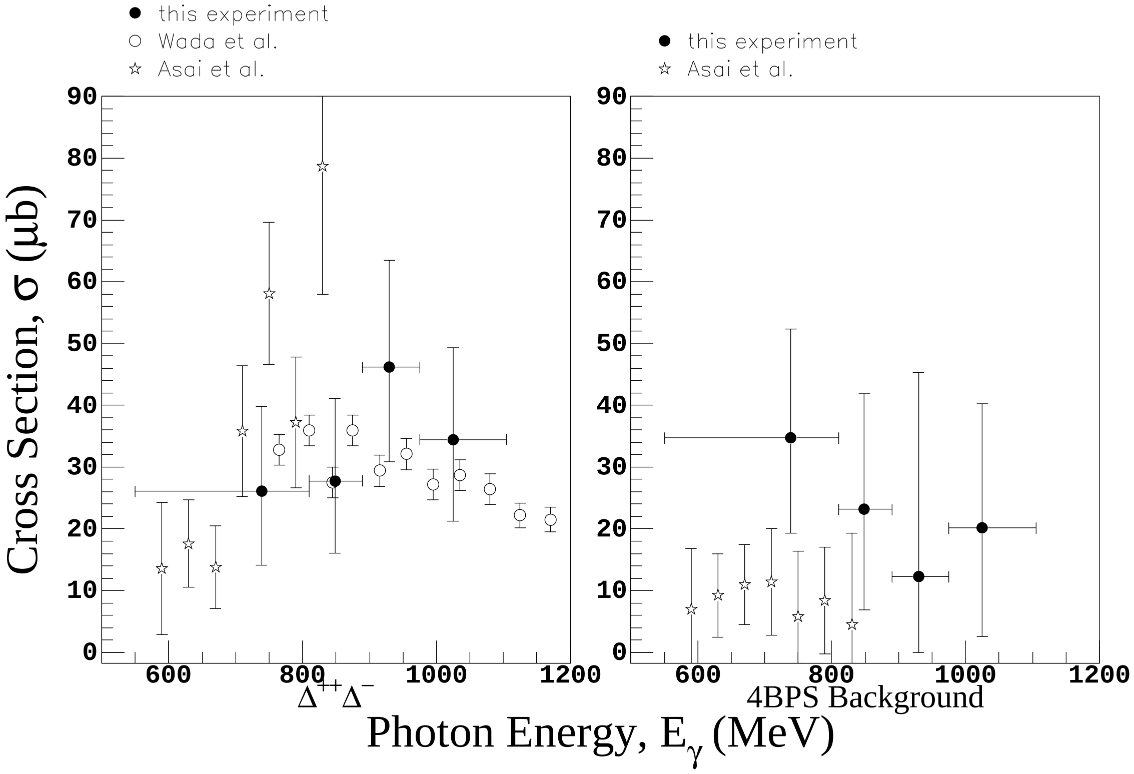

Figure 4.14: The total cross section for the reaction $\gamma d \to \Delta^{++}\Delta^{-}$ and the $(\pi^+\pi^-pn)_{\rm 4BPS}$ background. Full circles are the present result. Open circles are from Wada *et al.* [46] and open stars are from Asai *et al* [47].

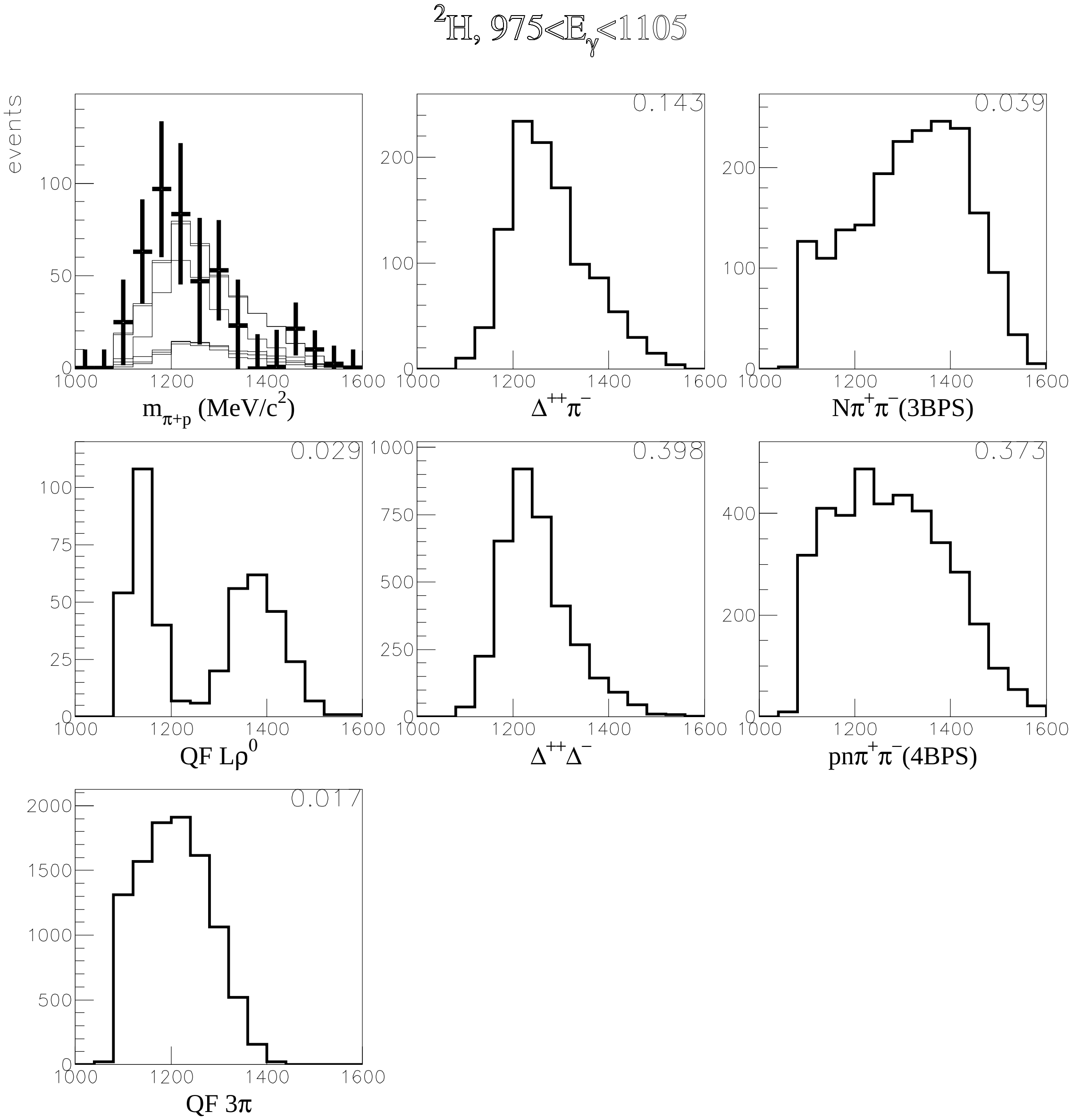

Figure 4.15: The π^+p invariant mass distribution in the high missing-mass region, $m_X \geq$ 2000 MeV/c^2. To interpret this figure, please refer to Fig.4.1.

tion with large errors, which does not violate the upper limits of the production cross section derived from the DESY experiment.

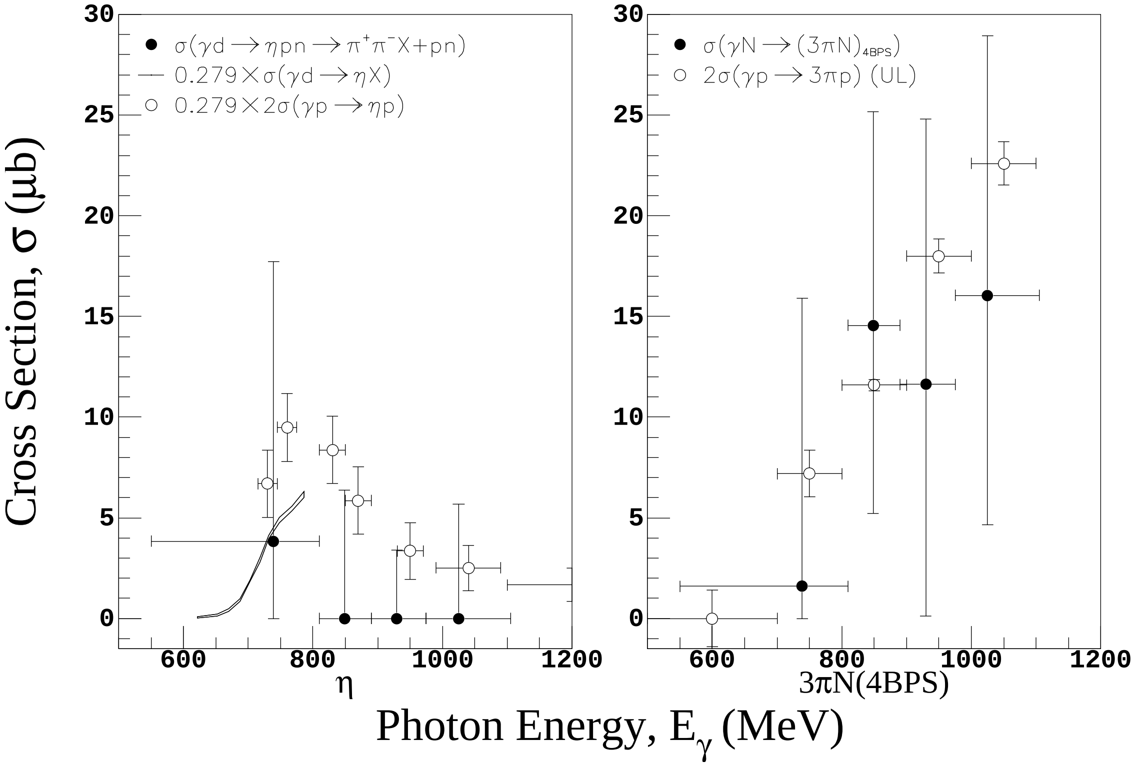

Figure 4.16: The photo production cross sections for the η and the $(3\pi N)_{\rm 4BPS}$ background. Full circles are from the present experiment. The smooth curve is a rough drawing from the inclusive MAMI experiment by B. Krusche *et al* [48]. The value is multiplied by 27.9%, which is a sum of the branching ratios for $\eta \to \pi^+\pi^-\pi^0$ and $\eta \to \pi^+\pi^-\gamma$ [1]. The open circles are from the $p(\gamma,\pi^+\pi^-p)$ experiment by the ABB-HHM collaboration [33]. The upper limit (UL) $\gamma p \to 3\pi p$ cross section is a sum of the $\gamma p \to \pi^+\pi^-\pi^0 p$ and $\gamma p \to \pi^+ 2\pi^- n$ UL cross sections. They implicitly include η production.

Direct evidence of three pion production, however, may be seen from the events with a proton detected. Because the neutron is the only undetected particle in addition to the third pion, the missing mass,

$$M_X = \sqrt{(k + p_A - k_1 - k_2 - p_p)^2}$$

should give a peak around $m_n + m_\pi \simeq 1080$ MeV/c^2 when another pion is created. Fig.4.17 clearly shows a small hump beside the neutron peak around 1100 MeV/c^{2}[§].

[§] In Fig.4.17, the Monte Carlo spectrum does not agree with the data very well. It is suspected that

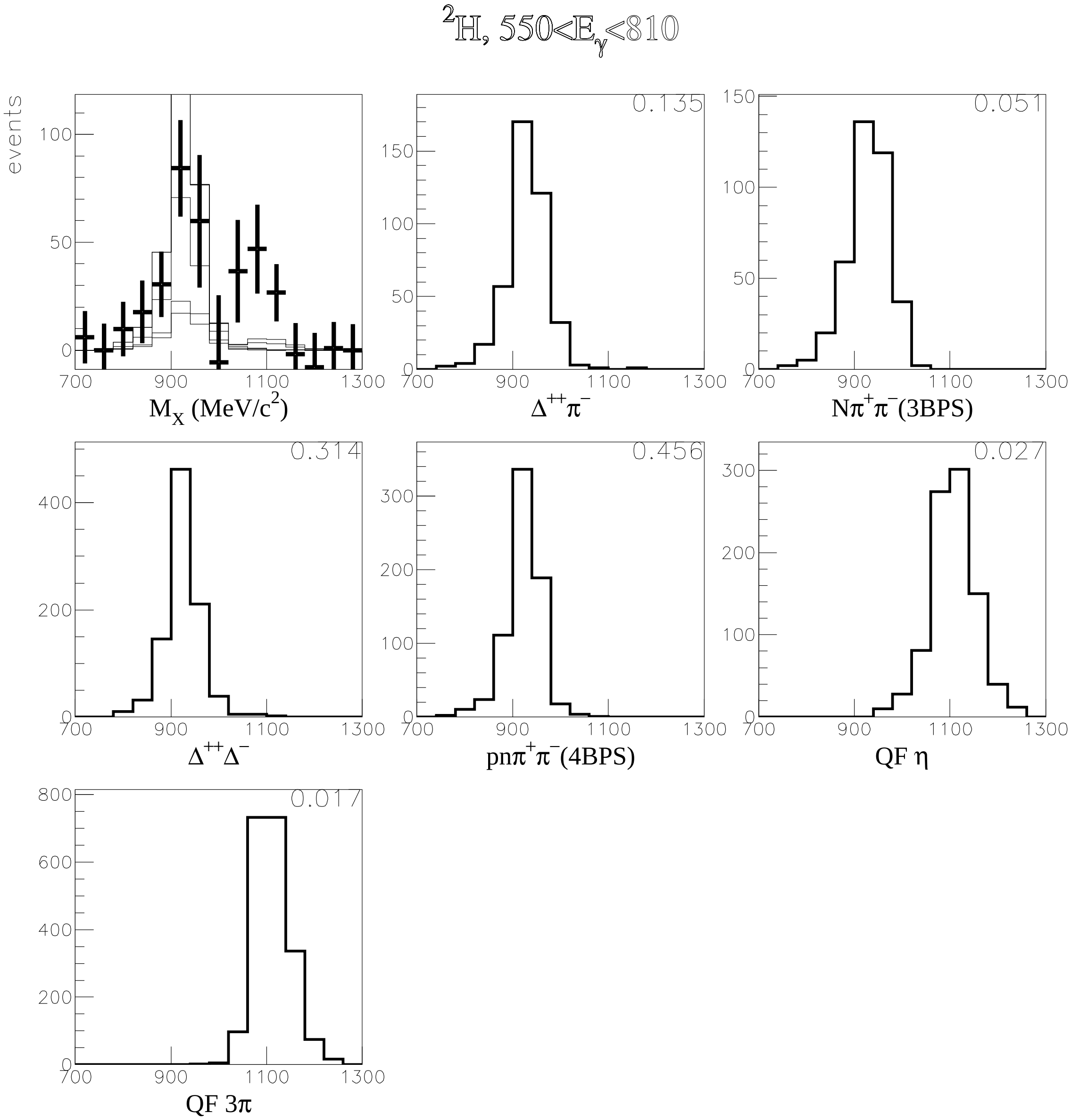

Figure 4.17: Distribution of the missing mass, M_X when the proton track is detected. The missing-mass cut $m_X \geq 2000$ MeV/c^2 is applied. M_X should not be confused with m_X. To interpret this figure, please refer to Fig.4.1.

Distinguishing the η signal from that of the N3π(4BPS) background is relatively easy because of the mass of η. The three-pion invariant mass is fixed at relatively low values so that the dipion invariant mass peaks at very small value compared to the background. As a result, a sharp contrast is seen in the opening angle in the laboratory frame as shown in Fig.4.18.

4.2.4 $\pi^+\pi^- X$ Cross Section

As a final check, our total double pion photo-production cross section is also compared with established references. Fig.4.19 displays the inclusive (meaning it includes the triple pion production) total cross section obtained by this experiment. It is superimposed with the twice the value of double pion photo-production off the proton by the ABBHHM collaboration and with Carbonara's total quasifree cross section. This experiment gives a systematically smaller cross section than the references but the error bars are large.

The absolute number of events obtained for the fitting analysis is fixed. The fitting procedure basically tries to separate these events into the 15 processes. The quasifree reaction processes generally have a larger TAGX acceptance than the high missing-mass reaction channels so that if some of the quasifree events in the real data were misidentified as the high missing-mass process, the total $d(\gamma, \pi^+\pi^-)X$ cross section would have become larger. But the fitting seems to yield the opposite result. Therefore, it should be safe to conclude that the fitting result does not underestimate the quasifree cross section.

4.3 Carbon Data Analysis

There are 14 Monte Carlo processes considered for the fitting. The fitting result is listed in Tab.4.2. The reduced χ^2 are found to be quite small ($\chi^2/\mathrm{ndf} \lesssim 0.4$) because of a large error in each fitting channel in the five dimensions. This is a result of the poor statistical quality of the data. As has already been seen in the deuteron result, the reproduction of the one dimensional distributions generally appears to be very good in the carbon case as well. By looking at the simulation and the data in the missing-mass

---

this shows the limitation of constructing the deuteron spectrum out of the $(\gamma, \pi^+\pi^-)$ TAGX detection acceptance ratios (see sec.2.3.5). A more reliable extraction of the deuteron M_X spectrum can be derived from the $(\gamma, \pi^+\pi^- p)$ TAGX detection acceptance ratios.

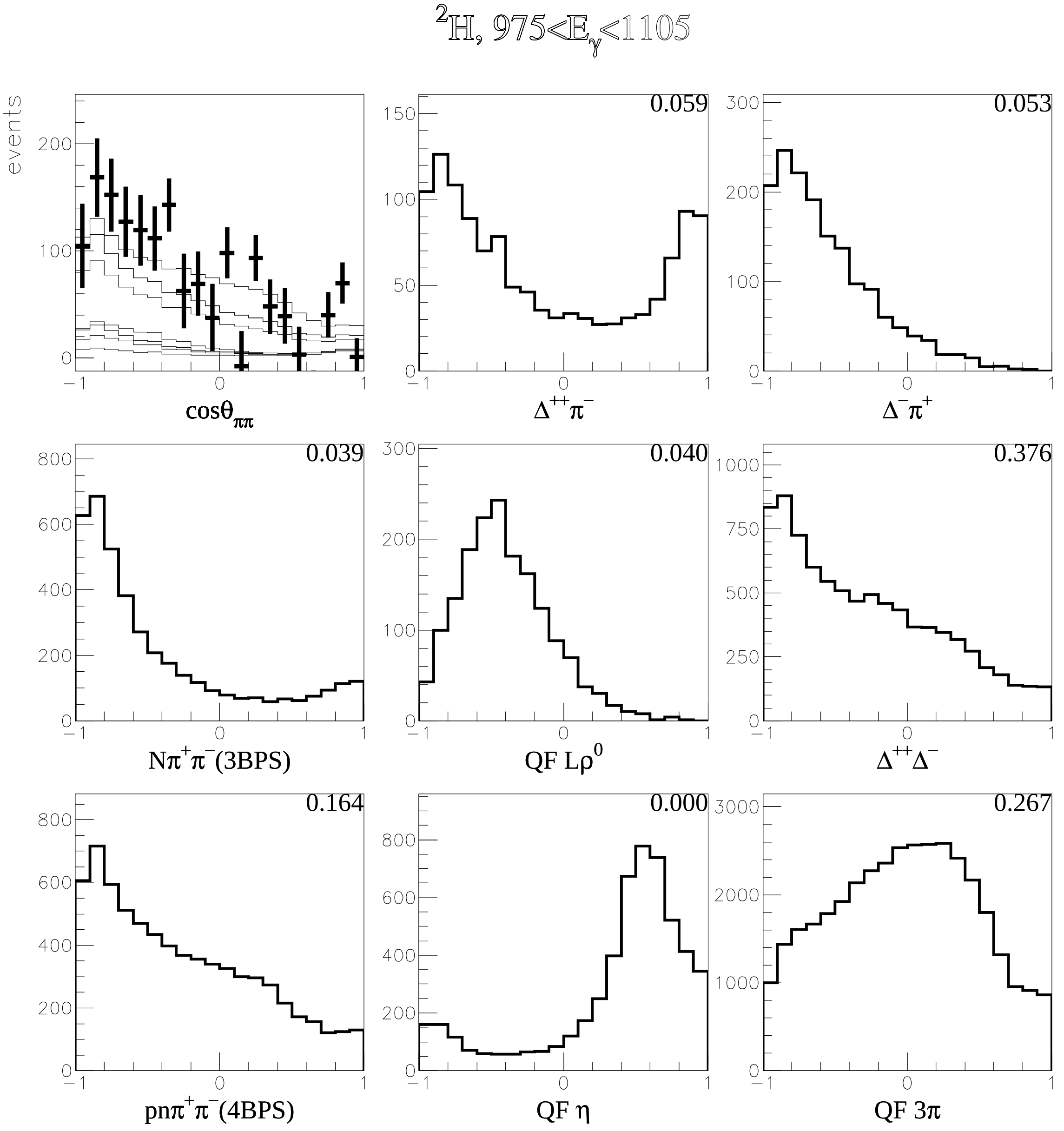

Figure 4.18: Cosine distribution of the laboratory opening angle in the high missing-mass region. Smaller readings at $\cos\theta_{\pi\pi} = \pm 1$ are due to the cut of the difference of azimuthal scattering angle described in sec.2.3.3. To interpret this figure, please refer to Fig.4.1.

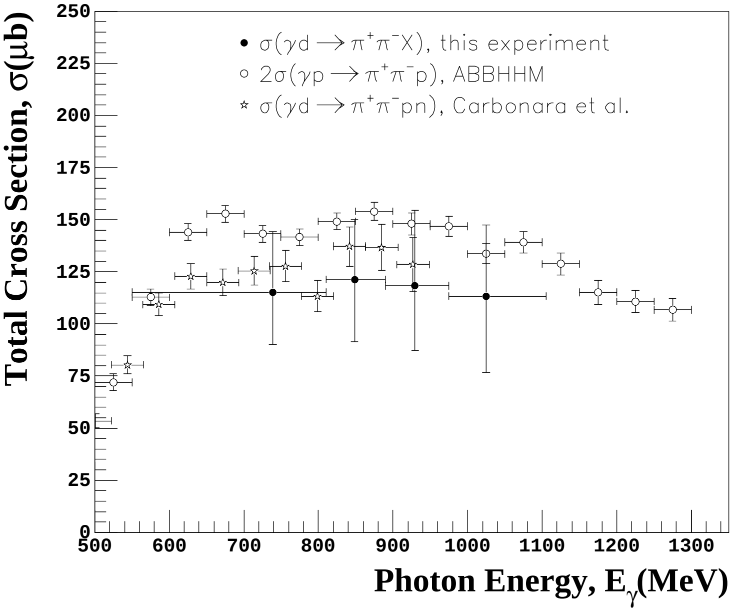

Figure 4.19: The total $d(\gamma,\pi^+\pi^-)X$ cross section obtained by this experiment (closed circles). Open circles are twice the value of the total cross section for $d(\gamma,\pi^+\pi^-p)$ by the ABBHHM collaboration [33]. Open stars are the total cross section for the $d(\gamma,\pi^+\pi^-p)n$ reaction by F. Carbonara *et al* [39].

spectrum as shown in Fig.4.20, the results are separated into three regions as follows:

$$\begin{aligned} m_X &\leq 11178\ \mathrm{MeV/c^2} && \text{(coherent region)} \\ 11178 \leq m_X &\leq 11400\ \mathrm{MeV/c^2} && \text{(quasifree region)} \\ m_X &\geq 11400\ \mathrm{MeV/c^2} && \text{(high missing-mass region)} \end{aligned}$$

As was done in the deuteron analysis, the fitting results presented in Tab.4.2 will be examined in the following sections for each missing-mass region.

4.3.1 Coherent Region

In Fig.4.21, the total $\gamma\mathrm{C} \to \pi^+\pi^-\mathrm{C}$ cross sections are plotted. Each datum is a sum of the coherent Drell-type background and the ρ^0 production cross sections. One observes that the total $\gamma\mathrm{C} \to \pi^+\pi^-\mathrm{C}$ cross section measured by this experiment appears to agree with Benz's [49] total $\gamma\mathrm{d} \to \pi^+\pi^-\mathrm{d}$ cross section multiplied by a factor $(12/2)^{2/3}$ which approximates the ratio of the geometrical nuclear cross sections. Benz's slightly smaller cross sections may be due to the t cut or possibly the geometrical factor.

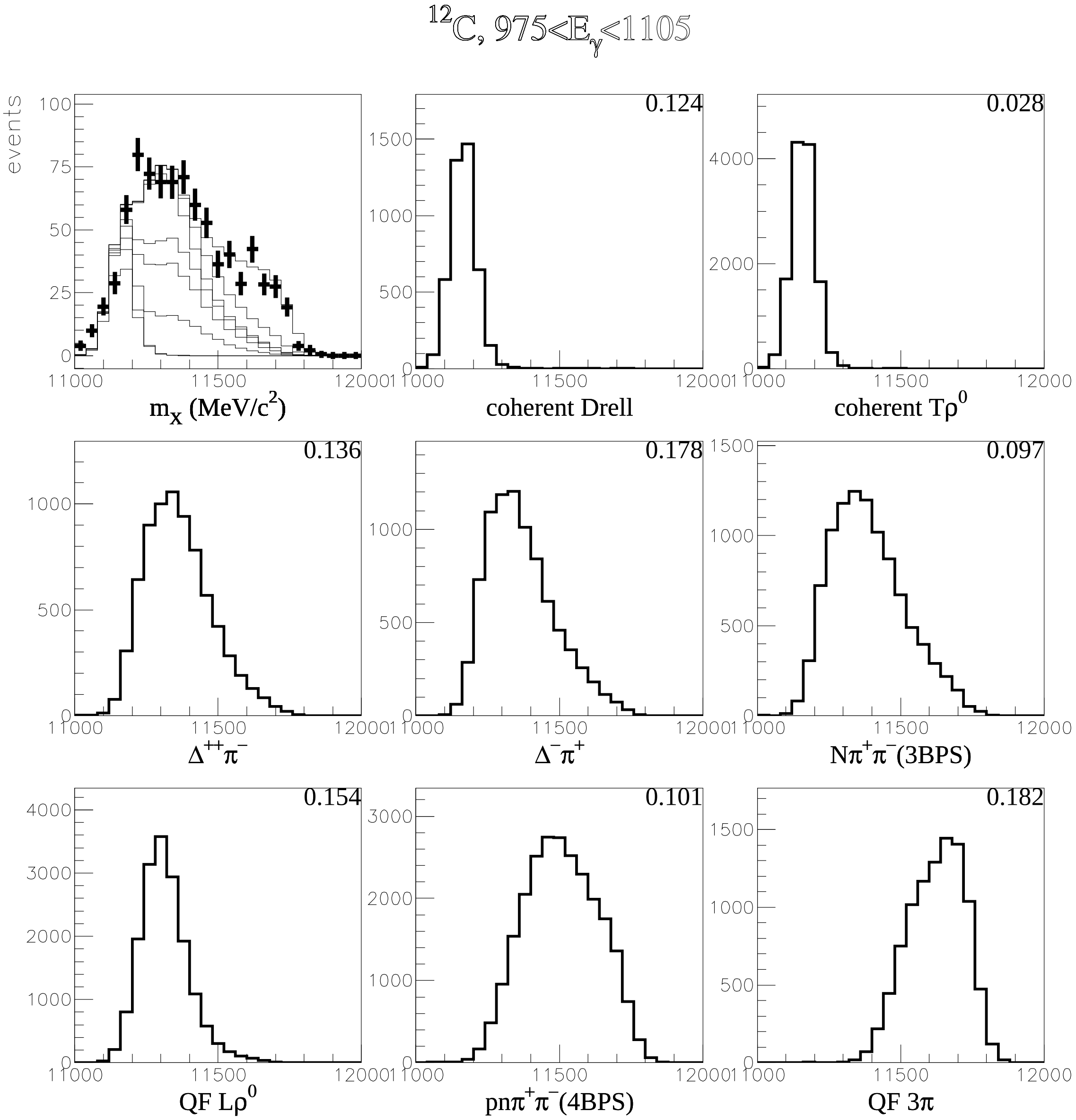

Figure 4.20: The carbon missing-mass distribution spectra. Data (+) and cumulative Monte Carlo simulation (rectangle lines) are superimposed in the top left panel. Each component of the simulation is displayed in the rest of the panels. The strength P_j for this particular data set is given in the upper right corner in each Monte Carlo panel.

Table 4.2: Carbon fitting result. “T” and “L” in front of ρ^0 signifies transverse and longitudinal, respectively.

$E_\gamma = 550\text{– }810$ MeV $\chi^2/\text{ndf} = 0.055$		
process	$P_j[\%]$	$\sigma[\mu\text{b}]$
coherent Tρ^0	$0.1^{+1.51}_{-0.14}$	$0.1^{+1.03}_{-0.09}$
coherent Lρ^0	$1.3^{+1.45}_{-1.26}$	$0.9^{+1.27}_{-0.92}$
coherent Drell	$4.8^{+2.35}_{-2.35}$	$5.2^{+3.43}_{-2.84}$
$\Delta^{++}\pi^-$	$20.1^{+7.70}_{-7.70}$	$61.6^{+33.37}_{-27.70}$
$\Delta^-\pi^+$	$20.2^{+7.47}_{-7.47}$	$72.0^{+37.80}_{-31.46}$
QF Tρ^0	$5.9^{+12.16}_{-5.90}$	$9.9^{+24.09}_{-9.91}$
QF Lρ^0	$0.0^{+3.19}_{-0.00}$	$0.0^{+5.41}_{-0.00}$
QF Drell	$16.0^{+10.01}_{-10.01}$	$38.0^{+30.52}_{-25.19}$
QF ρ^0(655)	$0.0^{+6.51}_{-0.00}$	$0.0^{+11.18}_{-0.00}$
N$\pi^+\pi^-$(3BPS)	$22.6^{+13.75}_{-13.75}$	$68.8^{+54.95}_{-44.93}$
$\Delta^{++}\Delta^-$	$3.8^{+9.87}_{-3.84}$	$13.1^{+39.70}_{-13.05}$
pn$\pi^+\pi^-$(4BPS)	$0.0^{+4.15}_{-0.00}$	$0.0^{+21.33}_{-0.00}$
QF η	$2.7^{+6.15}_{-2.73}$	$9.1^{+23.87}_{-9.10}$
QF 3π	$2.4^{+7.68}_{-2.39}$	$17.8^{+65.30}_{-17.82}$
total multiπ	$100.0^{+0.00}_{-0.00}$	$296.6^{+114.40}_{-91.25}$

$E_\gamma = 810\text{– }890$ MeV $\chi^2/\text{ndf} = 0.106$		
process	$P_j[\%]$	$\sigma[\mu\text{b}]$
coherent Tρ^0	$1.5^{+3.19}_{-1.53}$	$0.9^{+2.03}_{-0.86}$
coherent Lρ^0	$0.8^{+2.22}_{-0.84}$	$0.7^{+2.01}_{-0.68}$
coherent Drell	$8.7^{+2.08}_{-2.08}$	$10.6^{+3.79}_{-3.27}$
$\Delta^{++}\pi^-$	$22.4^{+6.02}_{-6.02}$	$66.3^{+25.77}_{-22.15}$
$\Delta^-\pi^+$	$28.4^{+6.46}_{-6.46}$	$93.5^{+31.92}_{-27.62}$
QF Tρ^0	$5.2^{+12.32}_{-5.25}$	$9.7^{+25.80}_{-9.67}$
QF Lρ^0	$2.4^{+6.78}_{-2.36}$	$3.8^{+12.38}_{-3.82}$
QF Drell	$9.4^{+18.43}_{-9.44}$	$23.9^{+53.18}_{-23.93}$
QF ρ^0(655)	$0.0^{+5.50}_{-0.00}$	$0.0^{+9.87}_{-0.00}$
N$\pi^+\pi^-$(3BPS)	$6.8^{+23.38}_{-6.78}$	$22.5^{+86.95}_{-22.45}$
$\Delta^{++}\Delta^-$	$0.0^{+7.77}_{-0.00}$	$0.0^{+36.73}_{-0.01}$
pn$\pi^+\pi^-$(4BPS)	$8.3^{+9.85}_{-8.34}$	$40.5^{+55.80}_{-40.55}$
QF η	$5.6^{+4.51}_{-4.51}$	$24.4^{+23.52}_{-20.01}$
QF 3π	$0.3^{+10.34}_{-0.33}$	$1.9^{+64.89}_{-1.88}$
total multiπ	$100.0^{+0.00}_{-0.00}$	$298.6^{+120.10}_{-93.66}$

$E_\gamma = 890\text{– }975$ MeV $\chi^2/\text{ndf} = 0.088$		
process	$P_j[\%]$	$\sigma[\mu\text{b}]$
coherent Tρ^0	$3.5^{+1.40}_{-1.40}$	$2.5^{+1.31}_{-1.12}$
coherent Lρ^0	$0.0^{+1.29}_{-0.00}$	$0.0^{+1.52}_{-0.00}$
coherent Drell	$13.8^{+1.81}_{-1.81}$	$21.7^{+5.32}_{-4.63}$
$\Delta^{++}\pi^-$	$22.9^{+5.53}_{-5.53}$	$76.8^{+27.79}_{-23.87}$
$\Delta^-\pi^+$	$8.6^{+5.27}_{-5.27}$	$30.8^{+23.49}_{-19.85}$
QF Tρ^0	$2.5^{+8.86}_{-2.45}$	$4.6^{+18.72}_{-4.63}$
QF Lρ^0	$9.0^{+4.16}_{-4.16}$	$16.6^{+9.94}_{-8.48}$
QF Drell	$0.0^{+4.89}_{-0.00}$	$0.0^{+15.37}_{-0.01}$
QF ρ^0(655)	$0.0^{+2.35}_{-0.00}$	$0.0^{+4.75}_{-0.00}$
N$\pi^+\pi^-$(3BPS)	$13.4^{+13.51}_{-13.36}$	$50.8^{+61.18}_{-50.81}$
$\Delta^{++}\Delta^-$	$0.0^{+3.28}_{-0.00}$	$0.0^{+17.27}_{-0.00}$
pn$\pi^+\pi^-$(4BPS)	$19.3^{+7.33}_{-7.33}$	$107.1^{+53.74}_{-46.29}$
QF η	$6.4^{+3.30}_{-3.30}$	$39.6^{+25.89}_{-22.05}$
QF 3π	$0.6^{+5.87}_{-0.60}$	$3.6^{+38.96}_{-3.59}$
total multiπ	$100.0^{+0.00}_{-0.00}$	$354.1^{+100.50}_{-94.49}$

$E_\gamma = 975\text{–}1105$ MeV $\chi^2/\text{ndf} = 0.329$		
process	$P_j[\%]$	$\sigma[\mu\text{b}]$
coherent Tρ^0	$2.8^{+1.88}_{-1.88}$	$2.5^{+1.96}_{-1.75}$
coherent Lρ^0	$0.0^{+1.61}_{-0.00}$	$0.0^{+2.92}_{-0.00}$
coherent Drell	$12.4^{+1.80}_{-1.80}$	$23.3^{+5.31}_{-4.73}$
$\Delta^{++}\pi^-$	$36.1^{+10.95}_{-10.95}$	$47.1^{+25.15}_{-19.58}$
$\Delta^-\pi^+$	$17.8^{+3.81}_{-3.81}$	$70.4^{+20.52}_{-18.42}$
QF Tρ^0	$0.0^{+1.12}_{-0.00}$	$0.0^{+2.29}_{-0.00}$
QF Lρ^0	$15.4^{+4.05}_{-4.05}$	$31.9^{+10.70}_{-9.68}$
QF Drell	$0.0^{+2.92}_{-0.00}$	$0.0^{+9.95}_{-0.00}$
QF ρ^0(655)	$0.0^{+2.03}_{-0.00}$	$0.0^{+4.60}_{-0.00}$
N$\pi^+\pi^-$(3BPS)	$9.7^{+20.44}_{-9.74}$	$40.4^{+92.49}_{-40.40}$
$\Delta^{++}\Delta^-$	$0.0^{+1.35}_{-0.00}$	$0.0^{+7.21}_{-0.00}$
pn$\pi^+\pi^-$(4BPS)	$10.1^{+6.95}_{-6.95}$	$58.8^{+45.80}_{-41.37}$
QF η	$0.0^{+1.68}_{-0.00}$	$0.0^{+14.94}_{-0.00}$
QF 3π	$18.2^{+6.61}_{-6.61}$	$108.2^{+48.43}_{-43.35}$
total multiπ	$100.0^{+0.00}_{-0.00}$	$382.5^{+82.66}_{-79.49}$

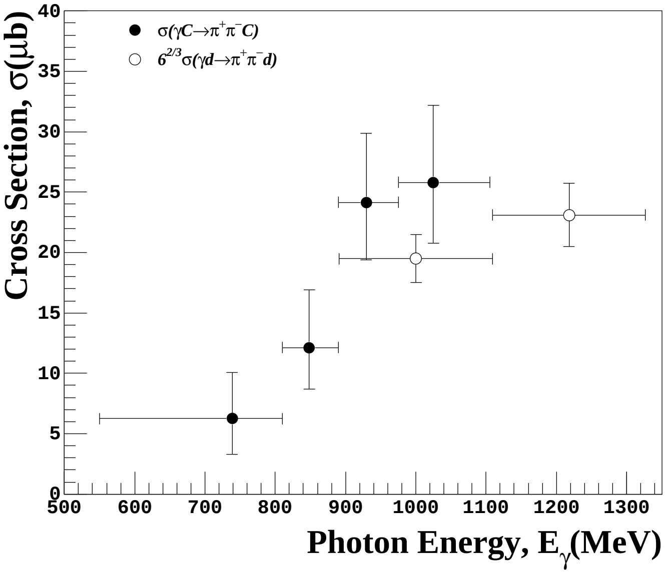

Figure 4.21: Total γC $\to$ $\pi^+\pi^-$C cross sections obtained by this experiment (closed circles) in comparison with the deuteron results measured by P. Benz *et al.* [49] multiplied by $(12/2)^{2/3}$ (open circles). In Ref.[49], all data are subjected to a cut of $-0.2 \le t \le -0.04$ GeV^2.

Fig.4.22 presents the dipion invariant mass distribution. The strength P_j at the corners of the Monte Carlo panels in this figure indicate that the missing-mass cut enhances the total coherent reactions to about 90%. Most of this portion is from the Drell-type background, apparently because its distribution is the most similar to the data. The figure is for the highest photon energy bin ($975 \le E_\gamma \le 1105$ MeV) but all the other photon energy bins also show the dominant Drell background.

The coherent ρ^0 production cross sections are shown in Fig.4.23. In order to compare with Benz's deuteron cross section, an approximate ratio, $R_{\mathrm{C/D}}$, is calculated from the coherent amplitude given by eq.(3.9). Assuming that the forward scattering dominates ($q_b = 0$) and $\sigma_{VN} \approx 30$ μb [60], one may find,

$$R_{\mathrm{C/D}} \equiv \frac{\sigma(\gamma\mathrm{C} \to \rho^0\mathrm{C})}{\sigma(\gamma d \to \rho^0 d)} = \frac{|f_c(A=12)|^2}{|f_c(A=2)|^2} \approx 1.5,$$

at $E_\gamma = 1.0$–1.1 GeV. In the derivation, the nuclear matter density is roughly approximated by a uniform and sharp sphere of radius $1.12A^{1/3}$ fm. The obtained value is very small compared to the conventional scale factor, $A^{3/2}$ (note that this is not $A^{2/3}$). In the high energy domain of the coherent photo production ($E_\gamma \gtrsim 4$ GeV), it is customary to express the forward differential cross section as roughly proportional to $A^{3/2}$ (see, e.g.,

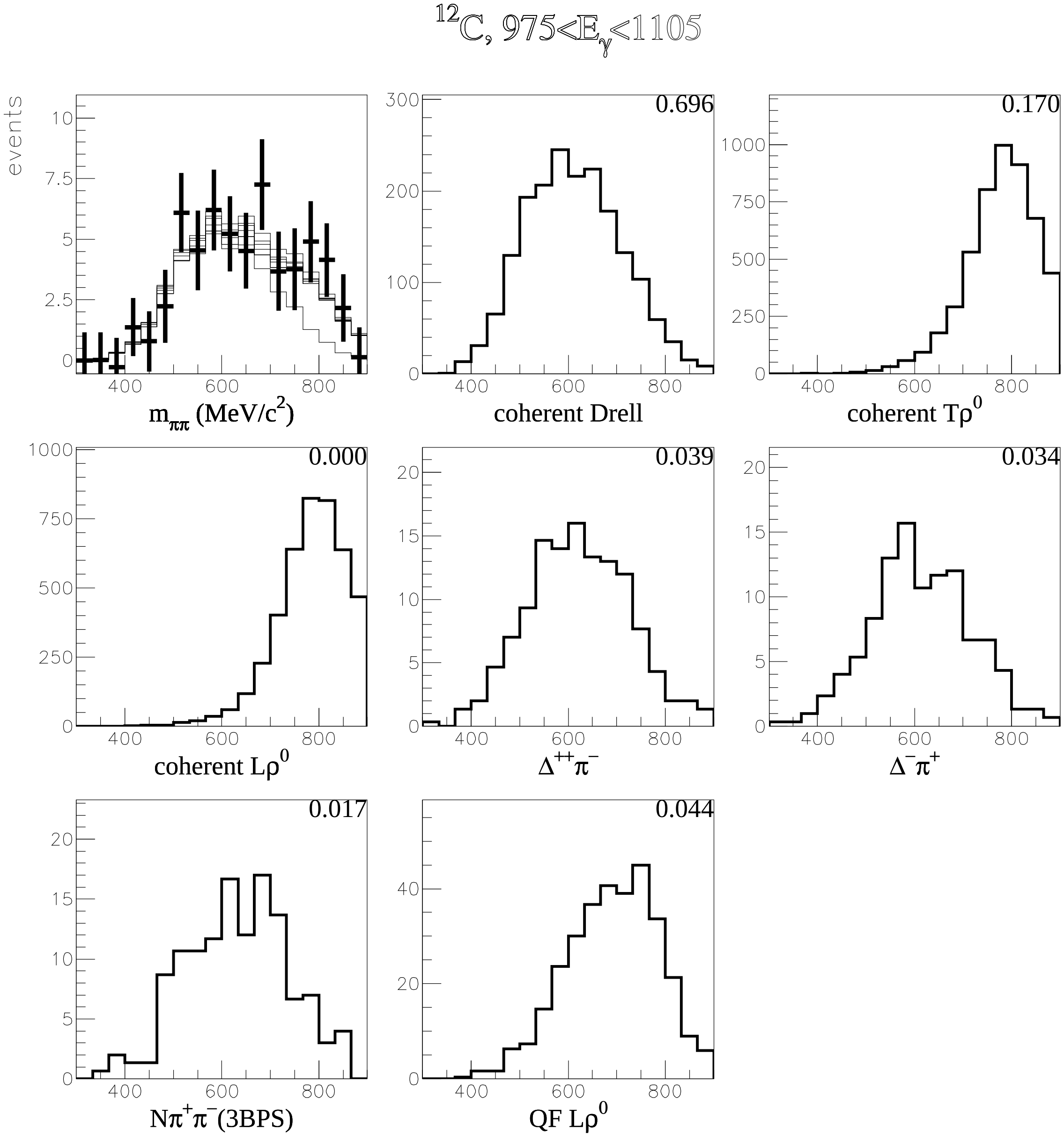

Figure 4.22: The dipion invariant mass distribution in the missing-mass range of $m_X \leq$ 11178 MeV/c^2. For how to read this figure, please refer to Fig.4.20.

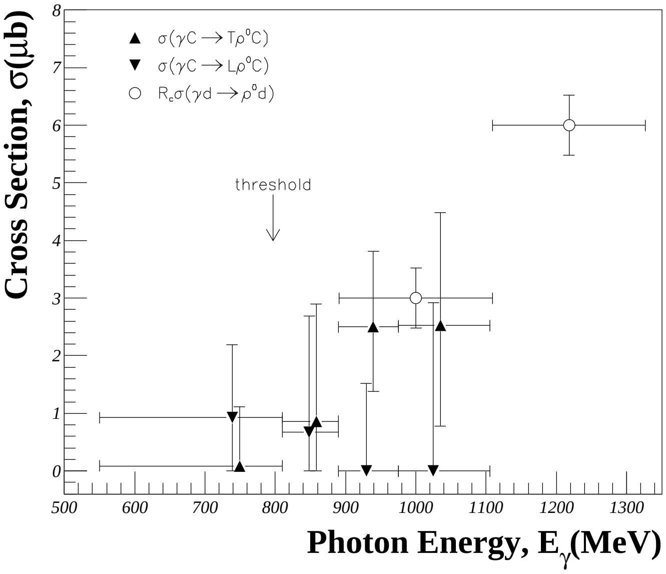

Figure 4.23: The γC $\to$ ρ^0C cross sections obtained by this experiment (filled triangles) in comparison with the deuteron result from P. Benz *et al.* [49] multiplied by $R_{\mathrm{C/D}} = 1.5$ (open circles) as explained in the text. "T" and "L" in front of ρ^0 stand for transverse and longitudinal, respectively. The centroid of the Tρ^0 values are shifted by 10 MeV toward higher E_γ for clarity.

[52]). It gives a manageable scale for $|f_c|^2$ when the momentum transfer is small. The scale factor breaks down near the threshold region because the dominant part of the formula, $\exp\left\{-\frac{\sigma_{VN}}{2}\int_z^\infty \rho(b,z')dz'\right\}$ is taken over by the factor $e^{iq_z z}$. When the energy becomes sufficiently small, the momentum transfer $|\vec{q}|$ is required to take large values in order to create a ρ^0 mass. The large momentum transfer generates a rapid oscillation by the latter and a larger cancellation occurs for a larger nucleus. Thus, the optical model predicts a much smaller ratio than $(12/2)^{3/2} \simeq 14.7$ near threshold.

In Fig.4.23, the present coherent cross sections are plotted with the factor $R_{\mathrm{C/D}}$ against the deuteron results. One can see that the ratio successfully describes the carbon cross sections relative to the deuteron. The large errors seem to be associated with poor statistics, which may be evident from the invariant-mass distribution in Fig.4.22.

This figure also appears to illustrate that the ρ^0 is transversely polarized above the coherent threshold, $E_{\gamma\mathrm{th}} = 797$ MeV, but is longitudinal below the threshold. Fig.4.24 shows the $\cos\theta_{cH}$ distribution for the invariant mass region $m_{\pi\pi} \geq 700\mathrm{MeV/c}^2$ in the highest photon energy bin. One can see at first from the values of P_j that the invariant mass cut enhances the proportion of the ρ^0 data. Because the Drell-type simulation does not include any polarizations, the similarity between the Drell simulation and the Tρ^0 is simply due to the effect of the TAGX acceptance. Nonetheless, the data distribution appears to support the transverse polarization over that of the longitudinal.

4.3.2 Quasifree Region

In order to compare the quasifree cross sections on carbon with the elementary cross sections, particularly with the $p(\gamma, \pi^+\pi^- p)$ results by the ABBHHM collaboration [33] and the $d(\gamma, \pi^+\pi^- p)n$ results by Carbonara *et al.* [39], the present carbon results somehow have to be converted to the average nucleon cross sections. Here, inspired by Ref.[67] which investigated the (π, K) reaction, an effective number of nucleons is devised. It takes the absorption of the outgoing two pions into account. The pion absorption has been written by eq.(3.12) with the exponent given by eq.(3.16). The effective number of nucleons is then given by

$$A_{\text{eff}} = \int \rho(\vec{r}) e^{-\chi(k_1, \vec{r})} e^{-\chi(k_2, \vec{r})} d^3 r, \tag{4.8}$$

where the pion momenta, k_1 and k_2, are distributed in accordance with a particular quasifree reaction. The computation of eq.(4.8) is made with the Monte Carlo method. The obtained values are listed in Tab.4.3. The effective number of protons, Z_{eff} (neutrons, N_{eff}) may be found by halving the values listed.

$\Delta\pi$ Cross Section

Fig.4.25 shows the quasifree cross sections per nucleon for the $\Delta\pi$ productions as well as the 3BPS background and the total quasifree reactions determined by this experiment. Comparisons are made with the present deuteron results, the $d(\gamma, \pi^+\pi^- p)n$ measurement by Carbonara *et al.* [39], and the $p(\gamma, \pi^+\pi^- p)$ results by the ABBHHM collaboration [33]. One can see that this result is generally in agreement with other data when the effect of absorption is considered. It seems that the effective number of target nucleons works well for this purpose. It should be pointed out, however, that the deuteron data ($\star$) include the non-quasifree processes. Since the carbon simulations explicitly include the effect of FSI, this seems to be a relevant comparison as also explained in the deuteron section.

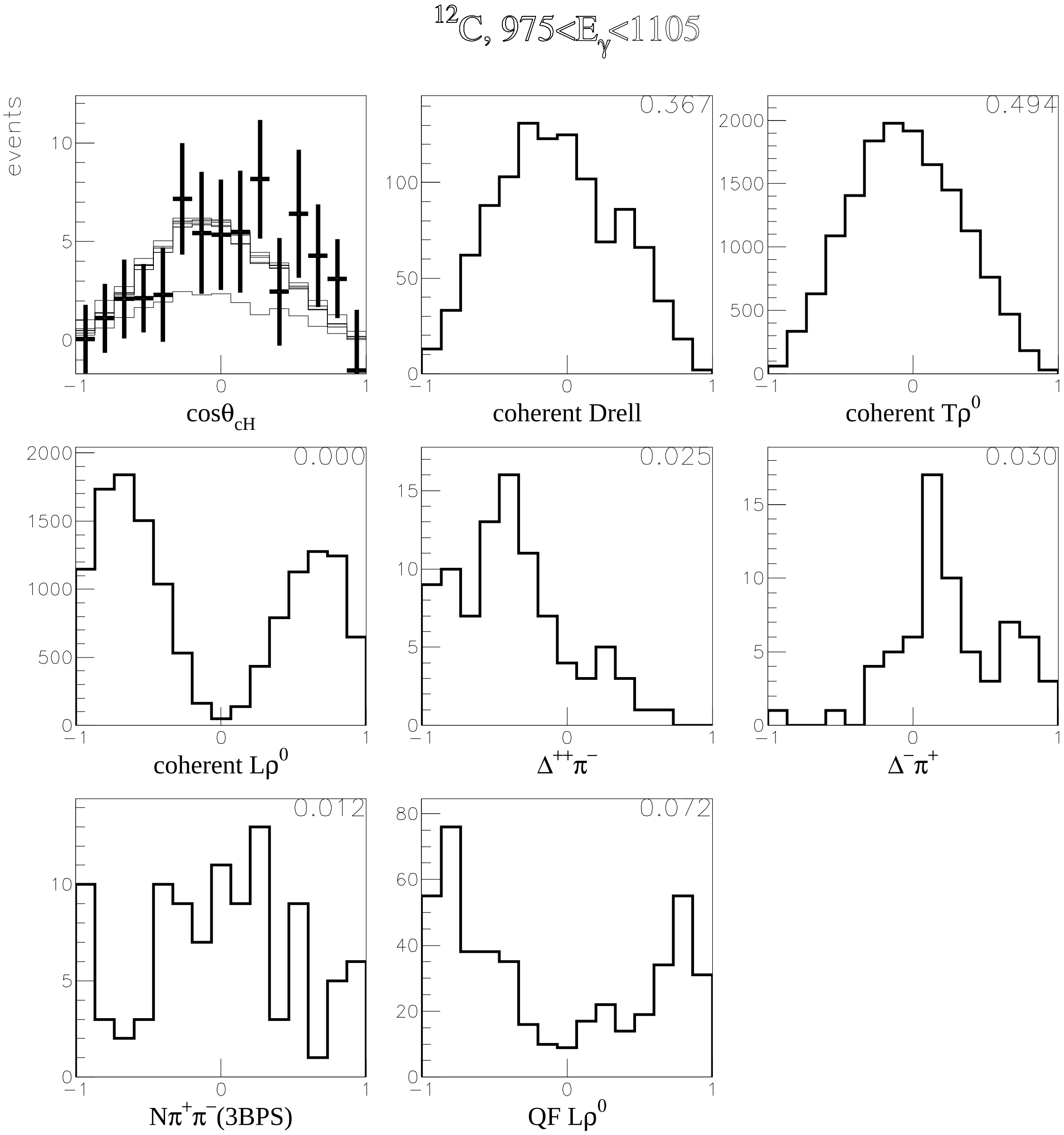

Figure 4.24: Carbon $\cos\theta_{cH}$ distribution in the coherent region. The missing-mass cut $m_X \leq 11178$ MeV/c^2 and the dipion invariant mass cut, $m_{\pi\pi} \geq 700$ MeV/c^2 are applied. To interpret this figure, please refer to Fig.4.20.

Table 4.3: The effective number of nucleons in carbon for each of the quasifree reactions as given by eq.(4.8). "QF AVR" gives the cross-section weighted average. "T" and "L" in front of ρ^0 signifies transverse and longitudinal, respectively.

E_γ = 550– 810 MeV	
process	A_{eff}
$\Delta^{++}\pi^-$	4.10
$\Delta^-\pi^+$	4.13
$(N\pi^+\pi^-)_{\text{3BPS}}$	4.36
$T\rho^0$	4.69
$L\rho^0$	5.08
Drell	6.39
$\rho^0(655)$	4.75
QF3π	5.13
QF AVR.	4.59

E_γ = 810– 890 MeV	
process	A_{eff}
$\Delta^{++}\pi^-$	4.15
$\Delta^-\pi^+$	4.12
$(N\pi^+\pi^-)_{\text{3BPS}}$	4.33
$T\rho^0$	4.57
$L\rho^0$	5.02
Drell	6.41
$\rho^0(655)$	4.74
QF3π	5.10
QF AVR.	4.44

E_γ = 890– 975 MeV	
process	A_{eff}
$\Delta^{++}\pi^-$	4.14
$\Delta^-\pi^+$	4.08
$(N\pi^+\pi^-)_{\text{3BPS}}$	4.42
$T\rho^0$	4.66
$L\rho^0$	5.14
Drell	6.42
$\rho^0(655)$	4.71
QF3π	5.14
QF AVR.	4.33

E_γ = 975–1105 MeV	
process	A_{eff}
$\Delta^{++}\pi^-$	4.15
$\Delta^-\pi^+$	4.16
$(N\pi^+\pi^-)_{\text{3BPS}}$	4.34
$T\rho^0$	4.63
$L\rho^0$	5.10
Drell	6.44
$\rho^0(655)$	4.71
QF3π	5.06
QF AVR.	4.62

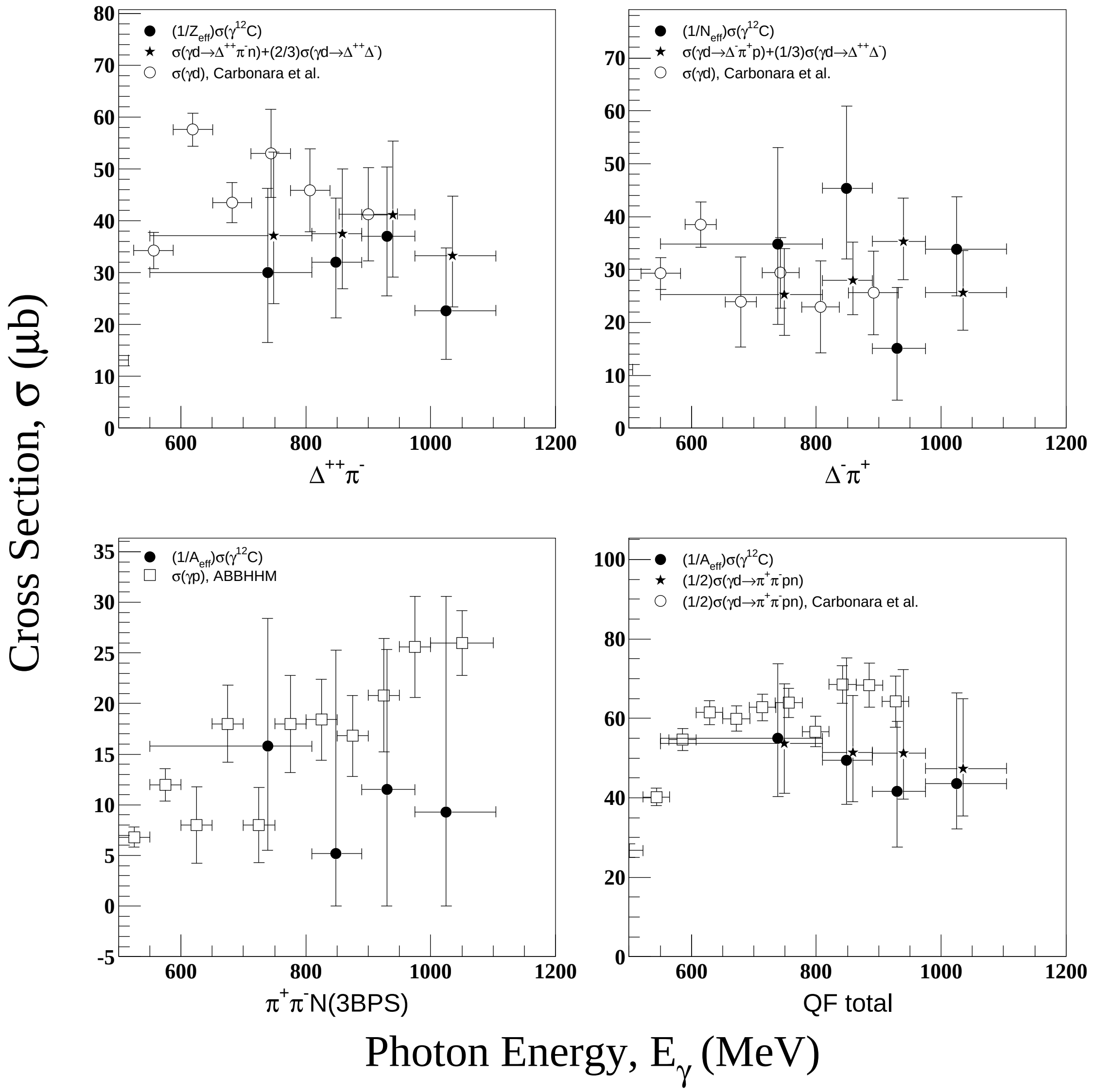

Figure 4.25: The quasifree cross sections per nucleon on carbon determined by this experiment (closed circles). The filled stars are our deuteron results: their central values are shifted by 10 MeV toward higher photon energy for clarity. The open circles are also from the deuteron results by Carbonara *et al* [39]. The open squares are from proton results by the ABBHHM collaboration [33]. For details of the effective number of nucleons (A_{eff}), protons (Z_{eff}), and neutrons (N_{eff}), please see the text.

The result is also checked with the data which include a proton track. Fig.4.26 presents the π^+p-invariant mass distribution in the quasifree region. The data and the simulation are roughly consistent each other.

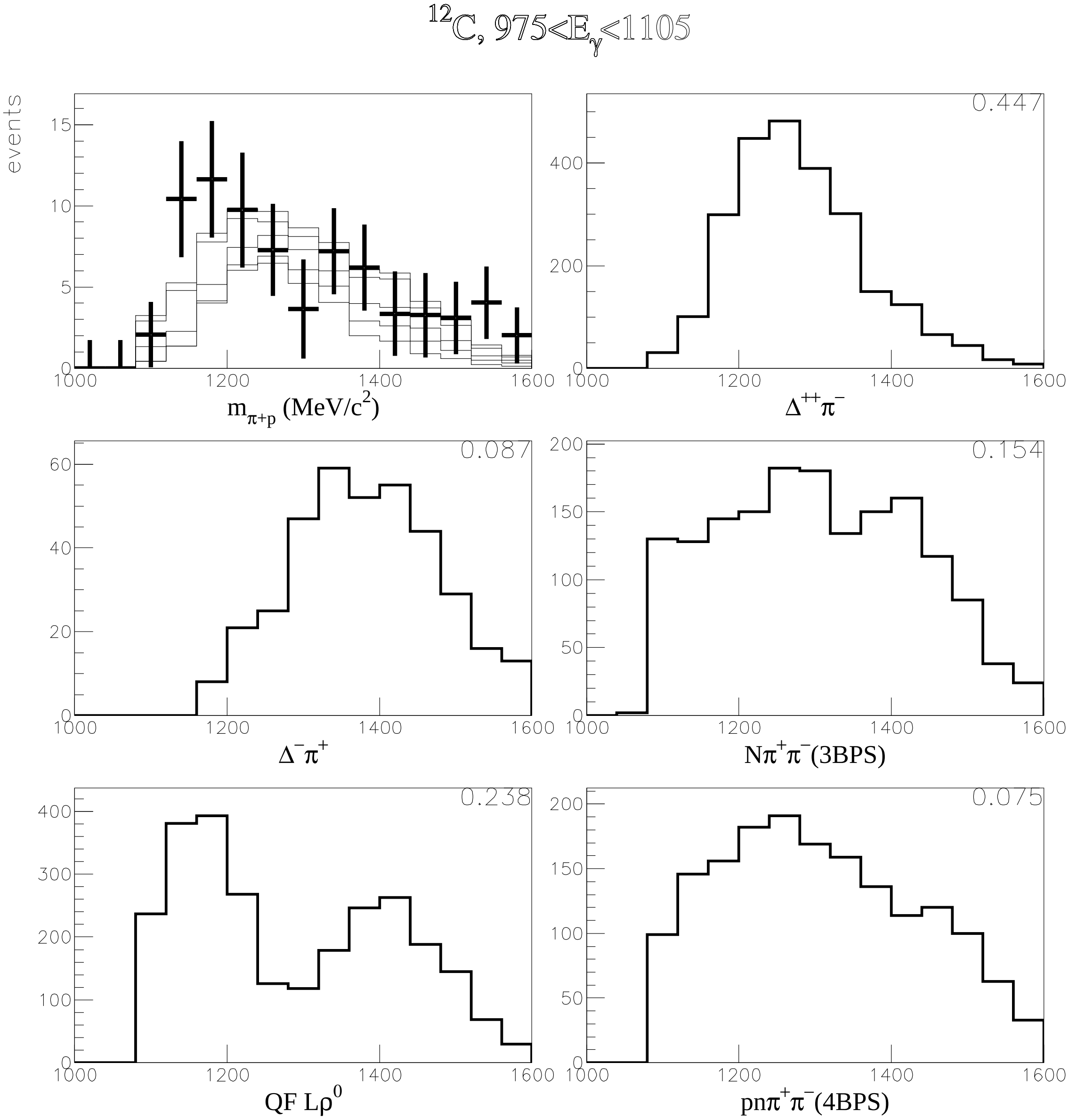

Figure 4.26: The π^+p invariant mass distribution in the quasifree region. For how to read this figure, please refer to Fig.4.20.

ρ^0 Cross Section

Fig.4.27 displays the quasifree cross sections for the ρ^0 production and the Drell-type background. They are all divided by the effective number of nucleons, A_{eff}, given in

Tab.4.3 to make a comparison with the $\gamma p \rightarrow \rho^0 p$ data by the ABBHHM collaboration [33]. The figure shows a distinct increase in strength of the Lρ^0 as the energy increases,

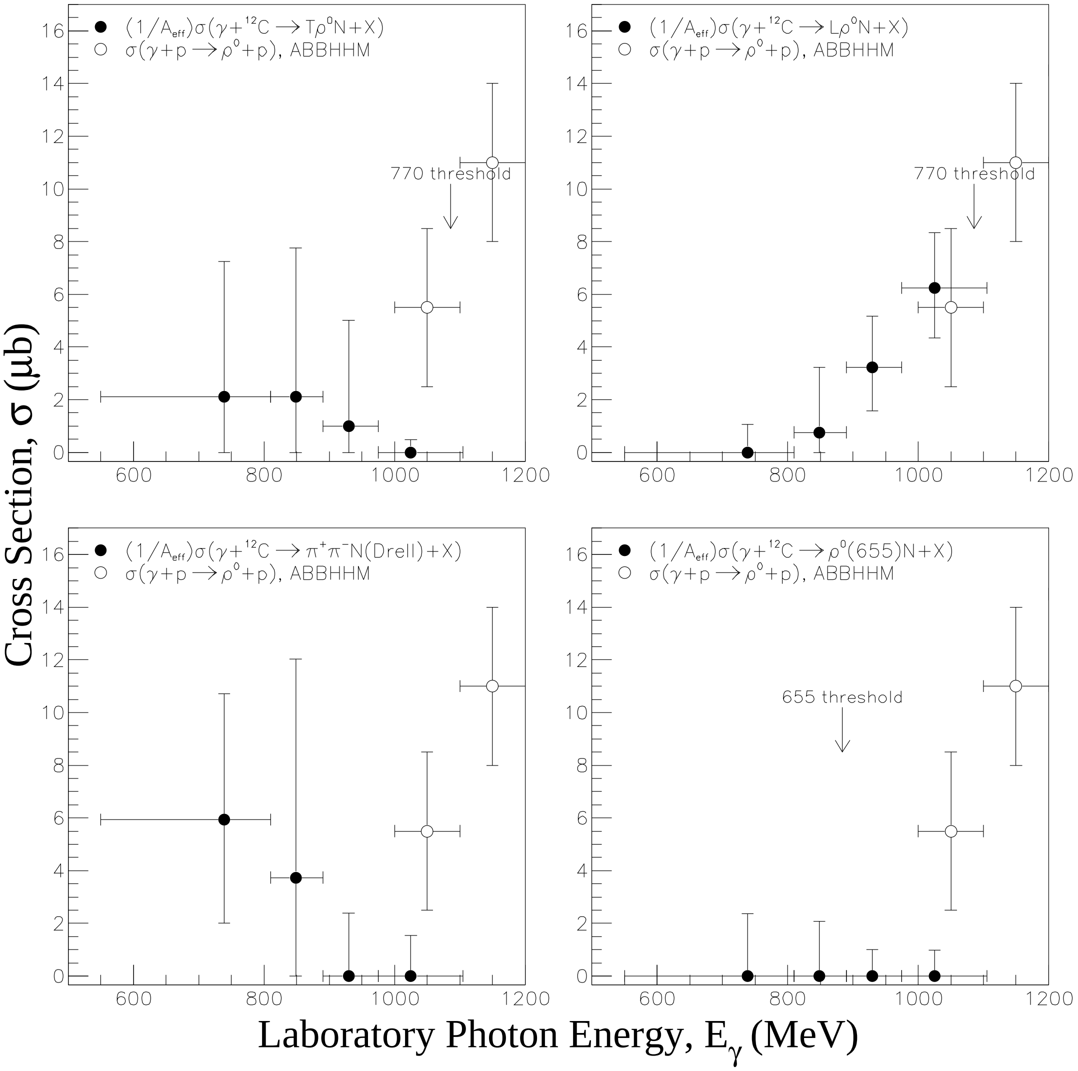

Figure 4.27: The carbon quasifree cross sections for the ρ^0 production and the Drell-type background. The closed circles are the present results, divided by A_{eff} given in Tab.4.3. All open circles are for the $\gamma p \rightarrow \rho^0 p$ reaction from the ABBHHM Collaboration [33].

which is consistent with the present deuteron results. The negligible strength in the $\rho^0(655)$ is also consistent. On the other hand, the Drell-type background and the Tρ^0 receive some strength well below the nominal threshold ($E_{\gamma\text{th}} = 1086$ MeV). This is not observed in the deuteron case. This contrast can suggest the true nuclear effect.

The Monte Carlo simulation reproduces all one-dimensional distributions very well.

Fig.4.28 shows the laboratory dipion opening angle in the lowest photon energy bin. Although it is certainly due to combinatory reasons that the Drell-type background has gained significant strength, it can be interpreted from this distribution that only the QF-Drell process can provide a reasonable population near $\cos\theta_{\pi\pi} = 0.5$ to fill in the data there. In Fig.4.29, the $\cos\theta'_{qH}$ distributions for the same photon energy bin are shown. In this figure, the QF-Tρ^0 provides a unique distribution among the quasifree simulations, because it populates near $\cos\theta'_{qH} = 0$. It is possible that the QF-Tρ^0 was brought forward because of this uniqueness. The data distribution may be flatter than the combined quasifree distributions without the QF-Tρ^0. According to the ρ-N resonance approach by W. Peters *et al.*, in which the ρ propagates through the N^*N^{-1} states in the nuclear medium similar to the pion in the Δ-hole model, the resonant ρ is "completely washed out" in the transverse channel while the longitudinal ρ retains its resonance character [11]. The present result actually supports such an idea because the combined effect of the QF-Drell and the QF-Tρ^0 could serve such a phenomenon. The definitive mass shift from 770 MeV/c^2 to 655 MeV/c^2, on the other hand, is not consistent with the data in this present analysis.

4.3.3 High Missing-Mass Region

Quasi-Deuteron Process

As is done for the quasifree processes, the effective number of quasi-deuterons, D_{eff} in the carbon nucleus has to be estimated. Perhaps, a simple model is that the main contribution to the cross section is from the absorption of created pions on the way out, just like how quasifree processes are treated. The number of quasi-deuterons the photon probes might be the number of proton-neutron pairs — six. Then one may use the same equation as eq.(4.8) but with a replacement,

$$\rho(\vec{r}) \to C\rho^2(\vec{r}), \quad C\int \rho^2(\vec{r})d^3r = D \quad (C = \text{const.}, \quad D = 6).$$

The computed D_{eff} values are listed in Tab.4.4. The cross sections per effective number of quasi-deuterons for $\Delta^{++}\Delta^-$ production and the 4BPS background are compared with the other deuteron experiments by Asai *et al.* [47] and Wada *et al.* [46] in Fig.4.30. As is seen, first of all, both the $\Delta^{++}\Delta^-$ process and the background are basically non-existent

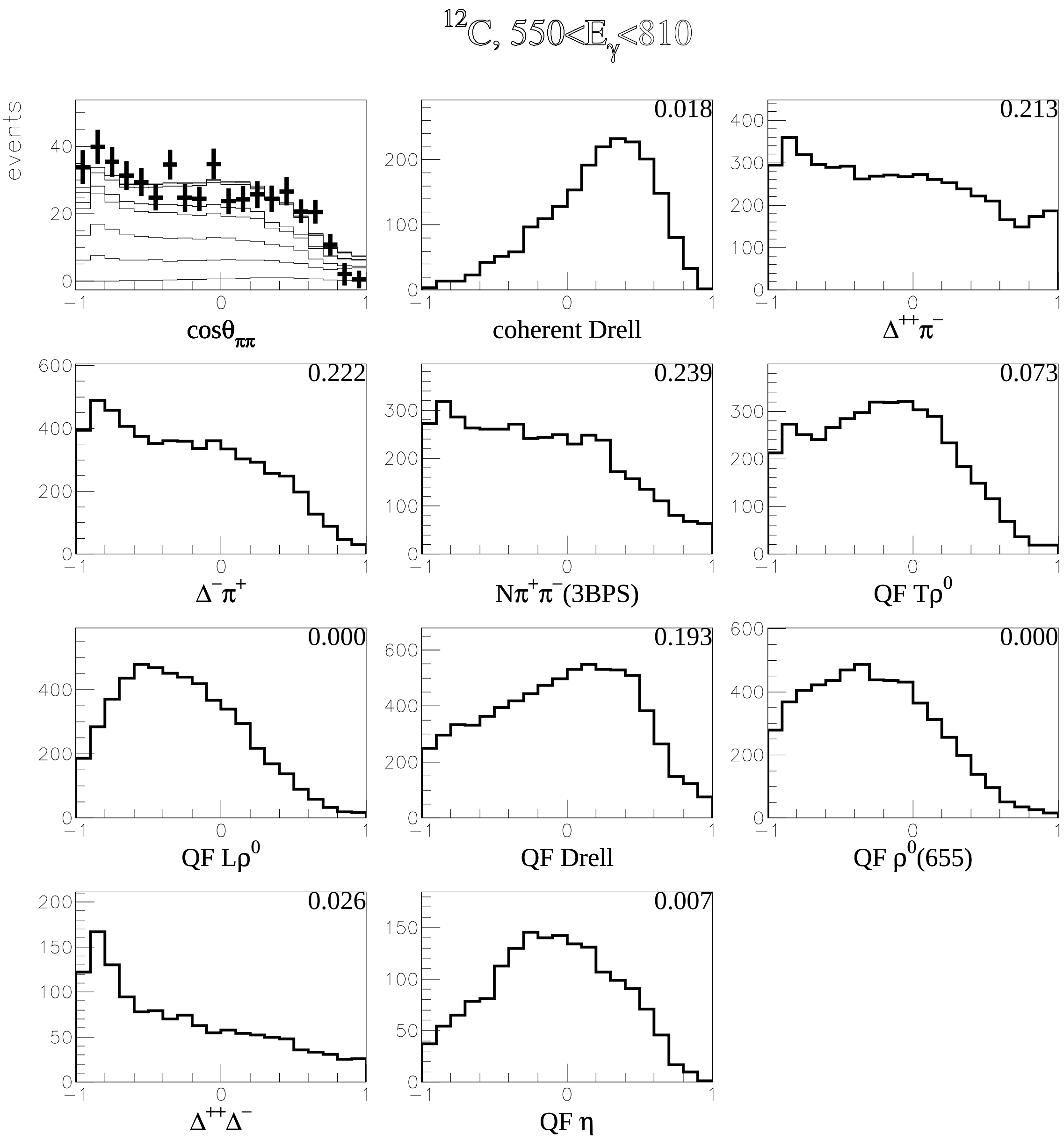

Figure 4.28: The $\cos\theta_{\pi\pi}$ (cosine of the laboratory opening angle) distribution in the quasifree region ($11178 \leq m_X \leq 11400$ MeV/c^2). To interpret this figure, please refer to Fig.4.20.

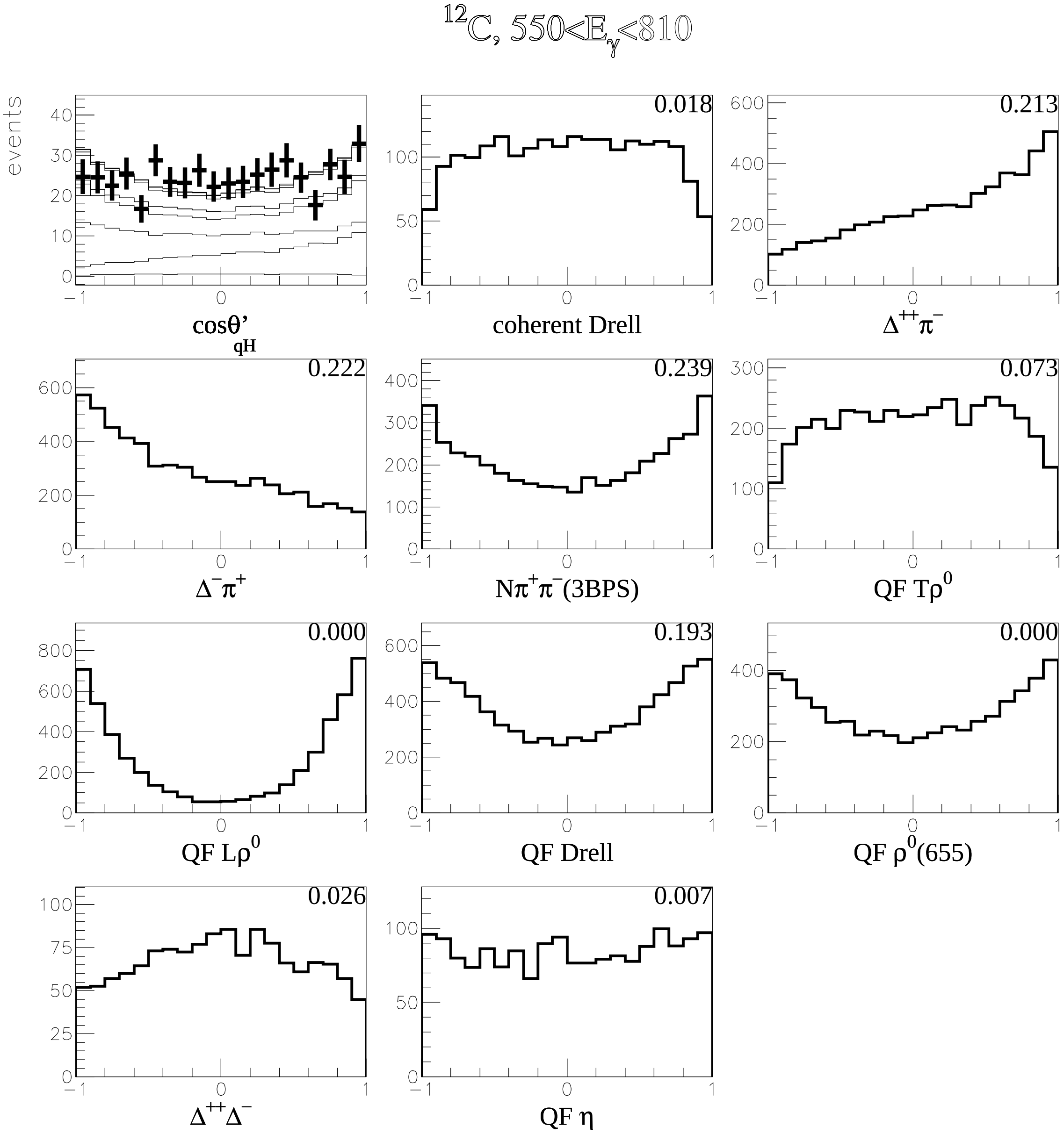

Figure 4.29: The $\cos\theta'_{qH}$ distribution in the quasifree missing-mass region. To interpret this figure, please refer to Fig.4.20.

Table 4.4: The effective number of quasi-deuterons in carbon, D_{eff}, for the quasi-deuteron processes.

E_γ [MeV]	$\Delta^{++}\Delta^-$	$(\pi^+\pi^-pn)_{4\text{BPS}}$
550– 810	1.64	1.91
810– 890	1.66	1.92
890– 975	1.65	1.93
975–1105	1.66	1.94

throughout the experiment photon energy range. In addition, the $\Delta^{++}\Delta^-$ production cross section is far from the expectation.

The fitting result is also compared to spectra with proton information for a possible misidentification. Fig.4.31 shows the missing momentum distribution when a proton is detected. Here the missing momentum is defined as

$$P_X \equiv \left|\vec{k} - \vec{p}_p - \vec{k}_1 - \vec{k}_2\right|_{\text{lab.}} .$$

The data and the simulation exhibit good agreement. Data from the proton events are generally well reproduced by the simulation and thus render a good support to the small quasi-deuteron process contribution.

In fact, this result should have been anticipated when the apparent agreement between the carbon and deuteron results on the $\Delta\pi$ cross sections were presented in Fig.4.25. There, an agreement is observed when the $\Delta^{++}\Delta^-$ is added to the deuteron data. Because the quasifree carbon simulations include the FSI, it implies that the $\gamma\text{C} \to \Delta^{++}\Delta^- X$ reaction is dominated by the mechanisms in which one of the exit pions created by the quasifree $\Delta\pi$ reaction forms another Δ with the other nucleon. Mechanisms which are difficult to be simulated by FSI would be the ones in which the photon interacts with the exchanged pion between the correlated nucleons. The process is usually called the meson exchange current (MEC) mechanisms [68]. Fig.4.32 illustrates these diagrams. These mechanisms are expected to be a small contribution based on Ref.[68], which states that it is about 10% on the deuteron. When one assumes that the $\Delta^{++}\Delta^-$ simulation for carbon is suitable only for the MEC mechanisms, our $\Delta^{++}\Delta^-$ cross section becomes understandable. It could be stated that the quasi-deuteron simulations are for the strongly or “purely” correlating nucleon pairs only. The

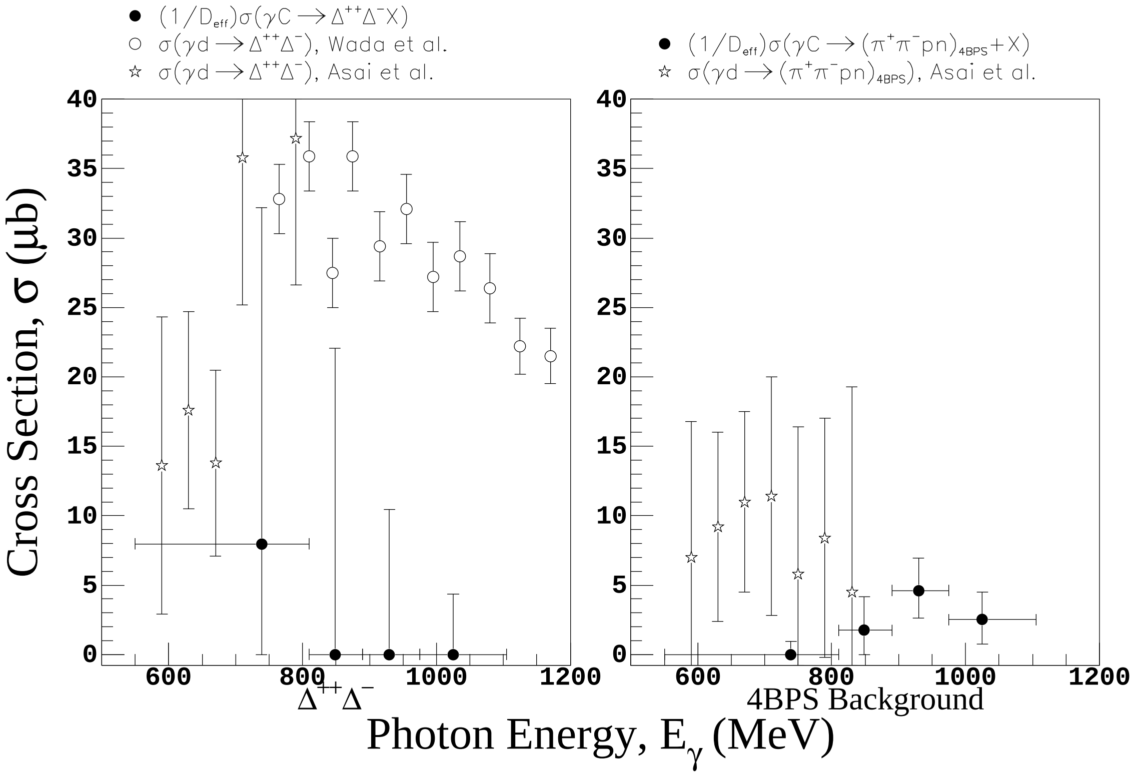

Figure 4.30: The quasi-deuteron cross sections per $D_{\rm eff}$ obtained by this experiment (closed circles). Open stars are from Asai *et al* [47]. Open circles are from Wada *et al* [46].

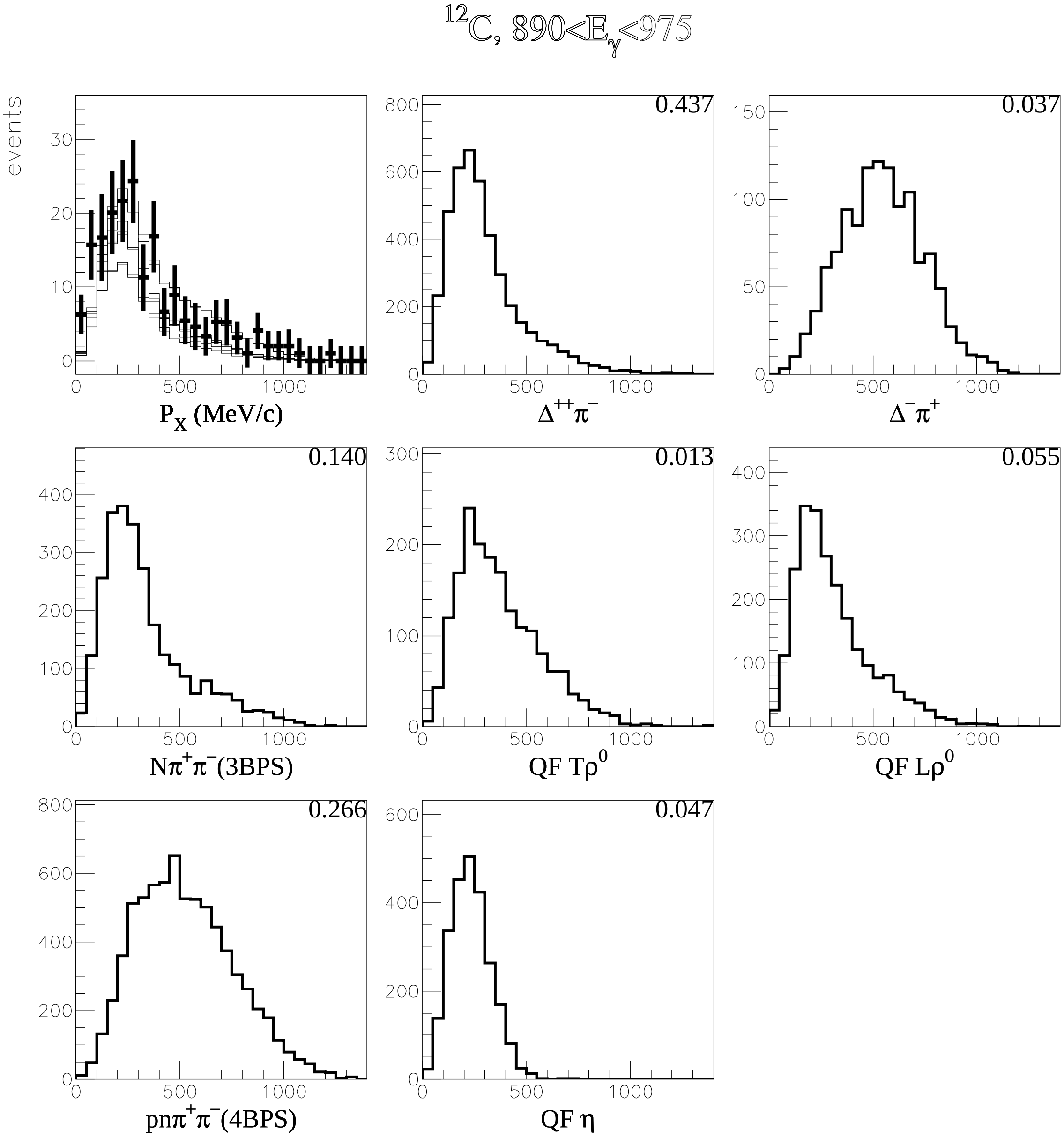

Figure 4.31: The laboratory missing momentum distribution when proton is detected. No missing-mass cut is applied. For how to read this figure, please refer to Fig.4.20.

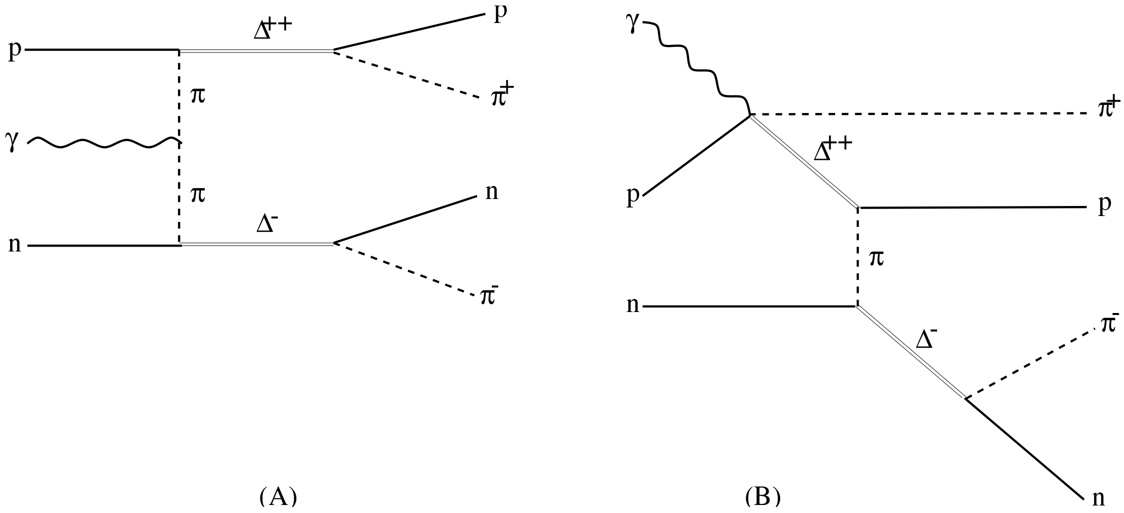

Figure 4.32: Diagrams for the double delta excitation. (A) Meson exchange current mechanism. (B) One of the dominant the double delta excitation process in which the second delta excitation is a rescattering process (FSI).

number of quasi-deuterons, D presented above then does not become a simple number of proton-neutron pairs.

Triple Pion Production

The total cross sections for quasifree η and triple-pion production are plotted in Fig.4.33. Here, a comparison is made with the inclusive η photo-production cross section off the carbon nucleus near threshold measured by Röbig-Landau *et al.* at MAMI [69]. Also, the upper limits of triple-pion production on the proton target from Ref.[33] are compared with our 4BPS cross sections, divided by the effective number of nucleons tabulated in Tab.4.3. The comparison appears to be in agreement, but the errors are very large. One of the best ways to check the strength of the triple-pion production process is to examine the missing mass distribution already presented in Fig.4.20. Good agreement at the high missing-mass region may be seen.

4.3.4 $\pi^+\pi^-X$ Cross Section

Inclusive double-pion photo-production cross sections are compared with the deuteron data as well as with the proton data obtained by the ABBHHM collaboration [33]. The result is shown in Fig.4.34. There, the carbon data are divided by the average effective

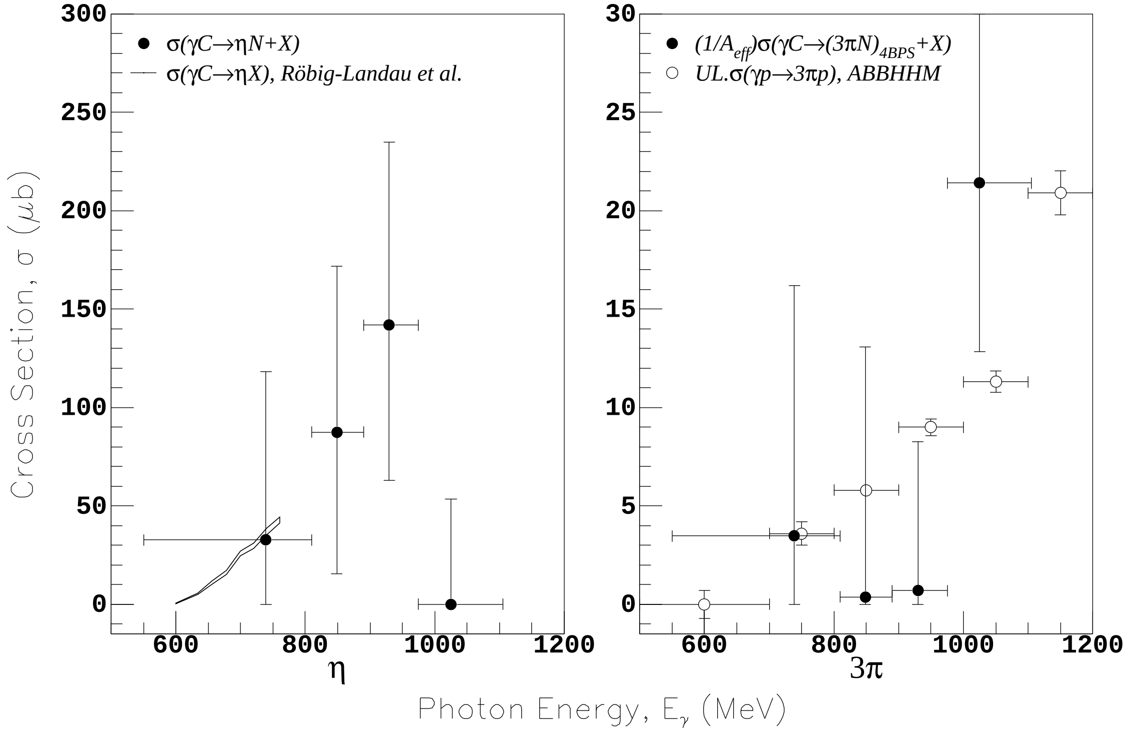

Figure 4.33: The η and triple-pion photo-production cross sections. The close circles are the quasifree carbon results by this experiment. The values are divided by 27.9% which is the $\eta \to \pi^+\pi^- X$ branching ratio. The double line is a rough drawing of the inclusive η measured by M. Röbig-Landau *et al* [69]. The open circles are from the $p(\gamma, \pi^+\pi^- p)$ experiment measured by the ABBHHM collaboration [33]. "UL" stands for upper limits (see Fig.4.16 for more detailed description for the $p(\gamma, \pi^+\pi^- p)$ result).

number of nucleons for the quasifree process presented in Tab.4.3. Because quasifree production contributes 70–90% of the cross section, this factor should be good enough for the present purpose. The deuteron cross sections are halved. All the data are within agreement, but all of our data have very large errors (~20%). The relative increase photon energy with respect to the proton cross sections is because the proton data are exclusive.

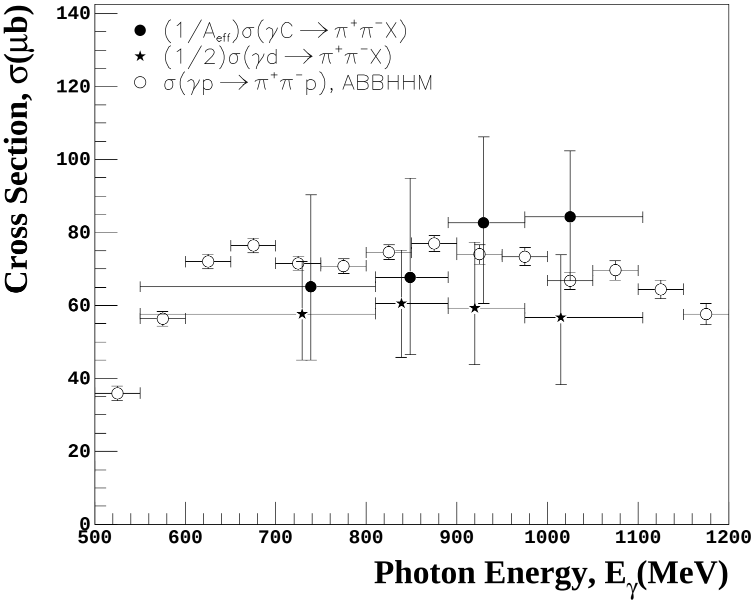

Figure 4.34: Inclusive double-pion photo-production cross section on carbon obtained by this experiment (closed circles) in comparison with the deuteron results (closed stars). The carbon cross sections are divided by the effective number of nucleons, A_{eff} (values for "AVR QF" in Tab.4.3). Deuteron cross sections are divided by two. The open circles are for the total double-pion photo production on proton from the ABBHHM collaboration [33].

Chapter 5

Summaries

5.1 Experiment and Data Calibration

Motivated by the theoretical interest in vector meson mass modifications in the presence of hadronic matter, as discussed in detail in Chapter 1, G. M. Huber and Z. Papandreou *et al.* proposed a simultaneous measurement of the $(\gamma, \pi^+\pi^-)$ reaction on carbon and deuteron. It was approved by the INS-ES PAC as ES144. In 1996, the TAGX collaboration conducted the ES144 experiment, two years after a similar experiment with ^{3}He target. During the experiment, the trigger rate and the efficiency of the on-line data acquisition were carefully monitored. Also, the tagging efficiency and off/on ratio were frequently measured between one run and another so that the photon flux is accurately determined. There were three stages of the experiment, each of which had a different ES energy in order to scan a wide range of the photon energy. As a result, a total of 36M events were collected within the tagged photon energy range of 550–1100 MeV.

Off-line calibration was necessary in order to accurately obtain the observed values of the charged particles. There were three major parts in the calibration. The first two parts were to find parameters for the Cylindrical Drift Chamber (CDC) and the Straw Drift Chamber. The parameters were for the offset of the TDC value (T_0) and for a relation called XT. It related the TDC value with the distance between the trajectory of a charged particle and the sense wire. The author mainly worked on a software development of the SDC calibration, taking over G. Garino's early work, which included a newly installed chamber and required a different technique than for the CDC. Once the chamber parameters were determined, the planar trajectories were reconstructed. Thus, the particle momenta were found by the curvature in the TAGX magnetic field. The third part of the calibration was to determine the T_0 values for the Inner Hodoscopes (IH) and the Outer Hodoscopes (OH). The OH were equipped with two PMT's and the TDC signal difference gives the vertical position of a charged particle. The time difference between the IH and OH provided the time of flight of the particle. After determining the parameters, the collected data were added with calibrated information. At the same time, events were rejected by a crude cut based on the vertex position and other elementary information. About 5% of the collected events survived and the data were condensed.

With the remaining events, further analyses were conducted to evaluate the integrated performance of the TAGX detector. It was found that the installation of the SDC resulted in the improvement of the planar momentum resolution by approximately 35%. From the EM background events, the time-of-flight resolution was evaluated to be less than 380 ps, which was found to be consistent with other respected references. The other important evaluations described here were the detection efficiencies for the SDC, the CDC, and newly installed aerogel and CO_2 gas Čerenkov counters. A very dramatic improvement was found at the vertex position resolution because the SDC was placed very close to the target center.

From the time-of-flight and the momentum information, the detected particles were identified to be either $\pi^\pm$, $e^\pm$, p, or other. Because only the hadronic events of the $(\gamma, \pi^+\pi^-)$ reaction were desired, the events with e^+ or e^- are considered to be EM background and rejected based on this particle identification. However, since the time-of-flight resolution was quite limited, some $e^\pm$ contamination in the $\pi^\pm$ region was unavoidable. Information on the vertex position, the planar opening angle, and the TDC values of the Čerenkov counters were also made use of to discard the EM background. The remaining data were separated into the graphite and CD_2 events and accidental background events. The graphite and CD_2 data were subtracted by the background to purify the foreground. The purified CD_2 data were subtracted by the carbon data to extract the deuteron data. Finally, the deuteron and carbon data were separated into four photon energy bins so that the energy dependence of the reaction could be investigated.

5.2 Simulation and Data Analysis

In order to interpret the data, the author developed a Monte Carlo simulation code following the initial work by G. M. Huber and K. Benslama. The simulation took into consideration all the TAGX detector performances which were evaluated in the off-line analysis. The same data analysis was exactly applied to the Monte Carlo so that the systematic error would be minimized. Each reaction process was simulated independently. There were about 15 processes simulated for each target. Specifically, they were

1. coherent processes (ρ^0, Drell)
2. quasifree processes $(\Delta\pi, (\pi^+\pi^-N)_{3\mathrm{BPS}}, \rho^0, \rho^0(655), \mathrm{Drell}, \eta, (3\pi N)_{4\mathrm{BPS}})$
3. $\Delta\Delta$ and $(\pi^+\pi^-pn)_{4\mathrm{BPS}}$.

In addition, the $\gamma d \to (\pi^+\pi^-d)_{3\mathrm{BPS}}$ simulation was added to compensate for the explicit t dependence, $d\sigma/dt \propto e^{At}$, embedded in the deuteron coherent simulations. Since our photon energies were in the N^* resonance region, the quasifree sector was realized roughly based on the N^* decay channels. The quasifree processes and the coherent ρ^0 productions were modeled after results from the γp and γA experiments performed at DESY, Frascati, SLAC, CEA, and Cornell in the 1960s and 1970s. Particular attention was paid to the ρ^0 polarization, and each ρ^0 process was separated into transverse and longitudinal channels. Primarily, the Drell-type background was to rectify the shape of the ρ^0, which is not well known, but it was possible to accommodate the in-medium modified ρ^0. Simulations for the double delta excitation and the $\rho^0(655)$ followed reports from the γd and γ^3He experiments at the TAGX. The MAMI experiments for the η photo production at Mainz supplies useful information to the η simulations. The carbon simulations contained the final state interactions (FSI) by imitating the distorted wave impulse approximation (DWIA). On the other hand, the deuteron simulations assumed the plane wave impulse approximation (PWIA) thus ignored the FSI because the four body reactions are explicitly considered. When each simulation is completed, the TAGX acceptance was obtained.

The data were fitted with a combination of the simulations in terms of the five-fold differential yield. The fitting determined a percentage in the data for each simulation.

Together with the acceptance, the cross section was determined. A technically unavoidable deficiency of the method is that the combination of the simulations was done as an incoherent sum. This renders the present analysis unsuitable for studying the effect of interference between the channels. To minimize this limitation, the intention was that the simulation follows the empirical differential cross sections whenever available. The data were separated into three missing-mass regions so that the fitting result could be easily scrutinized. Occasionally, events which detect a proton were also found useful as an added constraint and verification of assumptions made.

In the deuteron analysis, due to the present PWIA approach, a deviation from the data became visible in the missing-mass spectrum. However, the cross sections for the coherent and the double delta excitation were found to be in agreement with past experiments. The $\Delta\pi$ and total quasifree cross sections were found to be much smaller than those from a Frascati experiment which is the only resource available. It is pointed out that this is because the older experiment did not take the $\Delta\Delta$ into account. The $\Delta\pi$ plus $\Delta\Delta$ cross sections were in agreement with the Frascati data. In an analogy to the $\Delta\pi$ channel, smaller cross sections were found for the 3BPS background. This time, the $(\pi^+\pi^-pn)_{4\mathrm{BPS}}$ was added and a rough agreement with the ABBHHM data was found. The total quasifree cross sections were then within agreement with the Frascati data when both $\Delta\Delta$ and $(\pi^+\pi^-pn)_{4\mathrm{BPS}}$ were added. Both quasifree and coherent ρ^0 production seem to be dominated by the helicity flipping process below the threshold. The mass reduced ρ^0 does not appear to be present because both cross sections for the $\rho^0(655)$ and Drell-type background gave consistently zero contributions.

Since there is almost no literature information on carbon, the carbon cross sections were mostly compared with proton or deuteron results. The transverse polarization of the coherent ρ^0 above the threshold was observed. Within the error, its cross sections agreed with those for the deuteron by the ABHHM collaboration which were converted by a factor based on the optical model. An effective number of nucleons which took the absorption of the exiting pions into account was employed so that the quasifree carbon cross sections might be compared with those from proton and deuteron experiments. Satisfactory agreement was found. The behavior of the longitudinally polarized ρ^0 below the threshold was found to be similar to the deuteron case. However, the helicity-conserving ρ^0 seems to be stronger than helicity-flipping in the quasifree process when the photon energy is much lower than the nominal threshold. A strong presence of the Drell process was also found. This is unlike the deuteron result. It was argued that this is actually the indication of the medium modification based on the ρ-N resonance model by W. Peters *et al.* Another interesting finding is that the cross sections for the double delta excitation were found to be negligible. This is explained by the fact that the FSI is included to the simulation. The suitable process to the present quasi-deuteron simulations are for the meson exchange current (MEC) mechanism. It is expected to be a small effect.

Bibliography

[1] Particle Data Group, *Particle Physics Booklet*, Lawrence Barkeley National Laboratory, Berkeley, CA (2000).

[2] F. Halzen and A. D. Martin, *Quarks & Leptons: An Introductory Course in Modern Physics*, John Wiley & Sons, New York, (1984) p.170.

[3] F. Halzen and A. D. Martin, *Quarks & Leptons: An Introductory Course in Modern Physics*, John Wiley & Sons, New York, (1984) p.66.

[4] G. E. Brown and M. Rho, *Phys. Rev. Lett.* **66** (1991) 2720.

[5] T. Hatsuda and S. Lee, *Phys. Rev.* **C46** (1992) R34.

[6] G. Agakichiev *et al.* (CERES collaboraion), *Phys. Lett.* **B422** (1998) 405.

[7] G. E. Brown *et al.*, *Phys. Rev. Lett.* **60** (1988) 2723.

[8] K. Ozawa *et al.*, *Phys. Rev. Lett.* **86** (2001) 5019.

[9] M. A. Kagarlis *et al.* (TAGX collaboration), *Phys. Rev.* **C60** (1999) 025203;
G. J. Lolos *et al.* (TAGX collaboration), *Phys. Rev. Lett.* **80** (1998) 241;
G. M. Huber, G. J. Lolos and Z. Papandreou, *Phys. Rev. Lett.* **80** (1998) 5285;
G. J. Lolos *et al.* (TAGX collaboration), *Phys. Lett.* **B528**, (2002) 65.

[10] K. Maruyama *et al.*, *Hadron and Nuclear Physics with Electromagnetic Probes*, ed. by K. Maruyama and H. Okuno, Amsterdam, Elsevier, 2000.

[11] W. Peters *et al.*, *Nucl. Phys.* **A632** (1998) 109.

[12] R. Rapp and J. Wambach, *Adv. Nucl. Phys.* **25** (2000) 1.

[13] G. M. Huber and Z. Papandreou (TAGX collaboration), INS-ES PAC Proposal (1994) unpublished.

[14] K. Maruyama and S. Yamada, *Proceeding of the International Session of the 1992 Electron Synchrotron (ES) Symposium*, INS-J-179 (1992).

[15] Masayuki Muto, Journal of Science of the Hiroshima University, A51-2 (1987) 187.

[16] G. Garino *et al.*, *Nucl. Instr. and Meth.* **A388** (1997) 100.

[17] H. Yamashita *et al.*, *Nucl. Instr. and Meth.* **A379** (1996) 276.

[18] H. Wind, *Nucl. Instr. and Meth.* **115** (1974) 431.

[19] M. Iurescu, Master thesis, University of Regina, 1997.

[20] H. Asher Weinerman, Master thesis, University of Regina, 1996.

[21] Y. Murata, *TAGX-Note 93*, 1987. (not published.)

[22] Y. Murata, *TAGX Internal Circular*, 1987. (not published.)

[23] B. Jean-Marie, V. Lepeltier and D. L'Hote, *Nucl. Instr. and Meth.* **159** (1979) 213.

[24] W. Mendenhall, R. L. Scheaffer, D. D. Wackerly, *Mathematical Statistics with Applications*, Duxbury, Boston, Mass. (1981).

[25] K. Miyamoto, *TAGX Notes 96-001*, 1996. (not published.)

[26] M. Asai *et al.*, *Phys. Rev.* **C42** (1990) 837.

[27] Application Software Group Computing and Networks Division, *HBOOK Reference Manual Version 4.22*, CERN Geneva, (1993).

[28] K. Miyamoto, the TAGX group meeting report, (1995) (unpublished).

[29] K. Maruyama *et al.*, *Nucl. Instr. and Meth.* **A376** (1996) 335.

[30] R. Gluckstern, *Nucl. Instr. and Meth.* **24** (1963) 381.

[31] M. E. Peskin and D. V. Schroeder, *An Introduction to Quantum Field Theory*, Addison-Wesley Pub. (1995) p.106.

[32] S. Frullani and J. Mougey, *Advances in Nuclear Physics*, vol.14 ed. by J. W. Negele and Erich Vogt, Plenum Press (1985) 1995.

[33] Aarchen-Berlin-Bonn-Hamberg-Heidelberg-München Collaboration, *Phys. Rev.* **175** (1968) 1669;
Aarchen-Berlin-Bonn-Hamberg-Heidelberg-München Collaboration, *Phys. Rev.* **188** (1969) 2060.

[34] Cambridge Bubble Chamber Group, *Phys. Rev.* **163** (1967) 1510.

[35] G. Gialanella *et al.*, *Nuovo Cimento* **63A** (1969) 892.

[36] D. Lüke and P. Söding, *Springer Tracts in Modern Physics*, vol.59 ed. by G. Höhler, Springer-Verlag (1971) 39.

[37] A. Braghieri *et al.*, *Phys. Lett.* **B 363** (1995) 46.

[38] A. Piazza *et al.*, *Nuovo Cimento* **3** (1970) 403.

[39] F. Carbonara *et al.*, *Nuovo Cimento* **36A** (1976) 219.

[40] D. Lüke, M. Scheunert, and P. Stichel, *Nuovo Cimento* **58A** (1968) 234.

[41] K. Gottfried and J. D. Jackson, *Nuovo Cimento* **33** (1964) 309.

[42] N. Bianchi *et al.*, *Phys. Rev.* **C54** (1996) 1688.

[43] T. Ericson and W. Weise, *Pions and nuclei*, Oxford, Clarendon, (1988) p.152.

[44] J. A. Gómez Tejedor and E. Oset, Nucl. Phys. **A571** (1994) 667;
J. A. Gómez Tejedor and E. Oset, *Nucl. Phys.* **A600** (1996) 413;
J. A. Gómez Tejedor, M. J. Vicente-Vacas and E. Oset, *Nucl. Phys.* **A588** (1995) 819.

[45] J. D. Jackson, *Nuovo Cimento* **34** (1964) 1644.

[46] Y. Wada representing the SAPHIR collaboration, *Particles and Nuclei Internatinal Conference*, Williamsberg, Virginia, (1996) (unpublished).

[47] M. Asai *et al.*, *Z. Phys.* **A** (1993) 334.

[48] B. Krusche *et al.*, *Phys. Lett.* **B358** (1995) 40.

[49] P. Benz *et al.* (Archen-Bonn-Hamburg-Heidelberg-München Collaboration), *Nucl. Phys.* **B79** (1975) 10.

[50] P. E. Ulmer, *Monte Carlo for Electro-Nuclear Coincidence Experiments* (1997) (CEBAF Hall-A circular, not published).

[51] E. Oset and M. J. Vicente-Vacas, *Nucl. Phys.* **A454** (1986) 637.

[52] G. McClellan *et al.*, *Phys. Rev. Lett.* **22** (1969) 374;
G. McClellan *et al.*, *Phys. Rev. Lett.* **22** (1969) 377.

[53] H.-J. Behrend *et al.*, *Phys. Rev. Lett.* **24** (1970) 336.

[54] H. Alvensleben *et al.*, *Phys. Rev. Lett.* **23** (1969) 1058;
H. Alvensleben *et al.*, *Nucl. Phys.* **B18** (1970) 333.

[55] F. Bulos *et al.*, *Phys. Rev. Lett.* **22** (1969) 490.

[56] L. Foá, *Springer Tracts in Modern Physics*, vol.59 ed. by G. Höhler, Springer-Verlag (1971) 112.

[57] Cambridge Bubble Chamber Group, *Phys. Rev.* **146** (1966) 994.

[58] J. Ballam *et al.*, *Phys. Rev.* **D5** (1972) 545.

[59] M. Davier *et al.*, *Phys. Rev.* **D1** (1970) 790.

[60] G. Wolf, *Springer Tracts in Modern Physics*, vol.59 ed. by G. Höhler, Springer-Verlag (1971) 77.

[61] K. Schilling, P. Seyboth and G. Wolf, *Nucl. Phys.* **B15** (1970) 397.

[62] New Muon Collaboration, *Nucl. Phys.* **B429** (1994) 503.

[63] P. Söding, *Phys. Lett.* **19** (1966) 702.

[64] S. D. Drell, *Phys. Rev. Lett.* **5** (1960) 342.

[65] M. Effenberger, E. L. Bratkovskaya and U. Mosel, *Phys. Rev.* **C60** (1999) 044614.

[66] F. Klingl, N. Kaiser and W. Weise, *Nucl. Phys.* **A624** (1997) 527.

[67] C. B. Dover, *Phys. Rev.* **C22** (1980) 2073.

[68] J. A. Gómez Tejedor, E. Oset and H. Toki, *Phys. Lett.* **B346** (1995) 240.

[69] M. Röbig-Landau *et al.*, *Phys. Lett.* **B373** (1996) 45.

[70] H. Feshbach, *Theoretical Nuclear Physics*, New York, Wiley (1992) p.354.

[71] H. Feshbach, *Theoretical Nuclear Physics*, New York, Wiley (1992) pp.806–812.

[72] H. Feshbach, *Theoretical Nuclear Physics*, New York, Wiley (1992) pp.355–393.

Appendix A

Tagging Efficiency Spectrum

Typical spectra of the tagging counter scaler, off/on ratio, tagging efficiency and photon energy are shown in Fig.A.1.

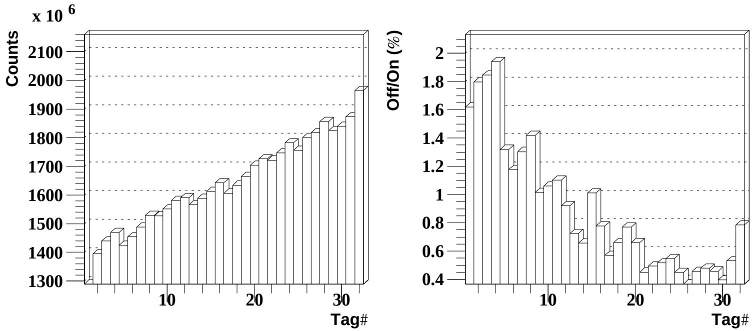

Tag Scaler *Off/On Ratio*

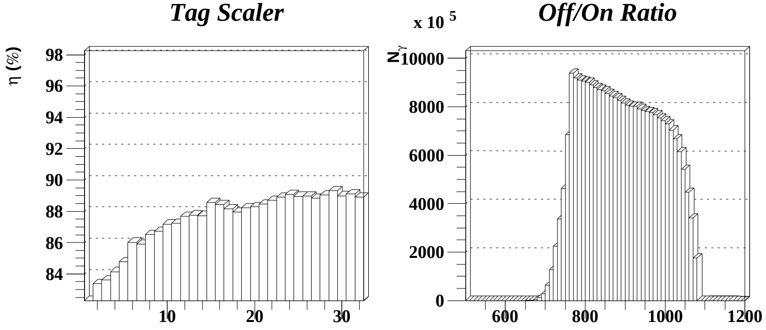

Tagging Efficiency *Number of Photons*

Figure A.1: The actual number of tagging scaler counts, off/on ratios, tagging efficiencies, and photon energy spectrum. Data are from a set of runs with $E_e(\text{top}) = 1180$ MeV.

Appendix B

Theorem of Probability Distribution Function

Theorem Let X and Y be independent random variables. Suppose X and $U = Y - X$ have known probability distribution functions, $f_X(x)$, and $f_U(u)$, respectively. Then the probability distribution function of Y is found to be

$$f_Y(y) = \int f_U(y-x) f_X(x) dx.$$

Proof If $X \in [x, x+\Delta x]$ and $U \in [u, u+\Delta]$, then $Y \in [x+u, x+u+\Delta x+\Delta u]$. Since X and U are independent, probability of having $Y \leq y$ is given by

$$\mathrm{P}(Y \leq y) = \lim_{\Delta x \to 0} \lim_{\Delta y \to 0} \sum_{x+u \leq y} \mathrm{P}(x \leq X \leq x+\Delta x) \mathrm{P}(u \leq U \leq u+\Delta u).$$

Because

$$\lim_{\Delta x \to 0} \mathrm{P}(x \leq X \leq x+\Delta x) = f_X(x)dx$$

and

$$\lim_{\Delta u \to 0} \mathrm{P}(u \leq U \leq u+\Delta u) = f_U(u)du,$$

the following expression is found.

$$\mathrm{P}(Y \leq y) = \iint\limits_{x+u \leq y} f_X(x) f_U(u) dx du.$$

The region of integration is shown in Fig.B.1. The integration is done by

$$\mathrm{P}(Y \leq y) = \int_{-\infty}^{+\infty} f_X(x) \int_{-\infty}^{y-x} f_U(u) du dx. \tag{B.1}$$

Because

$$\mathrm{P}(Y \leq y) = \int_{-\infty}^{y} f_Y(y) dy,$$

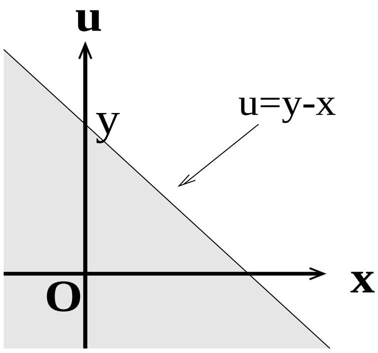

Figure B.1: The shaded area is the region of integration.

differentiating eq.(B.1) with respect to y, $f_Y(y)$ is now given by

$$f_Y(y) = \int_{-\infty}^{+\infty} f_X(x) f_U(y-x) dx.$$

Appendix C

Examples of the Data Distributions

Here are some observed spectra from the experiment. For details about the background and CD_2 data, please see sections 2.3.4 and 2.3.5.

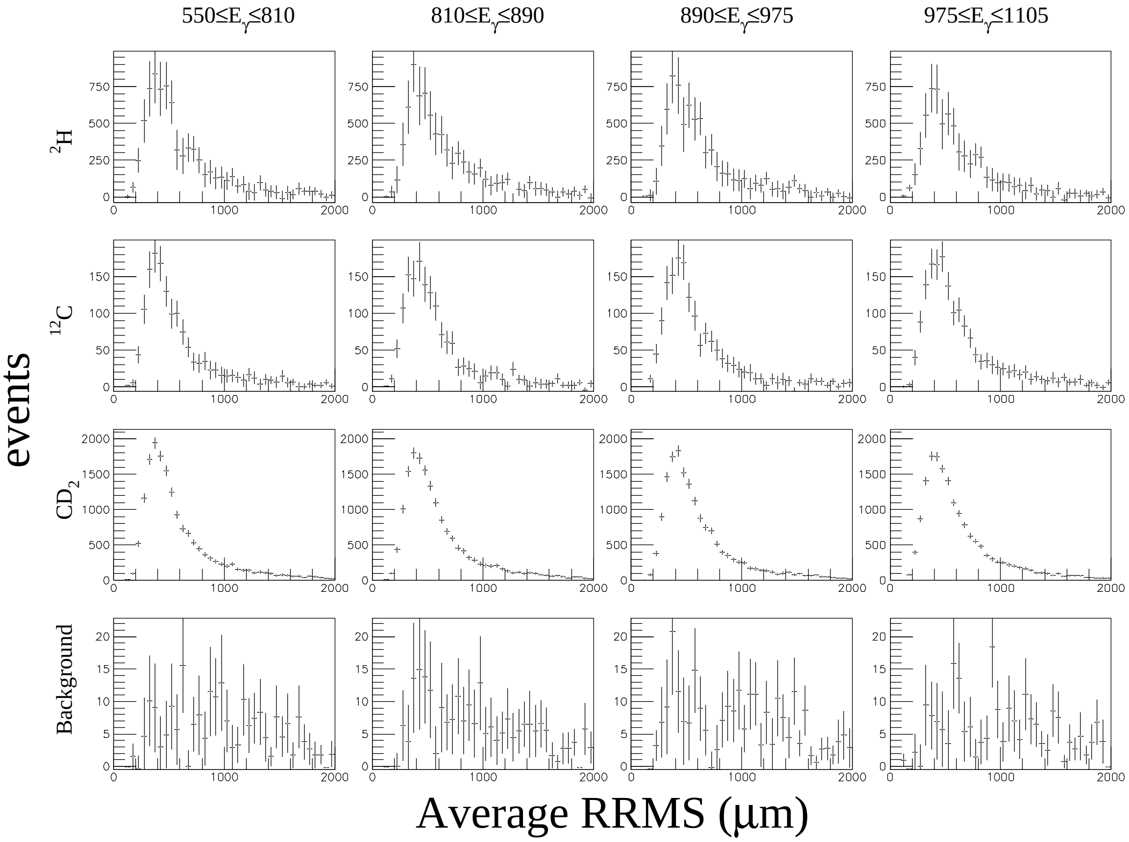

Figure C.1: Average residual RMS distributions. The average value is given by $(\text{RRMS}(\pi^+)+\text{RRMS}(\pi^-))/2$.

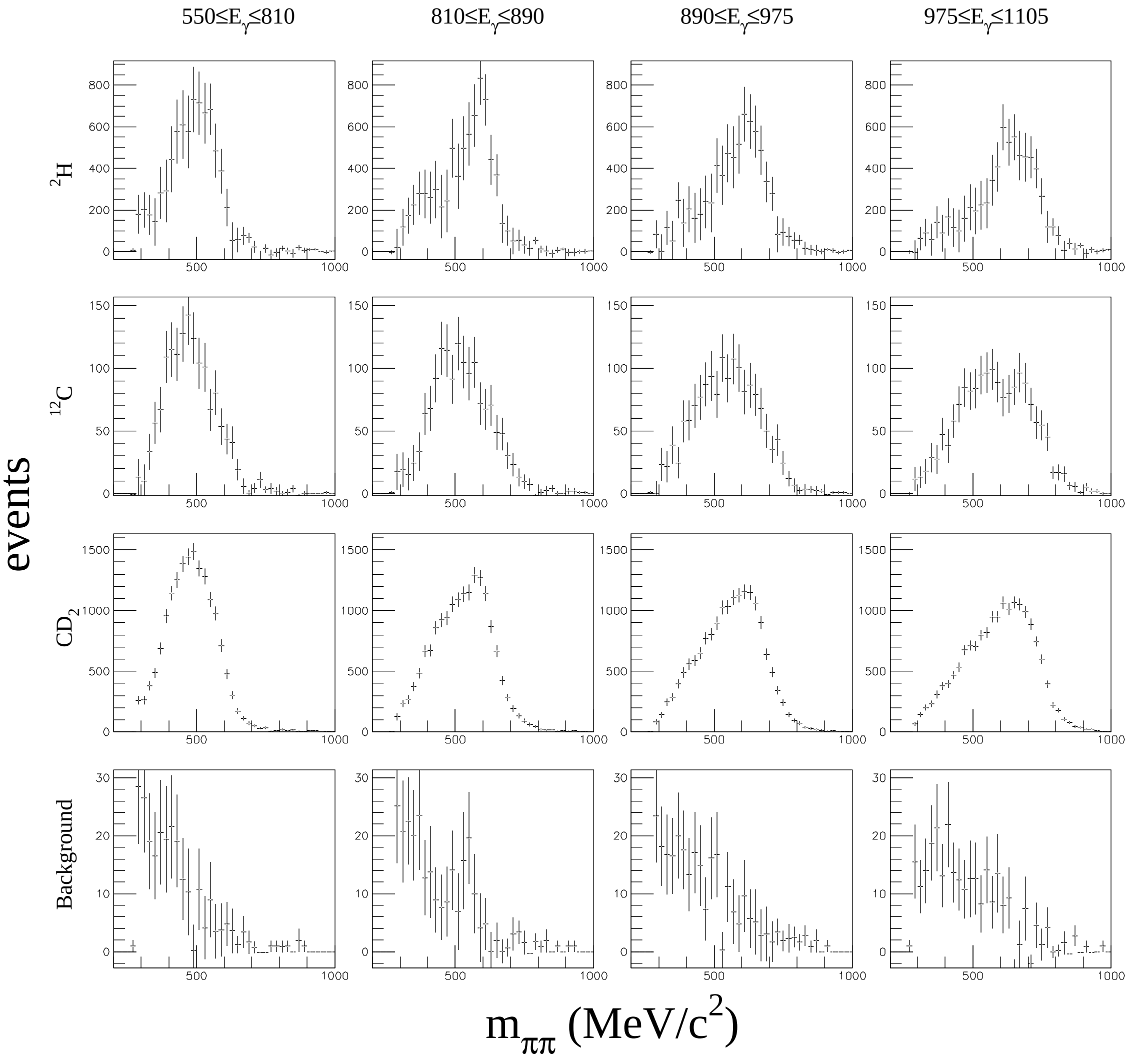

Figure C.2: Dipion invariant mass distributions.

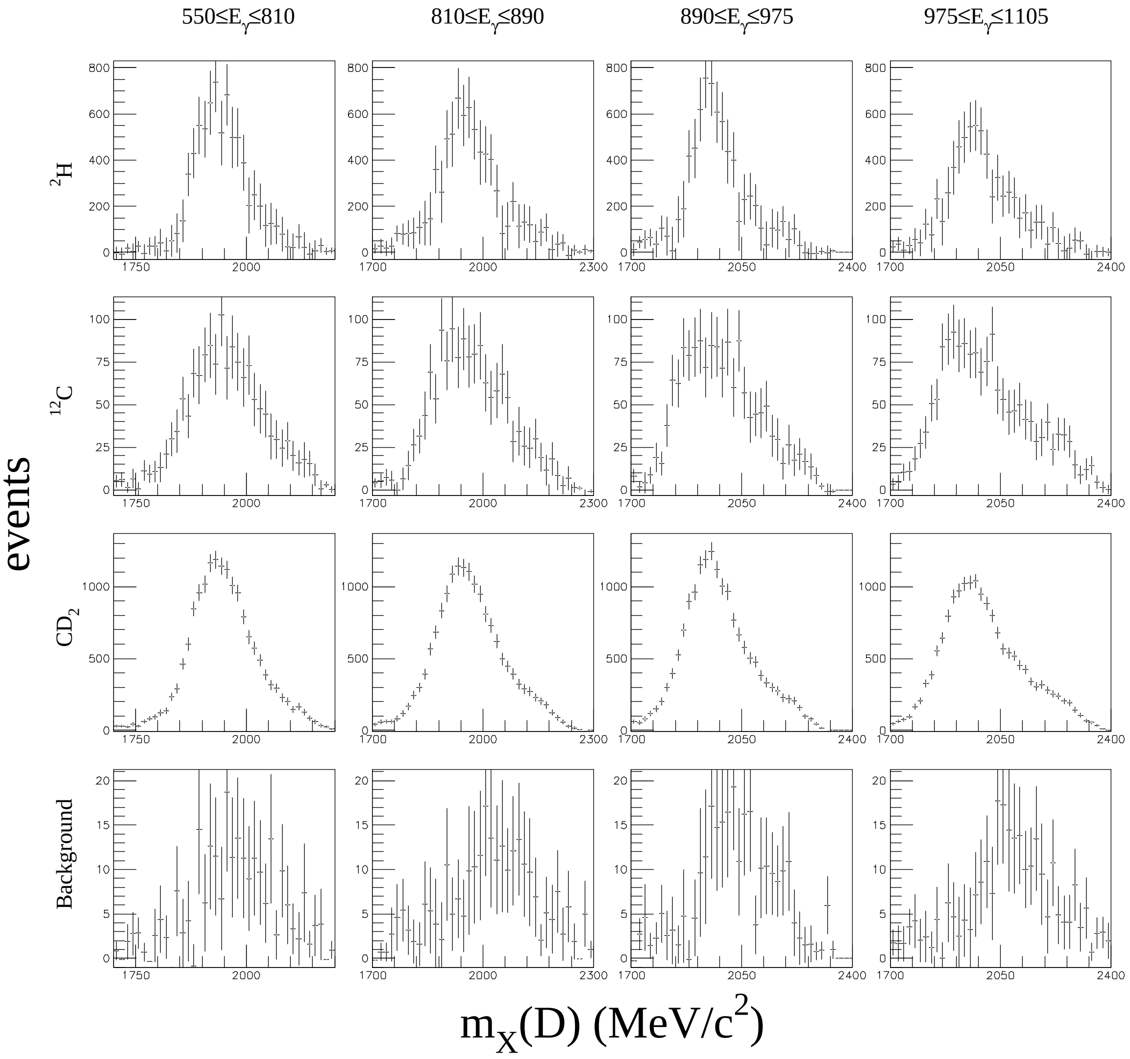

Figure C.3: Missing mass distributions. The target is assumed as the deuteron nucleus.

Appendix D

Calculation of the Dipion Decay Angle in the Helicity System

For the following discussion, it is useful to write a Lorentz boost of an arbitrary Lorentz vector x^μ in the following way:

$$x^{\mu'}(2) = \Lambda^{\mu'}_{\mu}(\vec{\beta})x^\mu(1), \quad \vec{\beta} = \frac{\vec{p_2}(1)}{p_2^0(1)},$$

where

$$\begin{array}{rclrcl} \Lambda^0_0(\vec{\beta}) & = & \gamma, & \Lambda^0_j(\vec{\beta}) & = & -\gamma\beta_j, \\ \Lambda^i_0(\vec{\beta}) & = & -\gamma\beta_i, & \Lambda^i_j(\vec{\beta}) & = & \delta_{ij} + \dfrac{\gamma^2}{\gamma+1}\beta_i\beta_j, \end{array} \quad i,j \neq 0, \quad \gamma = \frac{1}{\sqrt{1-\left|\vec{\beta}\right|^2}},$$

and $p_2^\mu(1)$ indicates a four-momentum of a particle called 2 in the rest frame of a particle called 1. Each particle is considered to travel with a different constant velocity. $\vec{\beta}$ indicates the three-velocity of the inertial frame of 2 in the inertial frame of 1. Note that this transformation preserves the direction of $\vec{\beta}$.

For any double pion photo production reaction, such as

$$\gamma(k) + N(p) \rightarrow \pi^+(k_1) + \pi^-(k_2) + N(p') \tag{D.1}$$

$$\gamma(k) + A(p_A) \rightarrow \pi^+(k_1) + \pi^-(k_2) + A(p'_A), \tag{D.2}$$

it is possible to define the helicity angles illustrated in Fig.3.6. When it is also possible to find the two pion momenta in the γ-N rest frame in case of reaction (D.1) or in the γ-A rest frame in case of reaction (D.2), the dipion momentum in the corresponding center-of-mass frame is given by the sum of the two:

$$k'^\mu(\mathrm{cm}) = k_1^\mu(\mathrm{cm}) + k_2^\mu(\mathrm{cm}).$$

One needs to Lorentz boost the four-vector of the positive pion momentum, $k_1^\mu(\mathrm{cm})$, from the center-of-mass frame to the dipion rest frame:

$$k_1^{\mu'}(\pi\pi) = \Lambda_\mu^{\mu'}(\vec{\beta})k_1^\mu(\mathrm{cm}), \quad \vec{\beta} = \frac{\vec{k}'(\mathrm{cm})}{k'^0(\mathrm{cm})}.$$

This Lorentz boost is parallel to the three-vector, $\vec{k}'(\mathrm{cm})$. This means that the direction of this three-vector does not change under the boost though $\left|\vec{k}'(\pi\pi)\right| = 0$. This common direction defines the quantization axis of the helicity system:

$$\hat{z}(\pi\pi) = \frac{\vec{k}'(\mathrm{cm})}{\left|\vec{k}'(\mathrm{cm})\right|}.$$

Hence, in effect, the polar helicity angle can be obtained from the scalar product of two three-vectors of different inertial frames:

$$\cos\theta_{qH} = \frac{\vec{k}_1(\pi\pi)\cdot\vec{k}'(\gamma N)}{\left|\vec{k}_1(\pi\pi)\right|\left|\vec{k}'(\gamma N)\right|}, \quad \cos\theta_{cH} = \frac{\vec{k}_1(\pi\pi)\cdot\vec{k}'(\gamma A)}{\left|\vec{k}_1(\pi\pi)\right|\left|\vec{k}'(\gamma A)\right|}.$$

The present quasifree Monte Carlo simulations generate events using the angle, θ_{qH}. Although the quasifree nucleons are off the mass-shell, it is still possible to find the appropriate axis from the dipion momentum in the final-state $\pi^+\pi^-N$ rest frame:

$$k'^{\mu'}(\gamma N) = \Lambda_\mu^{\mu'}(\vec{\beta})k'^\mu(A), \quad \vec{\beta} = \frac{\vec{k}(A)+\vec{p}(A)}{k^0(A)+p^0(A)} = \frac{\vec{k}'(A)+\vec{p}'(A)}{k'^0(A)+p'^0(A)}.$$

Note the A-rest frame is the laboratory frame. However, in the present experiment, the four-vector $p'^\mu(A)$ cannot be provided in most events so that the quasifree value of $k'^\mu(\gamma N)$ cannot be found from the data. This may be circumvented by assuming $\vec{p}(A) = (m_N, \vec{0})$, or the quasifree nucleon is replaced by a stationary on-shell nucleon. The resulting angle is denoted by θ'_{qH} in this thesis. The explicit calculation may be written by:

$$\cos\theta'_{qH} = \frac{\vec{k}_1(\pi\pi)\cdot\vec{k}'(\text{“}\gamma N\text{”})}{\left|\vec{k}_1(\pi\pi)\right|\left|\vec{k}'(\text{“}\gamma N\text{”})\right|},$$

with

$$k'^{\mu'}(\text{“}\gamma N\text{”}) = \Lambda_\mu^{\mu'}(\vec{\beta})k'^\mu(A), \quad \vec{\beta} = \frac{(E_\gamma, 0, 0)}{E_\gamma + m_N}$$

using the TAGX coordinate (see page 30). θ'_{qH} is found to be a good approximation to θ_{qH}.

Appendix E

Shape of the Quasifree ρ^0 Resonance

In sec.3.2.1, the differential cross section for the quasifree reaction, $\gamma A \to \rho^0 N + B$, is written by

$$d\sigma = \frac{S(\vec{p}, E)}{4(k \cdot p)} e^{at} W(\cos\theta_{qH}, \phi_{qH}) f_\rho(m) d\Phi_4(k + p_A; k_1, k_2, p', p_B)$$

where $m^2 = (k_1 + k_2)^2$ and $q(m)$ is the pion momentum in the ρ^0-rest frame. Definitions for other variables may be found in Fig.3.2 or in sec.3.2.1. By integrating this equation, one my find the following expression:

$$\frac{d\sigma}{dm^2} = \int \frac{S(\vec{p}, E)}{2^8 (2\pi)^7} \frac{e^{at_0} - e^{at_1}}{a(k \cdot p)^2} \frac{q}{m} f_\rho(m) \frac{d^3 p}{\sqrt{\vec{p}^2 + m_B^2}}. \tag{E.1}$$

This is essentially because the elementary process has the differential cross section given by

$$\frac{d\sigma}{dm^2} = \frac{1}{2^5 (2\pi)^4} \frac{e^{at_0} - e^{at_1}}{a(k \cdot p)^2} \frac{q}{m} f_\rho(m), \tag{E.2}$$

which is a result of the form,

$$d\sigma = \frac{1}{4E_\gamma m_N} e^{at} W(\cos\theta_H, \phi_H) f_\rho(m) d\Phi_3(k + p; k_1, k_2, p').$$

In Fig.E.1, $f_\rho(m)$ assumes the Jackson-type Breit-Wigner form presented by eq.(3.7). Result of eq.(E.2) is shown in Fig.3.8.

Problem arises when one uses the Gaussian shape for the resonance. The result is shown in Fig.E.2. The Gaussian shape exhibits dramatically different result than the Jackson shape. This is because the Gaussian tail almost overpowers the tail of the momentum distribution. Since the Gaussian shape resonance is not a very realistic assumption, it cannot be realistic to assume that the peak position does not dramatically change under the different photon energies.

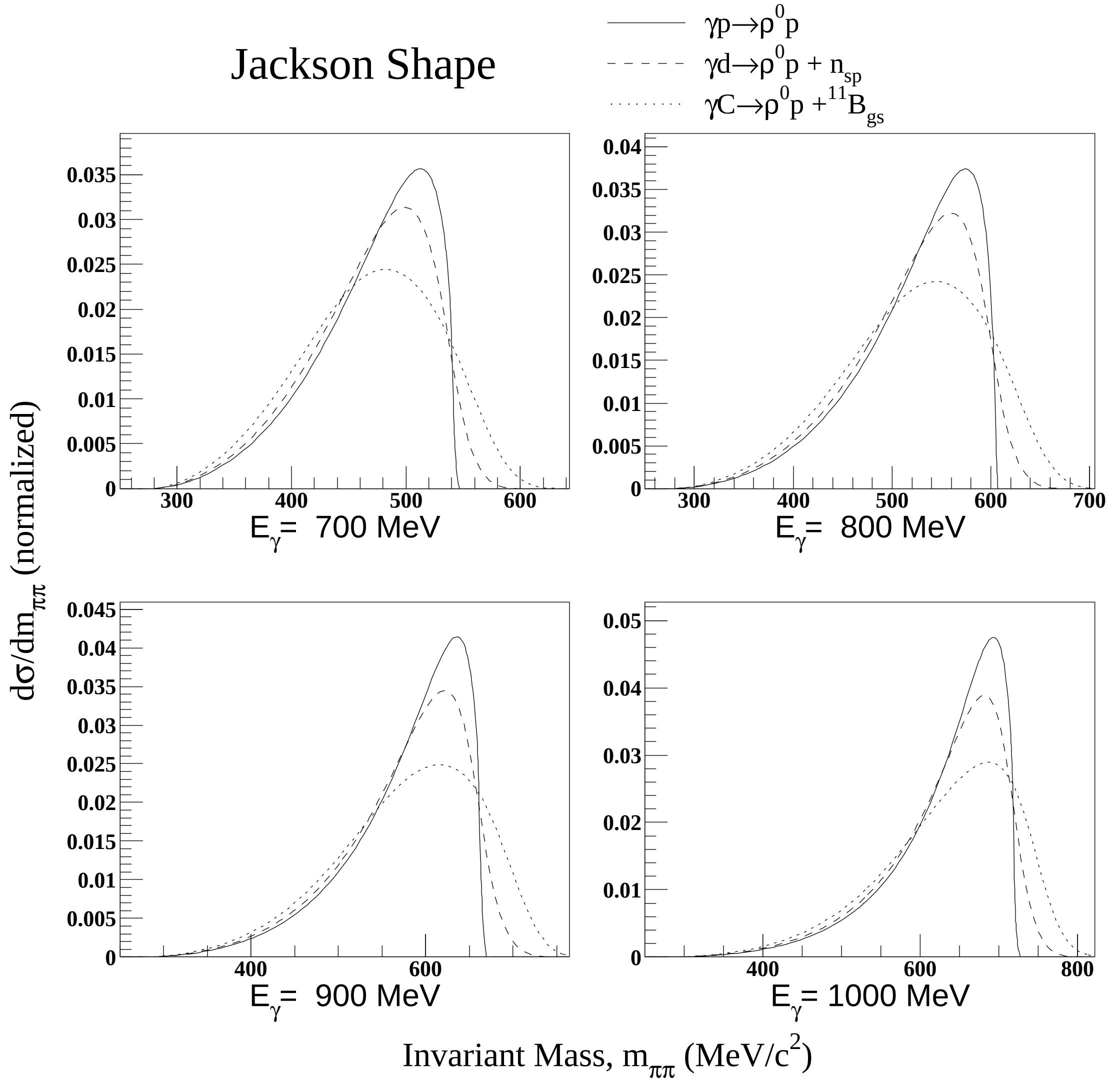

Figure E.1: Quasifree ρ^0 mass spectrum in the subthreshold region for Jackson-type resonance shape given by eq.(3.7). The solid line is the elementary process, $\gamma p \to \rho^0 p$. The dashed line is for the $\gamma d \to \rho^0 p + n_{sp}$ and the dotted line is $\gamma^{12}\mathrm{C} \to \rho^0 p + {}^{11}\mathrm{B}_{\mathrm{gs}}$.

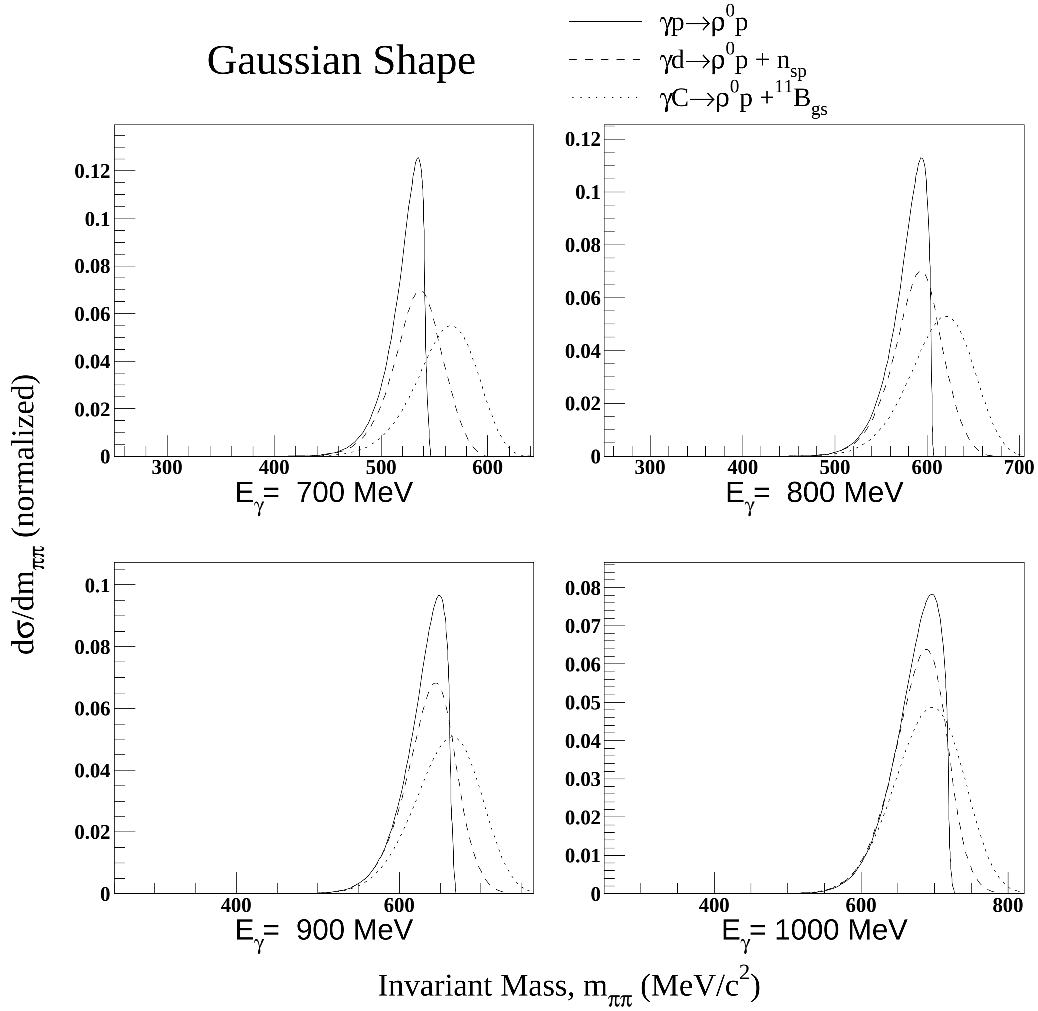

Figure E.2: Quasifree ρ^0 mass spectrum in the subthreshold region for the Gaussian shape resonance, $f_\rho(m) \propto \exp\left(-(m-m_\rho)^2/2\sigma_\rho^2\right)$, $\sigma_\rho = \Gamma_\rho/\sqrt{8\log 2}$. The solid line is the elementary process, $\gamma p \to \rho^0 p$. The dashed line is for the $\gamma d \to \rho^0 p + n_{sp}$ and the dotted line is $\gamma^{12}\mathrm{C} \to \rho^0 p + {}^{11}\mathrm{B}_{\mathrm{gs}}$.

Appendix F

The πN Scattering

F.1 Derivation of the Cross Section

Suppose a pion with momentum, $\vec{k}$ is elastically scattered by a nucleon and found to have momentum $\vec{k}'$ after the scattering. The physical quantities here would most easily be described in the rest frame of center of mass. Then an elastic scattering demands $k \equiv |\vec{k}| = |\vec{k}'|$. Generally, defining the scattering angle θ, and an unit vector normal to the scattering plane, $\hat{n}$, i.e.,

$$\cos\theta = \frac{\vec{k}\cdot\vec{k}'}{|\vec{k}||\vec{k}'|}, \qquad \hat{n} = \frac{\vec{k}\times\vec{k}'}{\left|\vec{k}\times\vec{k}'\right|},$$

one may express the scattering matrix for a spin-0 particle (π) scattered by a spin-1/2 particle (N) in terms of the spin-conserving term with f, and the spin-flip term with g, by [71],

$$\begin{aligned} M &= f(\theta)I + ig(\theta)\left(\vec{\sigma}\cdot\hat{n}\right) \\ f(\theta) &= \sum_{l=0}^{\infty}\left\{(l+1)f_{l,2l+1} + l f_{l,2l-1}\right\} P_l(\cos\theta) \\ g(\theta) &= \sum_{l=0}^{\infty}\left\{f_{l,2l+1} - f_{l,2l-1}\right\} P_l^{(1)}(\cos\theta) \end{aligned}$$

where I is the 2×2 identity matrix, $\vec{\sigma}$ the Pauli matrices, $f_{l,2j}$ the partial wave amplitude for the orbital angular momentum l with the total angular momentum $j = l \pm 1/2$. The unpolarized differential cross section is given by

$$\frac{d\bar{\sigma}}{d\Omega} = |f(\theta)|^2 + |g(\theta)|^2.$$

For the πN scattering, however, the scattering also depends on the total isospin $t = 1 \pm 1/2$. Specifically, from the isospin invariance, the concrete πN scattering matrix may be written by,

$$\begin{aligned}
M(\pi^+p\to\pi^+p) &= M(\pi^-n\to\pi^-n)=M_3\\
M(\pi^-p\to\pi^-p) &= M(\pi^+n\to\pi^+n)=\frac{1}{3}(M_3+2M_1)\\
M(\pi^-p\to\pi^0n) &= M(\pi^+n\to\pi^0p)=\frac{\sqrt{2}}{3}(M_3-M_1).
\end{aligned}$$

where M_{2t} is for the isospin-t channel. It should then be more appropriate to write $f_{2t}(\theta)$, etc. When the pion energy is low ($T_\pi \lesssim 400$ MeV), a good approximation for the πN scattering can be obtained only from the partial waves with $l=0,1$ (s and p waves). It then follows that,

$$\begin{aligned}
f_3(\theta) &\simeq f_{S31}+(2f_{P33}+f_{P31})\cos\theta\\
g_3(\theta) &\simeq (f_{P33}-f_{P31})\sin\theta\\
f_1(\theta) &\simeq f_{S11}+(2f_{P13}+f_{P11})\cos\theta\\
g_1(\theta) &\simeq (f_{P13}-f_{P11})\sin\theta.
\end{aligned}$$

Therefore, the unpolarized differential cross section for each elastic channel may be written by

$$\begin{aligned}
\frac{d\bar{\sigma}}{d\Omega}(\pi^+p\to\pi^+p) &= |f_3(\theta)|^2+|g_3(\theta)|^2\\
&= A_+\cos^2\theta+B_+\cos\theta+C_+,\\
A_+ &= 3\left\{|f_{P33}|^2+2\mathrm{Re}\left(f_{P33}f^*_{P31}\right)\right\}\\
B_+ &= 2\mathrm{Re}\left\{f_{S31}\left(f_{P33}+f_{P31}\right)^*\right\}\\
C_+ &= |f_{S31}|^2+|f_{P33}-f_{P31}|^2,\\
\frac{d\bar{\sigma}}{d\Omega}(\pi^-p\to\pi^-p) &= \frac{1}{9}\left(|f_3(\theta)+2f_1(\theta)|^2+|g_3(\theta)+2g_1(\theta)|^2\right)\\
&= \frac{1}{9}(A_-\cos^2\theta+B_-\cos\theta+C_-),\\
A_- &= 3\left[|f_{P33}+2f_{P13}|^2+2\mathrm{Re}\left\{(f_{P33}+2f_{P13})(f_{P31}+2f_{P11})^*\right\}\right]\\
B_- &= 2\mathrm{Re}\left\{(f_{S31}+2f_{S11})\left(2(f_{P33}+2f_{P13})+(f_{P31}+2f_{P11})\right)^*\right\}\\
C_- &= |f_{S31}+2f_{S11}|^2+|(f_{P33}+2f_{P13})-(f_{P31}+2f_{P11})|^2.
\end{aligned}$$

Integrating over the solid angle yields the total cross section given by,

$$\sigma(\pi^+p\to\pi^+p) = 4\pi\left(\frac{A_+}{3}+C_+\right)$$

$$
\begin{aligned}
&= 4\pi\left(|f_{S31}|^2 + 2|f_{P33}|^2 + |f_{P31}|^2\right),\\
\sigma(\pi^- p \to \pi^- p) &= \frac{4\pi}{9}\left(\frac{A_-}{3} + C_-\right)\\
&= \frac{4\pi}{9}\left(|f_{S31} + 2f_{S11}|^2 + 2|f_{P33} + 2f_{P13}|^2 + |f_{P31} + 2f_{P11}|^2\right).
\end{aligned}
$$

Similarly, the cross section for the charge exchange is given by,

$$\sigma(\pi^- p \to \pi^0 n) = \frac{8\pi}{9}\left(|f_{S31} - f_{S11}|^2 + 2|f_{P33} - f_{P13}|^2 + |f_{P31} - f_{P11}|^2\right).$$

The optical theorem yields the total cross section as follows:

$$
\begin{aligned}
\sigma_{tot}(\pi^+ p) &= \frac{4\pi}{k}\mathrm{Im} f_3(0)\\
&= \frac{4\pi}{k}\mathrm{Im}\left(f_{S31} + 2f_{P33} + f_{P31}\right),\\
\sigma_{tot}(\pi^- p) &= \frac{4\pi}{3k}\mathrm{Im}\left(f_3(0) + 2f_1(0)\right)\\
&= \frac{4\pi}{3k}\mathrm{Im}\left(f_{S31} + 2f_{S11} + 2(f_{P33} + 2f_{P13}) + f_{P31} + 2f_{P11}\right).
\end{aligned}
$$

Under the present approximation, one may find that the total cross section is the same as the total elastic cross section. This is because the partial wave amplitudes can be written in terms of the phase shifts as,

$$f_n = \frac{e^{i\delta_n}}{k}\sin\delta_n,$$

where n represents the quantum number for $(l, 2t, 2j)$. The parameterized form for the p-wave and s-wave phase shifts is available from Ref.[71]. It takes the following:

$$
\begin{aligned}
\tan\delta &= a\frac{\Gamma_0\sqrt{s_0}}{s_0 - s}\left(\frac{k}{k_0}\right)^{2l+1} + \left(\frac{k}{m_\pi}\right)^{2l+1}\left\{b + c\left(\frac{k}{m_\pi}\right)^2 + d\left(\frac{k}{m_\pi}\right)^4\right\},\\
&\left(s = \left(\sqrt{m_\pi^2 + k^2} + \sqrt{m_N^2 + k^2}\right)^2\right).
\end{aligned}
$$

There, the six parameters, a, b, c, d, k_0, Γ_0, and s_0, are tabulated with respect to n.

F.2 Generation of the Scattering Angle

As shown in sec.F.1, the probability distribution function for the scattering angle θ is written by,

$$f(\zeta) = a\zeta^2 + b\zeta + c, \quad (\zeta \equiv \cos\theta).$$

Let ξ be an uniform random number with $\xi \in [0,1]$ and ζ be a random variable following a probability distribution function, $f(\zeta)$. In general, these random variables are related via,

$$\xi = \int_{-\infty}^{\zeta} f(\zeta')d\zeta'.$$

Therefore, finding θ reduces to solving a cubic equation,

$$F(\zeta) \equiv \frac{a}{3}\zeta^3 + \frac{b}{2}\zeta^2 + c\zeta + d = \xi \quad \text{with} \quad \left\{ \begin{array}{rcl} F(-1) & = & 0 \\ F(1) & = & 1 \\ f(\zeta) & \geq & 0. \end{array} \right.$$

Writing $\zeta = z + \zeta_0$ simplifies the cubic equation to $z^3 - 3Pz - 2Q = 0$, where

$$\begin{aligned} \zeta_0 &= -\frac{b}{2a} \\ P &= -\frac{f(\zeta_0)}{a} = \zeta_0^2 - \frac{c}{a} \\ Q &= \frac{3}{2a}\left(\xi - F(\zeta_0)\right). \end{aligned}$$

Furthermore, writing $z = \omega + \dfrac{P}{\omega}$ yields $\omega^6 - 2Q\omega^3 + P^3 = 0$, which has solutions,

$$\omega^3 = Q \pm \sqrt{Q^2 - P^3}.$$

When only real solutions are interested, the following expression is then found:

$$z = \left\{ \begin{array}{ll} \sqrt[3]{Q + \sqrt{D}} + \sqrt[3]{Q - \sqrt{D}}, & (D > 0) \\ 2\sqrt{P}\cos\left(\dfrac{\chi + 2n\pi}{3}\right), & (D \leq 0) \end{array} \right. ,$$

where

$$D = Q^2 - P^3, \quad \cos\chi = \frac{Q}{\sqrt{P^3}}, \quad n = 0, \pm 1, \pm 2, \ldots.$$

In other words, when $D > 0$, there is only one real solution whereas there are three real solutions for $D \leq 0$. In the present case where only one solution uniquely satisfies $|\zeta| \leq 1$, one may choose the appropriate integer, n by restricting $0 \leq \chi \leq \pi$. Then,

$$n = \left\{ \begin{array}{lll} 3m+1, & \text{for} & a > 0, \quad \zeta_0 \geq 1 \\ 3m, & \text{for} & a > 0, \quad \zeta_0 \leq -1 \\ 3m-1, & \text{for} & a < 0 \end{array} \right. \quad \left(\begin{array}{l} \text{only if } |\zeta| \leq 1, \ f(\zeta) \geq 0, \\ 0 \leq \chi \leq \pi \end{array} \right).$$

Thus, when a random number $\xi \in [0,1]$ is generated, $\cos\theta = F^{-1}(\xi)$ is given.

Appendix G

Proton Wave Function in ^{11}B

Elastic scattering in the center of mass assumes the magnitude of initial and final proton momenta, $\vec{p}_r''$, $\vec{p}_r'$ are same:

$$|\vec{p}_r''| = |\vec{p}_r'| \equiv p_r.$$

Defining the coordinate system such that $\hat{z}//\vec{p}_r'$ and $\hat{y}//(\vec{p}_r' \times \vec{p}_r'')$, one may write,

$$\vec{q}_r \cdot \vec{r} = p_r b \sin\theta \cos\phi + p_r z(\cos\theta - 1),$$

where θ and ϕ are polar and azimuthal angles of $\vec{p}_r''$ and $b = \sqrt{x^2 + y^2}$. Integrating with respect to ϕ, eq.(3.18) is given by

$$\tilde{D}(\vec{p}) = 2\pi \int_0^\infty \int_{-\infty}^\infty \mathrm{e}^{i(p_r z(\cos\theta - 1) - \mathrm{Re}\chi)} \mathrm{e}^{\mathrm{Im}\chi} J_0(p_r b \sin\theta) \rho(\sqrt{b^2 + z^2}) dz b db,$$

where $J_0(x)$ is the zeroth order Bessel function which is provided by the CERN library and

$$\chi(\vec{r}) = \frac{m_p}{p_r} \int_0^\infty U(\vec{r} + \hat{p}_r' l) dl.$$

The double integration is performed with the Simpson's integral formula. The optical potential assumes the following form:

$$\begin{aligned} U(r) &= V_C(r) - V_0 f(r; R, a) - iW_0 f(r; R', a') \\ &\quad + (V_{so} + iW_{so}) \left(\frac{\hbar}{m_\pi c}\right)^2 (\vec{\sigma} \cdot \vec{l}) \frac{1}{r} \frac{d}{dr} f(r; R_{so}, a_{so}) \end{aligned}$$

where $V_C(r)$ is the electric potential due to an uniform charge density with total charge of Ze:

$$V_C(r) = \begin{cases} \dfrac{Ze^2}{4\pi\epsilon_0} \dfrac{(3 - r/R_C)^2}{2R_C} & (r \leq R_C) \\ \dfrac{Ze^2}{4\pi\epsilon_0} \dfrac{1}{r} & (r \geq R_C) \end{cases},$$

the function $f(r;R,a)$ has the Woods-Saxon form,

$$f(r;R,a)=\frac{1}{1+\exp\left(\frac{r-R}{a}\right)},$$

and $\vec{\sigma}$ and $\vec{l}$ are the spin and the orbital angular momentum of the proton. In general, the potential parameters, $R_C, V_0, W_0, V_{so}, W_{so}, R, R', R_{so}, a, a', a_{so}$ vary with the proton energy. Values are taken from Ref.[72]. Coulomb potential integration,

$$\chi_C(\vec{r})=\frac{m_p}{p_r}\int_0^{\infty} V_C(\vec{r}+\hat{p}_r' l)dl$$

is divergent. It is regulated with $\chi_C(\vec{r})-\chi_C(\vec{r}=0)$. Analytical form is easily found for $\chi_C(\vec{r})$. For example, when $b \leq R_C \leq r$, $z \leq 0$,

$$\chi_C(\vec{r})=\frac{m_p}{p_r}\frac{Ze^2}{4\pi\epsilon_0}\left[\frac{19}{3}\left(\frac{z_C}{R_C}-1\right)+\frac{2b^2 z_C}{3R_C^3}-\frac{3b^2}{R_C^2}\log\left(\frac{R_C+z_C}{b}\right)+\log\left(\frac{2R_C(r-z)}{(R_C+z_C)^2}\right)\right],$$

with $z_C=\sqrt{R_C-b^2}$. Simpson's integral formula is used for the integration of Woods-Saxon functions.